# Isolating Effects of Water Table Dynamics, Terrain, and Soil Moisture Heterogeneity on the Atmospheric Boundary Layer Using Coupled Models

By

Jehan Fouad Rihani

A dissertation submitted in partial satisfaction of the
requirements for the degree of
Doctor of Philosophy

in

Engineering - Civil and Environmental Engineering

in the

Graduate Division

of the

University of California, Berkeley

Committee in charge:

Professor Fotini Katopodes Chow, Chair
Professor Yoram Rubin
Professor Dennis Baldocchi
Professor Reed Maxwell

Fall 2010

# Abstract

Isolating Effects of Water Table Dynamics, Terrain, and Soil Moisture Heterogeneity on the Atmospheric Boundary Layer Using Coupled Models

by

Jehan Fouad Rihani

Doctor of Philosophy in Engineering - Civil and Environmental Engineering

University of California, Berkeley

Previous observational and modeling studies have demonstrated the sensitivity of atmospheric processes to land surface and subsurface conditions. The extent of the connection between these processes, however, is not yet fully understood. A sufficient understanding is needed of the circumstances under which these coupled processes might play a more significant role and when they might be simplified into the decoupled systems so frequently modeled in practice. This work focuses on the effects of terrain and soil moisture heterogeneity in changing water table depth and energy fluxes at the land surface, and how this might impact the development and structure of the atmospheric boundary layer. A three-dimensional, variably saturated groundwater model coupled to a three dimensional mesoscale atmospheric model (PF.ARPS) is used here to study the two-way feedback between the subsurface, land-surface, and atmosphere for both idealized cases and a real watershed. This is done by addressing the following key questions: How do terrain, soil moisture heterogeneity, and subsurface properties affect the planetary boundary layer? What are the effects of water table depth on land surface fluxes and boundary layer development and depth? What times of the diurnal cycle and which locations within a watershed demonstrate stronger feedbacks between the subsurface and the atmosphere? These questions are first addressed for idealized simulations designed to illustrate subsurface-surface feedbacks on one hand, and land-atmosphere feedbacks on the other hand. The coupled hydrologic model is then used to simulate real conditions over the Little Washita watershed in Oklahoma with the goal of addressing the above questions for a real watershed, and exploring the two-way feedback between the atmospheric boundary layer and the water table. The coupled simulations are compared to non-coupled atmospheric simulations initialized with simplified and realistic soil moisture profiles. Effects of a storm system on the coupling between subsurface, land surface, and atmosphere are also demonstrated. Results demonstrate the connection between water table dynamics and land surface energy fluxes. This connection has a clear signature on the structure of the atmospheric boundary layer and becomes most significant within transitional zones of a watershed which lie between fully saturated regions and dry regions with deep water table. The effects of realistic soil moisture forcing which reflects subsurface conditions on

boundary layer development can be equal to or greater than the effects from heterogeneous land-cover (soil and vegetation types), thus pointing to the need for improved soil moisture representations in current mesoscale atmospheric models.

# Dedication

To my parents for your endless support, patience, and believing in me.

To the rest of my family for your constant encouragement. Steve, Yolanda, and Veronica, for always being there. Jomana, Samir, and Reem for being my second home away from home, you made it all bearable, thank you.

To my host family, Jeff and Karen, for all your help especially during my first few weeks at Berkeley.

To Reed, Jen, and Cole for always thinking of me.

A special dedication for the friendship of Andrew and Madeline, and the memory of Linda Tompson. I will never forget your support and hospitality.

My deepest appreciation and love to my husband for pushing me further than I ever thought I could reach. I couldn't have made it this far without you.

# Acknowledgments

My deepest thanks go to my advisor, Prof. Tina Chow, for believing in me at a time when very few people did. Your investment, guidance, and faith in my ability to succeed have always meant a great deal to me and are the reason I am able to complete my degree.

I also wish to thank my co-advisor, Prof. Reed Maxwell, without whom I wouldn't be graduating today. I learned so much from you and will never forget your help and guidance during very difficult times.

I would like to acknowledge my committee members for their thorough review and invaluable feedback which elevated the quality of this work.

My personal thanks to Prof. Yoram Rubin for continuously pushing me to work harder and take my work to the next level.

I also wish to thank my department, especially Prof. David Sedlak and Prof. Mark Stacey, for not giving up on me when I was in between projects. You gave me the extra support and help I needed to get through those difficult times.

To our Graduate student adviser, Shelley Okimoto, for endless hours of listening, valuable advice, and help in getting through all the paperwork it takes to get a PhD.

I was also supported by a Pre-doctoral Fulbright Award (2003–05) and wish to thank the Fulbright Foundation for providing this great opportunity.

# Table of Contents

# List of Figures

# List of Tables

# Nomenclature

## Roman Symbols

$a$: Amplitude of sinusoid terrain [m]
$c_p$: Specific heat of dry air [J/kg.K$^2$]
$c_s$: Full acoustic wave speed [m/s]
$C_p$: Specific heat of dry air at constant pressure [J/kgK]
$C_{soilc}$: Transfer coefficient between the canopy air and underlying ground
E: Sum of evaporation from canopy and ground [kg/m$^2$s]
$E_c$: Evaporation from canopy [kg/m$^2$s]
$E_f^{pot}$: Potential evaporation from wet foliage [kg/m$^2$s]
$E_g$: Evaporation from ground [kg/m$^2$s]
$E_w$: Evaporation from wet foliage [kg/m$^2$s]
$E_{tr}$: Transpiration [kg/m$^2$s]
ET: Evapotranspiration [mm/d]
$f$ and $\tilde{f}$ : Coriolis parameters
$F_{\Delta,\mu}$ : Fraction of solar radiation absorbed by canopy [-]
$g$: Acceleration due to gravity [m/s$^2$]
G: Ground heat flux [W/m$^2$]
$h$: Height of terrain above reference level $h_o$ [m]
H: Average PBL depth [m]
$H_c$: Canopy sensible heat flux [W/m$^2$]
$H_g$: Ground sensible heat flux [W/m$^2$]
$J_1$, $J_2$, $J_3$, and $J_4$: Transformation Jacobians
$k$: Saturated hydraulic conductivity [m/s]
$k_r$: Relative (unsaturated) permeability [-]
$K_{sat}$: Saturated hydraulic conductivity [m/d]
$L$: Wavelength of sinusoid terrain [m]
L: Length Scale (e.g. horizontal domain length) [m]
$L_a^{\downarrow}$: Incoming atmospheric long wave radiation [W/m$^2$]
$L^{\uparrow}$ : Outgoing long wave radiation [W/m$^2$]
$L_d$: Dry fraction of foliage surface [-]
LE or LH: Latent heat flux [W/m$^2$]
LS: Land Surface Elevation [m]
$L_{SAI}$: Stem plus leaf area index [m$^2$/m$^2$]
$L_v$: Latent heat of evaporation [J/kg]
$\tilde{L}_w$ : Wetted fraction of the canopy [-]
$m$: Map projection factor
$m'$: Thickness of an interface separating the surface and subsurface [m]
n: Van Genuchten exponent [-]
$n$: Manning's coefficient [h/m$^{1/3}$]
$p$: Total pressure [Pa]

P: Precipitation [mm/day]
$q$: Water flux [m/s]
$q_a$ : Specific humidity of air at reference height $z_q$ [kg/kg]
$q_c$: Cloud water mixing ratio [kg/kg]
$q_e$: Surface-subsurface water exchange rate [m/s]
$q_g$: Specific humidity of air at the ground surface [kg/kg]
$q_{li}$: Total liquid and ice water mixing ratio [kg/kg]
$q_r$: is the source/sink rate (i.e. rainfall/evaporation) [m/s]
$q_s$: Source/sink term in Richard's equation [$s^{-1}$]
$q_{soil}$: Soil moisture at the land surface [-]
$q_{so}$: Initial soil moisture [-]
$q_v$: Water vapor mixing ratio [kg/kg]
$r_b$: Leaf boundary resistance [s/m]
$r_d$: Aerodynamic resistance of evaporation between the atmosphere and reference height $z_q$ [s/m]
$r_s$: Stomatal resistance [s/m]
R: Surface runoff [mm/day]
$R_d$: Gas constant for dry air [J/kgK]
$R_n$: Net radiation [$W/m^2$]
$R_v$: Gas constant for water vapor [J/kgK]
SH: Sensible heat flux [$W/m^2$]
$S_n$: Net solar radiation absorbed by the land surface [$W/m^2$]
$S_{n,c}$: Net solar radiation absorbed by vegetation [$W/m^2$]
$S_{n,g}$: Net solar radiation adsorbed by ground [$W/m^2$]
$S_q$ : Moisture source
$S_r$ or $S_{res}$: Residual saturation [-]
$S_{sub}$: Subsurface storage [mm]
$S_{surf}$: Surface storage [mm]
$S_s$: Specific storage [$m^{-1}$]
$S_{sat}$: Saturation at saturated conditions [-]
$S_w$: Relative saturation [-]
$S^{\downarrow}_{\Lambda,\mu}$ : Component of the incident solar radiation; visible (beam and diffuse) and near-infrared (beam and diffuse) [$W/m^2$]
$t$: Time (s)
T: Temperature [K]
$T_{adv}$: horizontal advection timescale [s]
$T_{af}$: Temperature in the canopy space [K]
$T_{air}$: Ambient Temperature at the land surface [K]
$T_c$: Leaf temperature [K]
$T_g$: Ground surface temperature [K]
$T_{diff}$: vertical diffusion timescale [s]
TKE: Turbulent Kinetic Energy [$m^2/s^2$]
$T_s$ or $T_{soil}$: top soil layer temperature [K]
$u$: Horizontal wind speed in the x-direction [m/s]
$u_{af}$ : Magnitude of the wind velocity incident on the leaves [-]
U: Average horizontal wind speed within the PBL [m/s]
$U^c$: Contravariant velocity component in the x-direction [m/s]

$v$: Horizontal wind speed in the y-direction [m/s]
$\vec{v}$ : Depth averaged surface water velocity [m/s]
$V^c$: Contravariant velocity component in the y-direction [m/s]
$w$: Vertical wind speed in the z-direction [m/s]
$W^c$: Contravariant velocity component in the z-direction [m/s]
$x,y$: Horizontal Cartesian coordinates
$x_\xi$ : Grid stretching factor in the $x$ direction
$y_\eta$ : Grid stretching factor in the $y$ direction
$z$: Vertical Cartesian coordinate

**Greek Symbols**

α: Van Genuchten soil parameter [$m^{-1}$]
$\overline{\alpha}_{\Delta,\mu}$ : Weighted surface Albedo over the grid [-]
δ: Step function (δ=1 for positive arguments and δ=0 for zero and negative arguments)
$\theta$: Potential temperature [K]
λ: Soil thermal conductivity [W/mK]
$\nu_T$: Average vertical eddy viscosity within the PBL[$m^2/s$]
$\xi,\eta,\zeta$: Mapped curvilinear coordinates
$\rho$: Total density [$kg/m^3$]
$\overline{\rho}$ : Base-state density [$kg/m^3$]
$\rho_a$: Intrinsic density of air [$kg/m^3$]
$\sigma_f$ : Vegetation fraction [-]
$\phi$: Effective soil porosity [-]
$\psi_p$: Soil pressure head [m]
$\psi_s$: Ponding depth of water at the land surface [m]
Ω: Angular rotation of the earth

**Acronyms**

ABL: Atmospheric Boundary Layer
ARPS: The Advanced Regional Prediction System
ARS: Agricultural Research Service
CAPS: Center for Analysis and Prediction of Storms
CCM1: Community Climate Model
CLM: Common Land Model
ET: Evapotranspiration
GW: Groundwater
LBC: Lateral Boundary Conditions
LES: Large Eddy Simulation
LSM: Land Surface Model
LW: Little Washita
ML: Mixed Layer

NARR: North American Regional Reanalysis
NCAR: National Center for Atmospheric Research
NLDAS: North American Land Data Assimilation System
NSIDC: National Snow and Ice Data Center
PBL: Planetary Boundary Layer
PBLD: Planetary Boundary Layer Depth
PF: ParFlow
PF.ARPS: ParFlow coupled to the Advanced Regional Prediction System (ARPS)
PF.CLM: ParFlow coupled to the Common Land Model (CLM)
RL: Residual Layer
SA: Semi-Arid
SBL: Stable Boundary Layer
SM: Soil Moisture
SMEX03: Soil Moisture Experiment 2003
SW: Surface Water
USGS: United States Geological Survey
USDA: United States Department of Agriculture
VG: Van Genuchten
WT: Water Table
WTD: Water Table Depth

# Chapter 1

# Introduction

Previous observational and modeling studies have demonstrated the sensitivity of atmospheric processes to land surface and subsurface conditions. The extent of the connection between these processes, however, is not yet fully understood. A sufficient understanding is needed of the circumstances under which these coupled processes might play a more significant role and when they might be simplified into the decoupled systems so frequently modeled in practice. In recent work, a three-dimensional, variably saturated groundwater model was coupled to a three dimensional mesoscale atmospheric model (Maxwell et al, 2007). The coupled model is a valuable research tool and is used here to study subsurface-land-surface-atmosphere two-way feedbacks. This work focuses on the effects of terrain, subsurface formation, land cover, and climate in changing water table dynamics, energy fluxes at the land surface, and how this might impact the development and structure of the atmospheric boundary layer.

## 1.1 Background

### 1.1.1 The planetary boundary layer

The planetary or atmospheric boundary layer (PBL or ABL) is the region of the atmosphere which is directly forced by land-surface fluxes on a short hourly time scale. It is the region in which pollution emitted on the earth's surface is dispersed, and it is the region in which weather events take place (Stull, 1988). There is therefore much interest in predicting and understanding boundary layer development for weather and air quality prediction. The PBL also represents the interface which couples land processes to global circulations, and thus has impact on the global scale and hence in climate studies.

Over land surfaces, the boundary layer can have a specific structure. A good description of this structure over high pressure regions and how it develops and changes with the diurnal cycle is provided by Stull (1988) (adapted in Figure 1.1). Three major components with different scales and flow dynamics can be observed within the PBL during a diurnal cycle: a turbulent mixed layer (ML), a residual layer (RL), and a nocturnal-stable boundary layer (SBL). The mixed layer is characterized by convectively driven turbulence from sources such as heat transfer from a warm ground surface and radiative cooling from cloud layers. Uprising thermals accompanied by entrainment of less turbulent air from above cause the boundary layer depth to grow, reaching a maximum in the late afternoon. During the evening, a cooling land surface creates a stable boundary layer, directly above the surface, characterized by inhibited mixing, intermittent turbulence, and very limited vertical flows. Above the nocturnal stable boundary layer lies the remainder of the well-mixed daytime convective boundary layer. This residual layer can be neutrally or slightly stratified with inhibited turbulence, and relatively equal mixing in all directions.

In any of these cases, land surface forcing plays a significant role in driving the development and structure of the PBL. Changes in land surface properties can affect the transfer of moisture and heat between the land surface and the atmosphere. To follow is a description of how land surface processes are usually implemented within atmospheric models as Land Surface Models (LSMs), and how this representation can be enhanced by the use of coupled hydrologic modeling.

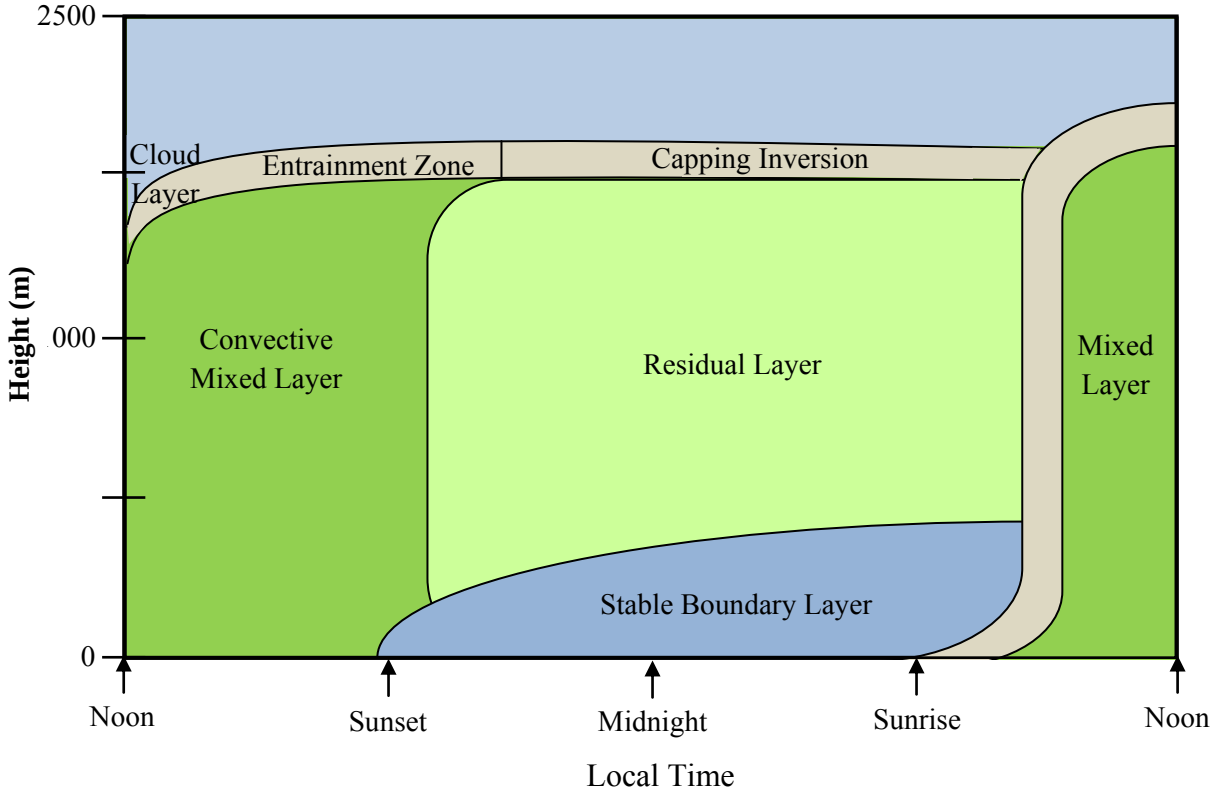


Figure 1.1: The diurnal evolution of the atmospheric boundary layer based on Stull (1988).

### 1.1.2 Land Surface Models

Land surface models (LSMs) are used to provide atmospheric and global circulation models with lower boundary fluxes of heat and moisture. LSMs have evolved in sophistication from the traditional bucket model (Manabe, 1969) into energy based LSMs that describe the root zone and vegetation in great detail. The electrical analogue is one of the most general approaches used in land-surface modeling. This approach assumes that the difference in potential of a quantity (e.g. vapor pressure or temperature) drives the rate of exchange between the land surface and the atmosphere. This rate of exchange now depends on resistances controlled by the local properties of soil, vegetation, and the surrounding atmosphere (see review by Overgaard et al, 2006). Models using this technique ranged from the Penman approach (1948), which assumes only one

atmospheric resistance, to more complex models which include surface resistances of soil and land cover (e.g. Monteith, 1965; Avissar and Pielke, 1989; Shuttleworth and Wallace, 1985; Gu et al., 1999; and Baldocchi and Harley, 1995). These include Soil-Vegetation-Atmosphere Transfer (SVAT) models which were developed to describe land surface exchanges with the atmosphere and focus on micro-scale plant processes such as photosynthesis, transpiration and stomatal conductance (Cowan, 1968; Waggoner et al. 1969; Shawcroft et al., 1974).

In Penman's approach the atmospheric resistance expresses the capability of the air to transport quantities away from the land surface. A higher resistance occurs in stable conditions (e.g. within a stable nocturnal boundary layer when vertical motions are dampened), as opposed to a lower resistance in unstable conditions (e.g. within a convective mixed boundary layer when rising thermals enhance vertical transport). Monteith (1965) added the land-surface controls of soil and vegetation to the Penman approach and developed what is called the Penman-Monteith approach. Models based on the Penman-Monteith approach generally do not distinguish between soil evaporation and transpiration and are thus considered one-layered models which treat the land surface as a single homogeneous unit (Overgaard et al, 2006). Consequently, patch-type LSMs were developed (Avissar and Pielke, 1989) in which the one-layered Penman Monteith approach is applied separately to different parts (patches) within a grid cell. Each part can be defined with different bare soil or vegetation properties; however, the patches in such models are generally not interactive. This led to the development of two-layered (Shuttleworth and Wallace, 1985) and then multi-layered LSMs (Gu et al., 1999; and Baldocchi and Harley, 1995) which assume that heat and moisture enter or leave the land surface through one or more canopy layers directly above it. The component fluxes are allowed to interact within the canopy layer(s) before being introduced into the atmosphere. In the multi-layer approach, canopy scale fluxes are obtained by integration of exchange rates calculated within each canopy layer (Overgaard et al, 2006).

A second generation of more physically-based LSMs were developed starting with the work of Deardorff (1978), who merged previous efforts (Bhumralkar, 1975; Blackadar, 1976; Legg and Long, 1975; Thom, 1972; and Monteith and Szeicz, 1962) and introduced a method for simulating soil temperature and moisture in two layers. This multiple soil layers approach was continued by Dickinson et al. (1986 and 1993) and Sellers et al. (1986) who built on Deardorff's work and developed LSMs (the Biosphere Atmosphere Transfer Scheme (BATS) and the Simple Biosphere Model (SiB), respectively) which form the basis of newer innovations in land surface modeling (e.g. the Common Land Model (Dai et al., 2003)).

Soil layering as well canopy layering is used to make LSMs more realistic by representing vertical gradients in a physically-based manner. Despite the increase in complexity and detailed representation of vegetation and the root zone, LSMs remain for the most part one-dimensional column models which ignore lateral water flow at the land surface and within the top soil layers. Processes effecting soil moisture variations such as shallow groundwater, runoff, overland flow, and subsurface lateral flow, are normally neglected.

### 1.1.3 Integrated Hydrologic Models (Coupled Surface Water-Groundwater Models)

Groundwater models allow advanced representations of subsurface heterogeneity and three-dimensional, variably saturated flow, thus accounting for both vertical and lateral transport of water in the subsurface. The traditional use of simplified boundary conditions at the land surface, however, has triggered the development of a new generation of integrated models, following the blueprint of Freeze and Harlan (1969), which take into account processes such as overland flow, runoff, soil heating and root-zone uptake (e.g. VanderKwaak and Loague, 2001; Morita and Yen, 2002; Panday and Huyakorn, 2004; Kollet and Maxwell, 2006; Qu and Duffy, 2007; Kollet and Maxwell, 2008). Surface runoff in this new generation of models is usually described using the shallow water equations in one- or two-dimensions, which are coupled to the three dimensional, variably saturated Richards equation (Maxwell, 2009; Ebel et al., 2009; Sulis et al., 2010). Most integrated hydrologic models use a first-order exchange coefficient coupling approach at the land surface (e.g. VanderKwaak, 1999; Panday and Huyakorn, 2004; Therrien et al., 2005; Ebel et al, 2009). A more physically-based approach is the continuity of pressure and flux boundary conditions at the land surface (e.g. Kollet and Maxwell, 2006; Maxwell and Kollet, 2008b; Dawson, 2008). PF.CLM is an integrated SW-GW code which uses the latter approach while taking into account vertical and lateral flow at the surface and subsurface (Maxwell and Kollet, 2008b). This is why PF.CLM is used in this work (chapter 2) to investigate surface-subsurface interactions in an idealized setting.

Although these recently developed integrated hydrological models describe interactions between surface and subsurface flows in great detail, they often have a simplistic representation of atmospheric processes which in many cases are introduced into the model as prescribed atmospheric conditions (Overgaard et al, 2006). Thus the groundwater is allowed to evolve in response to varied atmospheric forcing (including spatially variable precipitation, wind speed, etc), but this representation does not allow for the two-way feedback between the land surface and the atmosphere (e.g. Panday and Huyakorn, 2004; Graham and Butts, 2006).

### 1.1.4 Disconnected Models

Simplifications in atmospheric and hydrologic models described here are based on computational and practical requirements (Overgaard et al., 2006; Furman, 2008). Most field sites do not have a full set of field measurements and observations required for a fully coupled atmospheric-land surface-subsurface model. Furthermore, the computational costs of performing such fully coupled simulations are only verified in cases where such interactions and two way feedbacks are significant. Nonetheless, this implies there is still a gap in our models which describe different, yet interactive, parts of the terrestrial hydrologic cycle. Chapters 2 and 3 review the advancements made in coupled surface water-groundwater models and atmospheric-land surface models, respectively. Despite these advancements, there is still a need for enhancing our models to represent proper dynamic boundary conditions between surface, subsurface, and lower atmosphere, with the end goal of improving our understanding of cases where these feedbacks become most important.

This gap was addressed by Maxwell et al (2007) who designed the fully coupled subsurface-surface-atmospheric code PF.ARPS. This state-of-the-art code is unique in that it allows for vertical and lateral water flow both at the land surface and subsurface. Using this code to simulate the Little Washita watershed in Oklahoma, Maxwell et al (2007) were able to detect a close relationship between water table depth and atmospheric boundary layer depth. In this work, PF.ARPS is used to further explore this two-way connection between groundwater and the atmosphere by using lateral boundary forcing in the atmosphere (as explained in chapter 4).

## 1.2 Motivation and Outline

This work focuses on exploring the two-way feedback between the subsurface, land-surface, and atmosphere via fully coupled simulations of both idealized cases and a real watershed. The main motivation is the importance of land surface processes in controlling the transfer of water and energy between the lower atmosphere and the subsurface. In order to study this connection through the land surface, a coupled hydrologic model is used to address the following questions:

1. How do terrain, soil moisture heterogeneity, and subsurface properties affect the planetary boundary layer?

2. What are the effects of water table depth on land surface fluxes and boundary layer development and depth?

3. How do subsurface properties affect water table depth and boundary layer depth?

4. What times of the diurnal cycle show stronger feedbacks between the subsurface and the atmosphere?

These questions are first addressed for idealized simulations (described in chapters two and three) designed to illustrate land-atmosphere feedbacks and effects of surface and subsurface properties on atmospheric boundary layer development. The coupled hydrologic model (PF.ARPS) is then used to simulate real conditions over the Little Washita watershed in Oklahoma with the goal of addressing the above questions for a real watershed, and exploring the two-way feedback between the atmospheric boundary layer and the water table. The coupled hydrologic model used consists of atmospheric (the Advanced Regional Prediction System, ARPS), groundwater (ParFlow), and land surface (the Common Land Model, CLM) components which are coupled together in two different configurations: PF.ARPS and PF.CLM. PF.CLM consists of the groundwater model ParFlow coupled to the land surface model CLM and is used in chapter 2 to investigate subsurface and land surface feedbacks. PF.ARPS consists of the groundwater model ParFlow coupled to the atmospheric model ARPS and is used in chapter 4 to investigate coupled subsurface-surface-atmospheric processes for a real watershed.

Chapter 2 presents a set of idealized coupled simulations designed to isolate and characterize effects of terrain, land cover, subsurface layering, and climate on water table dynamics and land surface energy fluxes. Sinusoidal and hill-slope land forms are used to represent idealized valleys with various land properties.

In chapter three, results from the surface water-groundwater simulations of chapter two are used to obtain soil moisture fields at the land surface. These offline soil moisture profiles are used here to initialize atmospheric idealized simulations using the mesoscale atmospheric code ARPS. Effects of soil moisture heterogeneity, terrain, and water table dynamics on atmospheric boundary layer development and depth are demonstrated. Comparisons against atmospheric simulations initialized with uniform soil moisture profiles are conducted and the effects of using more realistic offline representations of soil moisture are demonstrated.

Chapter four compares fully coupled simulations of a real watershed (the Little Washita Watershed in Oklahoma) to non-coupled atmospheric simulations. This chapter explores which times within the diurnal cycle and which locations within the watershed show stronger feedbacks between the water table and the atmospheric boundary layer. How these feedbacks change over periods of time longer than a diurnal cycle and how a storm system affects the coupling are also demonstrated. Conclusions of feedbacks within the modeled hydrologic cycle and future recommendations are presented in chapter five. Governing equations for the Advanced Regional Prediction System (APRS) and ParFlow (PF) are presented in the appendix.

## 1.3 Summary of Contributions

The work presented here aims to increase our understanding of subsurface-surface-atmospheric interactions through idealized and real simulations. Effects of terrain, subsurface formation, land cover, and climate on water table dynamics, energy fluxes at the land surface, and the development and structure of the atmospheric boundary layer are isolated. Key contributions of this work include:

1. Understanding water table dynamics for a range of configurations of land form, subsurface properties, vegetation, and climate, and identifying critical zones which demonstrate strongest coupling between water table depth, land surface energy fluxes and atmospheric boundary layer depth.

2. Demonstrating the importance of having a realistic representation of water table dynamics through soil moisture initializations for atmospheric simulations.

3. Studying the relative effects of terrain, soil moisture heterogeneity, and subsurface properties on the atmospheric boundary layer and demonstrating which effect dominates during different times and locations within a watershed.

4. Investigating the two-way feedback between water table and atmospheric boundary layer dynamics in a real watershed using a fully coupled subsurface-surface-atmospheric code, and studying effects of a storm system on these feedbacks.

# Chapter 2

## Idealized Simulations to Identify Effects of Terrain and Subsurface Heterogeneity on Land Surface Energy Fluxes

This chapter investigates the role of terrain and subsurface heterogeneity on the interactions between groundwater dynamics and land surface energy fluxes using idealized simulations. A three-dimensional variably saturated groundwater code (ParFlow) coupled to a land surface model (Common Land Model) is used to account for both vertical and lateral water and pressure movement. This creates a fully-integrated approach, coupling overland and subsurface flow while having an explicit representation of the water table and all land-surface processes forced by atmospheric data. Because the water table is explicitly represented in these simulations, regions with stronger interaction between water table depth and the land surface energy balance (known as critical zones) can be identified. This study uses simple terrain and geologic configurations to demonstrate the importance of lateral surface and subsurface flows in determining land surface heat and moisture fluxes. Strong correlations are found between the land surface fluxes and water table depth across all cases, including terrain shape, subsurface heterogeneity, vegetation type and climatological region. Results show that different land forms and subsurface heterogeneities produce very different water table dynamics and land surface flux responses to atmospheric forcing. Subsurface formation and properties have the greatest effect on the coupling between the water table and surface heat and moisture fluxes. Changes in land form and land surface slope also have an effect on these interactions by influencing the fraction of rainfall contributing to overland flow versus infiltration. This directly affects the extent of the critical zone with highest coupling strength along the hillside. Vegetative land cover, as seen in these simulations, has a large effect on the energy balance at the land surface but a small effect on streamflow and water table dynamics and thus a limited impact on the land surface-subsurface interactions. Although climate forcing has a direct effect on water table dynamics and feedbacks to the land surface, in this study it does not overcome that of subsurface heterogeneity and terrain.

### 2.1 Introduction

The importance of modeling the terrestrial hydrologic cycle as a continuous system has long been recognized (Freeze and Witherspoon, 1966; Freeze and Harlan, 1969, Freeze, 1972). With advancing computer resources, the development of coupled hydrologic models has therefore been the subject of much recent research (e.g. Seuffert et al, 2002; Loague and VanderKwaak, 2004; Chow et al, 2006; Loague et al, 2006; Maxwell et al, 2007; Kollet and Maxwell, 2008; Kollet et al, 2009). There is, however, still much to be understood about the extent of surface-subsurface interactions and determining the locations within a watershed where they are most important.

Several key questions about the nature of surface-subsurface interactions are used to guide the work presented here: (1) What are the effects of terrain, subsurface properties, and land cover on

water table variability? (2) What affects the correlation between water table depth and land surface fluxes? (3) Which locations within a watershed show stronger feedbacks between the water table and the land surface? (4) How does climate and atmospheric forcing affect the coupling and feedbacks?

The answers to these questions have traditionally been sought using land-surface models or groundwater models in isolated configurations, which have limited ability to address true coupling feedbacks. Land surface models (Betts et al, 1996) were originally developed to form a lower boundary condition for general circulation models (e.g. Manabe et al, 1970) and typically consist of simple bucket-type formulations to store water beneath each atmospheric grid column. Historically, LSMs have relied on simplified parameterizations to represent subsurface flow, in general ignoring lateral water flow, spatial variability of land cover and surface soil moisture, and without an explicit representation of the groundwater table (Maxwell and Miller, 2005; Yeh and Eltahir, 2005; Gulden et al, 2007; Kollet and Maxwell, 2008).

Groundwater models, on the other hand, usually contain a complete representation of subsurface physics, but lack a good representation of surface processes. Early attempts have been made to represent coupled groundwater processes in LSMs, (e.g. Liang et al., 2003; Maxwell and Miller, 2005; Yeh and Eltahir, 2005; Gulden et al., 2007) or to fully couple groundwater models with land-surface processes (Kollet and Maxwell 2008). Water table depth has been identified as a critical factor affecting soil moisture variability at the land surface (Salvucci and Entekhabi, 1995; Liang et al, 2003; Chen and Hu, 2004; Yeh and Eltahir, 2005; Fan et al, 2007). Additionally, water table dynamics affect runoff generation, recharge, energy and moisture fluxes at the land surface, and resistance to changes in temperature and precipitation (Salvucci and Entekhabi 1995; Levine and Salvucci, 1999; Liang et al 2003; Chen and Hu, 2004; Maxwell and Kollet, 2008a; Kollet et al, 2009). Spatial variability of subsurface properties has also been shown to have a significant impact on water movement in hill slopes and on streamflow generation (Fiori and Russo, 2007). Salvucci and Entekhabi (1995) studied a range of topographic, soil, and climate conditions on idealized hillslopes using a spatially distributed flow model. They classified hillslope areas into three regions of distinct hydrologic behavior based on hydrologic fluxes: groundwater recharge, discharge, and midline regions in between with zero average recharge. A similar classification was observed by Kim et al (1999) who used a mixed analytical-numerical approach to investigate soil moisture patterns along a hillslope.

Coupled surface-groundwater models integrate variably-saturated groundwater models with surface-water routing and overland flow capabilities, thus allowing surface-subsurface flow simulations. A thorough review of the approaches used in coupled surface-water-groundwater models is given in Ebel et al (2009). The two most commonly used techniques are 1) first-order exchange coefficient coupling (e.g. VanderKwaak, 1999; Panday and Huyakorn, 2004; Therrien et al., 2005; Ebel et al, 2009) and 2) specifying surface-subsurface continuity of pressure and flux boundary conditions (e.g. Kollet and Maxwell, 2006; Maxwell and Kollet, 2008b; Dawson, 2008). Even though approaches differ, all these models use a rigorous, physically-based mathematical treatment of integrated surface-subsurface flow (Maxwell, 2009).

Here we use a model that combines aspects of each coupling approach, known as ParFlow-CLM (PF.CLM) (see Maxwell and Miller, 2005; Kollet and Maxwell, 2006; 2008). The three-

dimensional variably saturated groundwater code ParFlow is coupled to a land surface model (Common Land Model). The coupled model accounts for both vertical and lateral water and pressure movement. PF. CLM has been previously used with the Little Washita watershed (Oklahoma) to investigate spatial correlations between water table depth and the land-energy budget (e.g. latent heat flux) and identified a so-called critical zone of greatest interaction (Kollet and Maxwell, 2008). A shallow water table provides ample water for land surface processes so that they are not moisture limited. In such areas evaporation and transpiration rates operate at or close to potential values. A deep water table decouples groundwater from the land surface. The critical transition zone occurs between these two zones, where the spatial correlation between land surface energy fluxes and water table depth is highest. PF.CLM was also used to illustrate the role of lateral subsurface flow in climate change simulations and drought analysis (Maxwell and Kollet, 2008a). The three zone structure defined in Kollet and Maxwell (2008) resembles the classification observed in Salvucci and Entekhabi (1995) and Kim et al (1999). The definitions used, however, in classifying these zones are different, while the latter studies use recharge fluxes to define the midline region of zero recharge, Kollet and Maxwell (2008) use energy fluxes at the land surface and their correlation with water table depth to define the transition zone of strongest surface-subsurface interactions.

In an attempt to directly address the four questions introduced above, this work uses PF.CLM in idealized simulations to isolate effects of terrain, subsurface structure and heterogeneity, variability in subsurface properties, land cover, and climatology on land surface energy fluxes. The idealized cases are designed to cover basic land forms (hills and valleys) that typically occur in a watershed (similar to sinusoidal land forms studied by Toth, 1963). The coupled model simulates physical processes such as overland flow, runoff, recharge, root zone uptake, and evaporation in a fully interactive manner that is used here to understand the feedback between water table depth and land surface energy fluxes. We observe the three coupling regions of Kollet and Maxwell (2008). Our results demonstrate how the location and extent of the critical zone along the hillside is affected by subsurface formations, properties, terrain, and atmospheric forcing. Our cases also show situations where the decoupled zones may not appear such as when the water table is not deep enough.

## 2.2 Land surface-subsurface coupled model (PF.CLM)

ParFlow solves the three-dimensional, transient Richards' equation fully-coupled to the kinematic wave equation (*Kollet and Maxwell, 2006*). An implicit backward Euler scheme in time is used for both the subsurface and overland flow components, which are coupled via a pressure continuity boundary condition (second approach mentioned in the previous section). A cell-centered finite difference scheme in space, harmonic averages for hydraulic conductivity, and a one-point upwind of relative permeabilities are used for the variably-saturated flow solution with an upwind finite volume scheme in space used for the overland flow component. ParFlow solves for water pressure in the subsurface and gives the saturation field (from which the water table can be determined) at every time step in the simulation using a parallel, globalized Newton-Krylov method coupled to a multigrid preconditioned linear solver (*Ashby and Falgout, 1996; Jones and Woodward, 2001*). The pressure-saturation relationship is obtained from the Van Genuchten formulation (*Van Genuchten 1980*).

ParFlow has been integrated with the Common Land Model (Maxwell and Miller, 2005; Kollet and Maxwell 2008) to include the energy and mass balance at the land surface. Governing Equations for the coupled model are explained in Appendix A. In this coupled code, CLM is included as a module within ParFlow over the top-ten grid cells starting at the land surface and moving downward. ParFlow replaces both the soil moisture formulation and the TOPMODEL-based runoff scheme in CLM. The mass balance in the subsurface is calculated by ParFlow, which provides CLM with the soil moisture distribution, while the energy balance at the land surface is calculated by CLM which provides ParFlow with land surface fluxes (such as evapotranspiration and vegetation through-fall from precipitation). This passing of information is performed at each time step and is the basis of the coupling between the two models. The coupled code is mass and energy conservative. The model also takes into account water infiltrating at the land surface due to precipitation, canopy throughfall, and re-infiltration from overland flow (often called run-on, e.g. Maxwell and Kollet, 2008b).

Static parameters needed to generate the grid for ParFlow include subsurface hydraulic properties, land surface properties, and land-cover (vegetation type). The model is driven by an atmospheric forcing time series (temperature, precipitation, solar radiation, humidity, and barometric pressure).

## 2.3 Idealized Simulation Setup

The idealized simulations described here are designed to isolate effects of 1) subsurface formations , 2) terrain (including surface slope), 3) subsurface properties, 4) vegetative land cover, and 5) climatology on the hydrology (streamflow), water table dynamics, and coupling between water table and land surface energy fluxes. The coupled model inputs include atmospheric forcing, spatially uniform vegetation information, and a subsurface model setup to be consistent with the land surface formulation in PF.CLM.

Three types of subsurface layering are considered (Figure 2.1 and Figure 2.2): 1) homogeneous, 2) a two-layered subsurface (a high permeability-high porosity layer over a low permeability-low porosity layer), and 3) a three-layered subsurface (an aquitard separating a high-permeability, high-porosity layer from an underlying low permeability-low porosity layer). Input parameters include subsurface hydraulic properties (e.g. saturated hydraulic conductivity [L/T], porosity [-], and Van Genuchten parameters, chosen from ranges of values reported in *Schaap and Leij (1998)*) and land surface properties (Manning's coefficient [$T/L^{1/3}$] and surface slopes). The formations and properties used in each idealized case are summarized in tables 1 and 2. For the two and three layered formations, similar properties are used across all cases for the lower and aquitard layers (S7 and S1 in Table 2.2, respectively), but different parameters are used for the top layer. The top layer in these cases has a higher hydraulic conductivity and porosity than the underlying formation. To allow for a better comparison between different cases, subsurface properties are chosen for the homogeneous cases such that the hydraulic conductivity and porosity values lie in between those of the top and bottom layers of the layered cases.

All cases are two-dimensional in x-z with 100 m thickness in the y-direction. Two different landforms are considered for this study: uniform hill-slope and sinusoidal terrain (Figure 2.1 and Figure 2.2). Both are idealized landforms which may typically occur in a given watershed. Subsurface boundary conditions are no-flow on the sides and bottom of the domain. At the land surface the ParFlow overland flow boundary condition is applied (Kollet and Maxwell, 2006) and ponded water is routed along the land surface and allowed to exit the domain at outlet locations. The outlet for overland flow for the hill-slope cases is located at the bottom of the hill, while the outlets for the sinusoid cases are located at the valleys (left, middle, and right sides of the domain). The hill-slope cases have a domain size of (5000 m x 100 m x 310 m), with a horizontal grid spacing of 100 m and a vertical spacing of 0.1 m. Two domain sizes are considered for the sinusoidal terrain: (5000 m x 100 m x 80 m) and (5000 m x 100 m x 310 m) creating two different averaged slopes. The smaller domain with 80 m sinusoid height has an average land surface slope similar to the hill-slope cases and a finer grid discretization of 50 m in the x-direction.

Spatially-uniform atmospheric forcing is used to provide wind speed and direction, surface air temperature, incoming radiation, precipitation, pressure and humidity. Two atmospheric forcing data sets are used: a tropical forcing and a semi-arid forcing. Bare soil land cover was specified for all except two of the simulations which used the tropical forcing dataset with tropical forest and Savanna vegetation. These data sets are chosen to represent and compare surface-subsurface feedbacks for two very different climate systems: a very wet climate with little variation in solar radiation and temperature throughout the year, compared to a drier climate with a clear seasonal signature. Furthermore, the semiarid dataset was chosen because literature suggests a strong coupling between soil moisture and precipitation in semi-arid regions around the globe (Koster et al, 2004).

The tropical forcing time series is a year-long, synthetic dataset generated using the National Center for Atmospheric Research (NCAR) Community Climate Model (CCM1) for the Project for Inter-comparison of Land-surface Parameterization Schemes, PILPS (Pitman and Henderson-Sellers, 1995; Yang et al 1995). The data set was originally generated at 30-minute intervals for 1 year but was averaged into 3 hour timesteps for this study. The forcing covers the calendar year (12/31/1966 – 12/30/1967) and is representative of a tropical forest in the southern hemisphere (Pitman & Henderson, 1995). The forcing is characterized by large amounts of rain year round, and small temperature and incoming solar radiation variability within the year (see Figure 2.3). Some small seasonal variation is apparent in this type of climate such that the summer months show relatively less rainfall and cooler temperatures.

The semi-arid forcing data set was obtained from the North American Regional Reanalysis (NARR) data for the Little Washita watershed in Oklahoma, located in the Southern Great Plains in North America. It covers the water year (9/1/1998 – 8/31/1999), and has a total precipitation of 956 mm and mean temperature of 291 K (Kollet and Maxwell, 2008). The original dataset (NARR) has a three hour timestep which was interpolated to 1 hour timestep. The semi-arid forcing shows less rainfall throughout the year and greater temperature, solar radiation, and seasonal variations than the tropical dataset (see Figure 2.3).

Each configuration of the atmospheric forcing, land form, vegetation type, and land subsurface formation is initialized with a water table depth of 4 meters relative to the land surface. Then the model is run for several years, forced repeatedly with a single year of atmospheric data until the normalized change in yearly storage drops below 1%. For the simulations cases presented here, hydrologic and thermal equilibrium was reached within three to eleven years of spin-up. Results are shown for the year of simulation time when the model has reached equilibrium.

The simulation cases are organized into categories that isolate effects of subsurface formations, terrain, subsurface properties, land cover, and climatology. The terminology in Table 2.1 is used herein to describe and refer to each simulation case using five different categories that refer to the settings in each case as follows:

1. Land form: H (hill-slope), S (80 m-high sinusoid hills), or SE (elevated 310 m-high sinusoid hills).
2. Subsurface layering: H (homogeneous), 2L (two-layered), or 3L (three layered) formations.
3. Subsurface properties of top layer: S2, S3, S4, S5, or S6 (defined in Table 2.2).
4. Vegetation/Land cover: B (baresoil), S (savanna), or F (forest).
5. Atmospheric forcing: T (tropical) or SA (semi-arid).

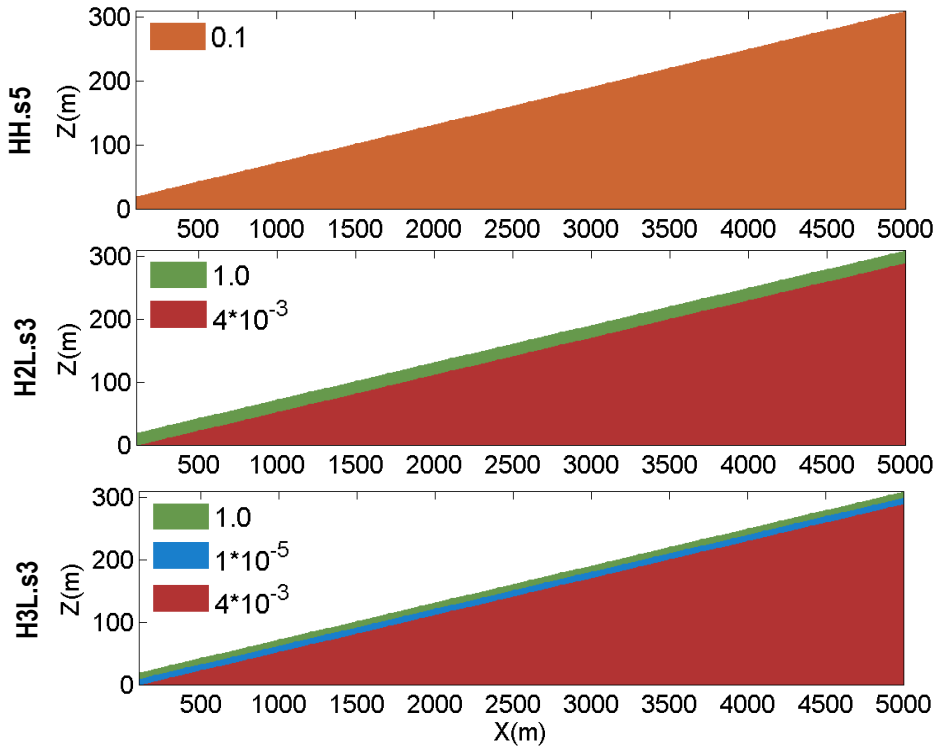


Figure 2.1: Subsurface formations for the hill-slope idealized simulation cases: homogeneous (HH.s5), two-layered (H2L.s3), and three-layered (H3L.s3). Colors indicate saturated hydraulic conductivity in (m/hour) for each layer.

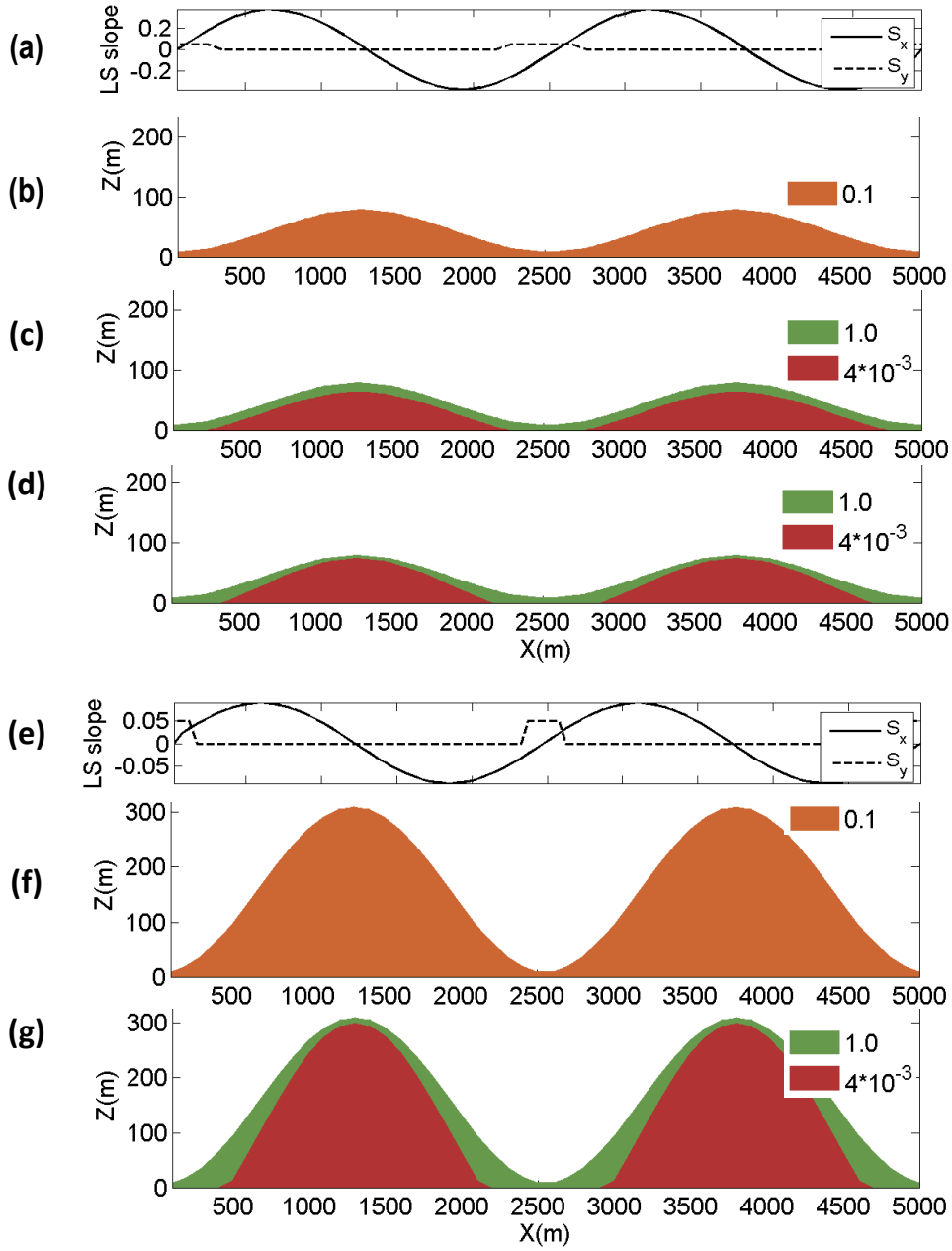


Figure 2.2: Subsurface formations for the sinusoid simulation cases and land surface x and y slopes: (a) Land surface (LS) slopes for the 80 m sinusoid cases, (b) case SH.s5, (c) case S2Lc.s3, (d) case S2L.s3, (e) LS slopes for the 310 m sinusoid cases, (f) case SEH.s5 and (g) case SE2L.s3. Colors indicate saturated hydraulic conductivity in (m/hour) for each layer.

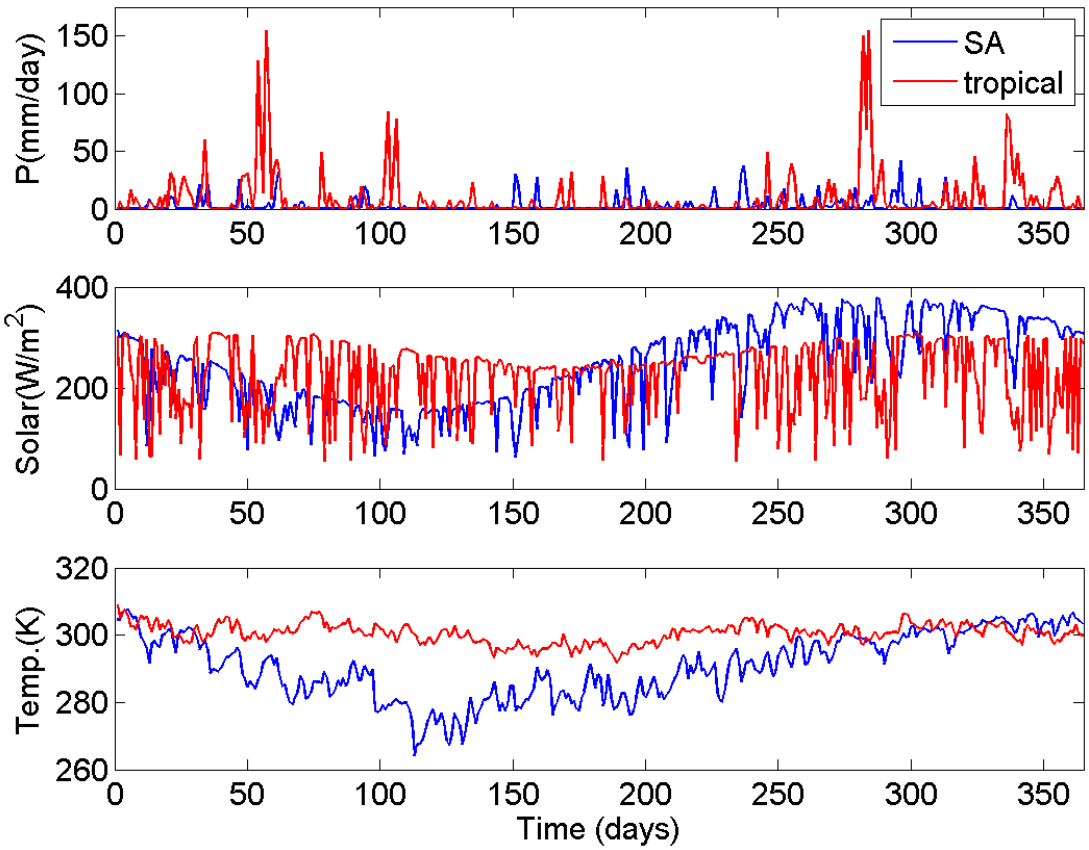


Figure 2.3: Daily-averaged precipitation (mm/day), incoming solar radiation ($W/m^2$), and ambient temperature (K) plotted against time in days of the year: starting on Sep. 1st for the semi-arid forcing and on Jan. 1st for the tropical forest forcing.

**Table 2.1:** Setup of terrain, subsurface layers and properties, vegetation, and atmospheric forcing for idealized simulation cases.

| Symbol | Terrain | Layers | Domain Height(m) | Average Slope | dx(m) | Land cover | Forcing | Subsurface properties* |
|---|---|---|---|---|---|---|---|---|
| HH.s5 | Hillslope | Homogeneous | 310 | 5.8% | 100 | Baresoil | Tropical | S5 |
| H2L.s3 | Hillslope | Two layers (2L) | 310 | 5.8% | 100 | Baresoil | Tropical | S3<br>S7 |
| H3L.s3 | Hillslope | Three layers (3L) | 310 | 5.8% | 100 | Baresoil | Tropical | S3<br>S1<br>S7 |
| SEH.s5 | Sinusoid | Homogeneous | 310 | 26.5% | 100 | Baresoil | Tropical | S5 |
| SE2L.s3 | Sinusoid | Two layers (2L) | 310 | 26.5% | 100 | Baresoil | Tropical | S3<br>S7 |
| SH.s5 | Sinusoid | Homogeneous | 80 | 5.8% | 50 | Baresoil | Tropical | S5 |
| S2L.s3 | Sinusoid | Two layers (2L) | 80 | 5.8% | 50 | Baresoil | Tropical | S3<br>S7 |
| S2Lc.s3 | Sinusoid | Two layers (2L)<br>Constant top layer thickness | 80 | 5.8% | 50 | Baresoil | Tropical | S3<br>S7 |
| S2L.s3.sav | Sinusoid | Two layers (2L) | 80 | 5.8% | 50 | Savanna | Tropical | S3<br>S7 |
| S2L.s3.for | Sinusoid | Two layers (2L) | 80 | 5.8% | 50 | Forest | Tropical | S3<br>S7 |
| S2L.s3.SA | Sinusoid | Two layers (2L) | 80 | 5.8% | 50 | Baresoil | Semi-Arid | S3<br>S7 |
| S2L.s2 | Sinusoid | Two layers (2L) | 80 | 5.8% | 50 | Baresoil | Tropical | S2<br>S7 |
| S2L.s4 | Sinusoid | Two layers (2L) | 80 | 5.8% | 50 | Baresoil | Tropical | S4<br>S7 |
| S2L.s6 | Sinusoid | Two layers (2L) | 80 | 5.8% | 50 | Baresoil | Tropical | S6<br>S7 |

* This column refers to the different subsurface properties listed in Table 2.2 for each layer. Layers are listed from top to bottom.

**Table 2.2:** Summary of subsurface properties (saturated hydraulic conductivity, porosity, and Van Genuchten parameters) used for different layers in cases from Table 2.1.

| Subsurface type | Ksat* (m/day) | porosity* | α** | n** | Sr** | Ss** | Description |
|---|---|---|---|---|---|---|---|
| S1 | 0.00024 | 0.5 | 1.51 | 2 | 0.196 | 1 | Very low K |
| S2 | 24 | 0.3 | 1.5 | 2 | 0.177 | 1 | Very high K |
| S3 | 24 | 0.3 | 3.55 | 3.16 | 0.177 | 1 | Very high K |
| S4 | 2.4 | 0.2 | 1.5 | 2 | 0.177 | 1 | High K |
| S5 | 2.4 | 0.2 | 2.45 | 2 | 0.14 | 1 | High K |
| S6 | 2.4 | 0.2 | 3.55 | 3.16 | 0.177 | 1 | High K |
| S7 | 0.096 | 0.01 | 10 | 2 | 0.1 | 1 | Low K |

* See equation A.9 in Appendix A.
** See equations A.4 and A.5 in Appendix A.

## 2.4 Results and Discussion

The results of different cases are compared to isolate effects of terrain, land cover, atmospheric forcing, subsurface formations and properties and investigate differences in water table dynamics, soil moisture and energy fluxes at the land surface. Yearly averages of mass and energy balance parameters are also compared (Table 2.3). It should be noted that subsurface pressure and saturation results were output at every other timestep during the simulations. Thus, the runoff results presented in Table 2.3 are estimated based on this six-hour interval.

### 2.4.1 Effects of subsurface formations

This first set of cases is chosen to illustrate the effect of subsurface formations. Using the simplest landform, a hillslope of uniform slope, we examine differences that result simply from having a homogeneous vs. layered subsurface. All three hillslope cases listed in Table 2.1 have bare soil land cover and were spun-up while forced with the tropical atmospheric data set.

The runoff time series in Figure 2.4 illustrates differences in baseflow and response to rainfall events. The homogeneous case (HH.s5) is the most responsive to storm events especially during summer months and has the largest average runoff and total storage (Table 2.3). This case has higher porosity and hydraulic conductivity values than the two layered cases at the land surface but smaller within the rest of the subsurface. Since overland flow is only generated once the land surface is fully saturated, the homogeneous case has the largest average runoff because it has a larger portion of the land surface under saturation conditions. This is different than baseflow which is a continuous outflow sustained by delayed shallow subsurface flow and deep subsurface discharge into the valley. Baseflow is largest for the two layered case (H2L.s3). The soil moisture (SM) time-series at the land surface in Figure 2.5 also demonstrate differences in

responsiveness to rainfall events between the three cases. A larger fraction of the hillside in the homogeneous case is under saturation conditions throughout the year. The layered cases on the other hand experience a larger number of dry periods especially during summer. It is interesting to note the three layered cases show sharp transitions between wet and dry soil at the land surface throughout the year. A storm with enough rainfall can saturate most of the land surface but this can quickly drain, drying the hillslope afterwards.

Figure 2.6 plots changes in vertical saturation profiles over time at the top of the hillslope (x = 5000 m). It is important to note that all panels in Figure 2.6 show a single column out of a 2D hillslope and that both lateral surface and subsurface flow occur but are not visualized in this figure. The effect of different rainfall events is visible through the resulting wetting fronts moving downward as time progresses. The water table is deepest (80 m) in the homogeneous case. The seasonal effect, however, is most clear in the two layered case (Figure 2.6b). The period of 180-300 days is the drier summer period during which the water table for this case declines below the top layer and falls within the bottom layer. This bottom layer is otherwise almost fully saturated during other times of the year. Since the bottom layer has lower permeability and porosity values than the top layer, its wetting/drying behavior will also be different, as reflected in the different saturation values from those in the top layer during the same times. Case H2L.s3, on the other hand, shows that the low-permeability (S7) formation beneath the top layer responds more slowly to storm events and is thus saturated during most of the year, only starting to dry during the latter part of summer. The aquitard in case H3L.s3 drains much more slowly than the underlying S7 formation. This produces an interesting effect where a perched aquifer forms above the S7 formation at the top of the hillside. This flow behavior is possible because lateral surface and subsurface flow are included in the coupled model formulation. Water is drained downhill from the S3 (top) and S7 (bottom) formations faster than it is drained from the aquitard formation. The bottom formation is now connected with the land surface through this leaky-perched aquifer. These cases show how the water table becomes more dynamic as more subsurface heterogeneity is introduced.

To examine subsurface-surface coupling, Figure 2.7 plots yearly-averaged latent heat flux, soil temperature, soil moisture and water table depth as a function of *x* for the three hillslope cases. The homogeneous case (HH.s5) shows three distinct zones along the hill-slope which indicate different coupling strengths between water table depth and energy fluxes at the land surface. These three regions correspond to the three zones presented in Kollet and Maxwell (2008) who described the middle region as a critical zone where the coupling between water table and land surface energy fluxes is greatest. The lower part of the hillside, including the outlet cells, is a region that is fully saturated for most of the year. Land surface energy processes within this first region (called zone 1) have ample water and stay relatively constant, showing no dependence on the water table. At the top of the hill on the other hand, the water table is sufficiently deep (zone 3) such that the energy fluxes are essentially decoupled from the water table. The middle part of the hillside (zone 2) is the critical region where the water table depth has the greatest effect on land surface fluxes (seen as a transition between the two constant regions in Figure 2.7). It should be noted that the different zones shown in Figure 2.7 are not an artifact of yearly averaging as we also see the critical zone on instantaneous timescales throughout the year with varying signs of correlation.

This also follows agrees with the findings of Salvucci and Entekhabi (1995) and Kim et al (1999) who defined these zones in terms of hydrologic fluxes and recharge into the saturated zone. Because the model used here explicitly calculates the energy balance at the land surface, we are able to define the zones in terms of different interactions between water table and energy fluxes. Consequently, the three zones are qualitatively similar; however the middle zones in both definitions (midline and transition) might not occur at the same location or have the same extent along the hillside. This could also be caused by differences in the models used and domain setup. Zone 1 is clear in Figure 2.7 for the lower part of the hill-slope for cases HH.s5 (between X = 0 and 1800 m) and H2L.s3 (between X = 0 and 150 0m), and for most of the hillslope for case H3L.s3 (between X = 0 and 4100 m) where the water table is shallow for a large region of the domain. Zone 3 is also apparent for cases HH.s5 and H2L.s3 (between X = 2800 and 5000 m), but does not appear in case H3L.s3 because the water table is not deep enough at the top of the hill due to the existence of the perched aquifer. The critical zone however is clearly shown for all three cases in Figure 2.7. As the water table becomes deeper within this region, evaporation becomes more soil moisture limited and latent heat flux decreases. The energy balance at the land surface dictates that as latent heat flux decreases in these regions, sensible heat flux will increase in turn causing ground surface temperatures to increase. This region is wider in the H2L.s3 case because the water table is generally shallower than in the HH.s5 case, and the change in depth is more gradual because of the effect of the low-permeability layer. This critical zone occurs at the highest part of the hillside for the H3L.s3 case. This occurs where the perched aquifer is formed and thus subsurface storage has greatest effects on evaporation and energy fluxes at the land surface. The saturated land surface at and near the valleys have the highest latent heat flux values because evaporation is not limited there. This also means, for the yearly averages shown here, that these regions will have lower sensible heat flux values and thus the ground surface will be coolest at the valleys. Areas at and around the peaks are too dry and have a deep enough water table that it is decoupled from the land surface. Thus latent heat flux values are at a minimum in these areas, and the land surface is warmest.

The critical zones presented here for cases HH.s5 and H2L.s3 each show two different slopes which indicate different coupling strengths along the hillside. To further explore this, we use scatter plots of yearly-averaged water table depth and yearly-averaged latent heat flux to diagnose regions of connection between the subsurface and land surface. This is shown in Figure 2.8 and is similar to the analysis presented in Kollet and Maxwell (2008); Maxwell and Kollet (2008a) and Maxwell et al (2007). Note that we normalize the latent heat flux values by the spatial and yearly average (also shown in Table 2.3) to more-easily compare across cases. The critical zone occurs in all three cases at water table depths ranging from about 0.1 to 10 meters (0.08-9.5m for the homogeneous case, 0.1-11m for the two layered case, and 0.2-8.5m for the three-layered case). The two different slopes are more pronounced in this representation of the data and likely are due to the interplay of soil moisture within this part of the hillslope, the Van Genuchten saturation-pressure relationship and how this translates to bare soil evaporation.

Comparison of these three hillslope cases with different subsurface layered formations emphasizes the importance of lateral water transport (particularly in case H3L.s3); the differences in flow and moisture distribution would not have been apparent if only vertical water flow was taken into account. The comparisons also underscore that even for these idealized

cases, variations in subsurface layering and properties show a strong signature in the water table responses and on the spatial pattern of latent heat flux.

Table 2.3: Resulting yearly averages of water and energy balance components for spin-up cases in Table 2.1. The energy fluxes reported here are spatially averaged over the domain.

| **Case** | **P (mm/day)** | **R (mm/day)** | **ET (mm/day)** | **$S_{sub}$ (mm)** | **$S_{surf}$ (mm)** | **LE ($W/m^2$)** | **H ($W/m^2$)** | **G ($W/m^2$)** | **Rn ($W/m^2$)** |
|---|---|---|---|---|---|---|---|---|---|
| HH.s5 | 8.95 | 6.02 | 3.07 | 3.16E+04 | 0.38 | 89.07 | -17.63 | 0.16 | 71.59 |
| H2L.s3 | 8.95 | 5.93 | 3.03 | 7.59E+03 | 0.12 | 88.04 | -17.64 | 0.04 | 70.44 |
| H3L.s3 | 8.95 | 5.50 | 3.51 | 1.08E+04 | 0.33 | 101.99 | -25.53 | 0.04 | 76.51 |
| SEH.s5 | 8.95 | 6.11 | 2.78 | 1.94E+04 | 0.08 | 80.87 | -13.75 | 0.20 | 67.32 |
| SE2L.s3 | 8.95 | 6.44 | 2.49 | 6.15E+03 | 0.07 | 72.49 | -8.18 | 0.01 | 64.32 |
| SH.s5 | 8.95 | 5.84 | 3.02 | 7.87E+03 | 0.18 | 87.72 | -16.97 | 0.16 | 70.91 |
| S2L.s3 | 8.95 | 6.31 | 2.64 | 2.81E+03 | 0.08 | 76.78 | -10.49 | 0.02 | 66.30 |
| S2Lc.s3 | 8.95 | 6.36 | 2.59 | 2.79E+03 | 0.08 | 75.37 | -9.46 | -0.05 | 65.86 |
| S2L.s3.sav | 8.95 | 6.62 | 2.33 | 2.82E+03 | 0.08 | 67.59 | -3.76 | -0.02 | 63.82 |
| S2L.s3.for | 8.95 | 5.39 | 3.51 | 2.73E+03 | 0.07 | 102.10 | -22.97 | -0.03 | 79.11 |
| S2L.s3.SA | 2.29 | 0.56 | 2.35 | 2.08E+03 | 0.01 | 68.34 | 48.19 | 3.58 | 120.11 |
| S2L.s2 | 8.95 | 5.90 | 3.07 | 2.95E+03 | 0.07 | 89.10 | -18.02 | 0.06 | 71.14 |
| S2L.s4 | 8.95 | 5.49 | 3.45 | 2.78E+03 | 1.14 | 100.11 | -24.95 | 0.06 | 75.22 |
| S2L.s6 | 8.95 | 5.60 | 3.34 | 2.79E+03 | 1.48 | 96.97 | -23.59 | 0.05 | 73.43 |

P: precipitation, R=surface runoff, ET=evapotranspiration
$S_{sub}$=subsurface storage, $S_{surf}$=surface storage
LE=latent heat flux, H=sensible heat flux, G=ground heat flux, Rn=net radiation

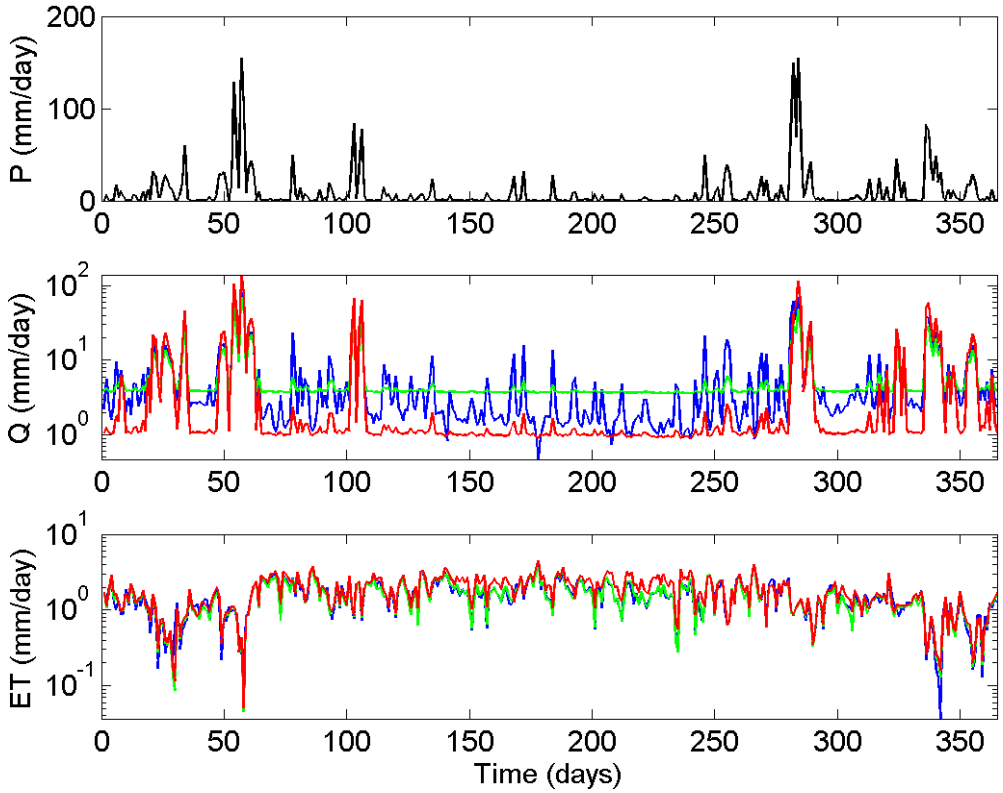


Figure 2.4: Daily-averaged outflow (Q) and evapotranspiration (ET) in (mm/day) on a log-scale from the hill-slope outlets of cases: HH.s5 (blue), H2L.s3 (green), and H3L.s3 (red). The top plot shows daily-averaged precipitation (P) in (mm/day).

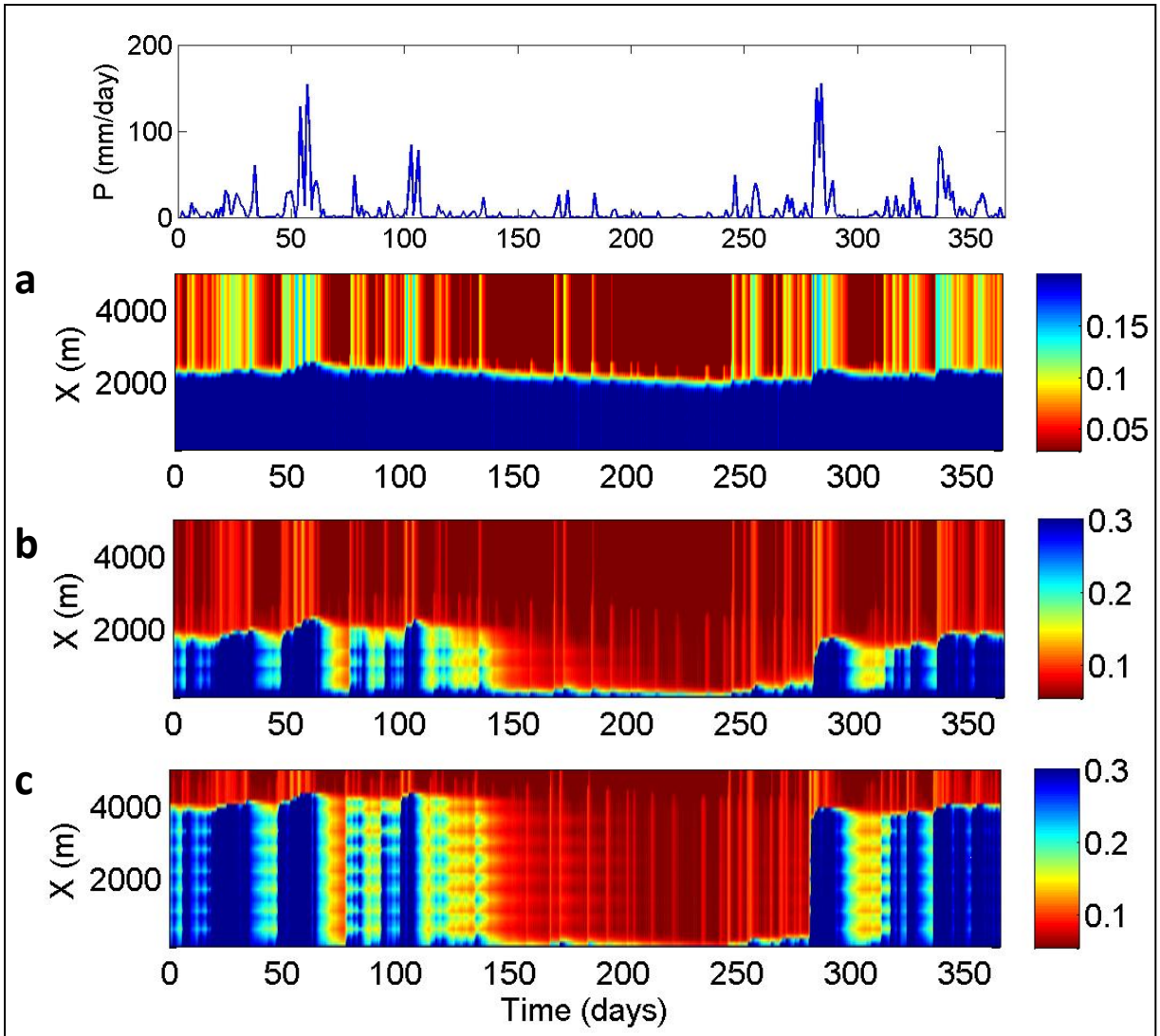


Figure 2.5: Soil moisture (SM) variations (colorbar) at the land surface in the x-direction versus time for the final spin-up year for cases: (a) HH.s5, (b) H2L.s3, and (c) H3L.s3. Blue regions show areas that are fully saturated. The top plot shows daily-averaged precipitation in (mm/day).

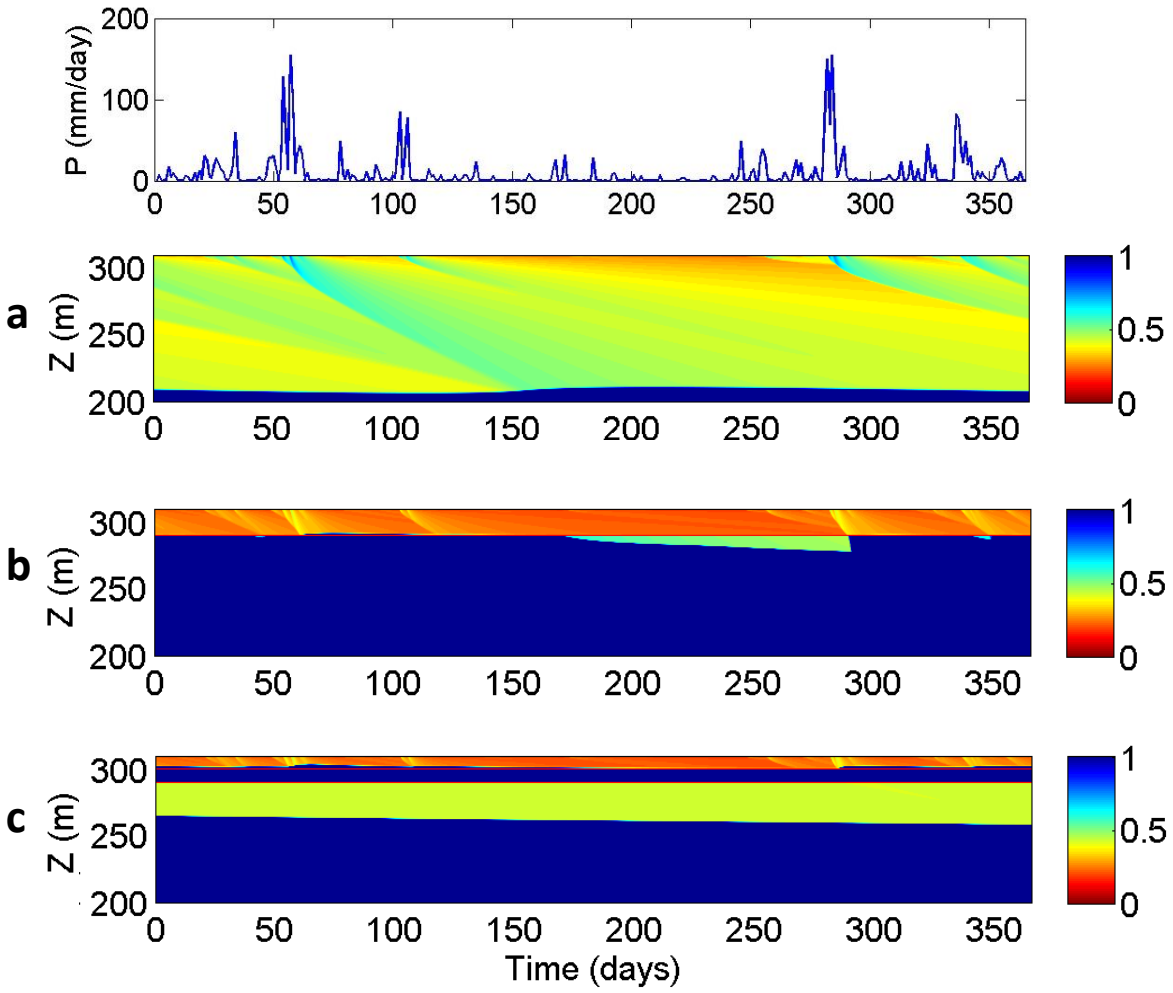


Figure 2.6: Vertical saturation variations in time at the top of the hillside (x=5000 m) for the final spin-up year for cases: (a) HH.s5, (b) H2L.s3, and (c) H3L.s3. Color bar shows saturation. The horizontal red lines show interfaces between different subsurface layers.The top plot shows daily-averaged precipitation in (mm/day).

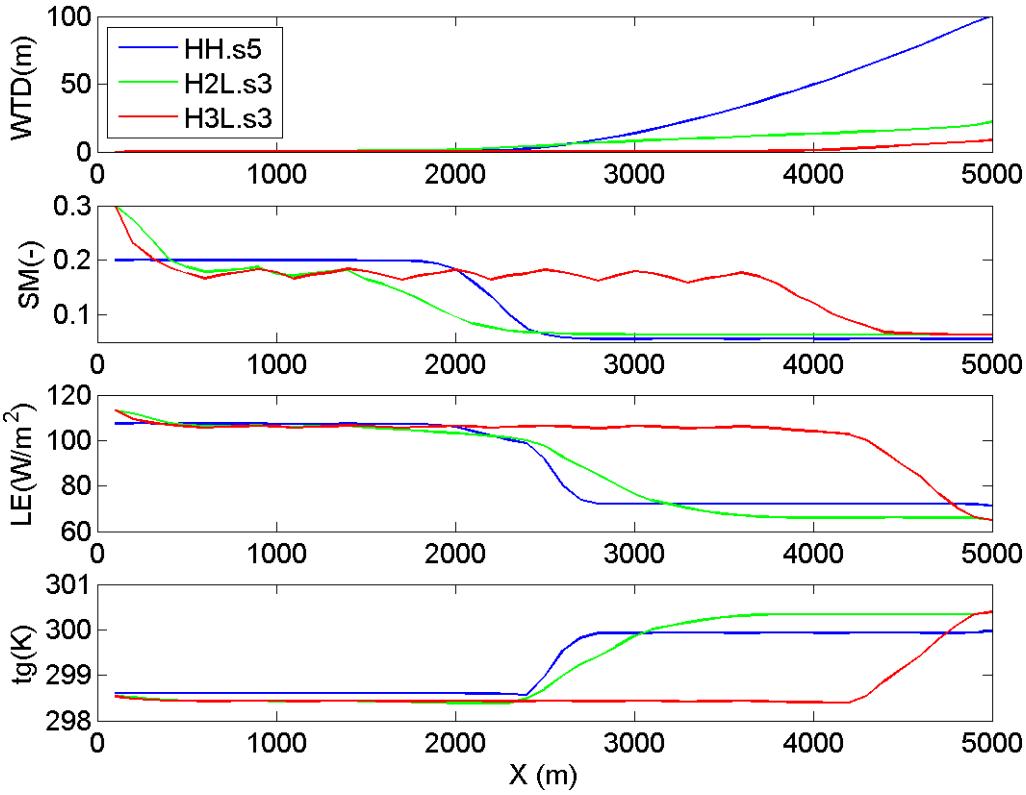


Figure 2.7: Water table depth (m), soil moisture at the land surface (-), latent heat flux ($W/m^2$), and ground surface temperature (K) versus X (m) for HH.s5, H2L.s3, and H3L.s3 cases.

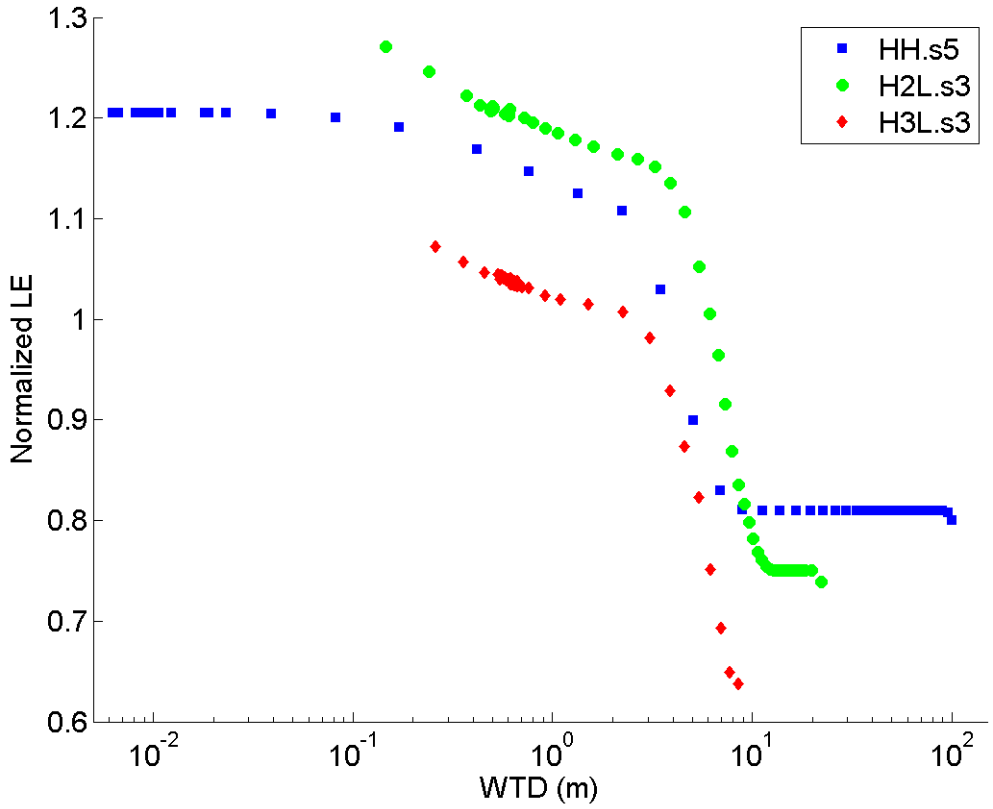


Figure 2.8: Semi-logarithmic scatter plots of yearly averaged latent heat flux normalized to its mean ($W/m^2$) versus water table depth (m) for cases: HH.s5, H2L.s3, and H3L.s3.

### 2.4.2 Effects of terrain and formation thickness

To examine the role of land surface slopes and introduce more complexity we consider an idealized sinusoidal valley, as an archetype feature in a watershed. The average slope is chosen to be similar to that of the hill-slope case. We compare the two-layered hill-slope case H2L.s3 (Figure 2.1b) to two layered sinusoid cases, one with a constant top layer thickness (S2Lc.s3, Figure 2.2c) and one with a variable top layer thickness (S2L.s3, Figure 2.2d). The variable top layer thickness was chosen to mimic a realistic geologic formation which is thinner at the hill tops and thicker at the valley bottom.

Figure 2.9 compares the runoff for the two-layer hillslope case with the two sinusoid cases. The two sinusoid cases produce very similar hydrographs, but they are both different than the hillslope case which has a more consistent baseflow sustained by the larger amount of subsurface storage for this case (Table 2.3). These differences are interesting because the average terrain slope is quite similar in all cases. The smaller slopes at the peaks of the sinusoidal hills, however,

create regions of higher infiltration than overland flow. The hill sides, having larger slopes, contribute more overland flow and subsurface lateral flow than infiltration.

Saturation snapshots at the end of the spin-up year (December 31$^{st}$) (Figure 2.10) show the effect of slope and top layer thickness more clearly. The cases with constant top layer depth (S2Lc.s3 and H2L.s3) show similar trends of water table variations throughout the year (not shown). Maximum water table depth for these cases occurs at the peak of the hill. It is interesting to note that the sinusoid case with variable top layer thickness (S2L.s3) has a deeper water table at the hill sides rather than at the peaks.

The resulting water table profiles (Figure 2.11) show different coupling zones along the hillsides of these cases. Water table depth for case S2Lc.s3 follows the expected general trend of deeper water table at hill tops, but shows narrower transition zones around the valleys compared to the transition zone in the hillslope case. . For case S2L.s3, these yearly averaged profiles show the maximum water table depth on the hillsides and this is reflected in the LE and temperature distribution, giving a small peak on each hill side. This pattern is a result of the land surface on the peak drying faster than the land surface on the hillside (Figure 2.10c). This makes evaporation at the peak moisture limited (and thus decoupled from water table dynamics) even though the water table depth there is shallow.

The scatter plot in Figure 2.12 shows that the transition zone occurs over the same range of water table depths (0.1 to 10 meters) for the cases with constant top layer thickness (S2Lc.s3 and H2L.s3). The patches of deep water table on the hillsides for case S2L.s3 results in a steeper transition zone that occurs at water table depths between (0.1 to 4.5 m). The second transition zone for this case is also apparent at higher water table depths (4.5 to 10.5 m).

Thus, we see that the variable top layer thickness in the sinusoidal cases does not have a great effect on integrated hydrology measures such as outflow or ET, but it greatly affects the water table distribution and profile along the hillside. This in turn had a large effect on the energy fluxes and evaporation at the land surface. These interactions became more complicated for case S2L.s3 than for cases S2Lc.s3 and H2L.s3. Since case S2L.s3 has a more realistic setup, it will now be used as a base case against which all subsequent cases will be compared.

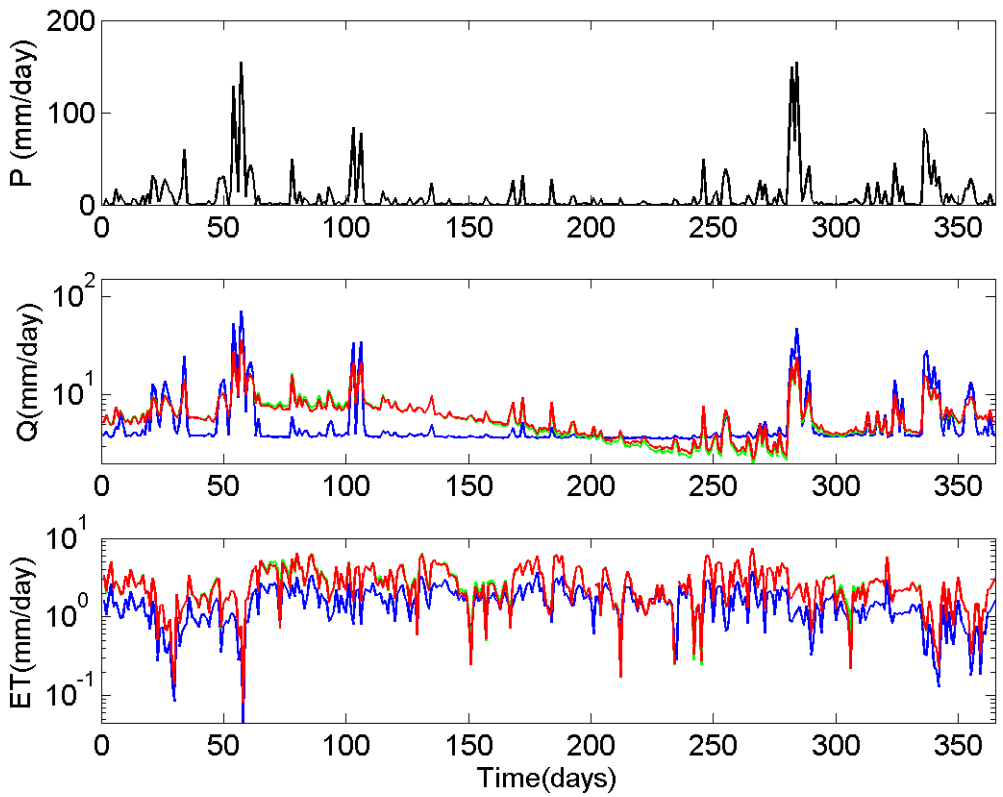


Figure 2.9: Daily-averaged outflow (Q) and evapotranspiration (ET) in (mm/day) on a log-scale from the valley outlets of cases: H2L.s3 (blue), S2L.s3 (green) and S2Lc.s3 (red). The top plot shows daily-averaged tropical precipitation (P) in (mm/day).

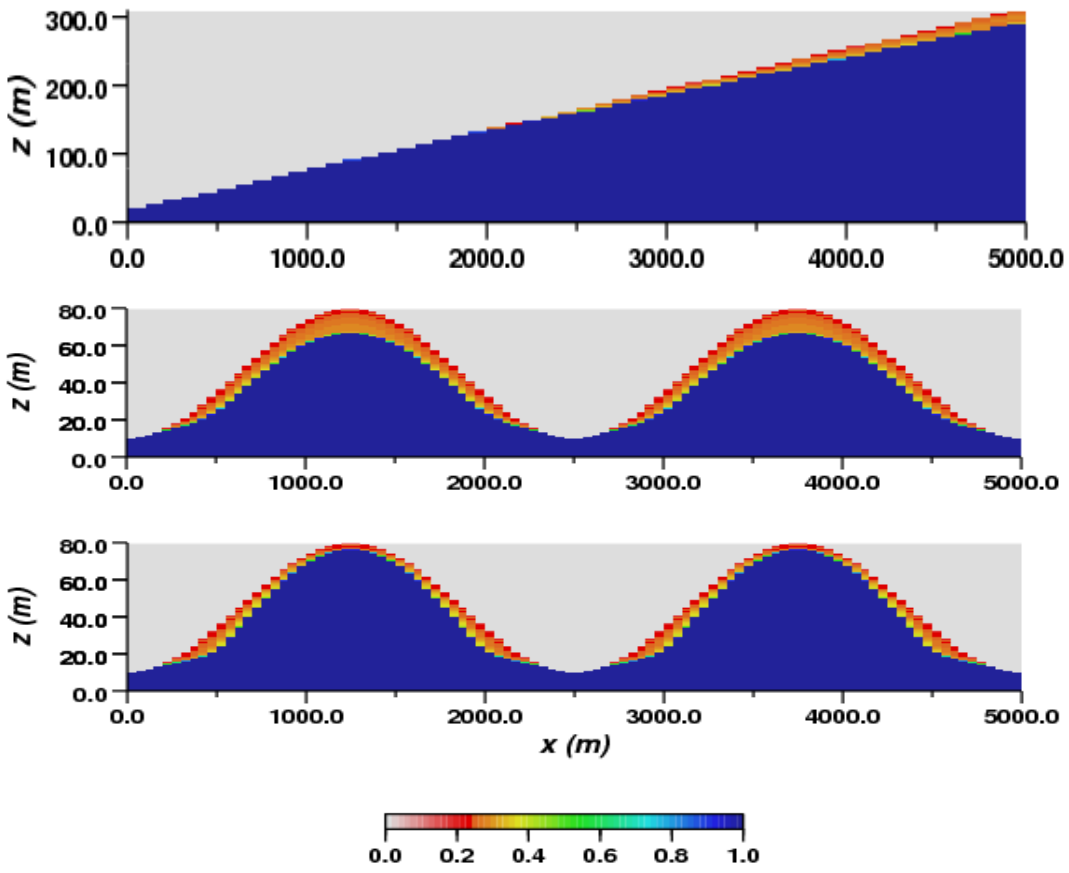


Figure 2.10: Saturation snapshots at the end of the spin-up year (December 31st) for the two layered cases: (H2L.S3), (S2Lc.s3), and (S2L.s3).

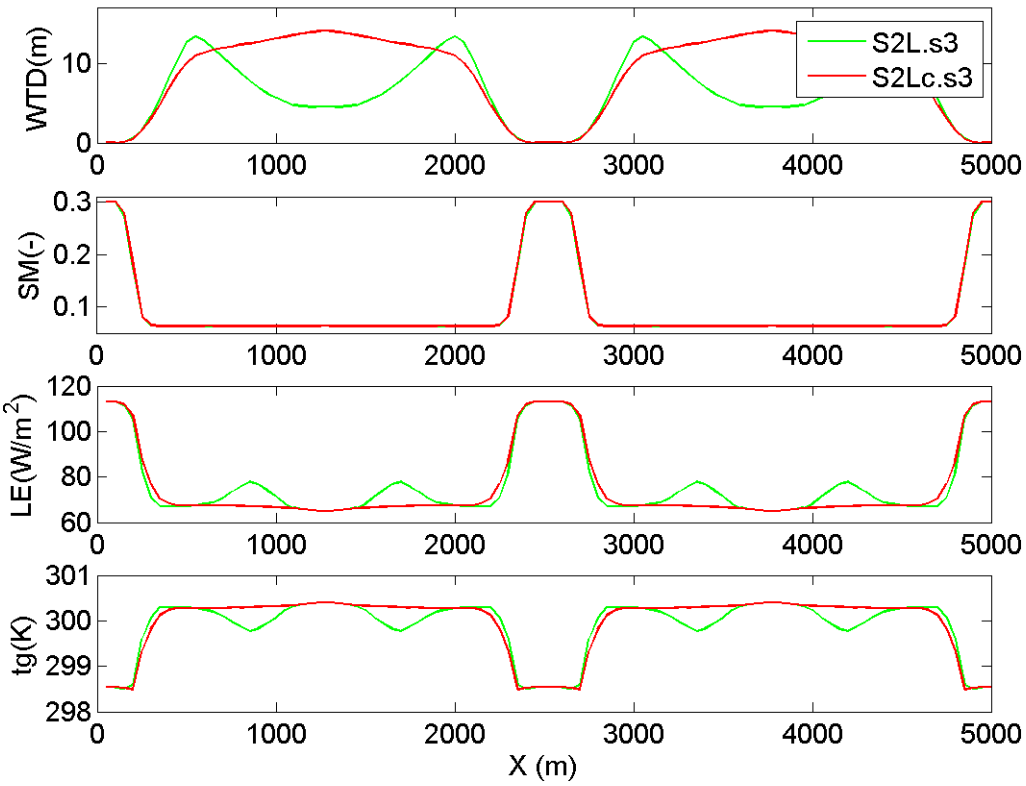


Figure 2.11: Water table depth (m), soil moisture at the land surface (-), latent heat flux (W/m$^2$), and ground surface temperature (K) versus X (m) for cases: S2L.s3 and S2Lc.s3. Note: The soil moisture curve for case S2L.s3 (green line) falls behind that for case S2Lc.s3 (red line).

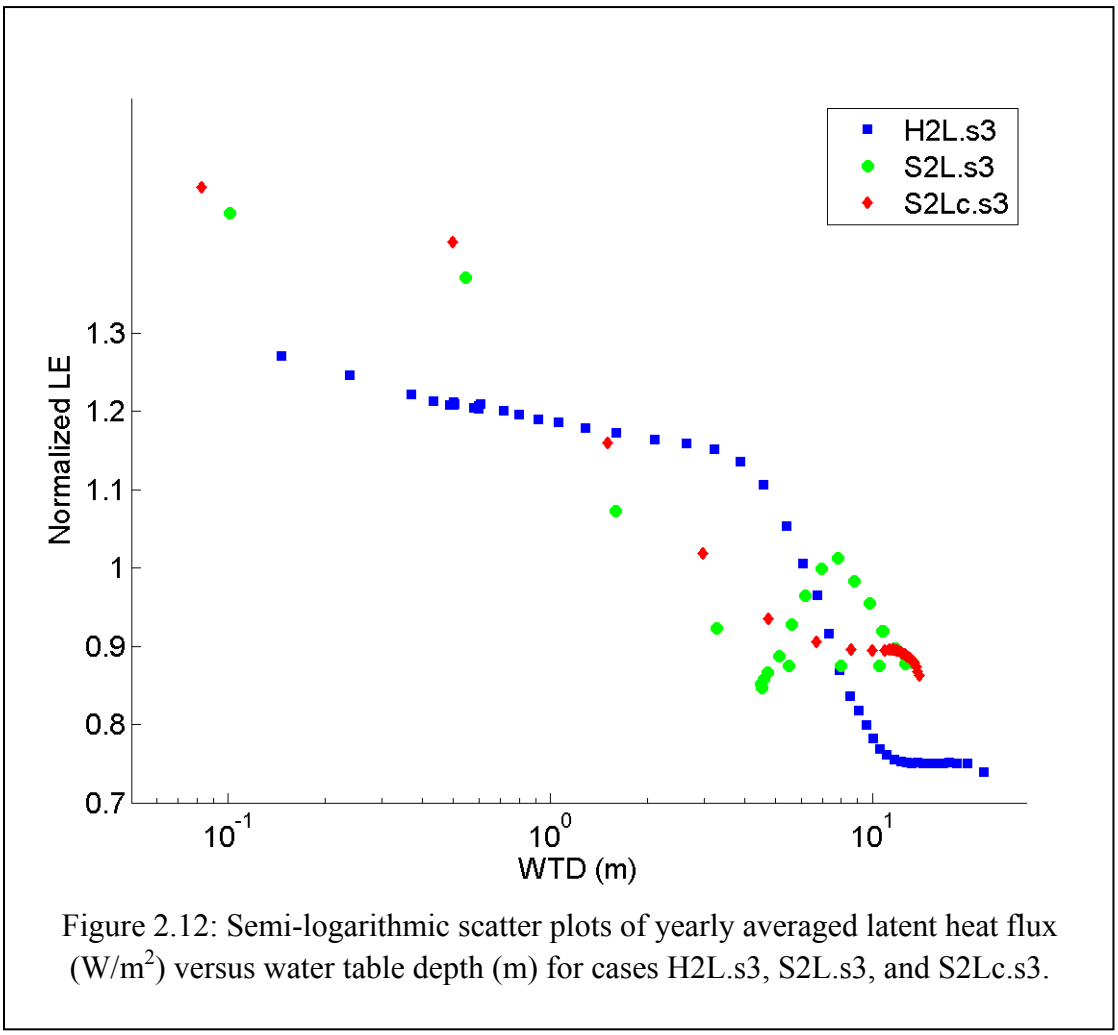


Figure 2.12: Semi-logarithmic scatter plots of yearly averaged latent heat flux ($W/m^2$) versus water table depth (m) for cases H2L.s3, S2L.s3, and S2Lc.s3.

### 2.4.3 Effects of terrain slope

Having illustrated the behavior of the valley and hillslope configurations with similar slopes in the previous section, we now compare sinusoid cases with different hill heights to study the effect of terrain slope. The two sinusoid domains have average slopes of 5.8% and 26.5%, as shown in Table 2.1. Because layering has a great effect on the coupling, homogeneous and two-layered cases are also considered here (Figure 2.2b, d, f, and g) for a total of four cases.

We see in Table 2.3 that land surface slopes have a direct effect on land surface hydrology. Greater land surface slopes result in larger yearly-averaged runoff rates as seen for cases SEH.s5 and SE2L.s3. Figure 2.13 plots the daily-averaged runoff and evapotranspiration and demonstrates that the 5.8% slope cases have a stronger seasonal trend and larger peak flows, while the steeper, 26.5% slope cases (SEH.s5 and SE2L.s3) have a more consistent baseflow and lower peak flows. Regardless of terrain height, the homogeneous cases (SH.s5 and SEH.s5) are more responsive to rainfall events than their respective two-layer cases. The homogeneous cases also have larger evaporation rates and larger subsurface storage values than the layered cases

(Figure 2.13 and Table 2.3). Because subsurface properties for the homogeneous cases were chosen to represent effective values of the layered cases, the porosity of the bottom formation in the layered cases (formation S7 in Table 2.2) is smaller than that for the homogeneous cases. Thus, the homogeneous cases have a larger pore volume, and a greater capacity to store water in the subsurface.

Resulting water table depth profiles in Figure 2.14 demonstrate that the homogeneous sinusoidal case, SH.s5, which has a comparable average slope to the homogeneous hill-slope case HH.s5, shows a similar water table behavior (as seen by comparing Figure 2.7 and Figure 2.14). Cases with greater land surface slopes on the other hand have deeper water table profiles. In fact, the water table for case SEH.s5 is too deep to show any direct response to rainfall events as exhibited by the other sinusoid cases (timeseries of saturation profiles not shown). While the valleys remain saturated during the year, the hill-sides are much drier, with the end result that narrower and more numerous transition zones are observed in the two sinusoid layered cases than in the homogeneous sinusoid cases and the hill-slope cases presented previously. The largest number of water table fluctuations in the x-direction appear in case SE2L.s3 (Figure 2.14). The homogeneous cases, on the other hand, show the same three zones as in the hill-slope cases in terms of coupling between water table depth and energy fluxes at the land surface. This behavior is also clear when considering the scatter plot in Figure 2.15. The two homogeneous cases show a trend similar to the homogeneous hillslope case HH.s5 (Figure 2.8) although the transition zone becomes very steep for case SEH.s5. The two transition zones are also clear for case S2L.s3 while the scatter becomes quite complex for case SE2L.s3 which has the largest number of WTD fluctuations. This analysis indicates that terrain height and steepness of hillslope are important factors in correlations between groundwater and land-energy fluxes.

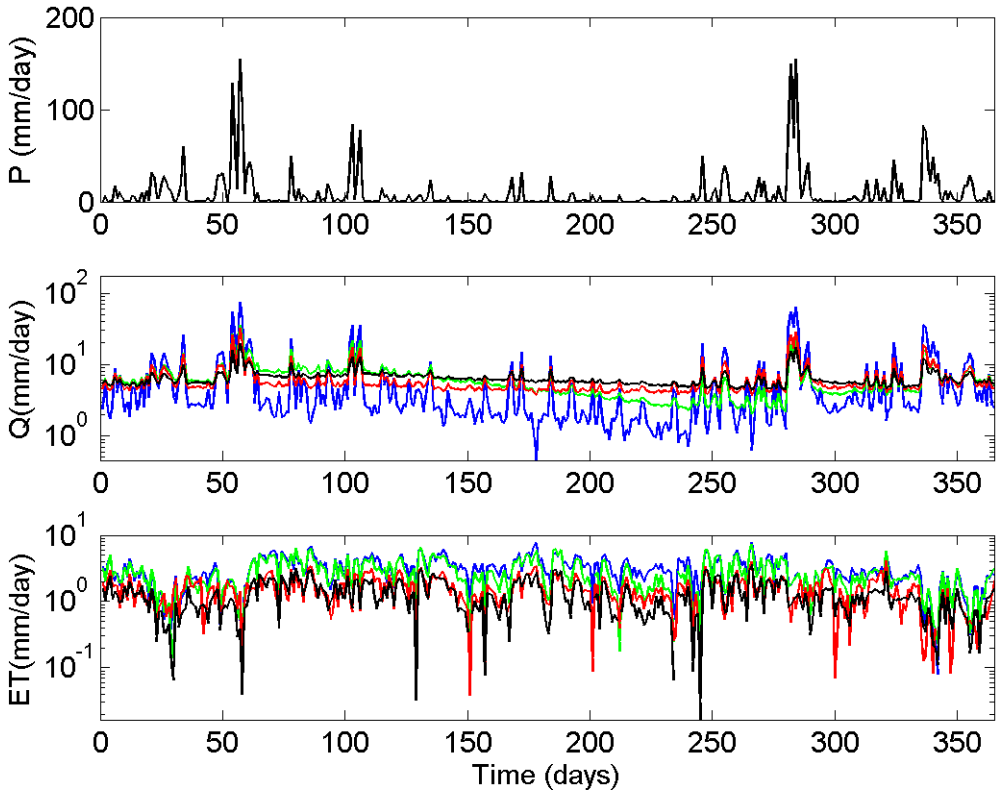


Figure 2.13: Daily-averaged outflow (Q) and evapotranspiration (ET) in (mm/day) on a log-scale from the valley outlets of cases: SH.s5 (blue), S2L.s3 (green), SEH.s5 (red), and SE2L.s3 (black). The top plot shows daily-averaged precipitation (P) in (mm/day).

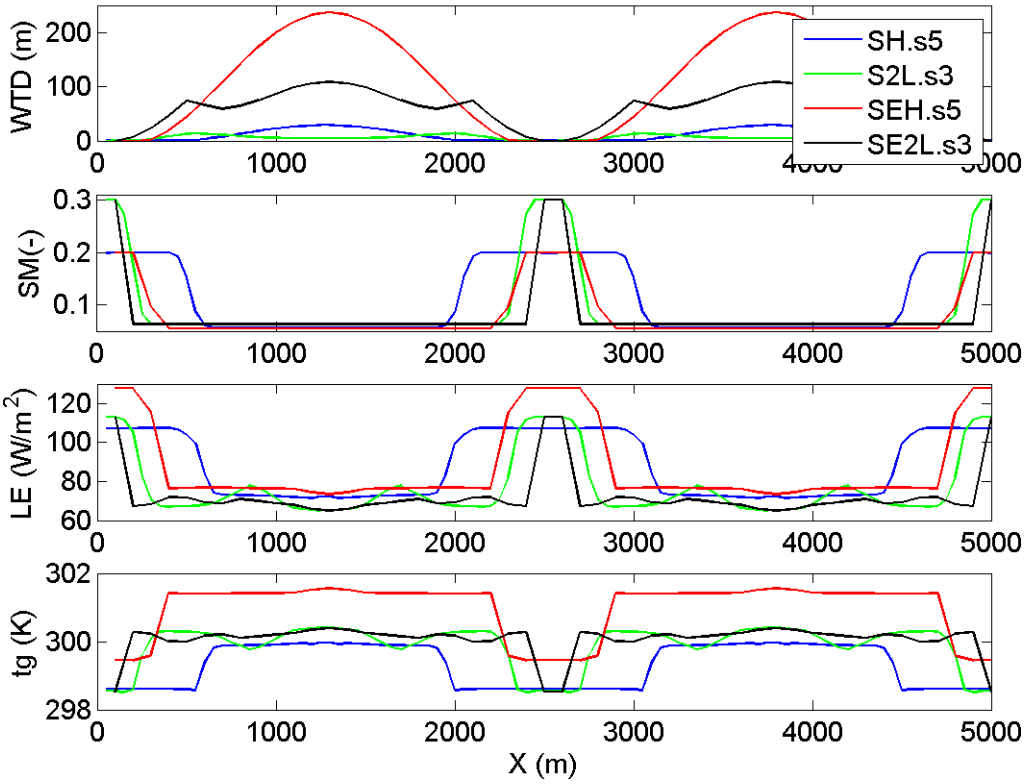


Figure 2.14: Water table depth (m), soil moisture at the land surface (-), latent heat flux ($W/m^2$), and ground surface temperature (K) versus X (m) for cases: SH.s5, S2L.s3, SEH.s5, and SE2L.s3.

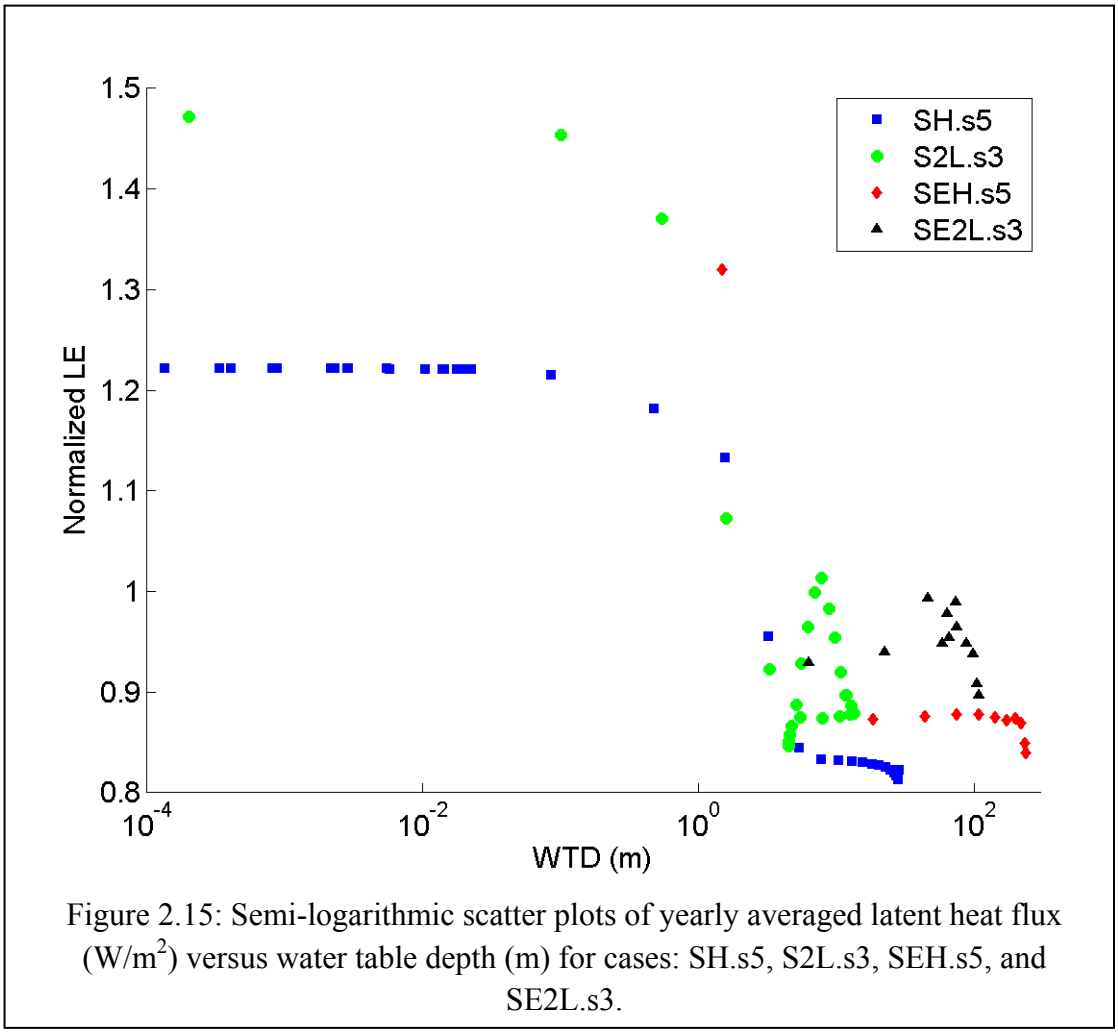


Figure 2.15: Semi-logarithmic scatter plots of yearly averaged latent heat flux ($W/m^2$) versus water table depth (m) for cases: SH.s5, S2L.s3, SEH.s5, and SE2L.s3.

### 2.4.4 Effects of subsurface properties

The base case S2L.s3 is compared here to three more cases (S2L.s2, S2L.s4, and S2L.s6 in Table 2.1) with the same domain and subsurface layering but different properties for the top layer. The subsurface properties considered here are saturated hydraulic conductivity ($K_{sat}$), porosity ($\phi$), and Van Genuchten parameters ($\alpha$ and n). All cases have bare-soil land cover and are forced with the tropical atmospheric data set.

Total runoff volume and evapotranspiration plots are shown in Figure 2.16, which shows that cases with similar $K_{sat}$ and $\phi$ have similar hydrographs (cases S2L.s2 and S2L.s3 on one hand, and cases S2L.s4 and S2L.s6 on the other hand). These parameters have a direct effect on how quickly the land surface will saturate during a storm and what fraction of precipitation will contribute to overland flow as opposed to infiltration or evaporation. The land surface is generally wetter for cases with smaller $K_{sat}$ and $\phi$ (S2L.s4 and S2L.s6). Because those cases are wetter, they have higher average evaporation rates throughout the year (Figure 2.16 and Table

2.3). It should also be noted that the differences in evapotranspiration during the middle of the winter are quite large (this is hard to see in Figure 2.16 because of the log scale).

Figure 2.17 shows difference in water table dynamics between the cases. Although porosity and hydraulic conductivity have a more pronounced effect on water table depth, the effect of Van Genuchten parameters $\alpha$ and n becomes more apparent for cases with higher $K_{sat}$ and $\phi$ values. For instance, case S2L.s3 and case S2L.s2 have similar responses to rainfall events, but the higher α and n for case S2L.s3 produce a shallower water table around the peak than for case S2L.s2 (Figure 2.17). The latter case dries out faster especially at the peaks and during summer.

Water table trends are similar for cases with similar $K_{sat}$ and $\phi$ values, and these are translated to the latent heat flux and ground surface temperature profiles and scatter plots shown in Figure 2.18 and Figure 2.19. Cases with smaller $K_{sat}$ and $\phi$ (S2L.s4 and S2L.s6) have much wider saturated areas around the valleys and thus a much wider zone 1. The effect of the shallow water table is also apparent for these two cases since the extent of the dry, decoupled zone 3 is very small. Most of the hillside for these cases is in the critical zone (zone 2). These figures also show the effect of Van Genuchten properties on the energy balance and coupling between water table depth and energy fluxes. Sharper transition zones and wider ranges of variability in LE and tg are observed for cases with higher Van Genuchten properties (S2L.s6 compared to S2L.s4, and S2L.s3 compared to S2L.s2).

These cases show that $K_{sat}$ and $\phi$ have a larger effect on streamflow and evaporation, water table dynamics, and coupling trends between water table depth and the land surface energy fluxes than the Van Genuchten parameters. The effects of α and n on the subsurface-land surface coupling, however, is still apparent and increases with increasing $K_{sat}$ and $\phi$.

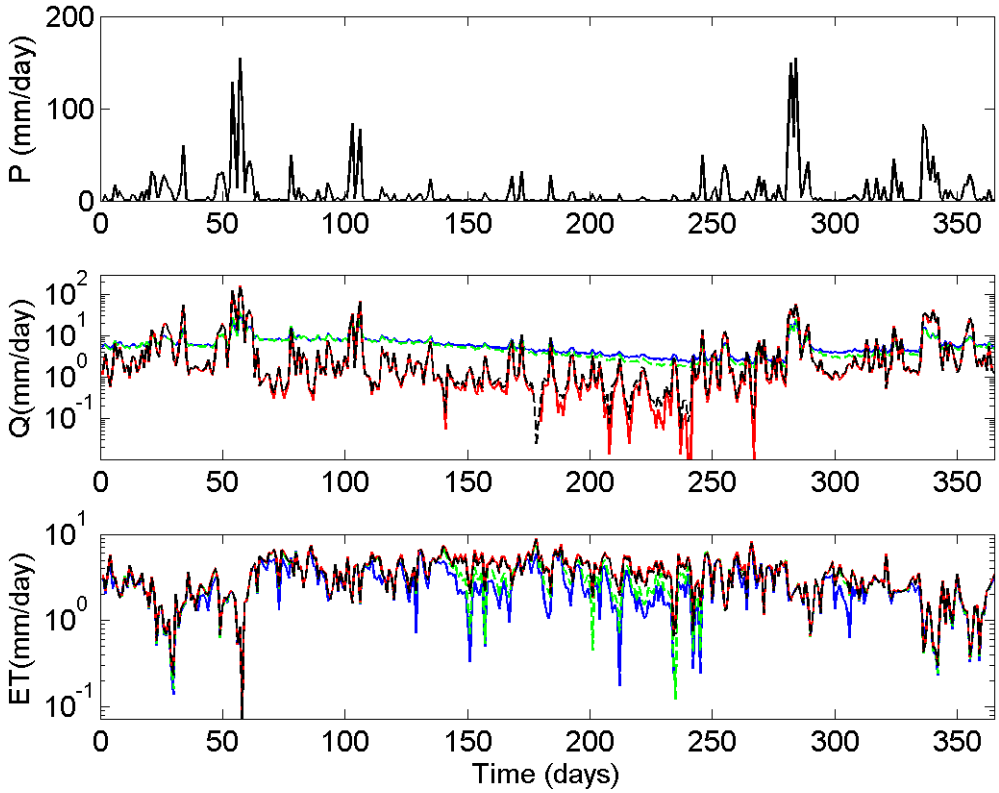


Figure 2.16: Daily-averaged outflow (Q) and evapotranspiration (ET) in (mm/day) on a log-scale from the valley outlets of cases: S2L.s3 (blue), S2L.s2 (green), S2L.s4 (red) and S2L.s6 (black). The top plot shows daily-averaged precipitation (P) in (mm/day).

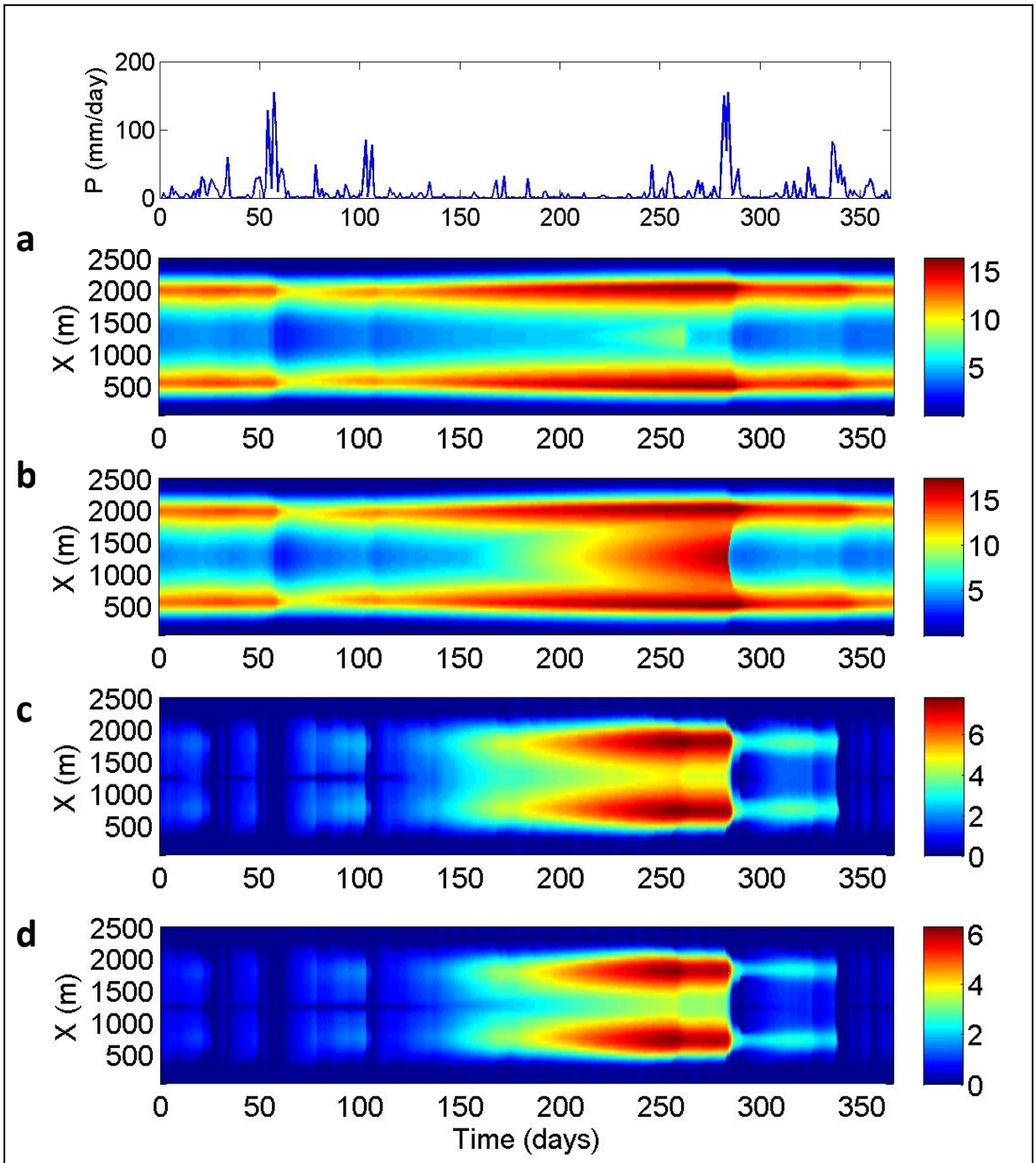


Figure 2.17: Water table depth variations in the x-direction with time for the final spin-up year for cases: (a) S2L.s3, (b) S2L.s2, (c) S2L.s4, and (d) S2L.s6. Color bar shows water table depth in meters. Note the plots are shown for the first sinusoid only. The top plot shows daily-averaged precipitation in (mm/day).

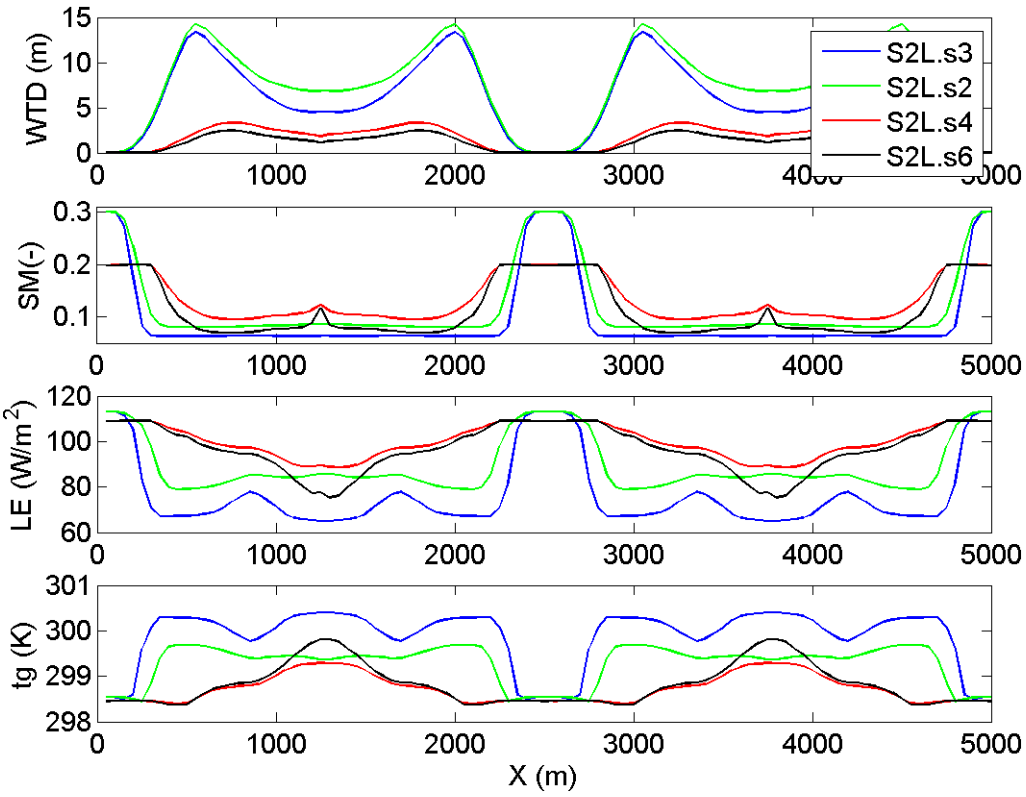


Figure 2.18: Water table depth (m), soil moisture at the land surface (-), latent heat flux ($W/m^2$), and ground surface temperature (K) versus X (m) for cases: S2L.s3, S2L.s2, S2L.s4, and S2L.s6. Small asymmetries in the averaged profiles are due to slight misalignment of the grid and topography.

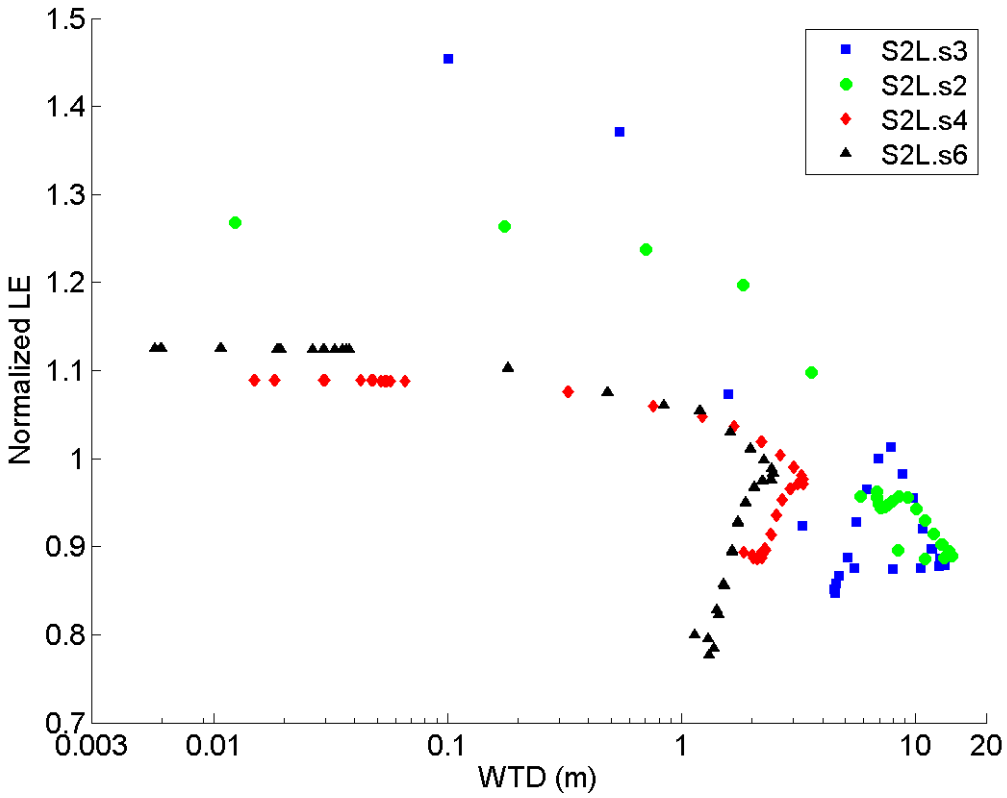


Figure 2.19: Semi-logarithmic scatter plots of yearly averaged latent heat flux ($W/m^2$) versus water table depth (m) for cases: S2L.s3, S2L.s2, S2L.s4, and S2L.s6.

### 2.4.5 Effects of land cover

So far we have demonstrated the effects of subsurface formation and properties on water distribution between the land surface and subsurface, and the subsequent effects on the energy fluxes at the land surface for bare soil. Vegetation also has an influence on the energy balance at the land surface and these correlations are highly dependent on the parameterizations used (Kollet and Maxwell, 2008). The effects of vegetation are demonstrated here by comparing the base case (S2L.s3) to two other cases with savanna and tropical forest land cover (S2L.s3.sav and S2L.s3.for in Table 2.1).

Time series of runoff and evapotranspiration in Figure 2.20 show that runoff trends are very similar between the three cases, except in the amount of baseflow produced. Savanna land cover produces more average runoff and baseflow than bare soil, while the forested case has the smallest baseflow of the three cases (Table 2.3). Figure 2.21 shows that the differences between the three cases are very small in terms of water table depth and soil moisture at the land surface.

Although all these cases have similar subsurface properties and atmospheric forcing, the water table for the forested case is slightly deeper because the trees tap into the deeper groundwater during dry summer months with limited rainfall.

While all three cases have similar latent heat profiles in terms of locations of transition zones coupled to water table depth, the effect of vegetation appears in shifted magnitudes of evapotranspiration and latent heat flux. The forest has the largest LE values, which is expected for this vegetation type. The savanna vegetation type has smaller LE values than bare soil (Figure 2.20 and Figure 2.21). This agrees with the findings of Kollet and Maxwell (2008) for grassland compared to bare soil. Although the latent heat flux increases in the transition zones for all cases, the ground surface temperature for the savanna case either remains constant or increases. This is because of the way grass and plant resistances are parameterized in CLM (and other LSMs) which results in bare soil evaporation being greater than evapotranspiration from grass cover (Kollet and Maxwell, 2008).

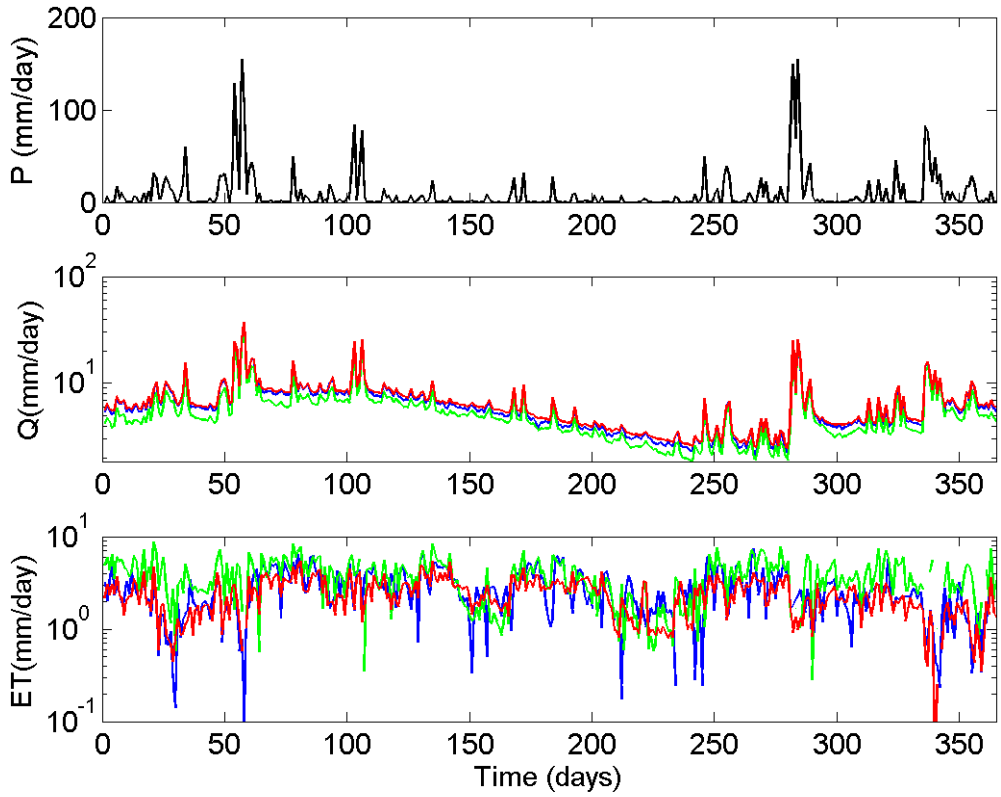


Figure 2.20: Daily-averaged outflow (Q) and evapotranspiration (ET) in (mm/day) on a log-scale from the valley outlets of cases: S2L.s3 (blue), S2L.s3.for (green), and S2L.s3.sav (red). The top plot shows daily-averaged precipitation (P) in (mm/day).

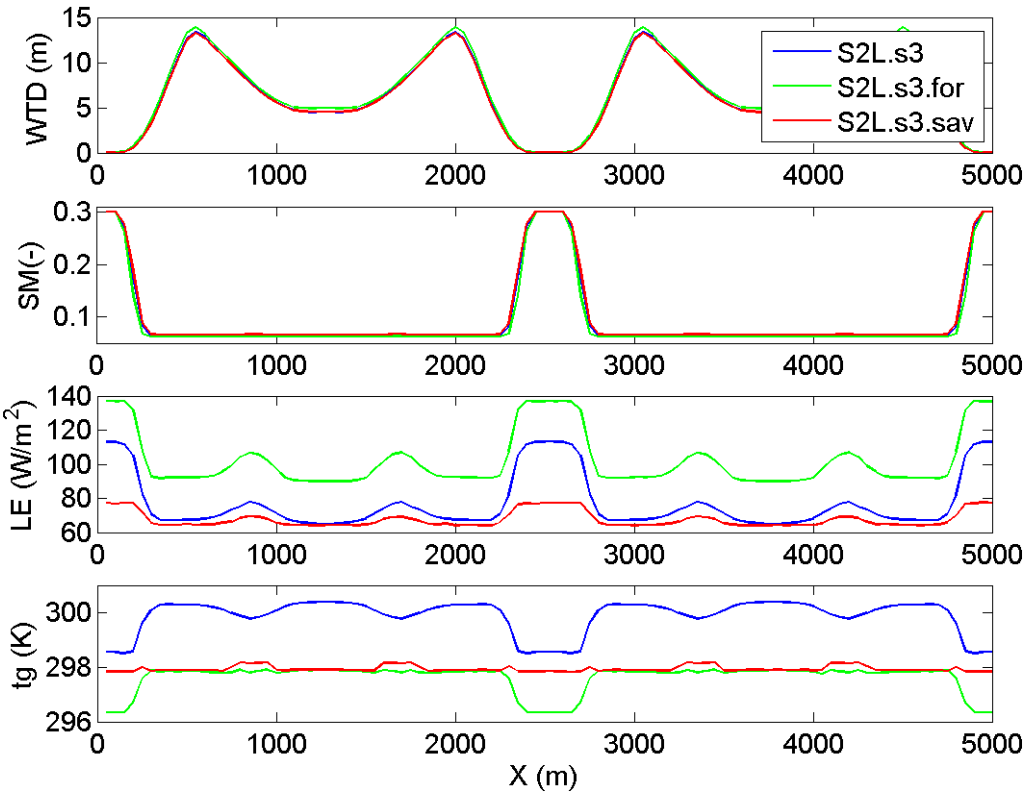


Figure 2.21: Water table depth (m) , soil moisture at the land surface (-), latent heat flux (W/m$^2$), and ground surface temperature (K) versus X (m) for cases: S2L.s3, S2L.s3.for, and S2L.s3.sav.

### 2.4.6 Effects of atmospheric conditions

Finally, the effect of different atmospheric forcing is studied by comparing two climatic regions: the base case (S2L.s3) forced by the tropical dataset and case (S2L.s3.SA) forced with the semi-arid dataset. The semi-arid dataset (Figure 2.3) is characterized by greater seasonal variation in the solar radiation and temperature, less rainfall, and lower ambient temperatures than the tropical forcing.

As would be expected, the runoff for S2L.s3.SA is much reduced (Table 2.3) as these are two very different climatologies with different amounts of precipitation. Despite these differences, both cases show similar trends in correlation between water table depth and latent heat flux (Figure 2.22 and Figure 2.23). Both cases have a maximum water table depth on the hillside rather than the peak (due to the variability in top layer thickness), but the water table is generally too deep in case S2L.s3.SA to have transition zones at these locations and thus we do not see any coupling with land surface fluxes on the hillside for this case. That the general pattern of water

table depth and surface fluxes are maintained despite the large difference in forcing, indicates that correlations between groundwater and land-energy fluxes are maintained across climatological regions.

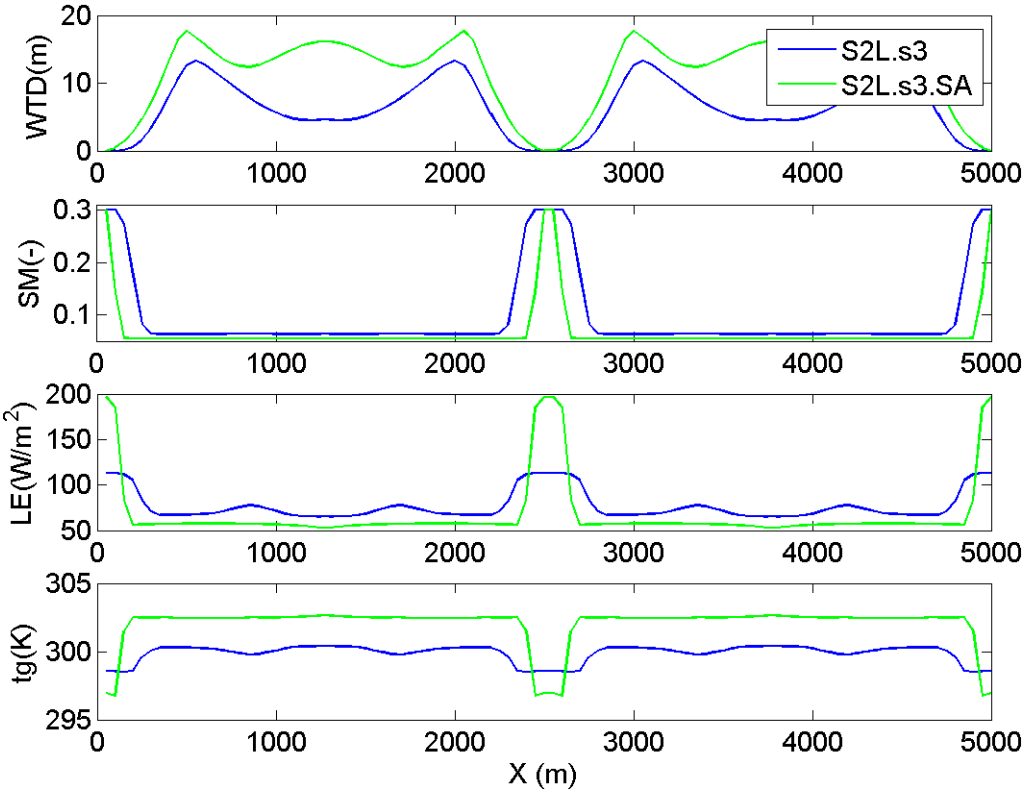


Figure 2.22: Water table depth (m) , soil moisture at the land surface (-), latent heat flux ($W/m^2$), and ground surface temperature (K) versus X (m) for cases: S2L.s3 and S2L.s3.SA.

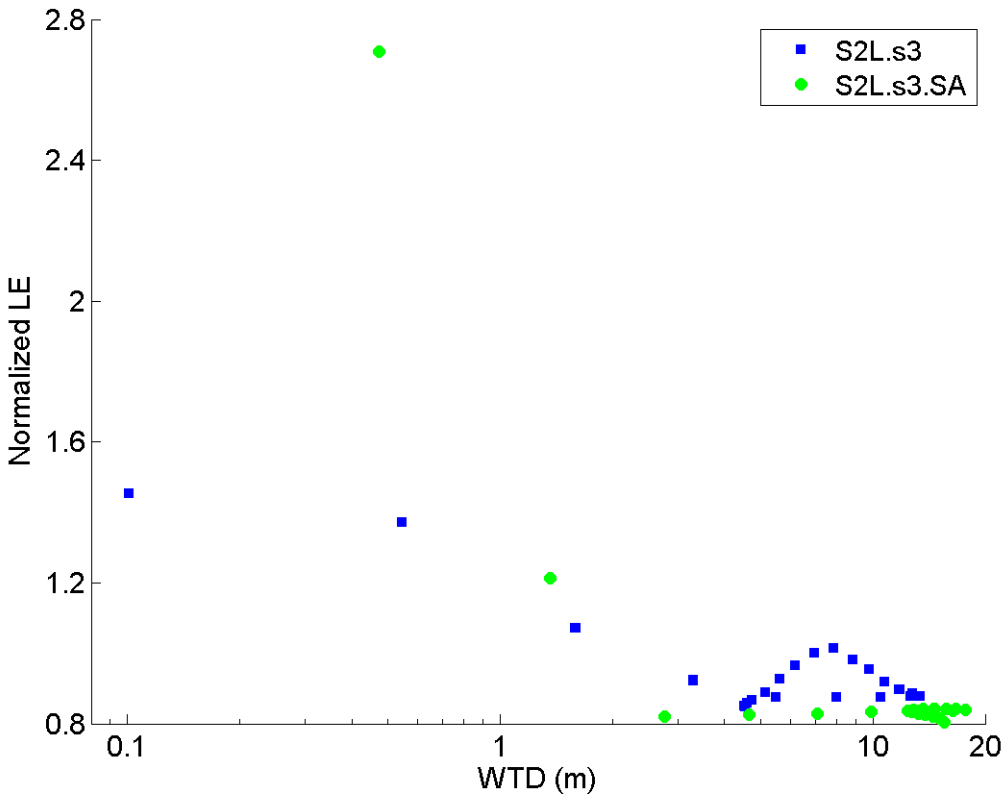


Figure 2.23**:** Semi-logarithmic scatter plots of yearly averaged latent heat flux ($W/m^2$) versus water table depth (m) for cases: S2L.s3 and S2L.s3.SA.

## 2.5 Conclusions

Idealized simulations were conducted with the coupled groundwater-land-surface code PF.CLM for different terrain, subsurface layering and soil properties, vegetation type, and atmospheric conditions to isolate the influences of these features on coupling of land-surface and subsurface processes. General conclusions that were reached in this work are summarized as responses to the four questions posed in the introduction:

(1) *What are the effects of terrain, subsurface properties, and land cover on water table variability?* Variations in terrain slope and top layer thickness directly affect the water table depth by changing the fraction of infiltration into the subsurface versus horizontal surface and subsurface flow within the top layer. Land surface slopes have some effect on the spatial variation of the water table, but a greater effect on overall runoff and ET. Subsurface properties like conductivity and porosity show a larger effect on water table

dynamics than the Van Genuchten parameters, although the latter become more pronounced at higher conductivity and porosity values. Vegetative land cover had a small effect on water table dynamics relative to subsurface properties and terrain. Based on our results, although terrain and land surface slope have a prominent effect, subsurface formations and properties have the strongest effect on changing water table dynamics and responses to atmospheric forcing.

(2) *What affects the correlation between water table depth and land surface fluxes?* Strong correlations are found between the land surface fluxes and water table depth across all cases, including terrain shape, subsurface heterogeneity, vegetation type and climatological region. Water table and surface soil moisture responses to atmospheric forcing become more pronounced and more complicated as more subsurface layers are introduced. Variable top layer thickness does not have a great effect on integrated measures such as outflow or total ET, but it affects the coupling and spatial variation of water table depth and latent heat flux at the land surface. In general these differences are smaller than the differences between a layered and homogenous system. Vegetative land cover affects the magnitude of energy fluxes at the land surface but not the general spatial pattern. Thus we find that the correlation between water table depth and land surface fluxes is mostly affected by subsurface formation (layering) and properties, with terrain shape and land surface slopes also having an effect. These effects are not overcome by different climate forcing or vegetation types.

*(3) Which locations within a watershed show stronger feedbacks between the water table and the land surface?* The results demonstrate a strong relation between water table depth and land surface energy fluxes, in particular in certain transitional areas (critical zones). These critical zones exist between regions of very shallow and very deep water table. Terrain, subsurface formations and soil properties are identified as having the strongest effect on the location, extent, and strength of coupling (critical zones) between water table depth and energy fluxes.

(4) *How does climate and atmospheric forcing affect the coupling and feedbacks?* Both the semi-arid and tropical forcing datasets produced similar correlations between land-energy balance and groundwater storage. Although steeper and narrower transition zones of coupling between water table depth and latent heat flux are observed for the drier climate, the general trends are similar to the wet climate and in fact resemble what those correlations would look like when observed on a dry day within the tropical climate.

Clearly the answers to these questions are even more complicated for a real watershed with highly variable terrain, vegetation, soil and atmospheric conditions. Our idealized results, however, demonstrate that lateral surface and subsurface flows have a great effect on land surface fluxes even for very simplistic terrain and geologic settings. Features such as subsurface heterogeneity combined with lateral flow under realistic conditions will certainly affect land surface fluxes, which will in turn have an effect on the atmosphere and alter the hydrologic feedback cycle (Maxwell and Kollet 2008a).

Our results indicate that observational studies should jointly consider taking measurements of land-energy and hydrologic variables as there is a great need for study sites with coexisting subsurface, surface, and atmospheric observations of flow and energy fluxes to validate coupled modeling studies. These studies should also characterize subsurface heterogeneity and use the findings presented here to guide the temporal and spatial resolution of observations. Furthermore, this work suggests that because terrain shape and subsurface heterogeneity alter surface fluxes, these in turn will impact development of the atmospheric boundary layer (see e.g. Maxwell et al 2007). This implied connection between the subsurface and the atmosphere is the subject of the following chapters.

# Chapter 3

## Idealized Simulations to Diagnose Land-Atmosphere Feedbacks

While chapter 2 examined the connection between the subsurface and the land surface, here we focus on the connection between the land surface and the atmosphere. Effects of terrain, subsurface properties, and soil moisture heterogeneity on the development and behavior of the atmospheric boundary layer are studied through a set of idealized numerical experiments. The mesoscale atmospheric model ARPS (Advanced Regional Prediction System) is used to perform three-dimensional simulations initialized with detailed soil moisture distributions obtained from offline spin-ups using a coupled land surface-subsurface model (presented in chapter 2). As expected, model results show terrain-induced convective circulations caused by variable heating and cooling at the land surface. However, results also indicate that water table dynamics and subsurface properties, reflected in soil moisture profiles at the land surface, produce a similar effect and can even have a clear signature over that of terrain particularly on land surface energy fluxes and the development of the mixed boundary layer during early morning hours.

### 3.1 Introduction

Land surface models are used as a lower boundary condition to provide heat and moisture fluxes for atmospheric models. This is typically done in an idealized fashion, and effects of water table and subsurface flows on the atmospheric boundary layer have not been considered until recently (Maxwell et al., 2007). Common practice is to decouple different parts of the hydrologic cycle in numerical models. Although previous studies have shown sensitivity of atmospheric processes to land surface and subsurface conditions (Taylor and Lebel, 1998; Clark et al, 2004; Yeh and Eltahir, 2005; Kollet and Maxwell, 2008; Seuffert et al., 2002; York et al., 2002; Maxwell et al., 2007), the extent of these interactions is not yet fully understood. A sufficient understanding is needed of the circumstances under which these coupled processes might play a more significant role and when they might be simplified into the decoupled systems so frequently modeled in practice. This chapter presents a set of idealized coupled simulations designed to isolate and characterize effects of soil moisture heterogeneity, terrain, and subsurface properties on atmospheric boundary layer development.

The importance of land surface processes to the overlying planetary boundary layer (PBL) has been recognized in the literature (see review by Pielke, 2001). Land surface heating and cooling control the development of turbulence and convective circulations which determine the structure of the PBL. The connection between land surface fluxes and soil moisture heterogeneity and land use has also been well documented (Ookouchi et al. 1984, Banta and Gannon 1995, Seuffert et al. 2002, Desai et al. 2006, Chow et al. 2006). This connection between surface soil moisture and PBL development has been shown to be more important than increasing a model's grid resolution for improving model results (Chow et al. 2006). Thus, it is important to have an accurate representation of surface hydrological processes and lateral water transport in the soil model (Seuffert et al. 2002).

Furthermore, the link between spatial distribution of rainfall on one hand, and land cover type and topography on the other has been observed (Da Silva et al, 2008; Clark et al, 2004; Avissar and Liu, 1996, Chen and Avissar, 1994). These studies suggest that increased deforestation in the Western part of Amazon basin induces significant decrease in precipitation during El-Nino events (Da Silva et al. 2008). Observations of Sahelian rainfall patterns show that successive rainfall events are not independent at convective length scales of approximately 10 km (Taylor and Lebel 1998). Taylor and Lebel argued that land–atmosphere feedbacks remain the most likely explanation for this rainfall persistence. Furthermore, coupled land-atmosphere simulations of semiarid conditions typical of the Sahel indicate strong feedbacks between spatial soil moisture variability caused by convective rainfall and boundary layer variability (Clark et al, 2004). D'Odorico and Porporato (2004) demonstrate similar observations of rainfall persistence and soil moisture-rainfall recycling in continental midlatitude regions. Avissar and Liu (1996) simulated different patterns of land surface wetness using a regional atmospheric mesoscale model and deduced that spatial distribution of clouds and precipitation is strongly affected by the landscape structure. They concluded that mesoscale circulations generated by landscape heterogeneities are stronger than thermal cells induced by turbulence. Accordingly, changes in landscape properties (vegetation and surface soil moisture) affect the climate system as much as atmospheric processes such as energy and moisture transport and cloud activity (Pielke, 2001).

Effects of terrain, land cover, and subsurface layering and properties on water table dynamics are demonstrated in chapter 2. Variability in water table depth induces variability in soil moisture at the land surface which closely relates to the PBL depth. For instance a shallow water table corresponds to wetter soils which induce higher evaporation rates, cooler soil temperatures, and thus a shallower PBL.Using a coupled groundwater-atmosphere model, Maxwell et al (2007) found a close relationship exists between water table depth and the atmospheric boundary layer depth, particularly during early morning hours.

Despite numerous field and modeling studies, however, the connection between the land surface and the atmosphere remains difficult to quantify. In particular, with real terrain and atmospheric conditions, it can be difficult to isolate the role of land-atmosphere feedbacks if other effects are dominant. Maxwell et al. (2007), for example, specifically chose to turn off lateral boundary forcing so that the influence of the soil moisture on the atmosphere would not be overshadowed by synoptic winds. A useful approach is often to use idealized simulations to study a particular physical mechanism in detail before attempting to analyze the mechanism in its normal context (a real case). The effect of soil moisture heterogeneity on the PBL was studied by Patton et al (2005) through a set of idealized numerical simulations on wet and dry convective boundary layers. They found that strip-like soil moisture heterogeneity dramatically alters the structure of the convective boundary layer by inducing significant organized circulations that modify turbulent statistics. Patton's results are part of the motivation behind this work which investigates these effects using realistic soil moisture profiles and terrain. Using detailed soil moisture profiles, induced by terrain and subsurface properties, allow for various effects to be recognized and isolated. The questions discussed in this chapter are:

1. What is the relative importance of terrain and soil moisture variability on the development and structure of the atmospheric boundary layer? What times within a diurnal cycle show stronger surface-atmospheric feedbacks?

2. How do subsurface properties (reflected in soil moisture initialization profiles) affect the structure and depth of the PBL?

3. Can we gain a better understanding of the processes which drive the atmospheric boundary layer by initializing atmospheric simulations with detailed soil–moisture profiles obtained from offline-simulations using realistic terrain and subsurface properties, rather than using uniform or simplified soil moisture profiles?

It should be noted since the simulations described in this chapter are uncoupled to the subsurface; effects of water table depth are included indirectly through soil moisture profiles extracted from the coupled land surface-subsurface simulations of chapter 2. Previous studies which looked into the influence of the land-surface on the atmospheric boundary layer have used offline hydrologic model results to force atmospheric simulations (e.g. Chow et al. 2006). The simulations described here are also based on idealized domains designed to illustrate land-atmosphere feedbacks and effects of surface and subsurface properties on atmospheric boundary layer development. Sinusoidal terrain is used to represent an idealized valley with various land properties. The modeling tool for this study consists of the atmospheric mesoscale model (ARPS) described below. The idealized simulations are designed to answer the questions posed above.

## 3.2 The Advanced Regional Prediction System (ARPS)

ARPS is a parallel, meso-scale atmospheric model designed for prediction of convective storms and serves as an effective tool for studying the dynamics and predictability of storm-scale weather in both idealized and more realistic settings. It was developed at the Center for Analysis and Prediction of Storms (CAPS) at the University of Oklahoma (Xue et al. 2000, Xue et al. 2001). ARPS solves the three-dimensional, compressible, non-hydrostatic, spatially-filtered Navier–Stokes equations and can be run in LES mode. Its governing equations (Appendix B) employ a terrain-following curvilinear coordinate system and include equations for conservation of mass, momentum, heat, water (vapor, liquid and ice), turbulent kinetic energy (TKE), and the equation of state of moist air. ARPS employs high-order monotonic advection schemes for scalar transport and fourth-order advection for other variables. A split-explicit time advancement scheme is used with leapfrog on the large time steps, and a forward-backward scheme for the smaller timesteps used to integrate the acoustic terms in the equations.

## 3.3 Conceptual approach

### 3.3.1 Atmospheric simulations

Simulations are setup with zero initial winds and no lateral forcing. Surface heat fluxes are provided by the ARPS land-surface model. Bare soil conditions were used, and the terrain is assumed homogeneous in the y-direction, and sinusoidal in x as follows:

$$h(x) = a\sin\left(\frac{2\pi x}{L} - \frac{\pi}{2}\right) + a \qquad \text{(Equation 3.1)}$$

where $h$ is the height of terrain above reference level $h_o$, $a$ is the amplitude, and $L$ is the wavelength. This idealized topography allows us to explore the role of land-atmosphere coupling in a domain that includes terrain-induced processes such as overland flow, surface runoff, lateral subsurface flow, and thermally induced slope flows in the atmosphere.

A hill height of 80 m is chosen to generate smoothly varying topography that allows realistic subsurface behavior for the given grid spacing (the hill slopes need to be well resolved). The atmosphere domain size (designed to match the x-horizontal subsurface grid from the 2D simulations in chapter 2) is 5 km x 2.5 km x 10 km. A horizontal grid size of 50 m is used for the atmospheric model. Stretching is applied in the vertical direction with an average grid size of 150 m and a minimum of 30 m at the land surface. Soil type for ARPS was chosen from the soil categories provided in the code (based on USDA definitions) and matched to subsurface input parameters (saturated hydraulic conductivity and porosity) used in the PF.CLM simulations in Chapter 2. Periodic lateral boundary conditions are applied while a rigid wall boundary is employed at the top of the model. The atmospheric model is initialized with constant dry moisture content (1 g/kg) and potential temperature starting at (300 K) at the land surface with a constant stable stratification (3 K/km) through the entire domain (Figure 3.1). The model is initialized with heterogeneous soil moisture profiles obtained from the offline simulations performed by the coupled groundwater-land surface model PF.CLM (chapter 2) as explained in the next section.

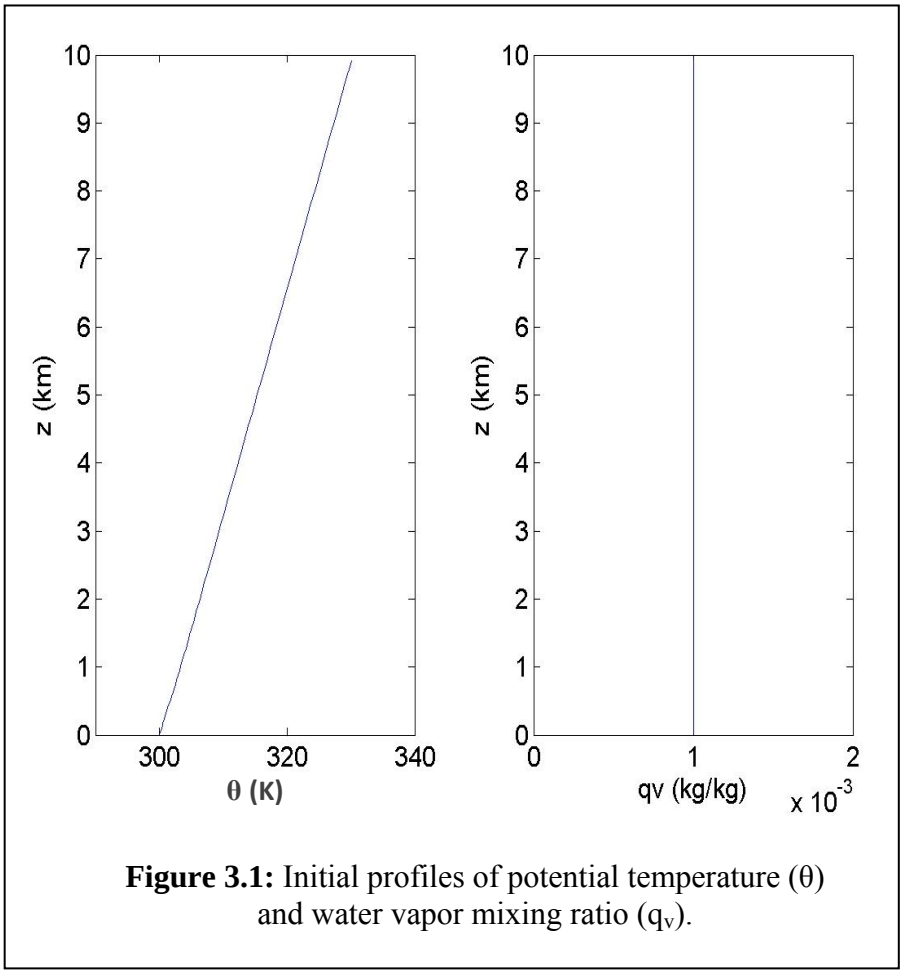


**Figure 3.1:** Initial profiles of potential temperature (θ) and water vapor mixing ratio ($q_v$).

### 3.3.2 Soil moisture initializations: PF.CLM offline spin-ups

ParFlow coupled to the Common Land Model, PF.CLM, (Dai et al. 2003, Maxwell and Miller, 2005) was used to initialize the atmospheric model with realistic soil moisture profiles. These soil moisture profiles were obtained by applying an offline spin-up process in which PF.CLM was repeatedly forced with an atmospheric data time series until water and energy equilibrium is reached. The model is considered spun-up when the change in water and energy storage between two consecutive years of simulation drops below a pre-determined threshold. Soil moisture profiles at the land surface are then extracted from these offline spinup cases, and are used as initial soil moisture conditions for the atmospheric simulations. This section recaps the spinup procedure (described more extensively in chapter 2) while highlighting properties of the three SW-GW cases used in this chapter to isolate effects of soil moisture heterogeneity and subsurface properties on the atmospheric boundary layer.

A two dimensional (x-z) domain was designed for the PF.CLM spin-up simulations such that the lateral grid matches the lateral extent of the atmospheric domain. A domain size of 5 km in x and 80 m in z is chosen with a lateral grid spacing of 50 m, vertical spacing of 0.1 m, and idealized

sinusoidal terrain as described in the previous chapter (Figure 3.2). Cases with flat terrain and similar grid are also simulated to compare against hilly (sinusoidal) terrain. Two subsurface formations are introduced in the PF.CLM spinups; a homogeneous low permeability-low porosity layer (hereafter referred to as the lower layer) underlying a homogeneous high permeability-high porosity layer (hereafter referred to as the top layer). Overland flow with no vegetation is applied at the land surface (top boundary) while no flow boundary conditions are applied for the lateral and bottom subsurface boundaries. PF.CLM allows river outflow to leave the domain (at the base of the valleys) as part of the overland flow boundary condition.

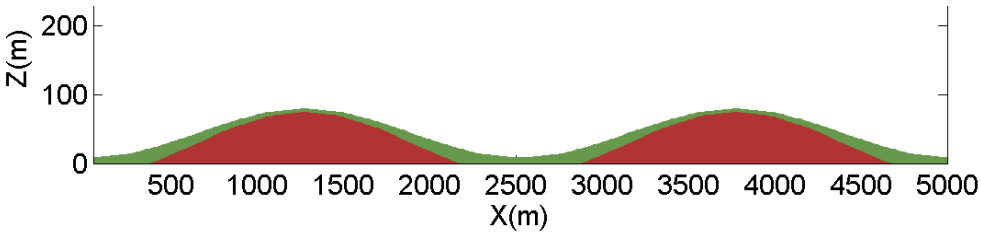


**Figure 3.2**: Subsurface formations for the idealized surface-subsurface sinusoid cases.

**Subsurface properties:**

Three cases with different idealized subsurface heterogeneities (Table 3.1) are used, to obtain different soil moisture initializations, by varying the saturated hydraulic conductivity [L/T], porosity [-], and Van Genuchten Parameters. The Van Genuchten formulation relates relative (unsaturated) permeability, $k_r$ [-] and relative saturation, $S_w$ [-], to the subsurface pressure head, $\psi_p$ [L], as follows (Van Genuchten, 1980; Kollet and Maxwell, 2006):

$$S_w(\psi_p) = \frac{S_{sat} - S_{res}}{(1 + (\alpha\psi_p)^n)^{(1-1/n)}} + S_{res} \qquad \text{(Equation 3.2)}$$

$$k_r(\psi_p) = \frac{\left(1 - \frac{(\alpha\psi_p)^{(n-1)}}{(1 + (\alpha\psi_p)^n)^{(1-1/n)}}\right)^2}{(1 + (\alpha\psi_p)^n)^{\frac{(1-1/n)}{2}}} \qquad \text{(Equation 3.3)}$$

Where $\alpha$ [$L^{-1}$] and $n$ [-] are the Van Genuchten soil parameters, $S_{sat}$ [-] is the saturation at saturated conditions and $S_{res}$ [-] is the residual saturation. $S_{res}$ ranges from zero (for completely dry soil) to one (for fully saturated soil) while $S_{sat}$ has the value of one.

Each of the three different cases in Table 3.1 has two layers as shown in Figure 3.2, a high-permeability, high-porosity layer overlying low-permeability, low-porosity layer, with

homogeneous subsurface properties within each layer. The values chosen are within ranges observed in Schaap and Leij (1998). Similar lower layer properties are used for all cases, but different parameters are used for the top layer. These three cases correspond to cases S2L.s2, S2L.s3, and S2L.s4 in chapter 2. For simplicity, in this chapter these cases are referred to as case1, case2, and case3, respectively. Comparing case1 to case3, for example, will highlight the effect of having different saturated hydraulic conductivity and porosity, while comparing case1 to case2 will show the effect of Van Genuchten parameters $\alpha$ and $n$.

**Table 3.1**: Properties of the three idealized PF.CLM cases used to initialize the ARPS atmospheric simulations

| Idealized case | Layers | $K_{sat}$ | Ø | α | *n* | $S_{res}$ | $S_{sat}$ |
|---|---|---|---|---|---|---|---|
| **Case1** | Top | 24 | 0.3 | 1.50 | 2.00 | 0.177 | 1 |
| | Bottom | 0.096 | 0.01 | 10.0 | 2.00 | 0.100 | 1 |
| **Case2** | Top | 24 | 0.3 | 3.55 | 3.16 | 0.177 | 1 |
| | Bottom | 0.096 | 0.01 | 10.0 | 2.00 | 0.100 | 1 |
| **Case3** | Top | 2.4 | 0.2 | 1.50 | 2.00 | 0.177 | 1 |
| | Bottom | 0.096 | 0.01 | 10.0 | 2.00 | 0.100 | 1 |

**$K_{sat}$**: Saturated Hydraulic conductivity (m/day)
**Ø**: Effective soil porosity
**α**: Van Genuchten alpha (1/m)
**n**: Van Genuchten exponent
**$S_{res}$**: Residual Saturation
**$S_{sat}$**: Saturation at saturated conditions

**Climatic conditions:**

Each of the cases in Table 3.1 was repeatedly forced with a year-long synthetic tropical data set (Pitman and Henderson-Sellers, 1995) as explained in Chapter 2. The forcing was set as spatially uniform and includes incoming shortwave and longwave radiation, precipitation, surface air temperature, wind velocity, surface pressure and humidity. The forcing is characteristic of a typical tropical region in the Southern hemisphere where incoming solar radiation and ambient temperature changes during the year are not large. It is also characterized by large amounts of precipitation with some seasonal effect.

The literature suggests that land surface-PBL feedbacks become stronger as soil moisture heterogeneity increases. The tropical forcing was chosen here because the large amounts of rain throughout the year, along with the chosen subsurface properties, are reflected in the water table response such that resulting soil moisture profiles at the land surface are very heterogeneous (Figures 3.3, 3.4, and 3.5). These profiles are characterized with abrupt transitions between wet and dry zones and are somewhat similar to the idealized patchy profiles simulated in Patton et al. (2005), though the "patches" here are generated by topography-driven hydrologic processes. This provides one extreme of soil moisture heterogeneity with very strong feedbacks. The

opposite extreme would be cases with homogeneous soil moisture initialization (e.g. fully saturated or fully dry).

**Saturation profiles**

Two times of the year are chosen to extract saturation profiles from the PF.CLM spinups; the beginning of a large storm on March 18$^{th}$, and during a small storm on November 4$^{th}$. Saturation profiles at the top two soil layers are extracted at these times for all three cases in Table 3.1 (as shown in Figures 3.3a, 3.4a, and 3.5a). Snapshots of the resulting saturation field for these times are also shown in Figures 3.3b, 3.4b, and 3.5b for the March 18$^{th}$ storm, and in Figures 3.3c, 3.4c, and 3.5c for the November 4$^{th}$ storm. It should be noted that the March 18$^{th}$ storm occurs during the rainy season and thus the subsurface is more saturated relative to conditions preceding the November 4$^{th}$ storm which actually occurs after a drier period.

The general trends are similar between the three cases as shown in these figures. For example, water table depth is shallow in the valleys and grows deeper along the hill sides and hill tops which results in fully saturated soils at and around the lowest valley points where outflow occurs during and after precipitation. Different subsurface properties between the three cases, however, produce clear differences in saturation profiles along the hill sides and hilltops, as well as differences in the dynamics of how a wetting front might move downhill during a storm. Profiles for all three cases are plotted against each other in Figure 3.6 to emphasize these differences. For instance, lower saturated hydraulic conductivity and porosity for case 3 results in a shallower water table for this case (Figure 3.5b and c) which now has a wider saturated region around the valleys than cases 1 and 2 during both times of the year (Figure 3.6). On the other hand, higher hydraulic conductivity and porosity values in cases 1 and 2 allow precipitated water to infiltrate more readily and flow laterally as well as vertically downhill through the high permeability layer. This results in sharper transitions between the wet (fully saturated) valleys and the drier region around the hilltops.

Another apparent difference is in the wetting behavior of these cases. The hill tops in cases 1 and 3 (with similar Van Genuchten properties) start saturating more quickly than surrounding areas. The transition in soil moisture between the peaks and hill sides is affected by both properties of the top layer and saturation and weather conditions preceding the storm. Case 1 with higher hydraulic conductivity and porosity exhibits a smooth transition during both storms and times of the year. In contrast, case 3 shows a very sharp transition during the wet season (March 18$^{th}$ storm) and much smoother transition during the drier season around the November storm. Case 2, on the other hand, with higher Van Genuchten properties than both cases 1 and 3 exhibits a different wetting behavior in which the hill sides saturate quicker than the hill top during both storms. This is also apparent in the saturation field in Figures 3.4b and c.

Each of the previously described saturation profiles are converted to soil moisture profiles at the land surface which are used to initialize a set of atmospheric simulation cases shown in Table 3.2. The table also shows two cases (flat and sinusoidal terrain) initialized with homogeneous soil moisture equal to half the saturation value. These cases are meant to demonstrate the effects of initializing an atmospheric model with realistic a soil moisture profile obtained from running a

hydrologic model offline, versus initializing with a uniform value throughout the domain. Each case is run for 36 hours starting at 8 am. The first day of simulation was intended as a spinup period, but the results are very clear and useful even during the spinup period which is why the results presented in the next section are from that first day.

Different effects are isolated and established in each case as explained in the following sections. Since no external forcing is imposed on the domain, boundary layer development is driven by diurnal variations of incoming solar radiation, terrain, and soil moisture heterogeneity.

**Table 3.2**: Idealized atmospheric simulation cases

| ARPS case | Terrain | Soil Moisture Initialization |
|---|---|---|
| Flat0 | Flat | homogeneous at half saturation |
| Flat1_Mar | Flat | PF.CLM case1 Mar 18$^{th}$ profile |
| Flat1_Nov | Flat | PF.CLM case1 Nov 4$^{th}$ profile |
| Sin0 | Sinusoid | homogeneous at half saturation |
| Sin1_Mar | Sinusoid | PF.CLM case1 Mar 18$^{th}$ profile |
| Sin1_Nov | Sinusoid | PF.CLM case1 Nov 4$^{th}$ profile |
| Sin2_Mar | Sinusoid | PF.CLM case2 Mar 18$^{th}$ profile |
| Sin2_Nov | Sinusoid | PF.CLM case2 Nov 4$^{th}$ profile |
| Sin3_Mar | Sinusoid | PF.CLM case3 Mar 18$^{th}$ profile |
| Sin3_Nov | Sinusoid | PF.CLM case3 Nov 4$^{th}$ profile |

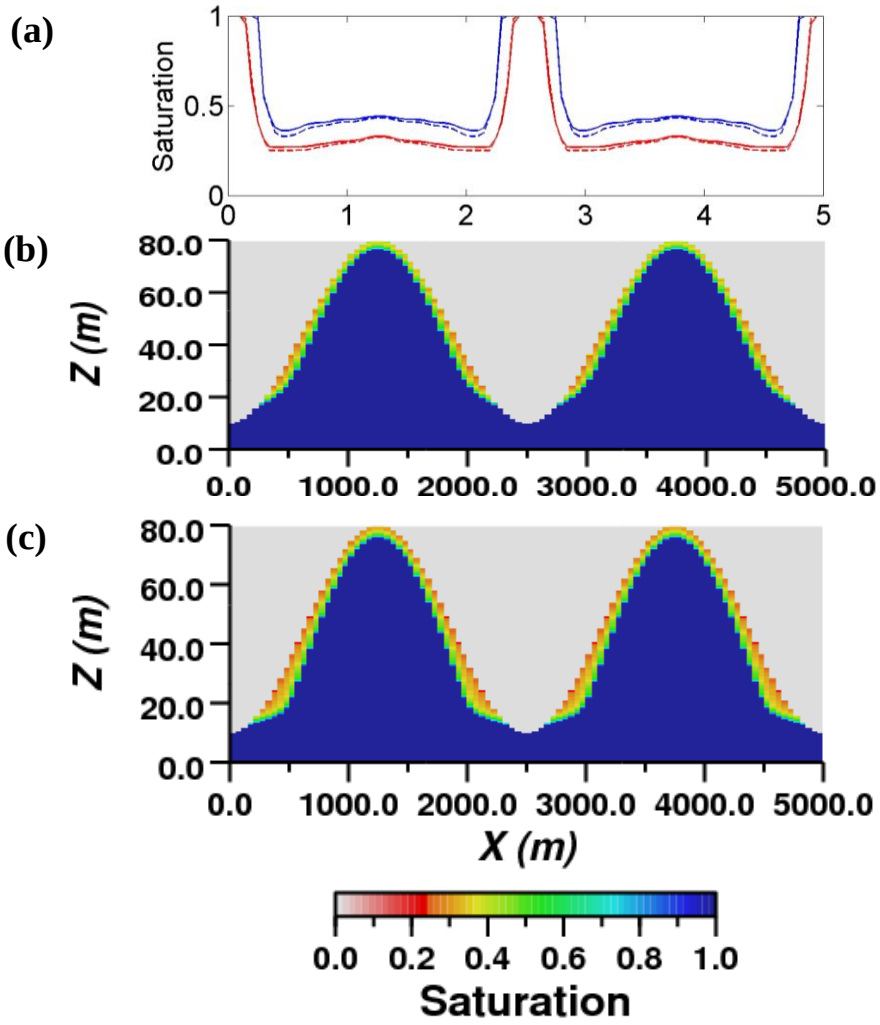


**Figure 3.3**: PF.CLM results for case1 used to initialize ARPS simulations: (a) Saturation profiles at the land surface for March 18th (blue lines) and November 4th (red lines). Solid lines are for the top soil layer, dashed lines are for the second soil layer, (b) Subsurface saturation field snapshot at the beginning of a large storm on March 18th, (c) Subsurface saturation field snapshot during a storm on November 4th. Vertical scale in (b) and (c) is exaggerated for clarity.

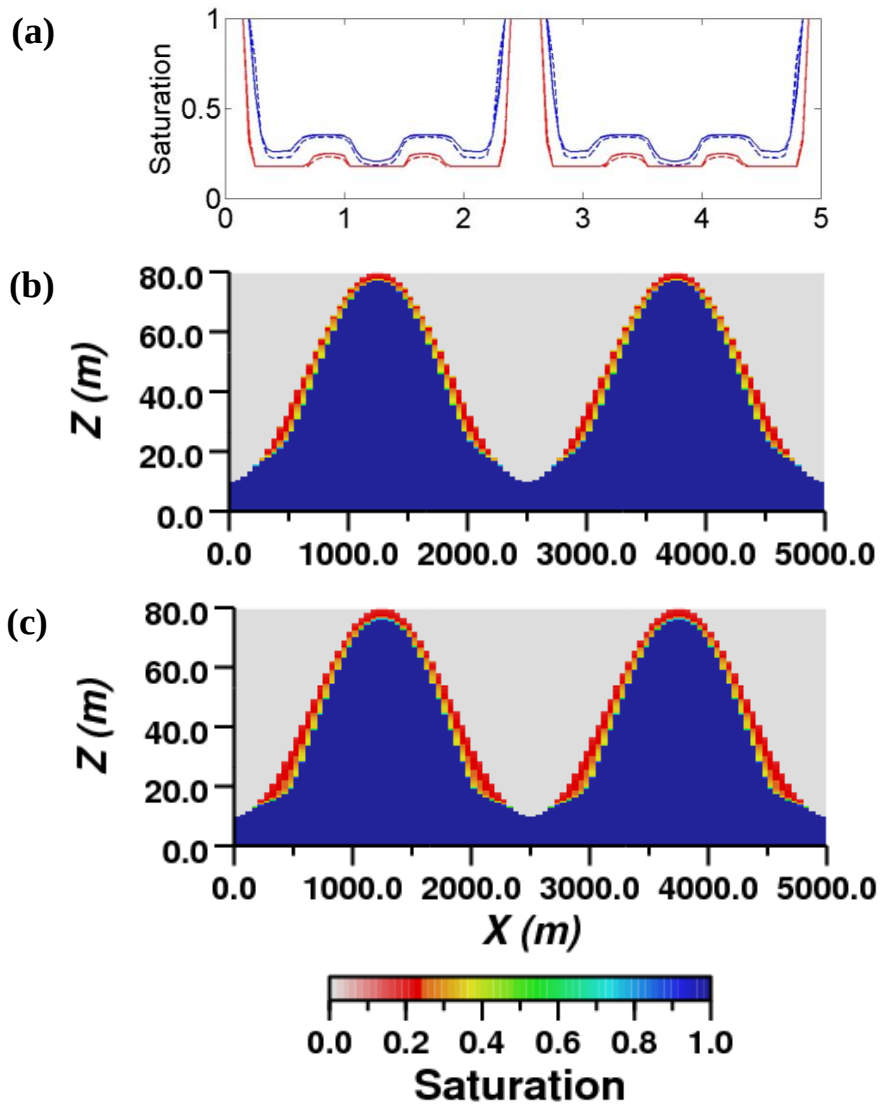


**Figure 3.4**: PF.CLM results for case2 used to initialize ARPS simulations: (a) Saturation profiles at the land surface for March 18th (blue lines) and November 4th (red lines). Solid lines are for the top soil layer, dashed lines are for the second soil layer, (b) Subsurface saturation field snapshot at the beginning of a large storm on March 18th, (c) Subsurface saturation field snapshot during a storm on November 4th. Vertical scale in (b) and (c) is exaggerated for clarity.

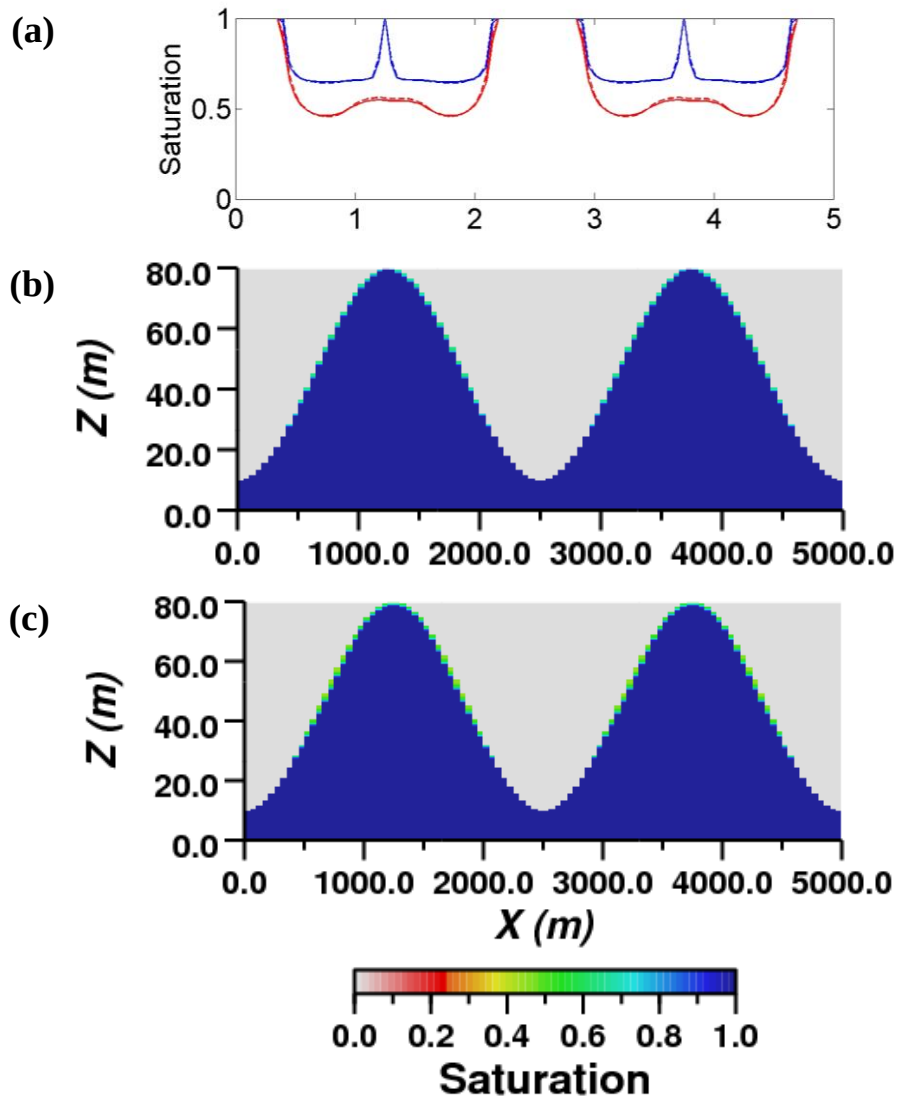


**Figure 3.5**: PF.CLM results for case3 used to initialize ARPS simulations: (a) Saturation profiles at the land surface for March 18th (blue lines) and November 4th (red lines). Solid lines are for the top soil layer, dashed lines are for the second soil layer, (b) Subsurface saturation field snapshot at the beginning of a large storm on March 18th, (c) Subsurface saturation field snapshot during a storm on November 4th. Vertical scale in (b) and (c) is exaggerated for clarity.

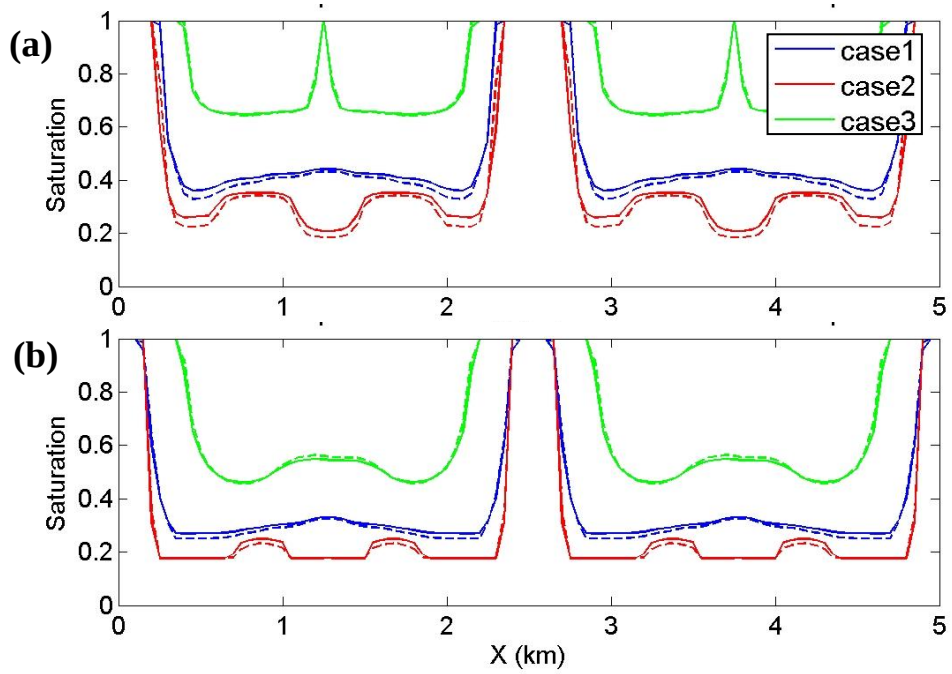


**Figure 3.6**: Saturation profiles at the land surface for the three PF.CLM spinup cases on: (a) March 18th and (b) November 4th. Solid lines are for the top soil layer, dashed lines are for the second soil layer.

## 3.4 Simulation results

In these simulations, the sinusoidal (hilly) terrain is aligned in the East-West direction and the valley axes point North-South. All cross sections and plots show values averaged in the y direction (North-South). Section 3.4.1 describes the processes that drive the development of the convective boundary layer during the first simulation day, night, and second day. Subsequent sections isolate different effects by cross comparing cases from Table 3.2.

### 3.4.1 Development and Structure of the PBL

Figure 3.7 shows a time series of water vapor mixing ratio contours for case sin1_Mar (Table 3.2). The series includes y-averaged snapshots from within the 36 hour simulation. Times are chosen at 2 hour intervals within the 36 hour simulation period except during morning hours during which the snapshots are at hourly intervals to show the development of the daily convective PBL from its stable nocturnal state as explained herein. The snapshots also include profiles in x of instantaneous soil moisture ($q_s$) at the top soil layer, initial soil moisture profile ($q_{so}$), top soil layer temperature ($T_s$), and latent heat flux (LH) at the land surface. The arrows overlaying $q_v$ contours illustrate x-z wind directions. These arrows show the circulations and

development of the PBL during the day and thus indicate the depth of the boundary layer. The yellow line in the contour plots also indicates PBL depth and is calculated based on minimum turbulent kinetic energy (TKE) over each vertical profile. Figure 3.8 shows vertical profile time series of potential temperature ($\theta$), water vapor mixing ratio ($q_v$), and turbulent kinetic energy (TKE). Profiles from the first day, first night, and second day are overlaid in Figures 3.8a, 3.8b, and 3.8c, respectively. Different colors indicate different times as indicated in the figure captions. The profiles are shown for both valley and hill top locations as indicated by subscripts V and H, respectively.

The hilly terrain induces variable heating of the land surface at different times of the day. During early morning hours (e.g. 10 am in figure 3.7) the sun more strongly heats the east side of the hills. This warms air just above the surface which rises in the form of upslope winds and induces evaporation (as shown in $\theta$ and $q_v$ profiles, Figure 3.8a). The West side of the hill is inclined away from the incident solar radiation and is therefore cooler during early morning hours, but starts to warm up as the sun rises and the day progresses to noon (refer to surface temperatures at 10 am, 11 am and 12 pm in Figure 3.7). Upslope winds start to form on the west side of the hill carrying warmer air to the peak where it meets the warm air rising along the East side. The flow converges upward at the warm and dry peaks and downward at the cooler wet valleys. These convective circulations, which continue through the afternoon, carry the signature of the terrain during the day and result in a lower PBL above the valleys and higher over the peaks, as expected.

Land surface temperature (Ts, solid red line in Figure 3.7) and latent heat flux profiles (LH, dashed red line) emphasize the effect of the heterogeneous soil moisture at the land surface. The effect of variable heating of the land surface caused by terrain on Ts and LH profiles is mostly apparent during early morning (10 am and 11 am) as there is a slight increase in evaporation on the east hill side compared to the west. These profiles, however, mostly carry the signature of soil moisture variation at the land surface (qs) such that wetter soils (e.g. in the valleys) induce more evaporation and thus lower land surface temperature, and vice versa. TKE profiles in Figure 3.8a show the effects of rising thermals around the hill tops during the day. Valley TKE profiles in the same figure show relatively inhibited turbulence compared to the hill top due to wetter and thus cooler soils in the valleys.

The boundary layer grows in depth during the day due to rising thermals from the heating land surface and entrainment from the free atmosphere above. The growing PBL depth is apparent in Figure 3.8a when comparing profiles at different times of the day. PBL depth is typically defined by maximum potential temperature gradient or minimum TKE (Sullivan et al, 1998). Both methods give similar results but the TKE minimum is more easily defined. Towards the end of the day, the PBL reaches its maximum depth as the convective circulations have formed a well mixed layer (Figure 3.7, 8 pm and 10 pm). As the land surface starts to cool during the night (e.g. starting at 10 pm in Figure 3.7), a shallow stable nocturnal boundary layer forms due to cool near-surface air underlying warmer residual mixed air from the daytime convective layer (Figure 3.8b). Positive buoyancy and upward vertical transport is inhibited within the stable layer as shown in potential temperature and TKE profiles in Figure 3.8b, compared to the turbulent convective layer seen in Figure 3.8a. Water vapor mixing ratio decreases between 0~500m heights because the cooling land surface at night induces condensation and due formation close

to the land surface. During morning hours on the second day, however, differential heating of the land surface starts again and the moisture retained in the valleys during the night is now carried by uphill flows (Figure 3.7 times 10 am and 11am) to the western sides of the hills which by noon are starting to heat and form rising thermals on both hill sides. Looking at the minimum TKE and maximum θ gradient in Figure 3.8c profiles, the second day convective PBL has a greater depth than the first day PBL. Furthermore, Figure 3.7 (times 2 pm and 4 pm on the second day) show the convective PBL on the second day is now moister than that on the first day due to continued evaporation from the ground ($q_v$ profiles in Figure 3.8c indicate this as well). In the following sections, comparisons are made between different cases to isolate effects of terrain and soil moisture variability.

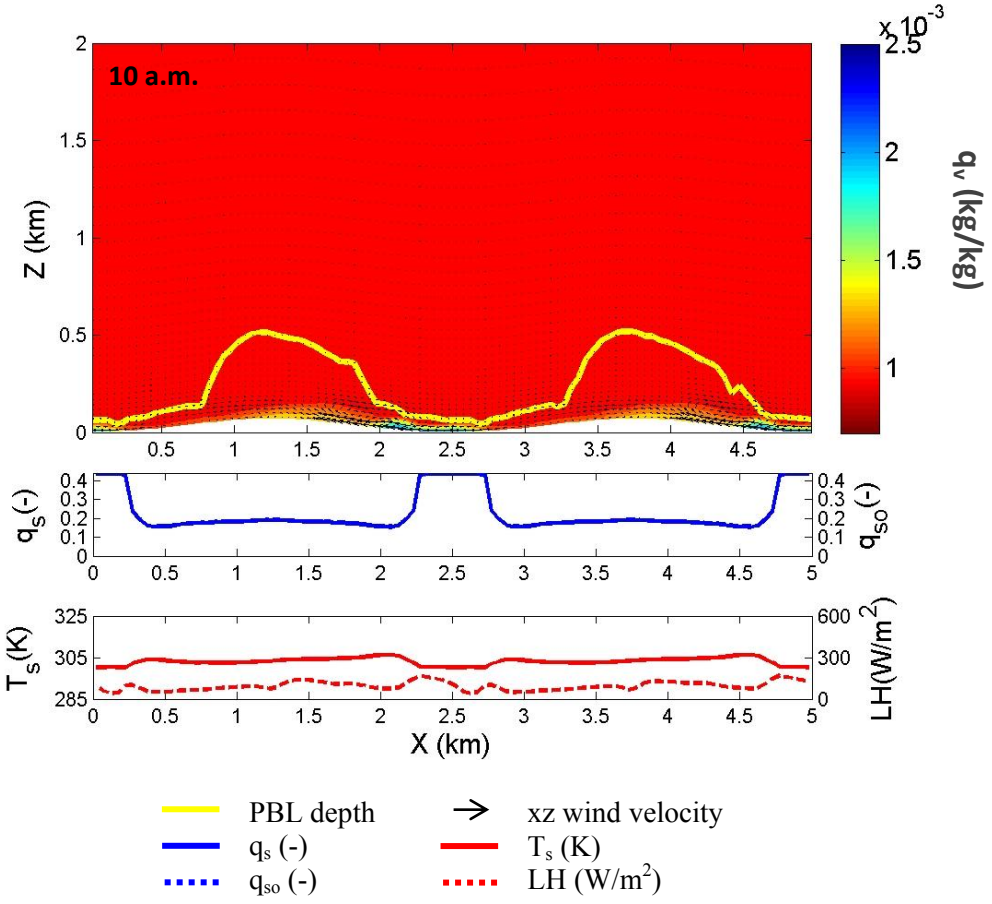


**Figure 3.7:** Snapshots of water vapor mixing ratio contours $q_v$ for case sin1_wet. Arrows show x-z wind directions (arrow size relative to the magnitude) and the yellow line overlaying the contours indicates PBL depth. Profiles beneath the contours show instantaneous soil moisture profiles $q_s$ at the top soil layer (solid blue line), initial soil moisture profile $q_{so}$ (dashed blue line), soil temperature $T_s$ (solid red line) and latent heat flux LH at the land surface (dashed red line). All values are y-averaged. Snapshots continued on pages (61 to 71) showing time series from 10am on the first day to 4pm on the second day.

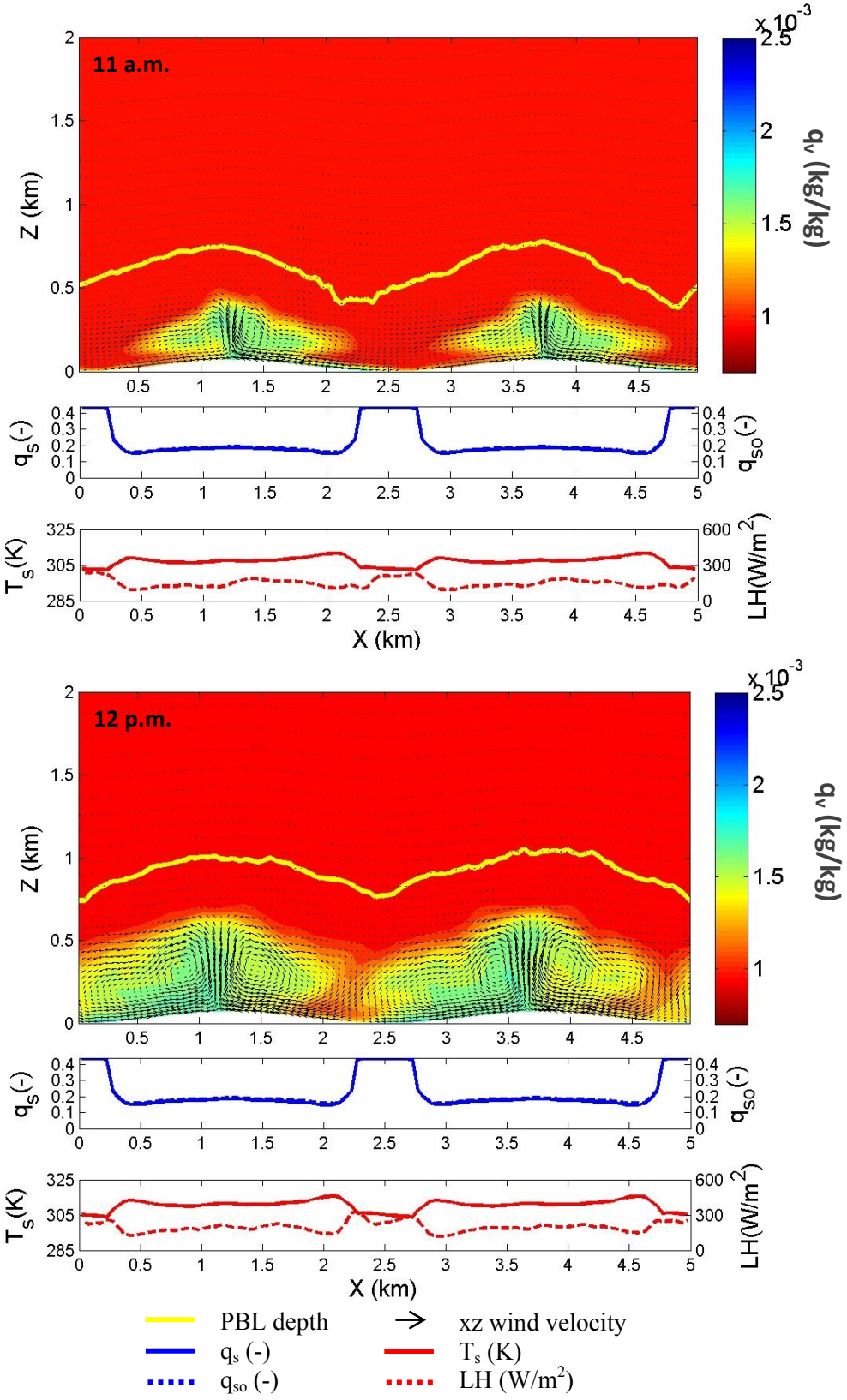


**Figure 3.7:** Continued times 11 am and 12 pm.

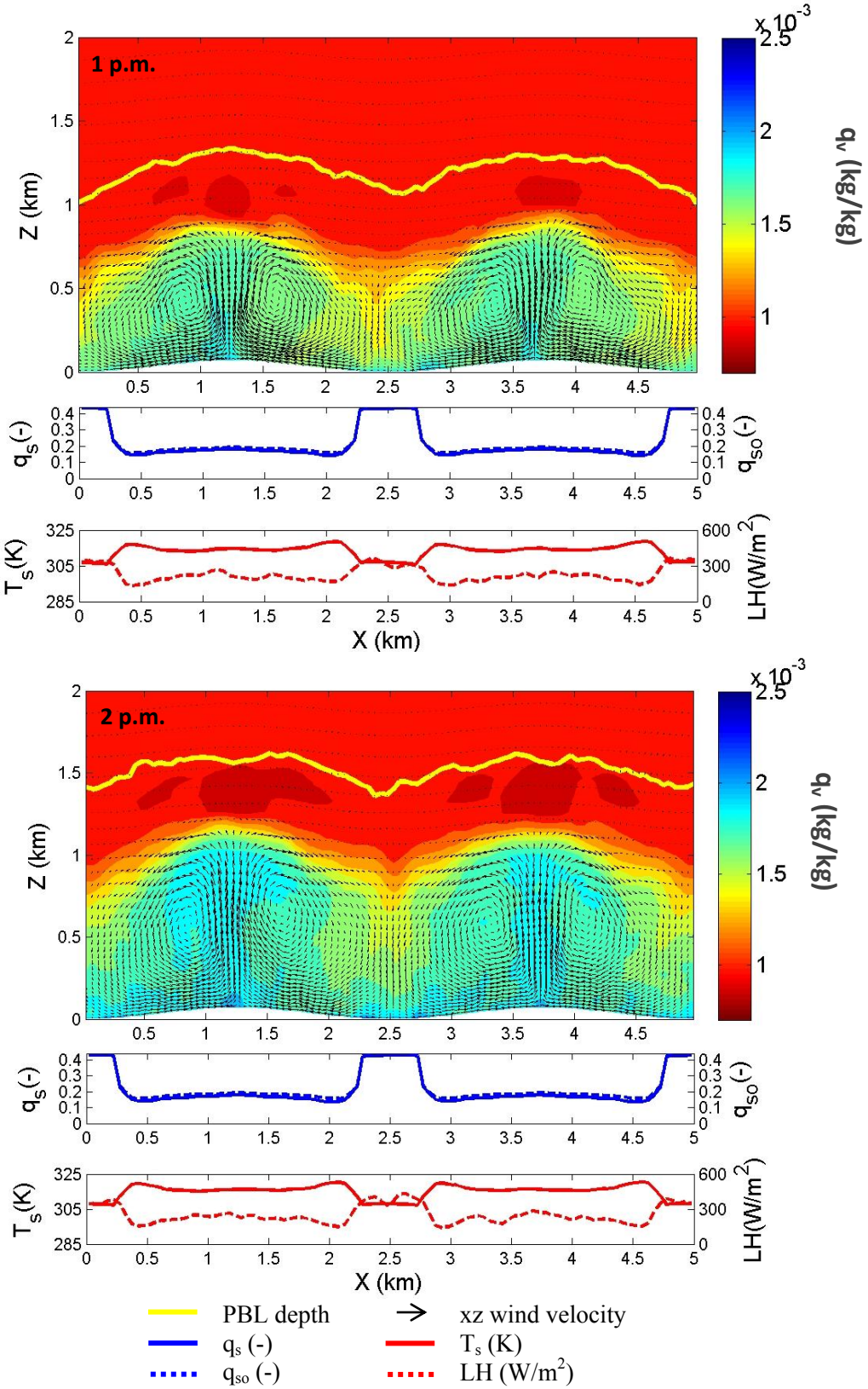


**Figure 3.7:** Continued times 1 pm and 2 pm.

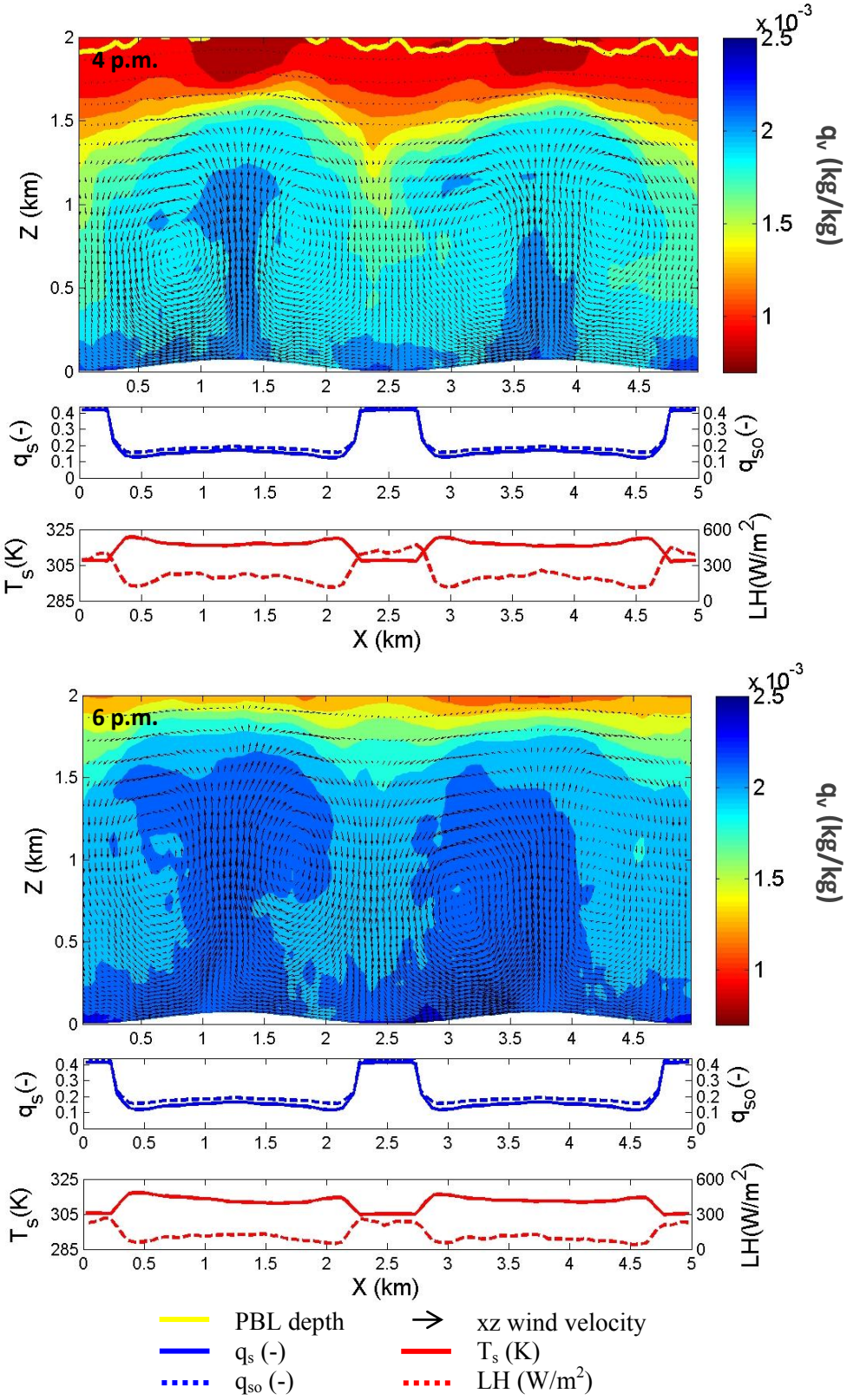


**Figure 3.7:** Continued times 4 pm and 6 pm.

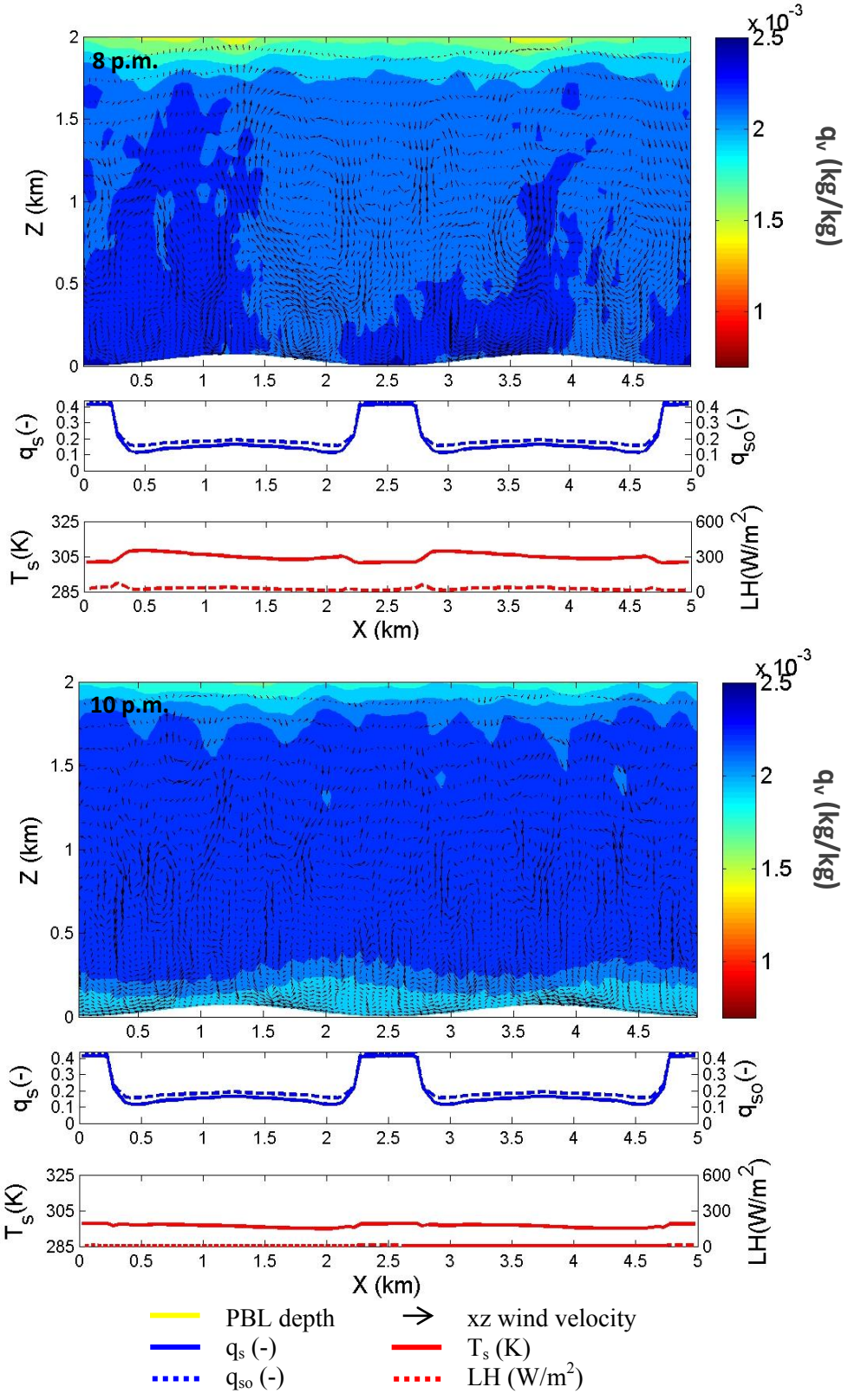


**Figure 3.7:** Continued times 8 pm and 10 pm.

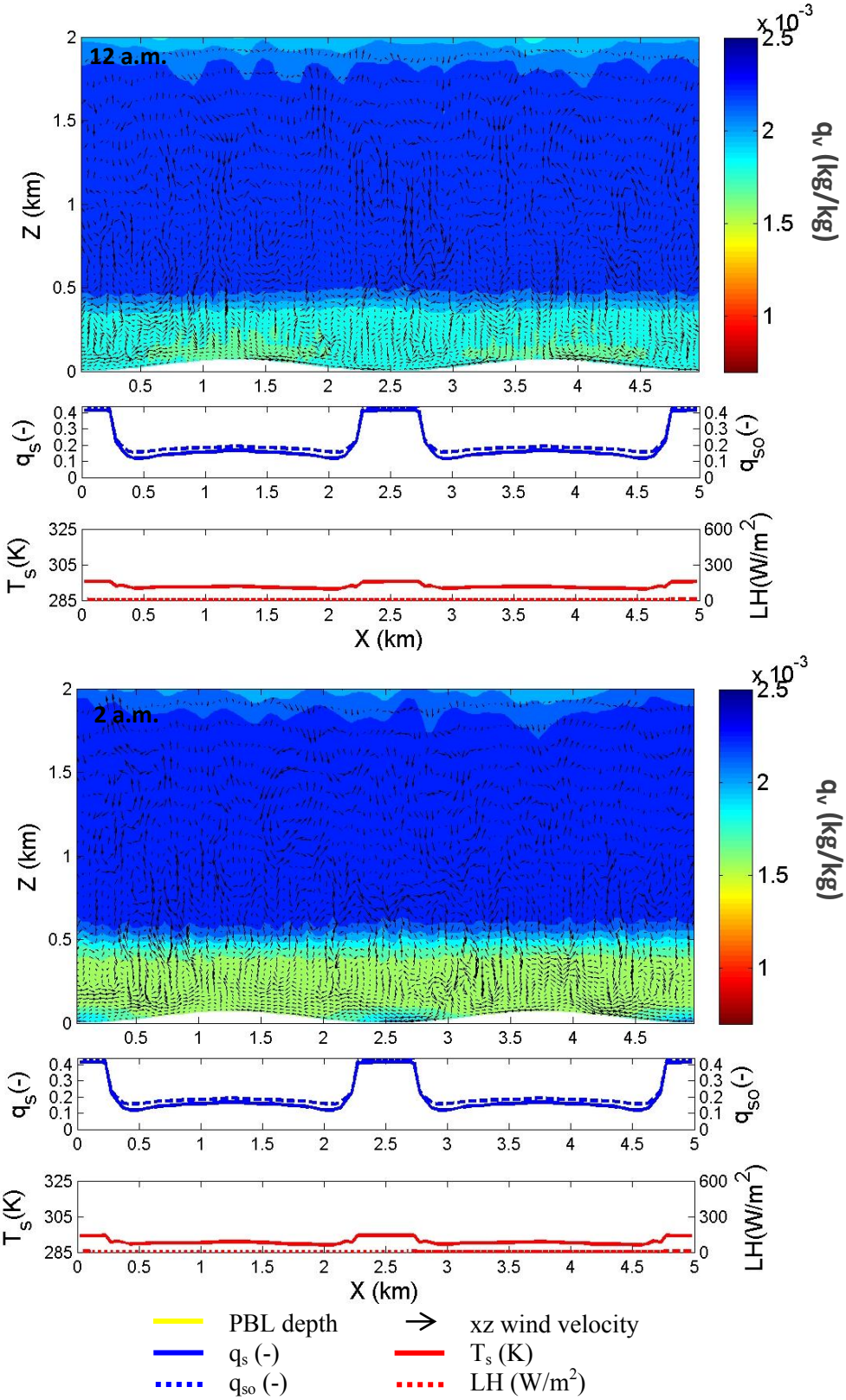


**Figure 3.7:** Continued times 12 am and 2 am.

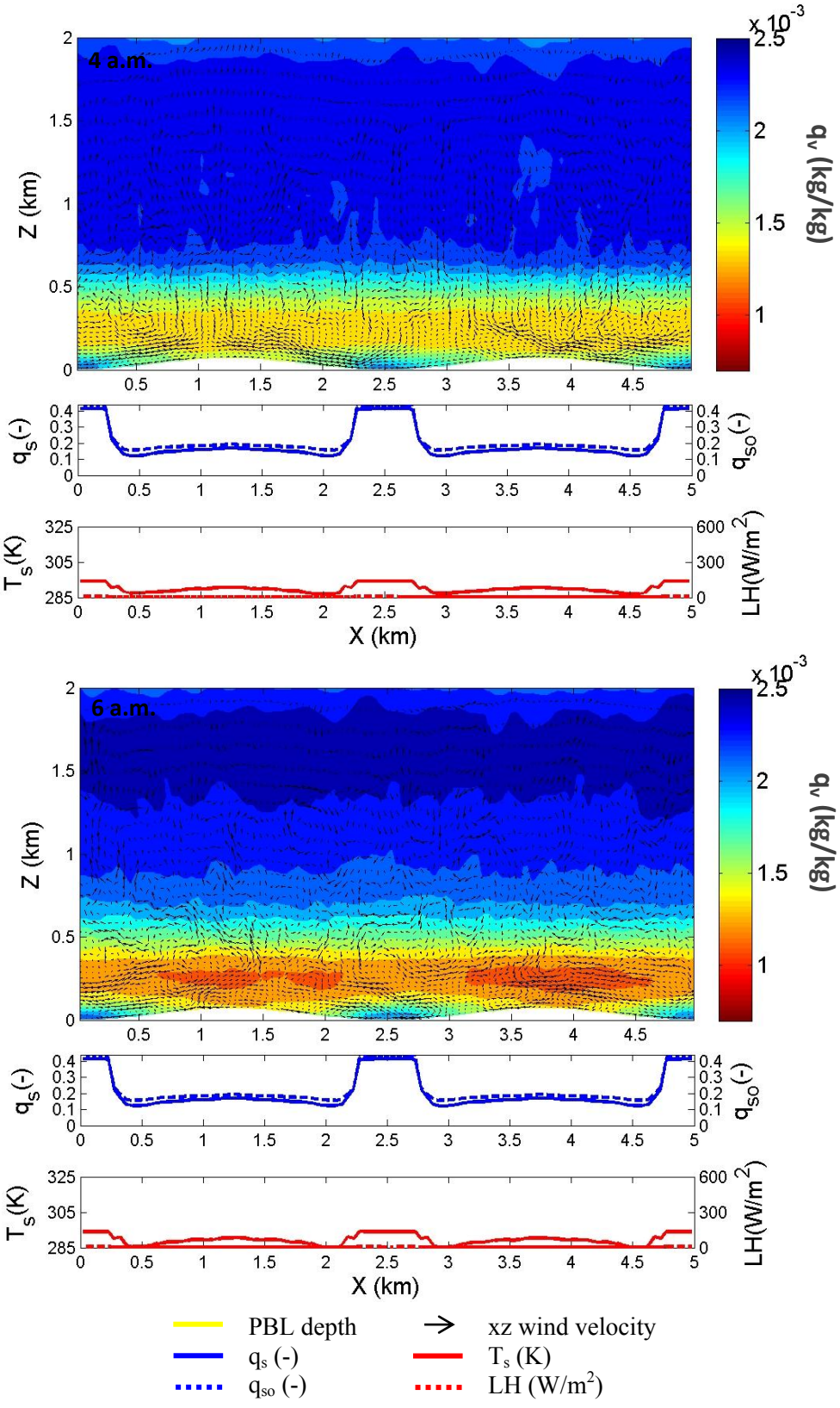


**Figure 3.7:** Continued times 4 am and 6 am.

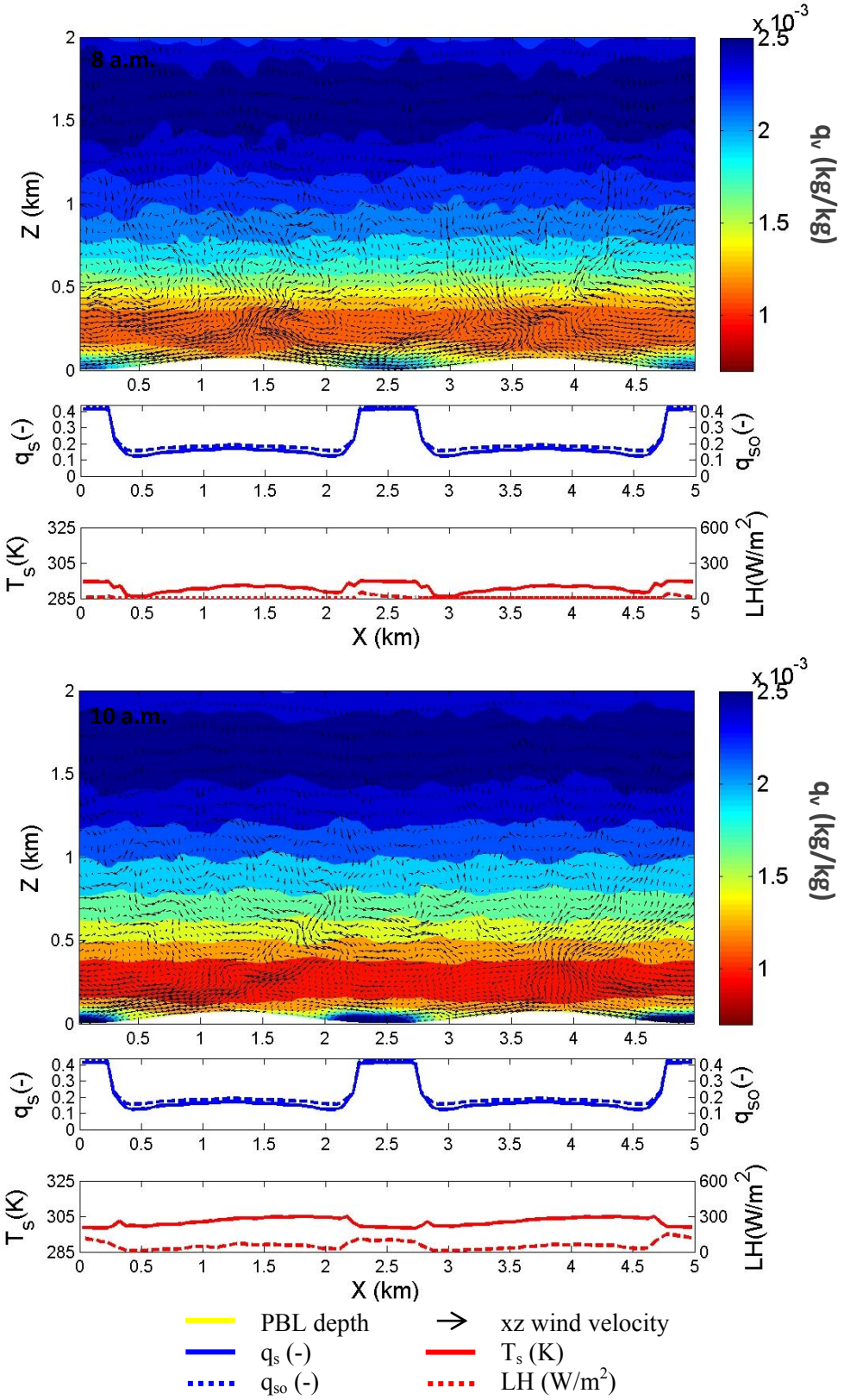


**Figure 3.7:** Continued times 8 am and 10 am.

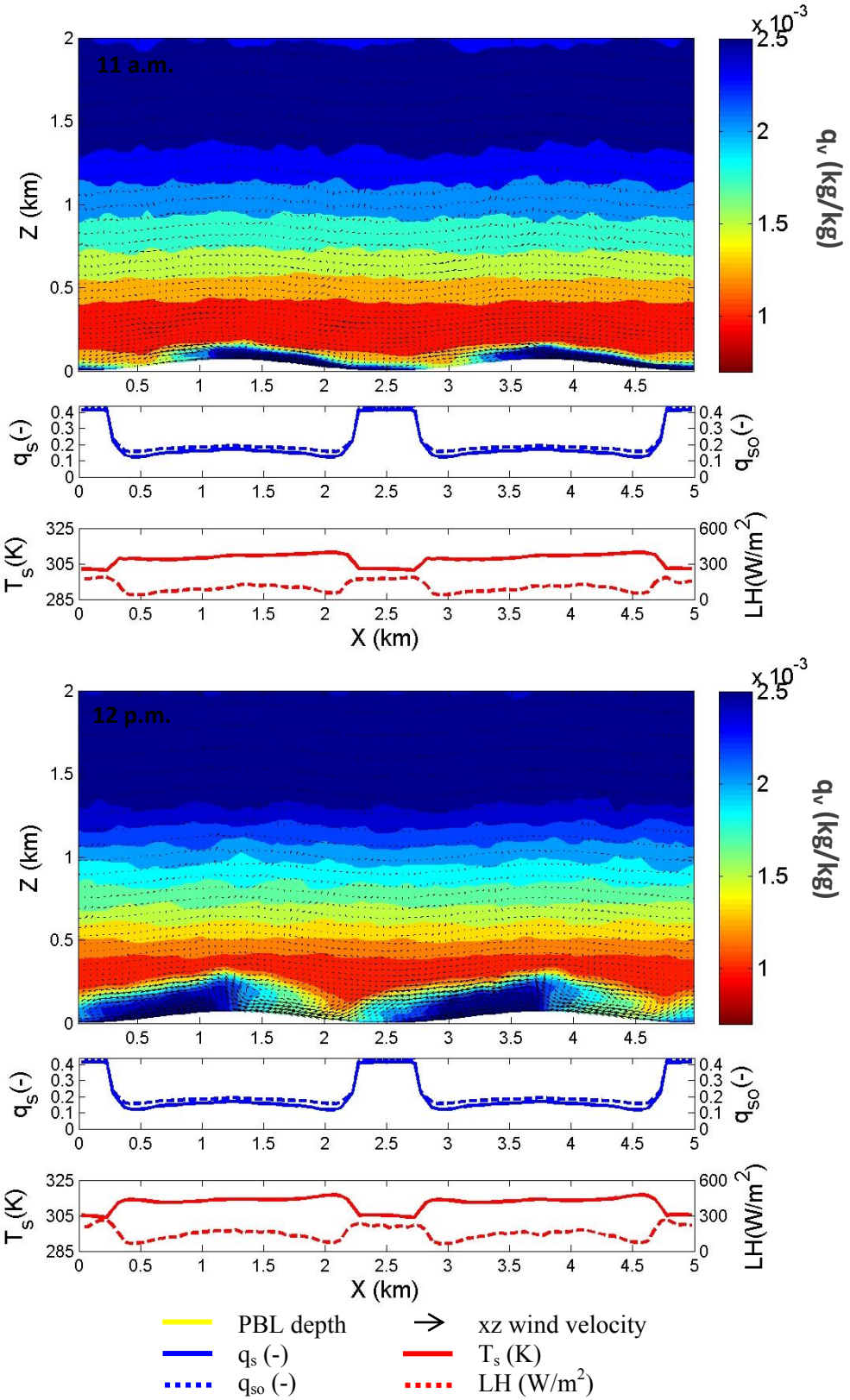


**Figure 3.7:** Continued times 11 am and 12 pm.

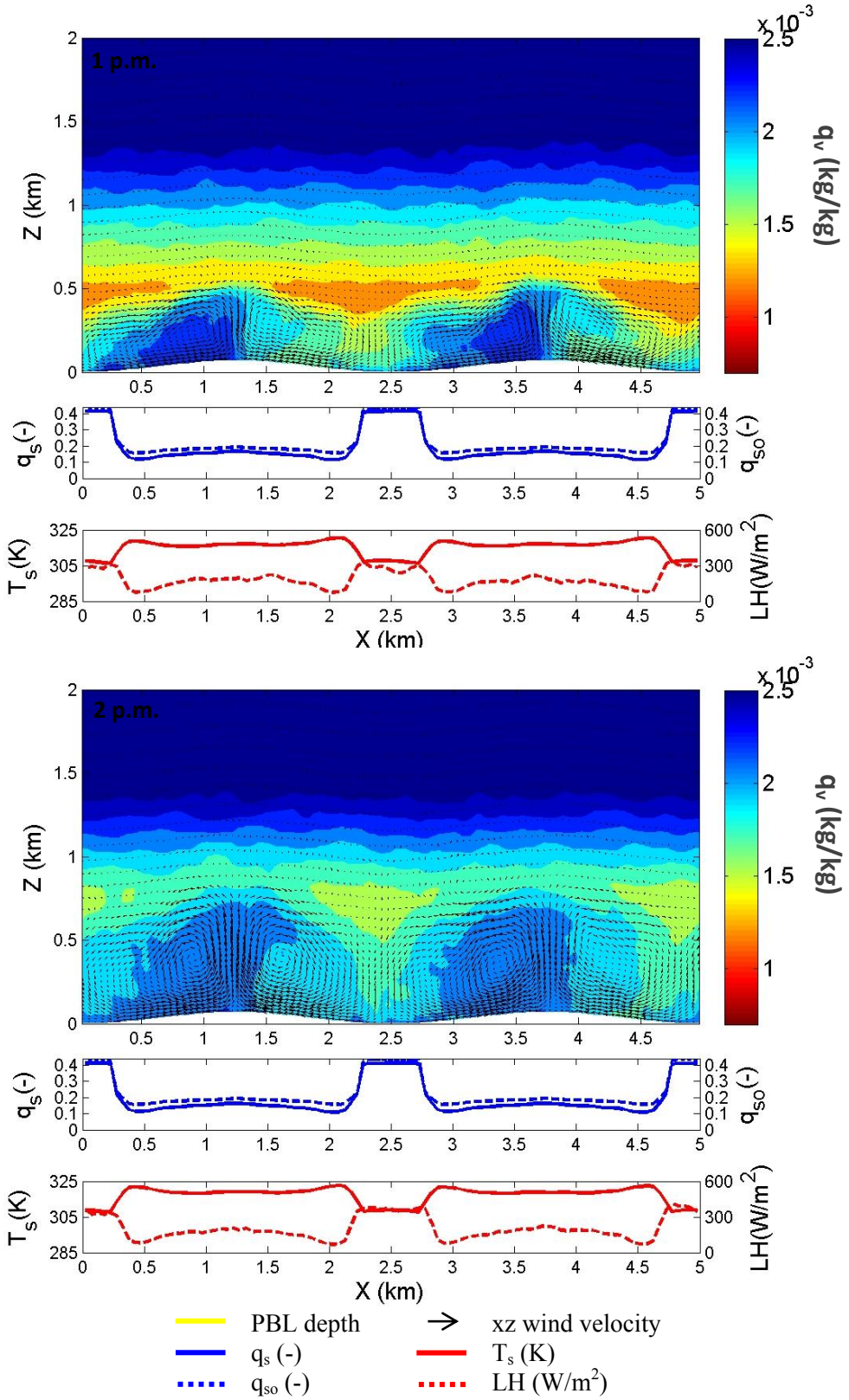


**Figure 3.7:** Continued times 1 pm and 2 pm.

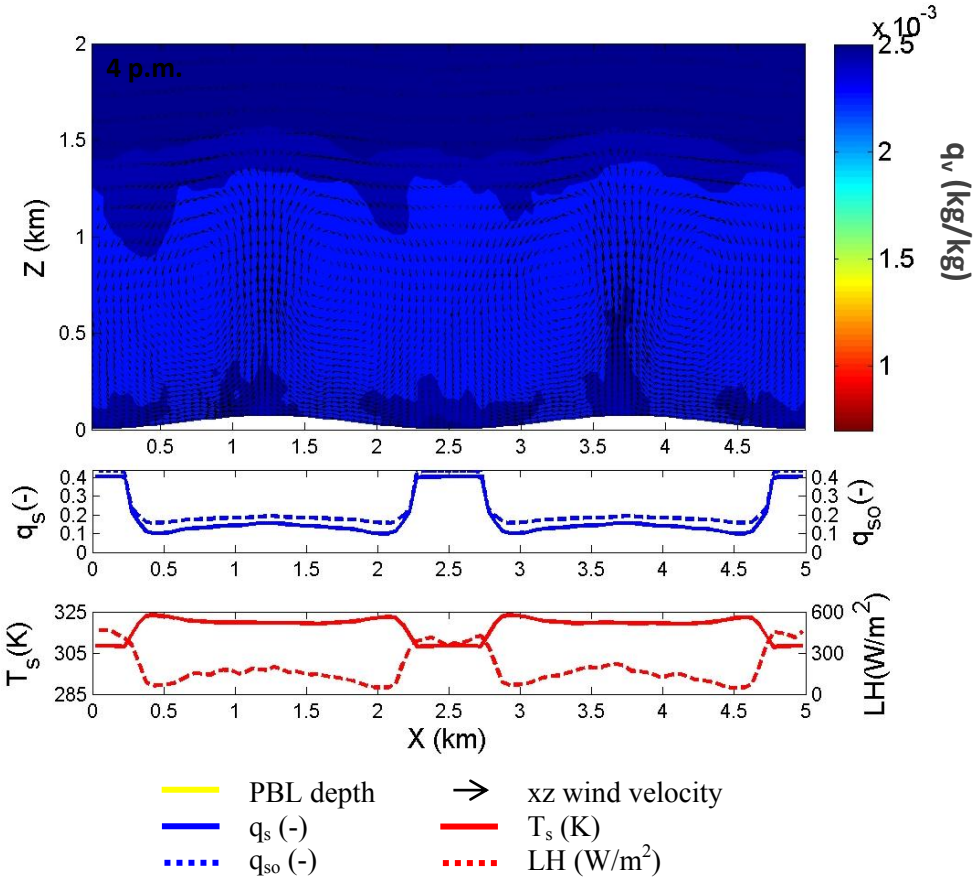


**Figure 3.7:** Continued times 4 pm.

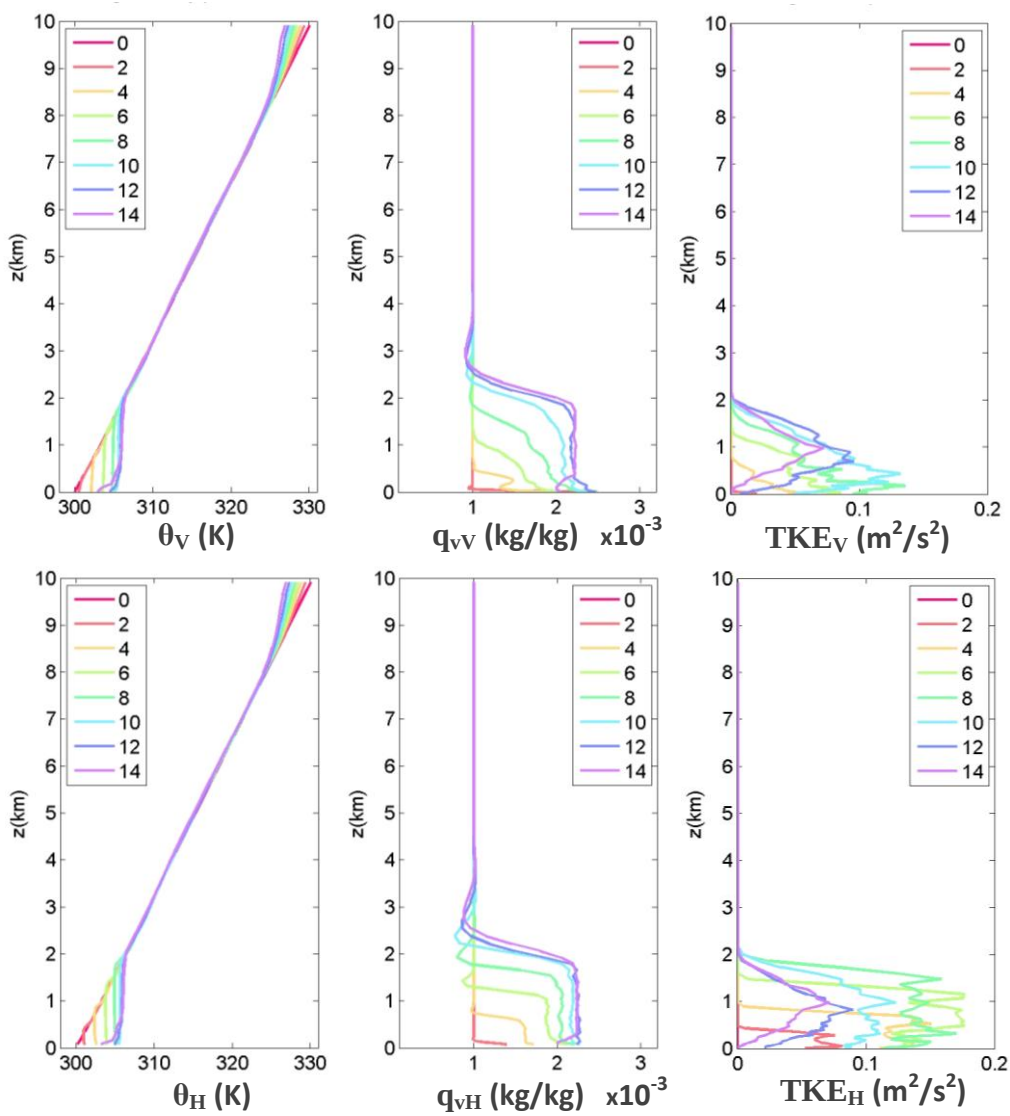


**Figure 3.8a:** Vertical profiles during the first simulation day of potential temperature (θ, K), water vapor mixing ratio ($q_v$, kg/kg), and turbulent kinetic energy (TKE, $m^2/s^2$). Subscripts V and H denote valley or hilltop profiles, respectively. Line colors indicate hours in simulation time: 0 (8 am), 2 (10am), 4 (12 pm), 6 (2 pm), 8 (4 pm), 10 (6 pm), 12 (8 pm), and 14 (10 pm).

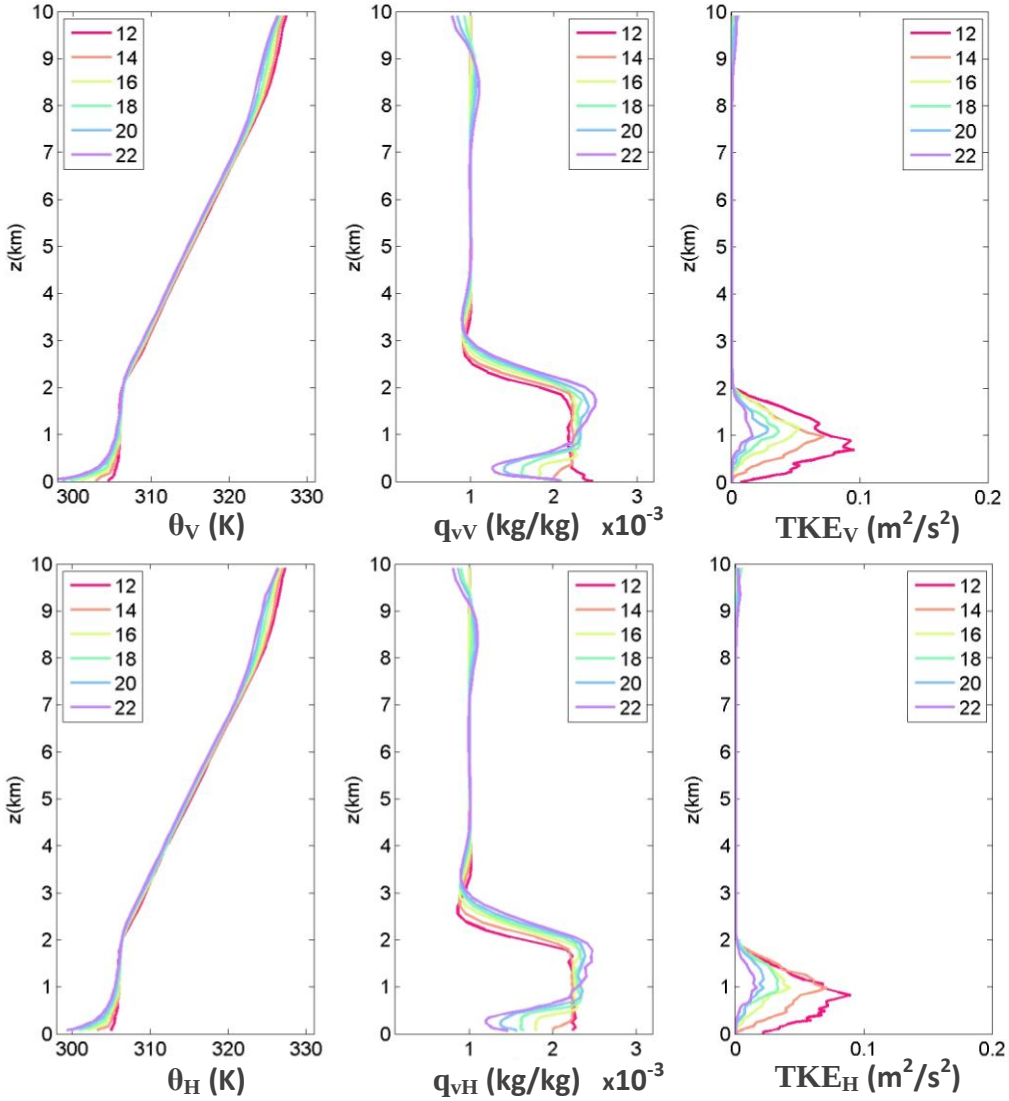


**Figure 3.8b:** Continued first simulation night profiles at times: 12 (8 pm), 14 (10 pm), 16 (12 am), 18 (2 am), 20 (4 am), and 22 (6 am).

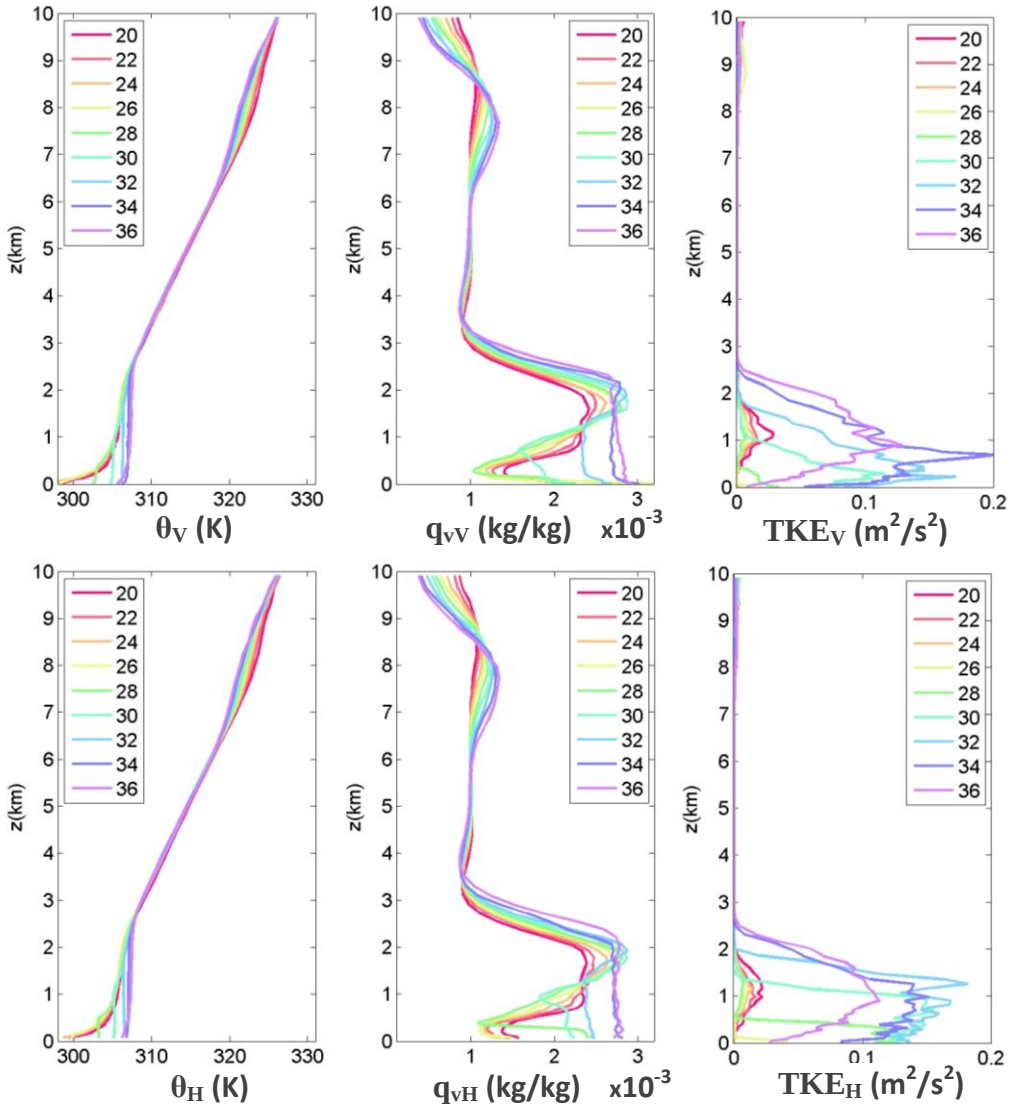


**Figure 3.8c:** Continued second simulation day profiles at times: 20 (4 am), 22 (6 am), 24 (8 am), 26 (10 am), 28 (12 pm), 30 (2 pm), 32 (4 pm), 34 (6 pm), and 36 (8 pm).

### 3.4.2 Effects of Terrain

Because the test case presented above includes both terrain and soil moisture variability, it is not entirely clear what the predominant mechanism is that drives the evolution PBL depth. To isolate the effect of terrain from soil moisture in driving the development of the convective boundary layer, flat and sinusoid cases initialized with similar soil moisture profiles are compared. In Figures 3.9 and 3.10, cases initialized with homogenous soil moisture profiles at the land surface (flat0 and sin0) are compared. Water vapor mixing ratio contours with profiles of soil moisture, soil temperature, and latent heat flux are shown at times 10 am, 11 am, and 12 pm in Figures 3.9a, 3.9b, and 3.9c, respectively. The effect of variable heating and cooling due to terrain are immediately apparent in the circulations that develop, as described previously. In the flat case, however, the land surface receives equal amounts of radiative heating and even though thermals form in this case, the convective cells have a smaller scale and the boundary layer depth is more uniform. The PBL depth, particularly over the hill tops is greater in the sinusoid case than in the flat case. This effect is further demonstrated when looking at contour plots of wind velocities in the x and z directions (Figure 3.10a and 3.10b, respectively). These are y-averaged plots, and the vertical axis here is cropped to 1km to emphasize the terrain effects on convective circulations. Winds tend to be of larger magnitude in the sinusoidal case and the circulation cells are better defined than in the flat case. Figure 3.10b shows clearly how rising thermals on the hilltops increase the boundary layer depth over the smaller scale circulations in the flat case.

Terrain effects are also clear even when soil moisture heterogeneity is included. Water vapor mixing ratio contours with profiles of soil moisture, soil temperature, and latent heat flux for cases flat1_Mar and sin1_Mar are shown in Figure 3.11a and 3.11b for times 11 am and 1 pm, respectively. At 11 am, the terrain signature is clear over soil moisture heterogeneity when looking at convective circulations forming around the hills in sin1_Mar compared to the smaller scale cells in flat1_Mar. The soil moisture signature is still apparent when looking at soil temperature and latent heat profiles, but there is more evaporation on the East side of the hills in case sin1_Mar due to variable heating and cooling caused by terrain. This effect does not continue however as the sun heats both sides of the hill evenly in the afternoon. By 1pm, the effect of terrain is overcome by the variability of soil moisture. Wetter soils at the valleys induce more evaporation than drier soils at the peaks. The effect of soil moisture which now drives the convective cells and rising thermals is also seen in the flat case. Land surface temperature is warmer in the dry regions. This heats the surrounding air and causes it to rise while cooler air descends at the wetter soil regions forming similar circulations for both sinusoid and flat terrain during the afternoon (Figure 3.11b).

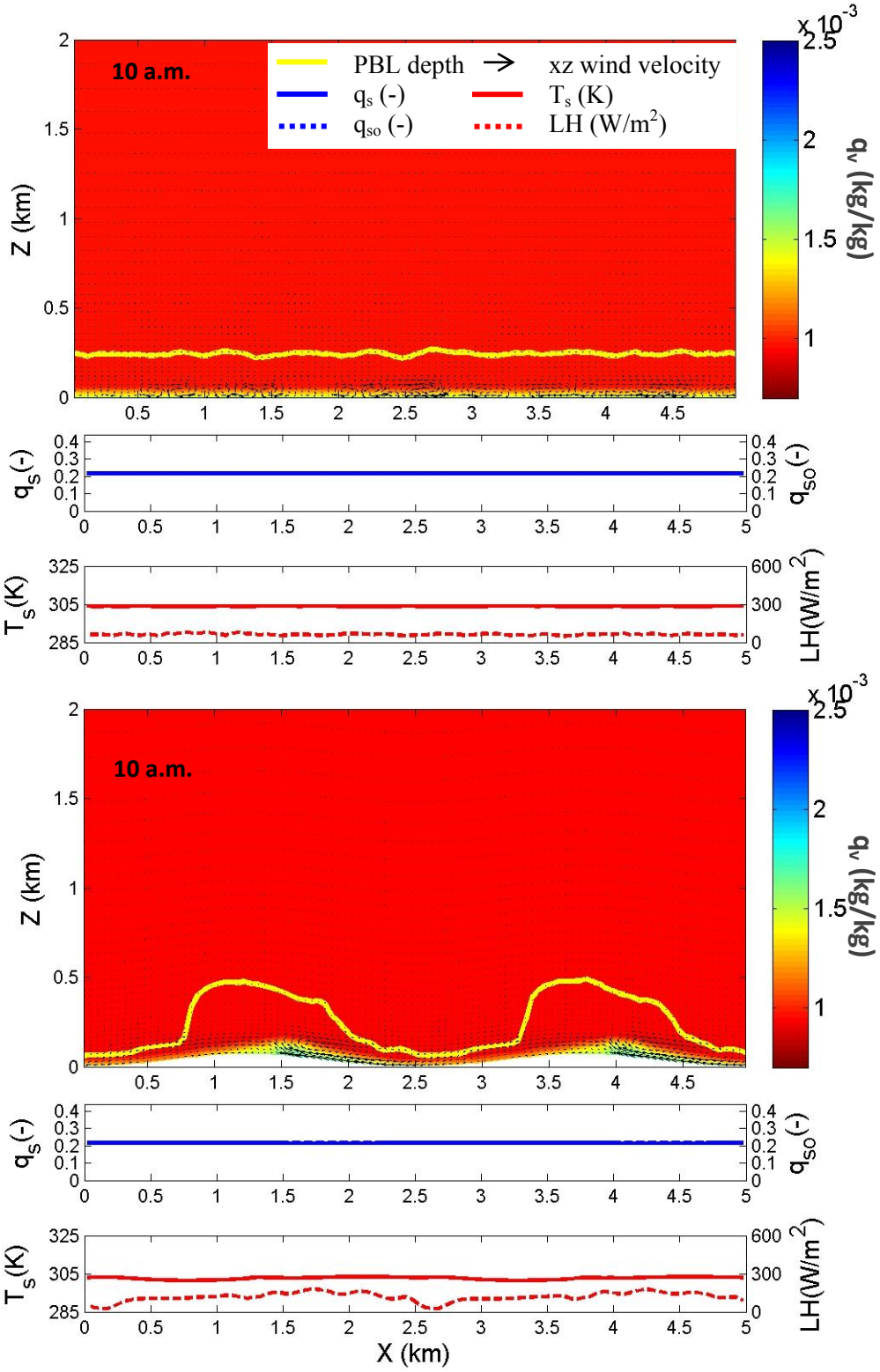


**Figure 3.9a:** 10am y-averaged snapshots of $q_v$ contours and profiles of soil moisture $q_s$ (solid blue), initial soil moisture $q_{so}$ (dashed blue), soil temperature $T_s$ (solid red), and latent heat flux LH at the land surface (dashed red) for cases flat0 & sin0.

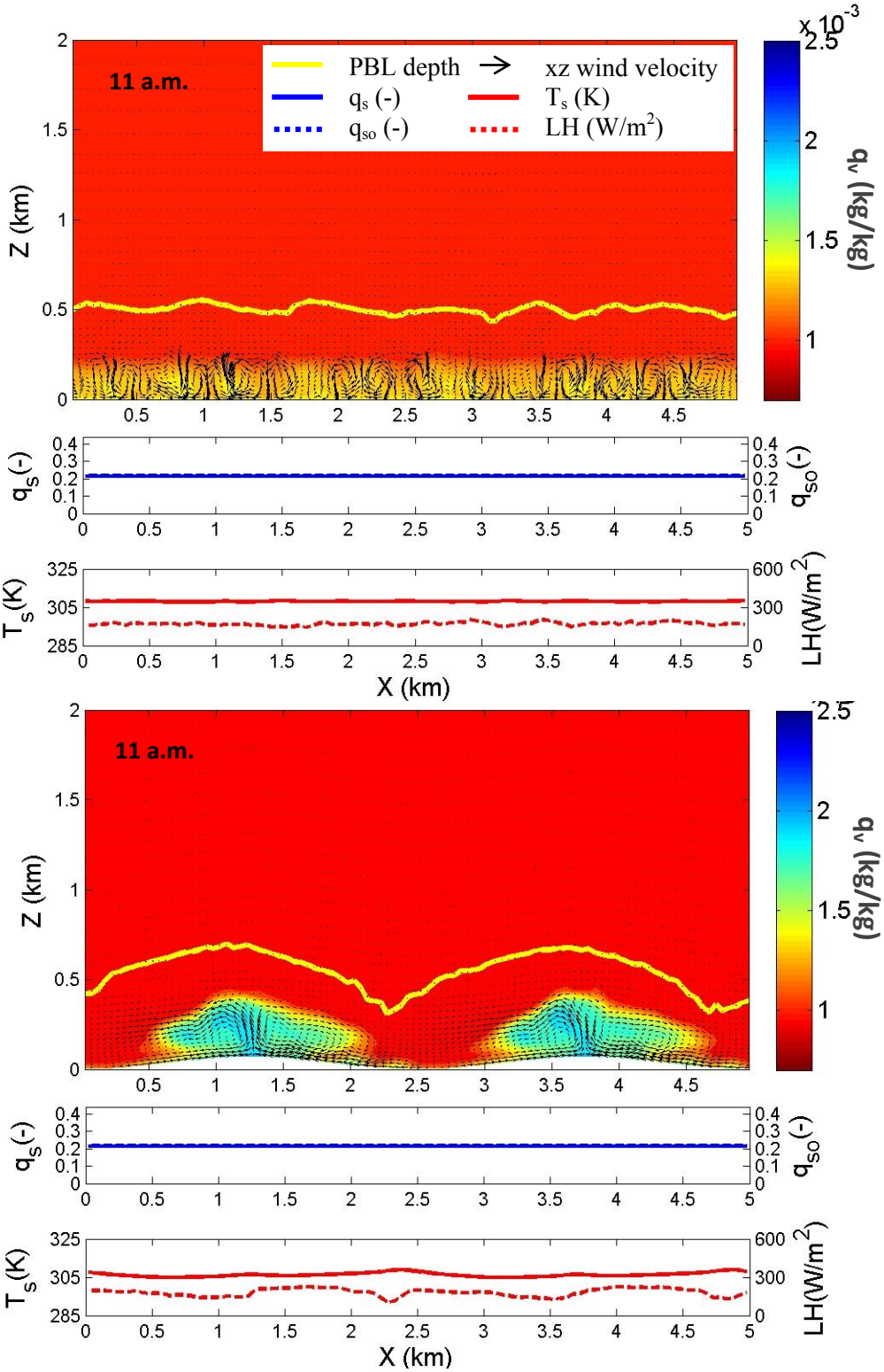


**Figure 3.9b:** 11am y-averaged snapshots of $q_v$ contours and profiles of soil moisture $q_s$ (solid blue), initial soil moisture $q_{so}$ (dashed blue), soil temperature $T_s$ (solid red), and latent heat flux LH at the land surface (dashed red) for cases flat0 & sin0.

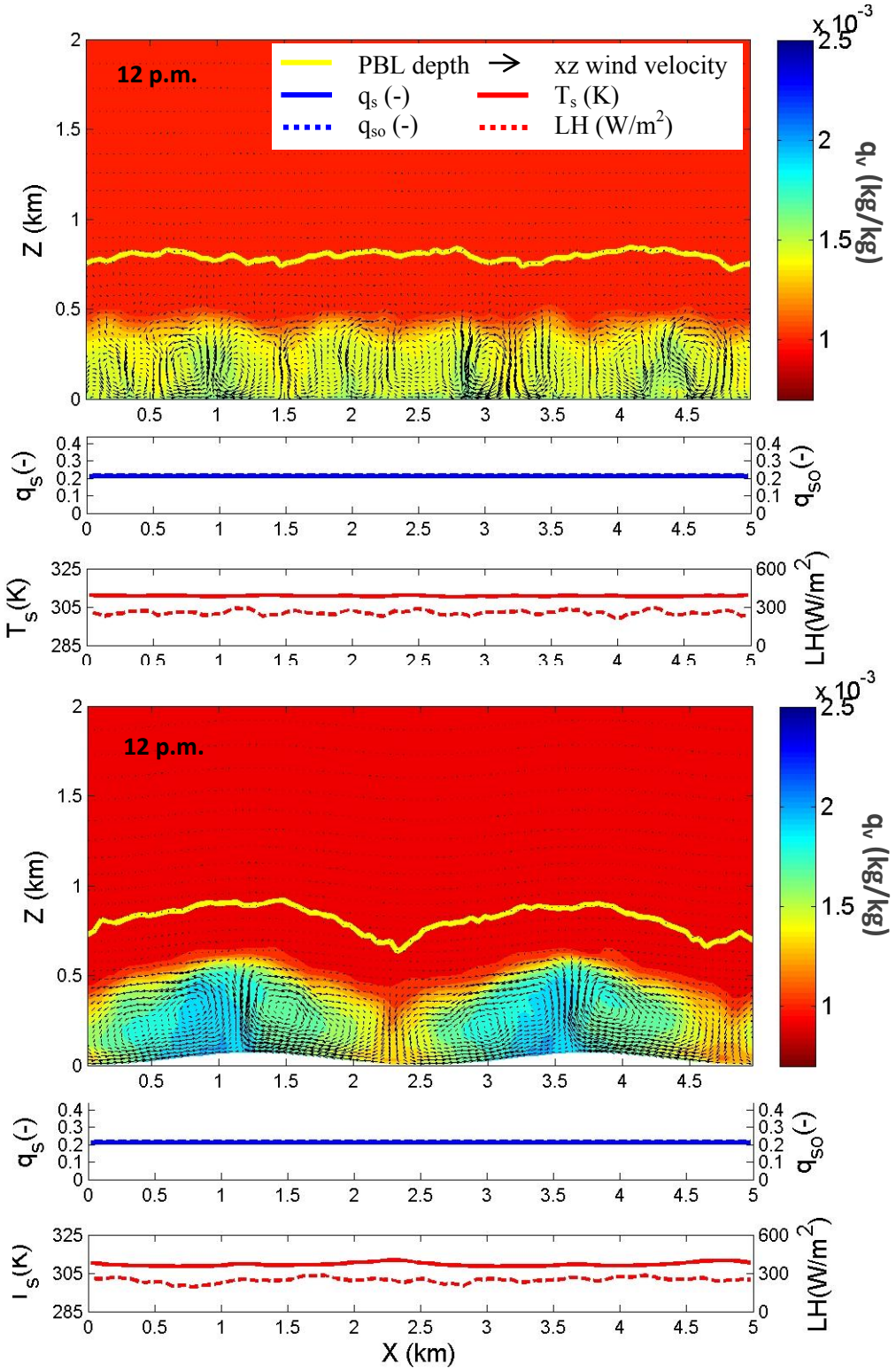


**Figure 3.9c:** 12pm y-averaged snapshots of $q_v$ contours and profiles of soil moisture $q_s$ (solid blue), initial soil moisture $q_{so}$ (dashed blue), soil temperature $T_s$ (solid red), and latent heat flux LH at the land surface (dashed red) for cases flat0 & sin0.

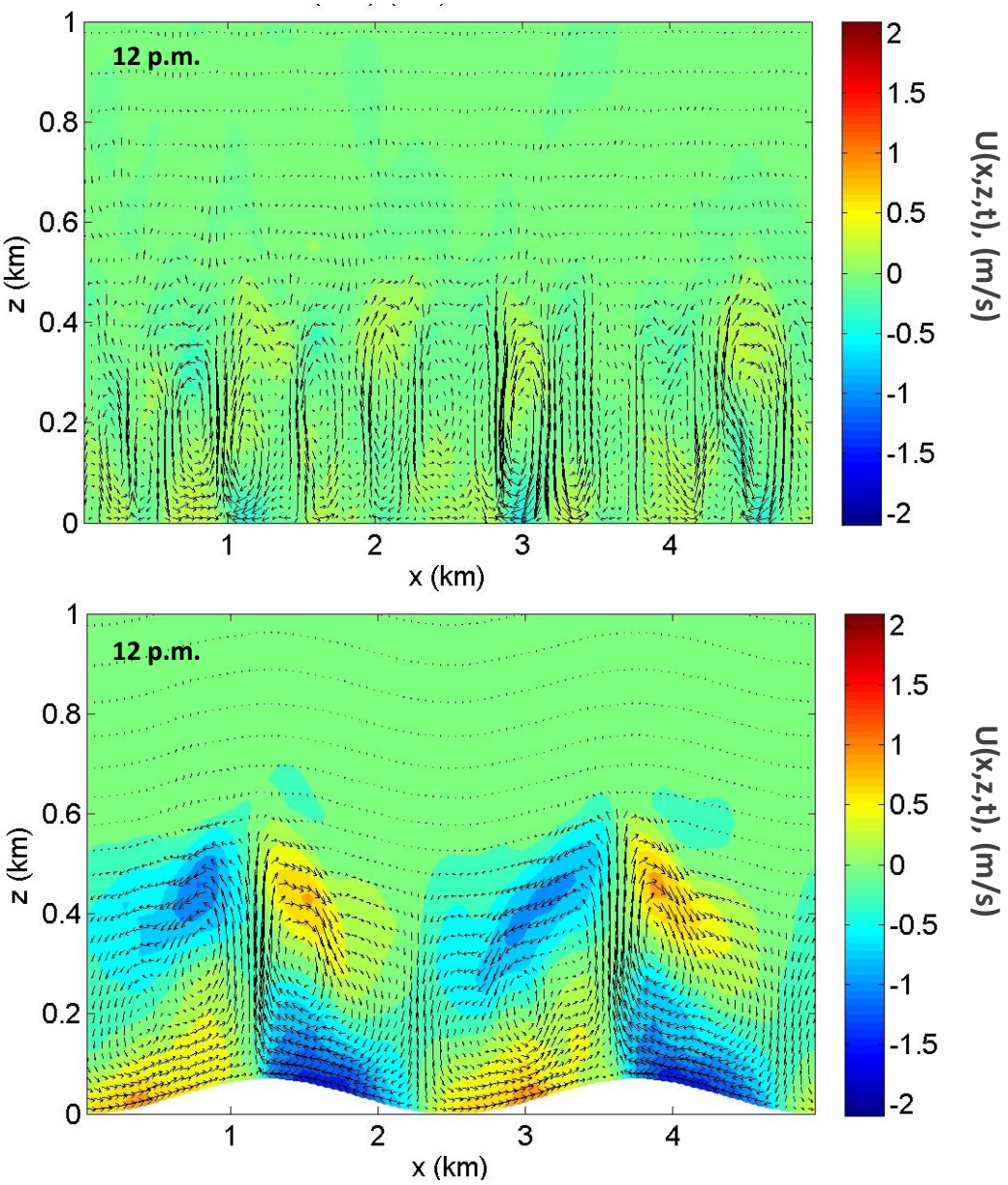


**Figure 3.10a:** Contours of y-averaged snapshots of wind velocity in the x-direction (u(x,z,t)) at 12 pm for cases flat0 & sin0.

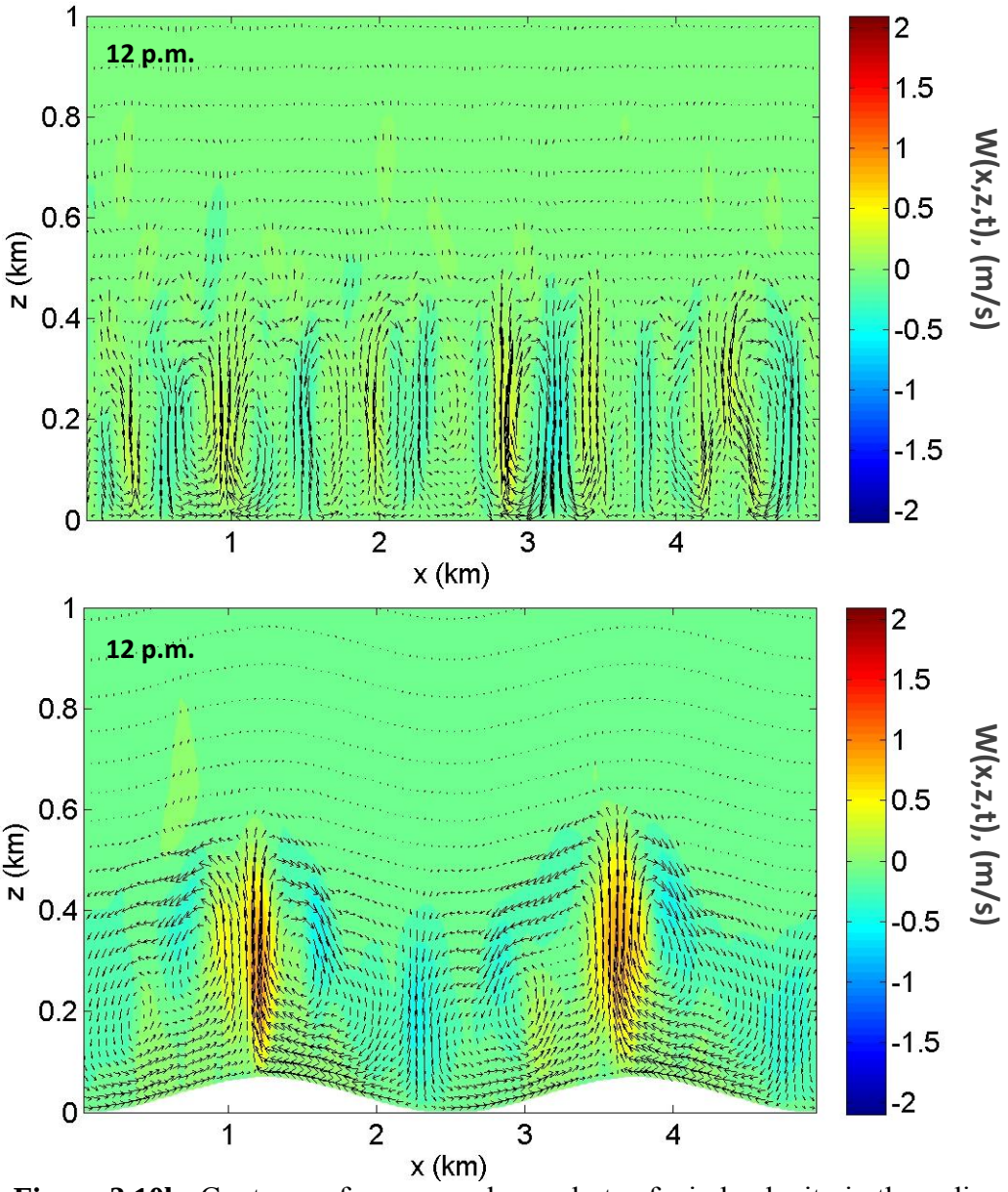


**Figure 3.10b:** Contours of y-averaged snapshots of wind velocity in the z-direction (w(x,z,t)) at 12 pm for cases flat0 & sin0.

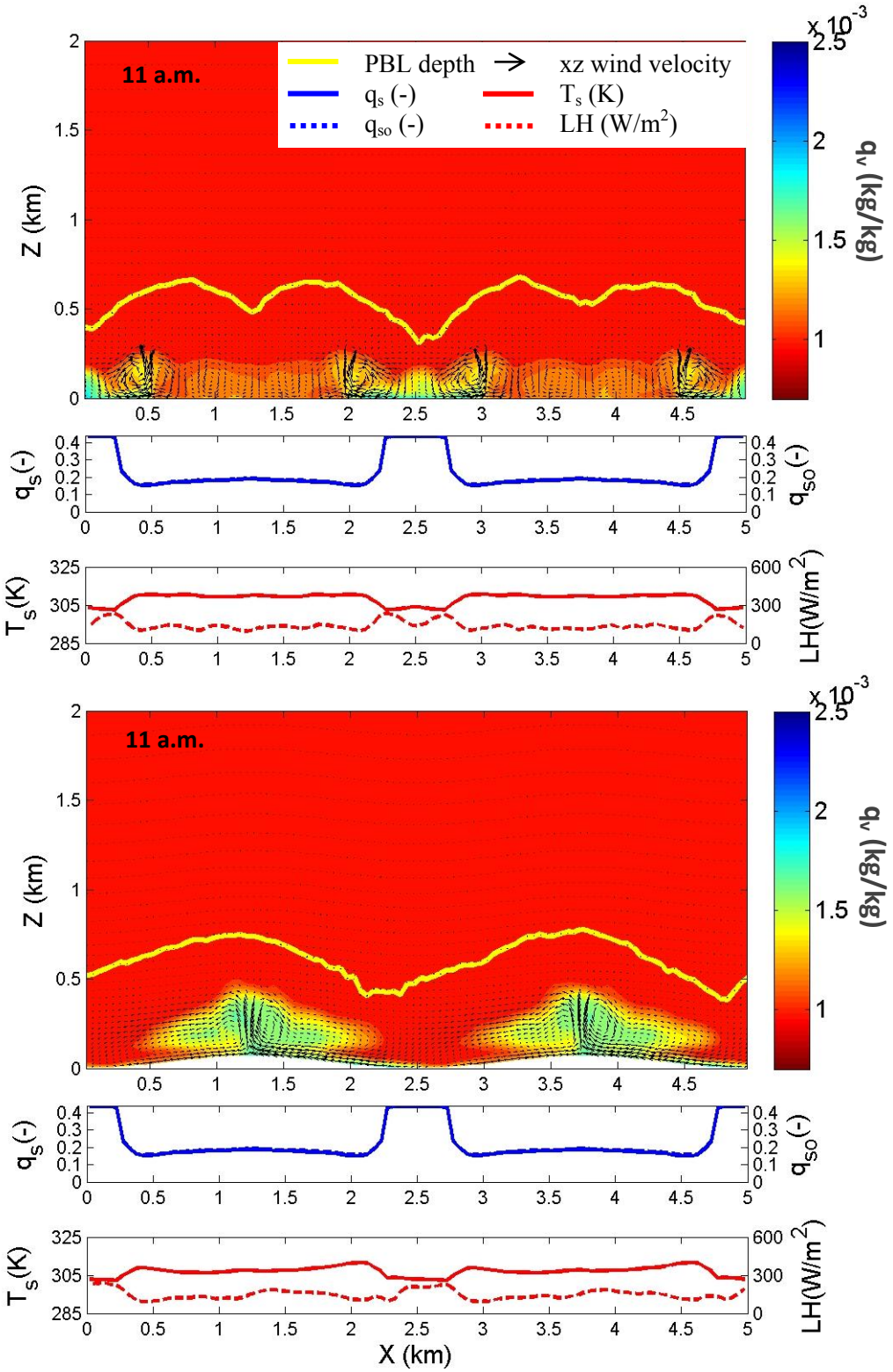


**Figure 3.11a:** 11am y-averaged snapshots of $q_v$ contours and profiles of soil moisture $q_s$ (solid blue), initial soil moisture $q_{so}$ (dashed blue), soil temperature $T_s$ (solid red), and latent heat flux LH at the land surface (dashed red) for cases flat1_wet & sin1_wet.

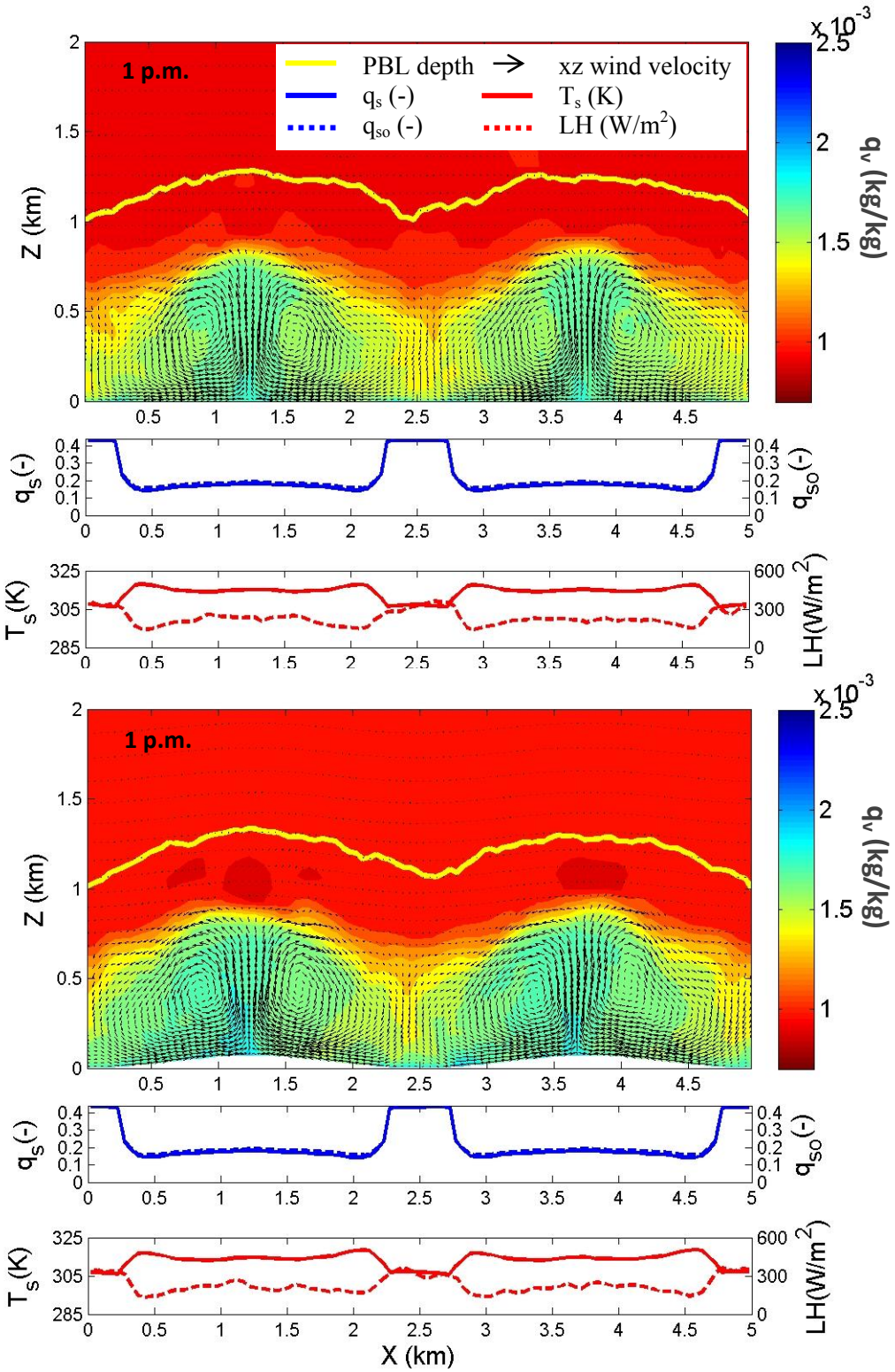


**Figure 3.11b:** 1pm y-averaged snapshots of $q_v$ contours and profiles of soil moisture $q_s$ (solid blue), initial soil moisture $q_{so}$ (dashed blue), soil temperature $T_s$ (solid red), and latent heat flux LH at the land surface (dashed red) for cases flat1_wet & sin1_wet.

### 3.4.3 Effects of Water Table Depth and Soil Moisture Heterogeneity

To isolate soil moisture heterogeneity effects and remove any terrain effects on PBL development, the next set of cases compared here includes two cases with flat terrain; one initialized with uniform soil moisture at half saturation (flat0), the other initialized with realistic heterogeneous soil moisture profile from PF.CLM case1 (flat1_Mar). Figures 3.12a and 3.12b show water vapor mixing ratio contours at 12 pm and 2 pm, respectively. Figure 3.12a shows that the land surface is heated uniformly and the PBL depth is uniform throughout the domain for case flat0. As described in the previous section, variable soil moisture initialization in case flat1_Mar drives downward flows and reduced PBL depth in the wetter valley regions. Dry patches on the other hand heat up faster than wet patches and cause thermals to rise. Without terrain to drive the thermals uphill, the thermals break up in the middle of the dry patch because of its large extent compared to the wet patches. As the afternoon progresses and the land surface continues to heat up, the circulations in case flat1_Mar increase in scale (compared to case flat0). By 2pm (Figure 3.12b), the resulting convective boundary layer carries the signature of these circulations resulting from the heterogeneous soil moisture profile at the land surface. Development of turbulent motions within these circulations is demonstrated by the TKE contour plots in Figure 3.13a and 3.13b. Strongest turbulent motions occur in the middle of the dry patch for case flat1_Mar.

The next test cases illustrate that soil moisture heterogeneity at the land surface affects the PBL even when terrain is added. Figure 3.14 compares the two sinusoid cases sin1_Mar and sin1_Nov. Initialization profiles for both cases come from PF.CLM case1, but at different times of the spinup year as explained in previous sections. The March 18$^{th}$ time (used for case sin1_Mar) is within the rain season and the water table is shallower than that during the November 4$^{th}$ storm. This is clear from the extracted saturation profiles at the land surface ($q_{so}$ in Figure 3.14); the saturated regions around valleys are wider in case sin1_Mar, and the dry patches have more moisture than in case sin1_Nov. Thus, the dry soil patches in case sin1_Nov heat up faster and induce more convection than the dry patches in case sin1_Mar. Even though both cases have the same PBL shape and scale of convective circulations, the result is a shallower and moister PBL for sin1_Mar. The same effect is demonstrated when comparing PBL development for cases sin3_Mar and sin3_Nov (Figure 3.15). These cases have smaller hydraulic conductivity and porosity than cases sin1_Mar and sin1_Nov. The hill top for both cases (sin3_Mar and sin3_Nov) becomes wetter than the hill sides, however in case sin3_Mar the peak reaches saturation at the beginning of the March 18$^{th}$ storm, and the hill sides are much wetter than those in case sin3_Nov. This induces more evaporation and thus cools the land surface in case sin3_Mar which inhibits turbulence and rising thermals resulting in a relatively uniform land surface temperature profile ($T_s$ in Figure 3.15) and a shallower, moister PBL for case sin3_Mar. The soil moisture profile has a greater effect on land surface fluxes in the drier case with greater variation in soil moisture between wet and dry patches. This is shown in the land surface temperature and latent heat flux profiles which are less uniform than the wetter case and follow the soil moisture heterogeneity ($T_s$ and LH in Figure 3.15).

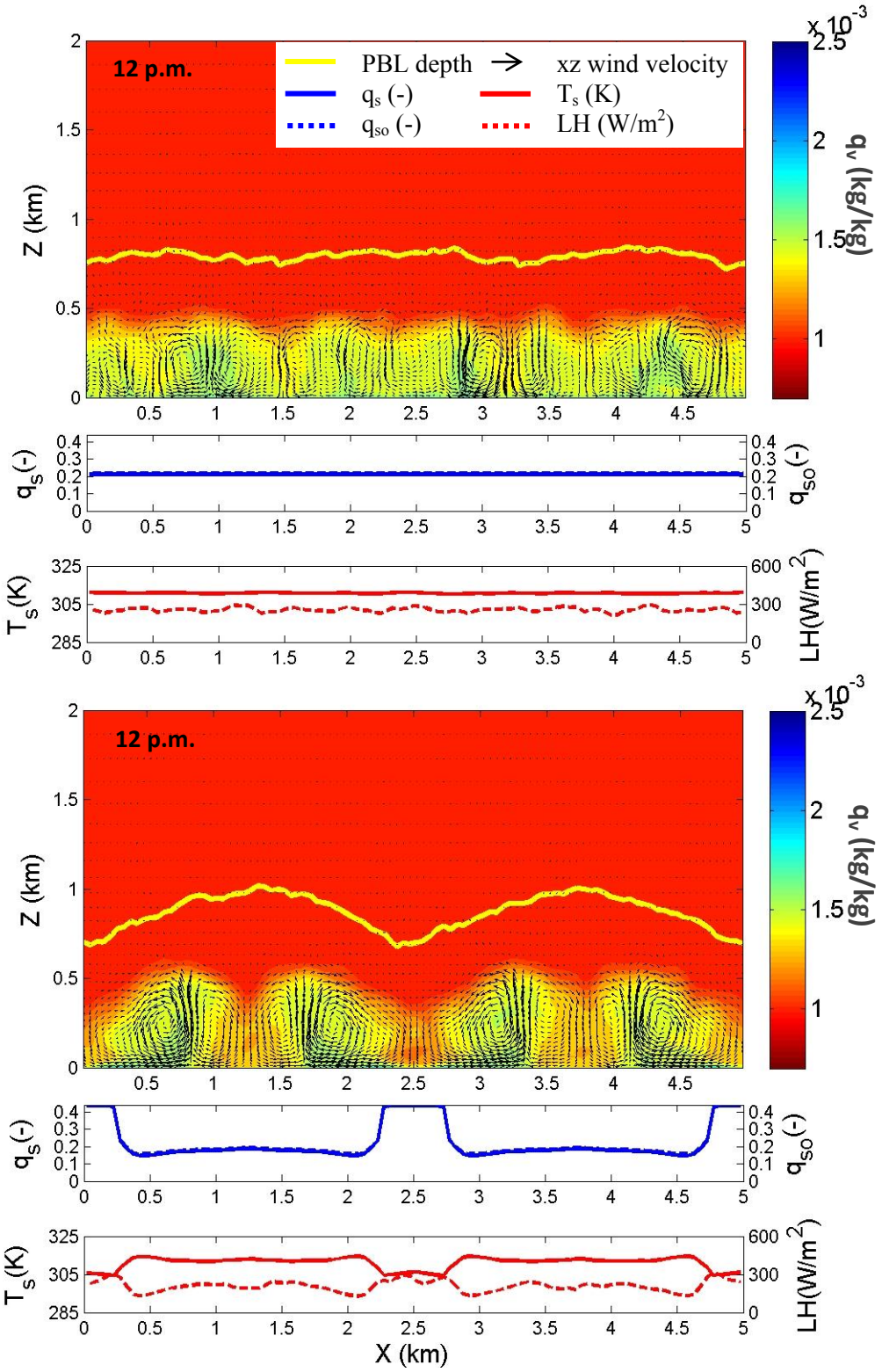


**Figure 3.12a:** 12pm y-averaged snapshots of $q_v$ contours and profiles of soil moisture $q_s$ (solid blue), initial soil moisture $q_{so}$ (dashed blue), soil temperature $T_s$ (solid red), and latent heat flux LH at the land surface (dashed red) for cases flat0 & flat1_wet.

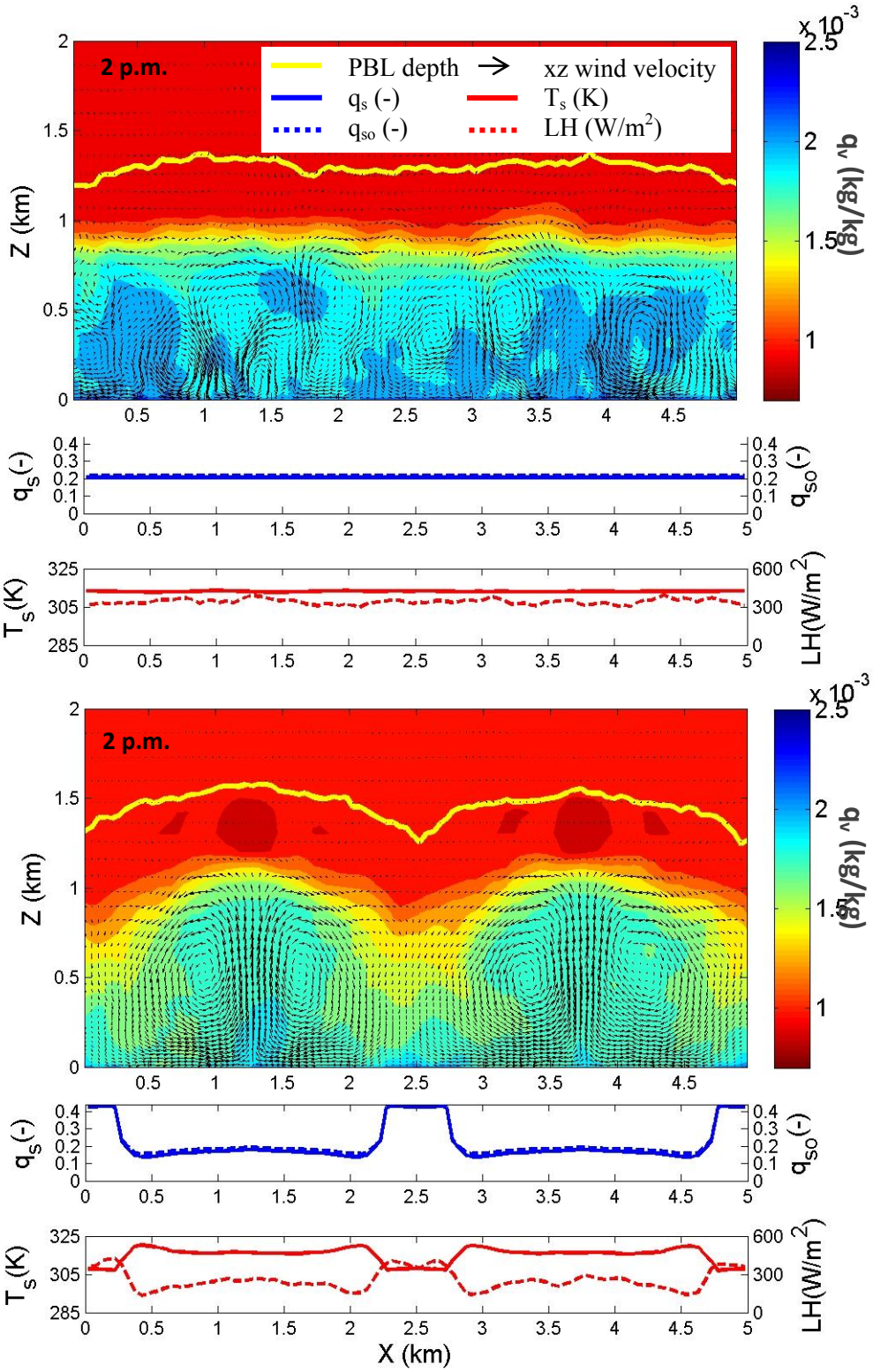


**Figure 3.12b:** 2pm y-averaged snapshots of $q_v$ contours and profiles of soil moisture $q_s$ (solid blue), initial soil moisture $q_{so}$ (dashed blue), soil temperature $T_s$ (solid red), and latent heat flux LH at the land surface (dashed red) for cases flat0 & flat1_wet.

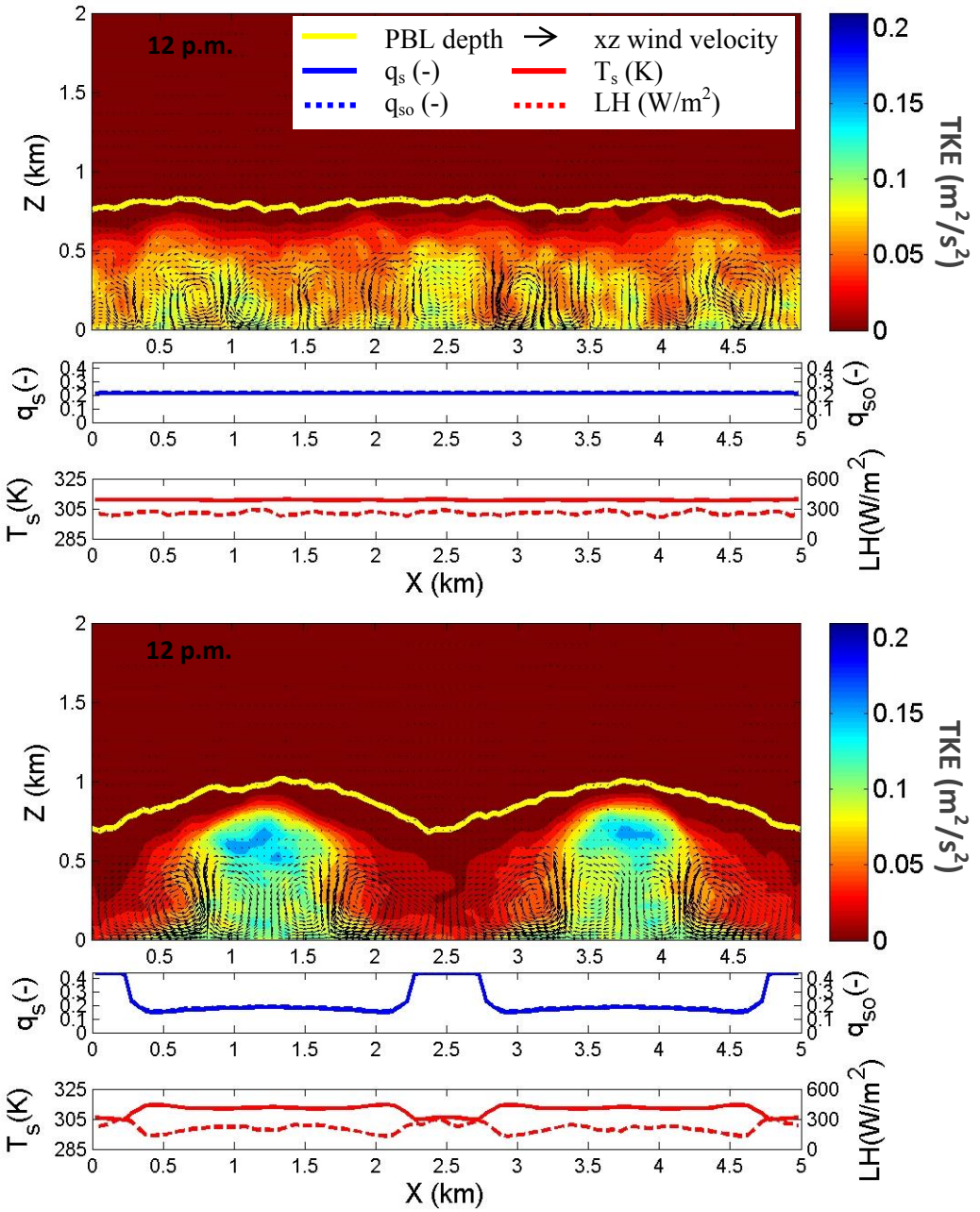


**Figure 3.13a:** 12pm y-averaged snapshots of TKE contours and profiles of soil moisture $q_s$ (solid blue), initial soil moisture $q_{so}$ (dashed blue), soil temperature $T_s$ (solid red), and latent heat flux LH at the land surface (dashed red) for cases flat0 & flat1_wet.

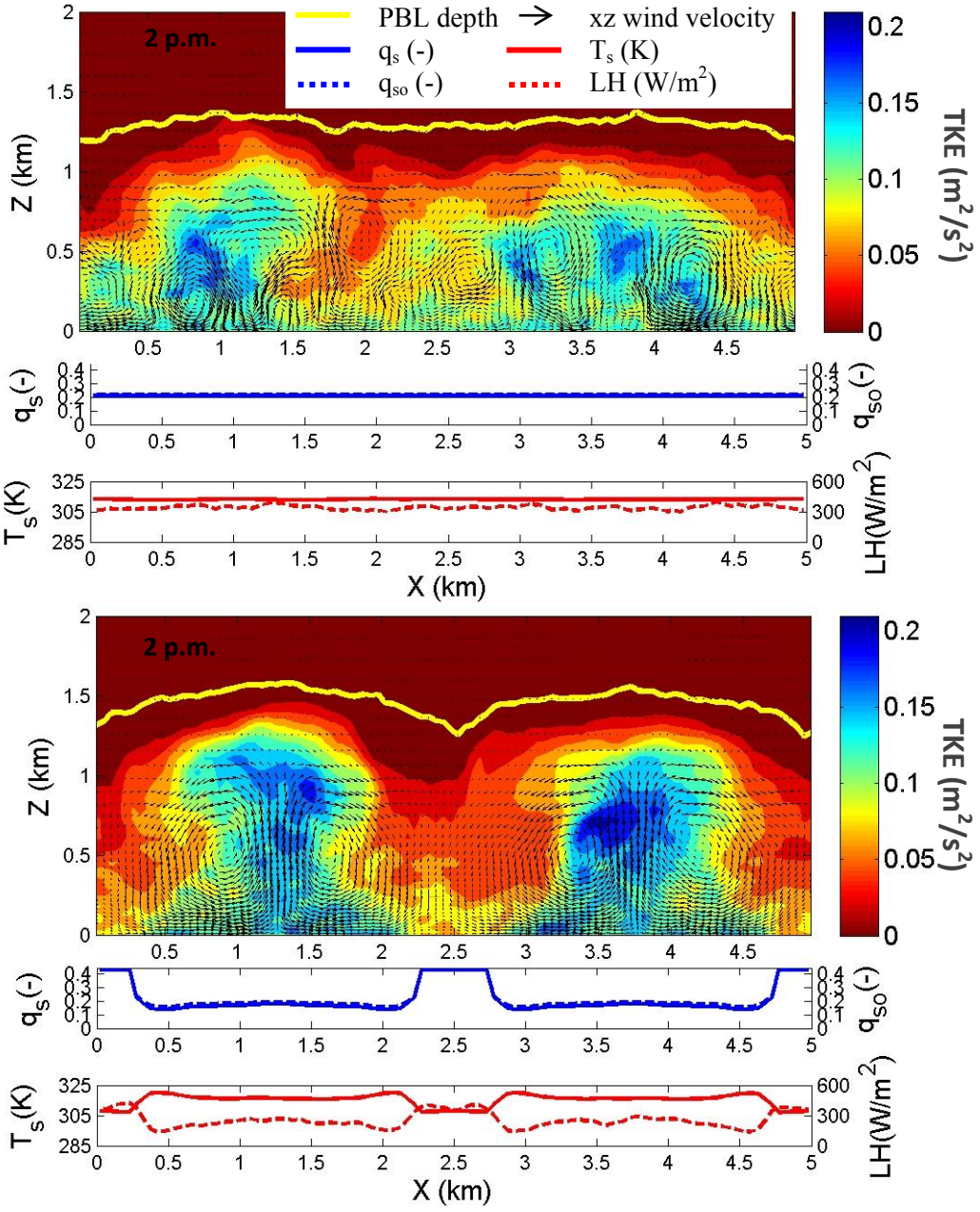


**Figure 3.13b:** 2pm y-averaged snapshots of TKE contours and profiles of soil moisture $q_s$ (solid blue), initial soil moisture $q_{so}$ (dashed blue), soil temperature $T_s$ (solid red), and latent heat flux LH at the land surface (dashed red) for cases flat0 & flat1_wet.

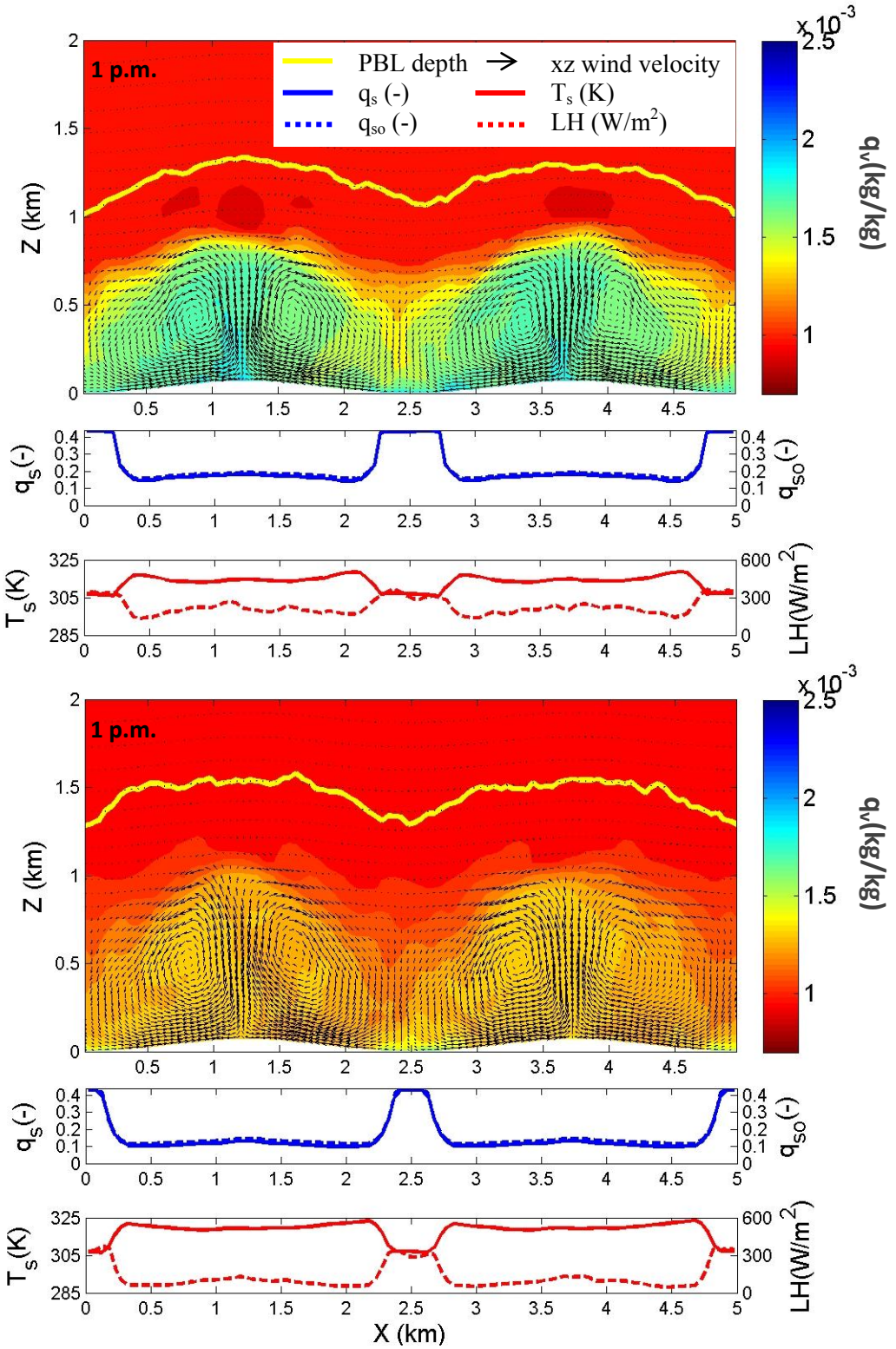


**Figure 3.14:** 1 pm y-averaged snapshots of $q_v$ contours and profiles of soil moisture $q_s$ (solid blue), initial soil moisture $q_{so}$ (dashed blue), soil temperature $T_s$ (solid red), and latent heat flux LH at the land surface (dashed red) for cases sin1_wet & sin1_dry.

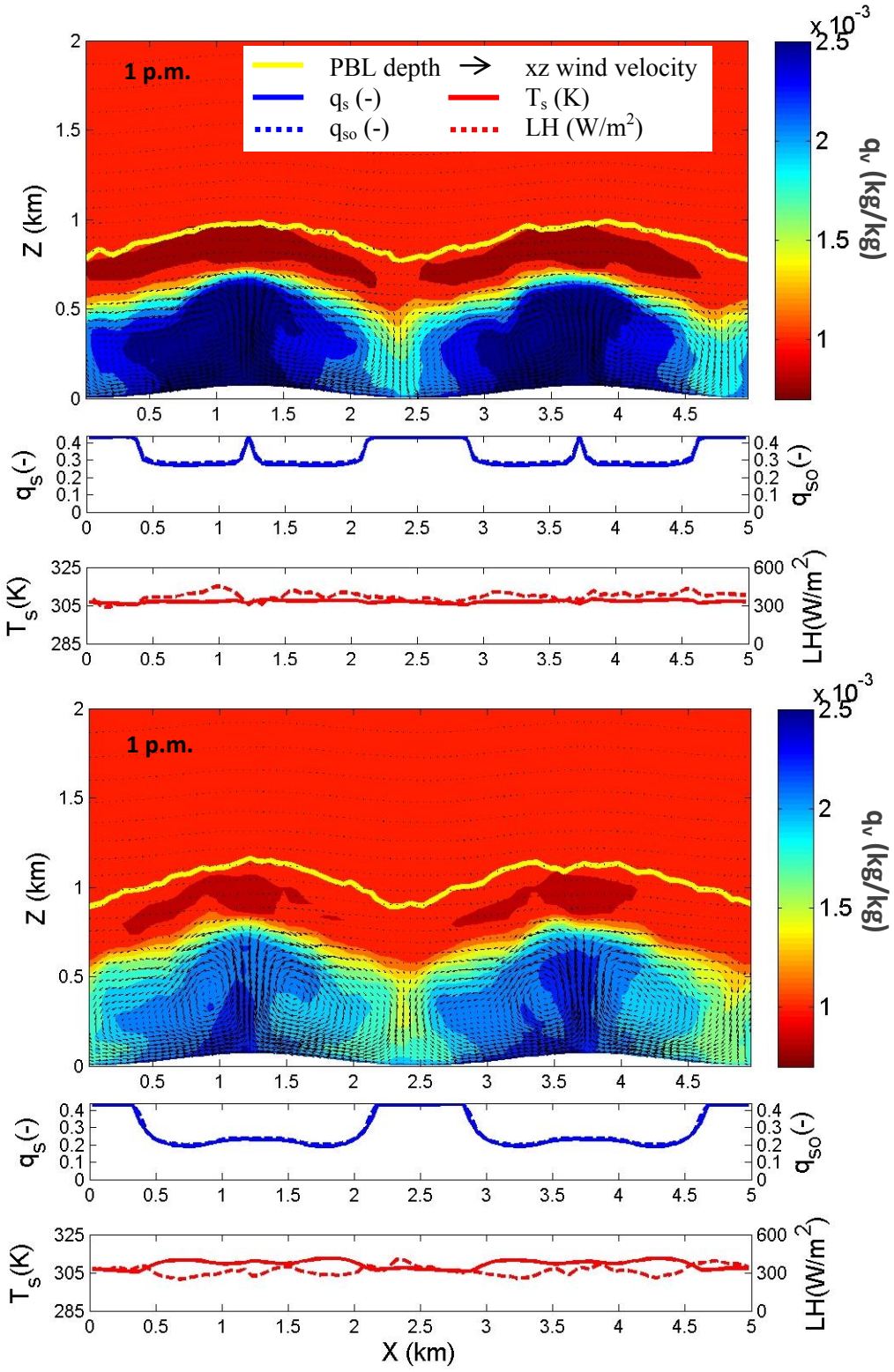


**Figure 3.15:** 1pm y-averaged snapshots of $q_v$ contours and profiles of soil moisture $q_s$ (solid blue), initial soil moisture $q_{so}$ (dashed blue), soil temperature $T_s$ (solid red), and latent heat flux LH at the land surface (dashed red) for cases sin3_wet & sin3_dry.

### 3.4.4 Effects of Subsurface Properties

The soil moisture profiles used to initialize the cases compared in this section come from systems with different subsurface properties (Table 3.1) and thus different water table depths. The indirect effects of subsurface properties are demonstrated here through the resulting soil moisture profiles used to initialize the atmospheric runs. Figure 3.16, for example, compares water vapor mixing ratio contours for cases sin1_Mar and sin3_Mar which are initialized with soil moisture profiles resulting from different saturated hydraulic conductivity and porosity. Both soil moisture profiles are taken during the March 18$^{th}$ storm. Even though the PBL development and shape are similar between the two cases, the land surface fluxes and depth of the PBL are different. Case sin3_Mar, initialized with profiles of lower conductivity and porosity and a shallower water table, has wetter soils at the land surface. As explained before, this results in a shallower PBL depth and more uniform soil temperature and latent heat flux at the land surface (bottom part of igure 3.16). Case sin1_Mar, initialized with profiles of higher conductivity and porosity, retains the soil moisture signature in land surface temperature and heat flux profiles (top part of Figure 3.16). The sharper transition from wet to dry patches in this case induce stronger rising thermals as demonstrated in Figure 3.17 which shows vertical wind velocity contours for both cases.

As it turns out, effects of high values of hydraulic conductivity and porosity are more pronounced in these cases than those of the Van Genuchten (VG) parameters ($\alpha$ and $n$). PF.CLM cases 1 and 2 have different VG properties but the same high conductivity and porosity (compared to case3). Comparing ARPS simulations initialized with profiles for these cases during the March 18$^{th}$ (sin1_Mar vs. sin2_Mar) and Nov 4$^{th}$ storms (sin1_Nov vs. sin2_Nov), as in Figures 3.18 and 3.19, respectively, we see that the sharp transitions from wet to dry patches in all these cases are retained in land surface heat and moisture fluxes ($T_s$ and LH profiles in figures 3.18 and 3.19). Cases sin2_Mar andsin2_Nov are initialized with a soil moisture profile using higher VG parameter values. These cases have drier soils and thus deeper PBL depth than cases sin1_Mar and sin1_Nov, respectively. Figure 3.20 shows that the higher VG parameters result in more vigorous turbulent motions for case sin2_Nov than case sin1_Nov.

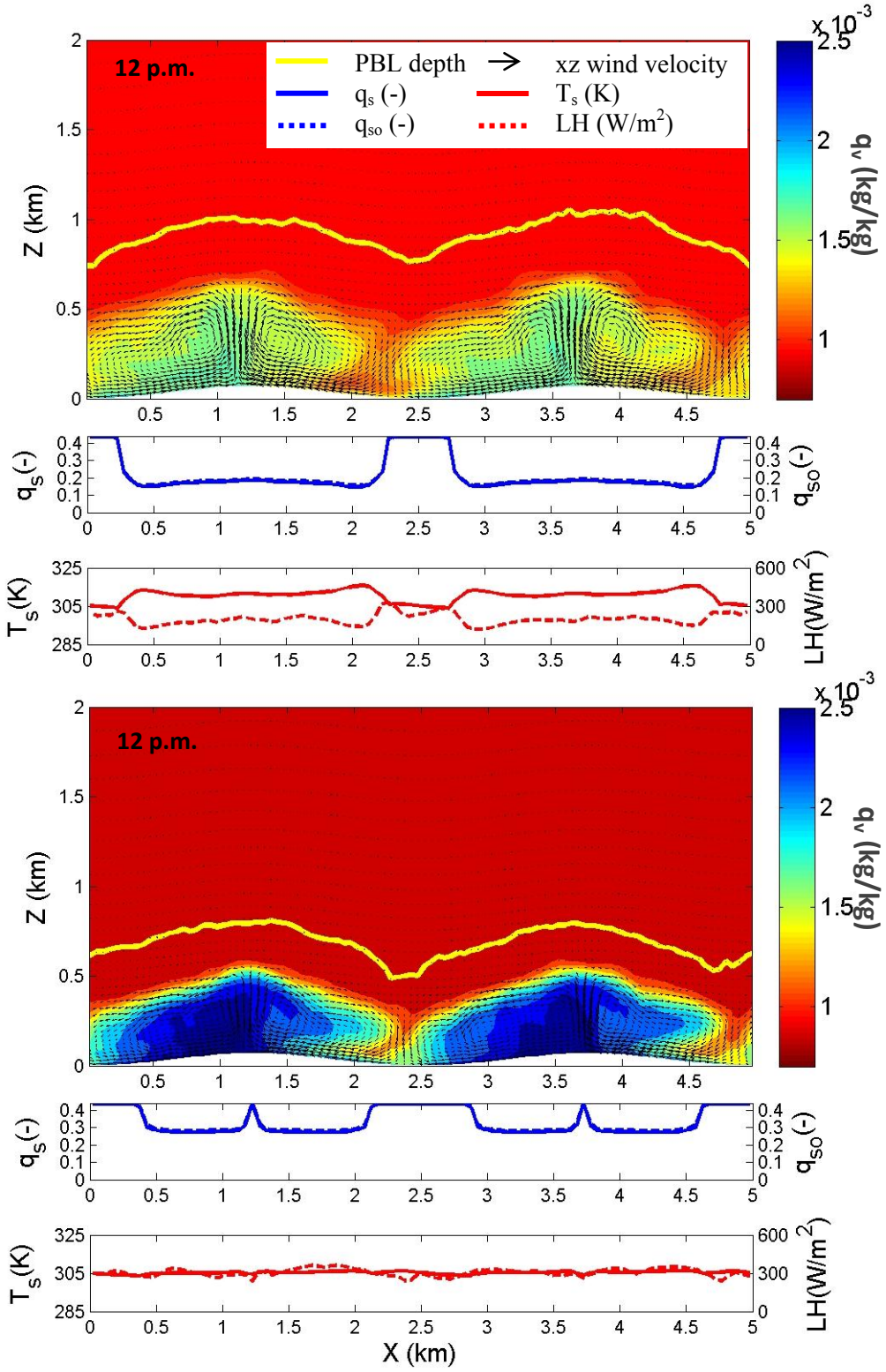


**Figure 3.16:** 12pm y-averaged snapshots of $q_v$ contours and profiles of soil moisture $q_s$ (solid blue), initial soil moisture $q_{so}$ (dashed blue), soil temperature $T_s$ (solid red), and latent heat flux LH at the land surface (dashed red) for cases sin1_wet & sin3_wet.

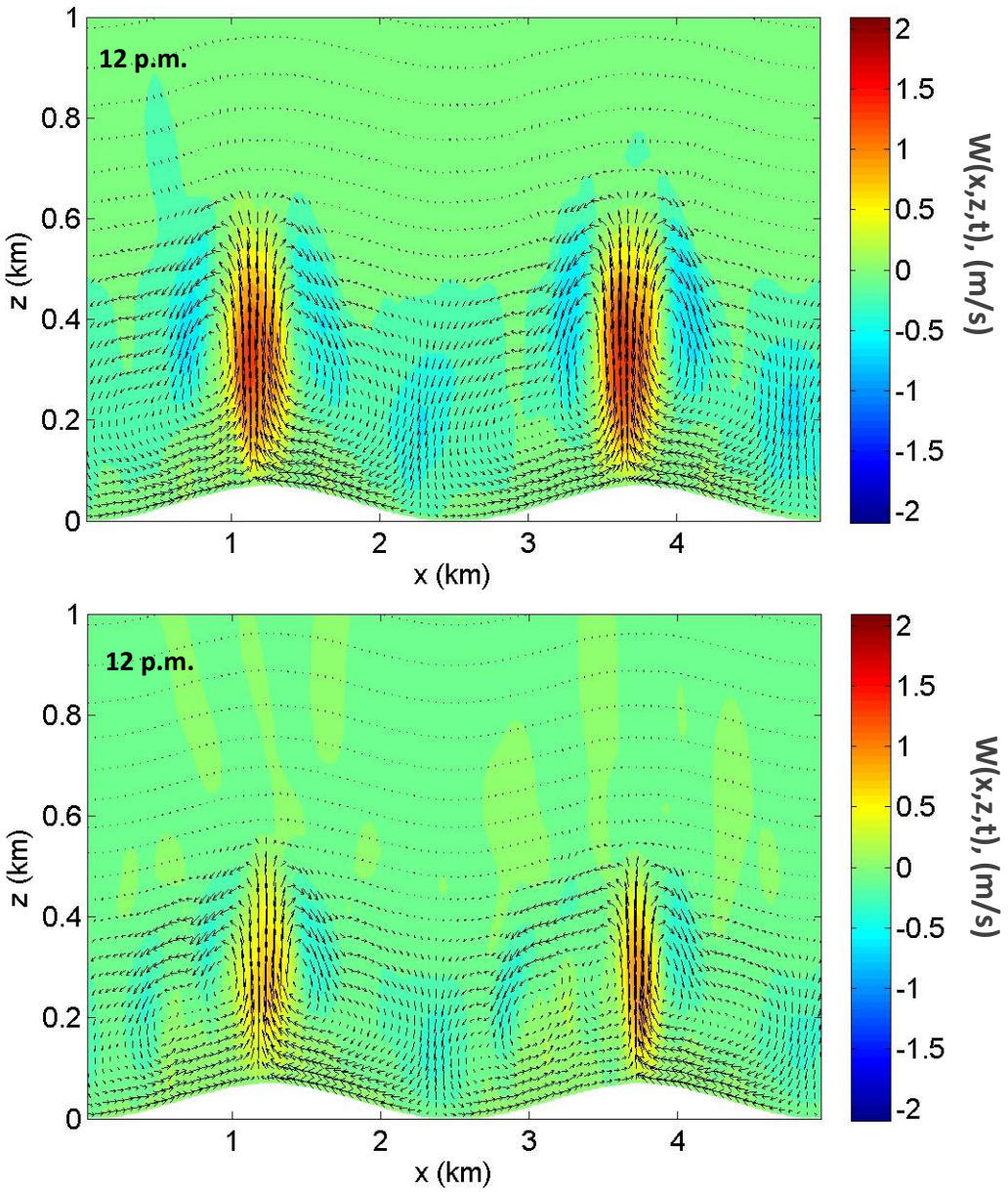


**Figure 3.17:** Contours of y-averaged snapshots of wind velocity in the z-direction (w(x,z,t)) at 12 pm for cases sin1_wet & sin3_wet.

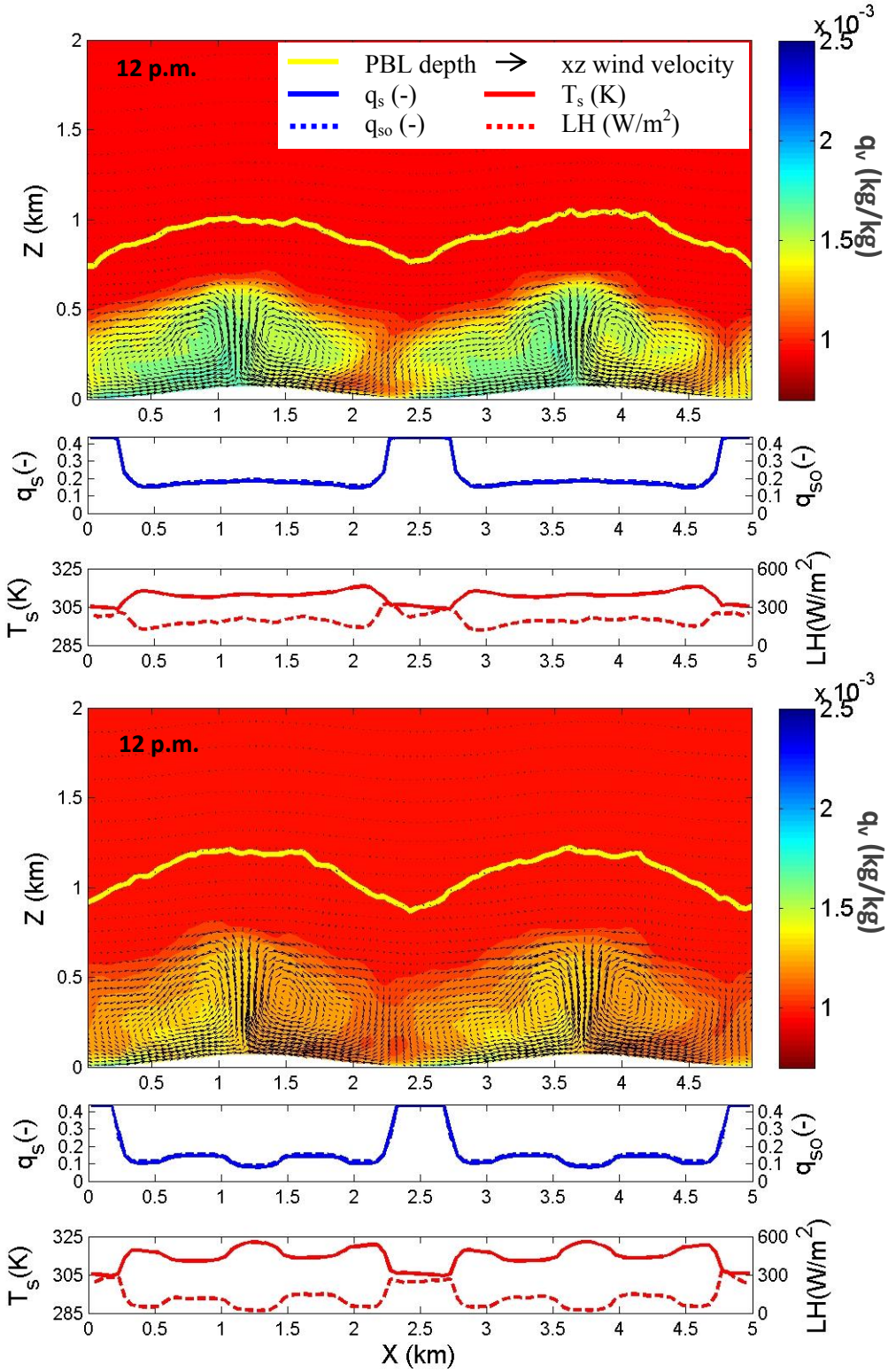


**Figure 3.18:** 12pm y-averaged snapshots of $q_v$ contours and profiles of soil moisture $q_s$ (solid blue), initial soil moisture $q_{so}$ (dashed blue), soil temperature $T_s$ (solid red), and latent heat flux LH at the land surface (dashed red) for cases sin1_wet & sin2_wet.

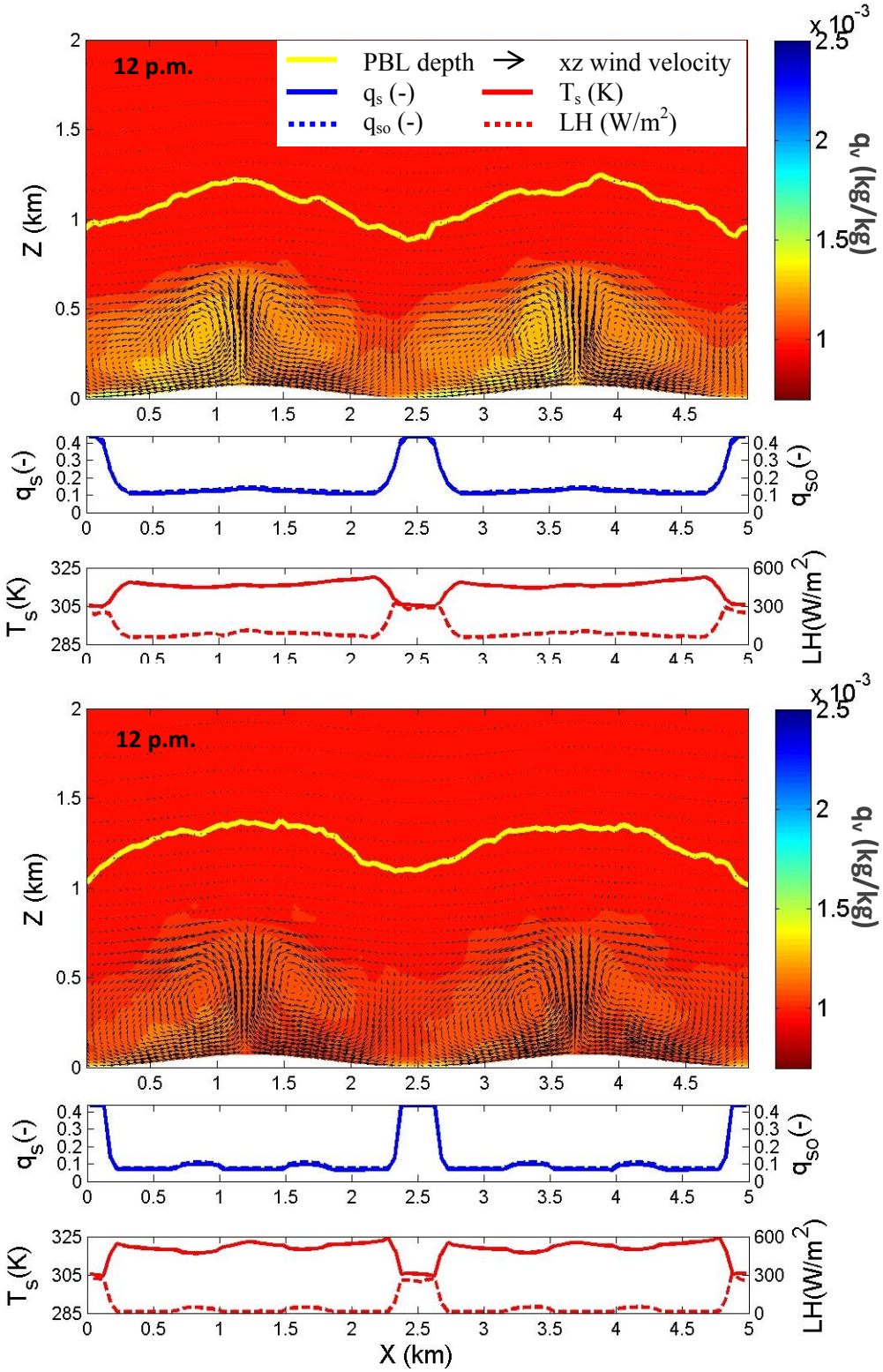


**Figure 3.19:** 12pm y-averaged snapshots of $q_v$ contours and profiles of soil moisture $q_s$ (solid blue), initial soil moisture $q_{so}$ (dashed blue), soil temperature $T_s$ (solid red), and latent heat flux LH at the land surface (dashed red) for cases sin1_dry & sin2_dry.

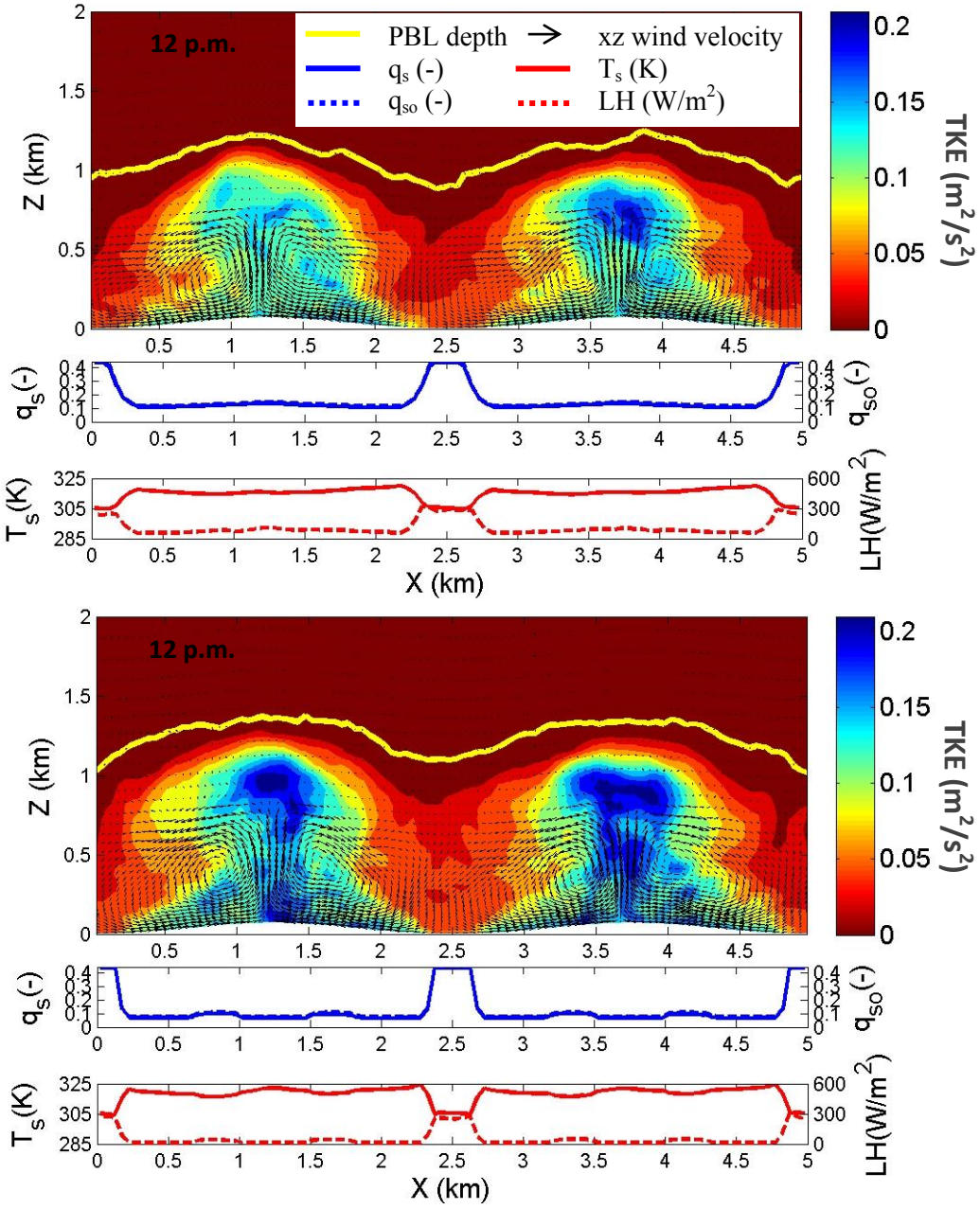


**Figure 3.20:** 12pm y-averaged snapshots of TKE contours and profiles of soil moisture $q_s$ (solid blue), initial soil moisture $q_{so}$ (dashed blue), soil temperature $T_s$ (solid red), and latent heat flux LH at the land surface (dashed red) for cases sin1_Nov & sin2_Nov.

## 3.5 Discussion and Analysis

To further demonstrate how terrain and soil moisture heterogeneity simultaneously affect the development of the boundary layer, profiles of energy and moisture variables are plotted and compared for two sinusoid cases with different soil moisture initializations (sin1_Mar and sin1_Nov). The profiles (shown in Figures 3.21 and 3.22 at 10am and 12pm, respectively) include boundary layer depth (PBLD), water table depth (WTD), soil moisture at the land surface ($q_{soil}$), land surface temperature (Ts), vertical wind velocity (w), latent heat flux (LH), land surface elevation (LS), and water table elevation (WT). These profiles demonstrate that terrain effects on boundary layer development and land surface fluxes are strongest during early morning hours for both cases (e.g. PBLD, Ts, w, and LH profiles at 10 am as shown in Figure 3.21). This effect is stronger for case sin1_Nov because of the larger differences in soil moisture between wet and dry patches than in case sin1_Mar. This implies that soil moisture heterogeneity enhances the effect of terrain on land surface fluxes and PBL development.

As the sun moves higher in the sky and the land surface heats more evenly around noon (Figure 3.22), soil moisture effects begin to overcome terrain effects. The latent heat flux and soil temperature profiles for case sin1_Nov begin to demonstrate a three zone structure (similar to that observed in chapter2); wet or saturated zones at the valleys, dry zones (at hill tops and most of the hill sides), and transition zones in between. Very small LH and Ts changes are observed within saturated valley locations as well as dry hillsides and peaks. Significant changes with WTD and soil moisture are observed however within the transition zones which are highlighted for case sin1_Nov in Figure 3.22. Case sin1_Mar on the other hand shows more numerous transition zones because the land surface is generally wetter and the water table is shallow for a larger extent along the hill side which renders the three-zone structure less clear for this case. These zones play an important role in boundary layer interaction with the land surface and subsurface as they drive the scale and strength of the convective cells which in turn drive the development of the PBL during different times in the diurnal cycle. For instance, the three zone structure in the drier case sin1_Nov, caused by sharper transitions between wet and dry soil patches, drives stronger convective fluxes during morning hours. This results in a PBL depth which is 200m higher for this case than sin1_Mar (Figure 3.22).

To further demonstrate effects of the three zone structure on these cases, Figure 4.23 shows scatter plots of boundary layer depth, latent heat flux, and vertical winds at the land surface against water table depth at 12 pm on the first simulation day. The top panel shows how terrain and soil moisture heterogeneity simultaneously affect the resulting PBL structure. Saturated valley regions (WTD=0) are decoupled from the land surface and thus show no correlation in these plots. Transition zones around the valley have a shallow water table and wet soils. These exhibit a clear positive correlation between PBLD and WTD as wetter soils have cooler land surface temperature which inhibits convective circulations and thus results in a shallower PBL. As water table depth peaks at the sides of the hills rather than at the peaks (note WTD profiles in Figures 4.21 and 4.22), the correlation flips and becomes negative at higher elevations. So although the hill sides are drier than the peaks in these cases, the water table is deep enough such that it becomes decoupled from the land surface. Thus, terrain effects become dominant within this zone such that PBLD increases with terrain rather than with increasing WTD. Effects of terrain are also shown in the two-line structure of each of these plots which demonstrate similar

trends but with slightly different values for each side of the hill; during morning hours, the eastern side of the hill would heat up more and exhibit a slightly higher PBLD. The difference between shaded and non-shaded hillsides is emphasized for the case with drier soil moisture at the land surface (e.g. 3 K difference in land surface temperature and more than 100 $W/m^2$ difference in latent heat flux between two hill sides for case sin1_Nov). This case also has a generally higher PBLD as explained above.

When looking at scatter plots of latent heat flux and vertical winds at the land surface however (Figure 4.23), strong correlations are observed within the transition zone (negative correlation for LH versus WTD, and positive for w versus WTD). Little or no correlation is observed however at and around the decoupled peaks and hillsides as well as at the saturated valley regions. This trend is similar to that observed in chapter 2. These results show how these trends extend through the land surface into the atmospheric boundary layer and affect its properties alongside other factors such as terrain.

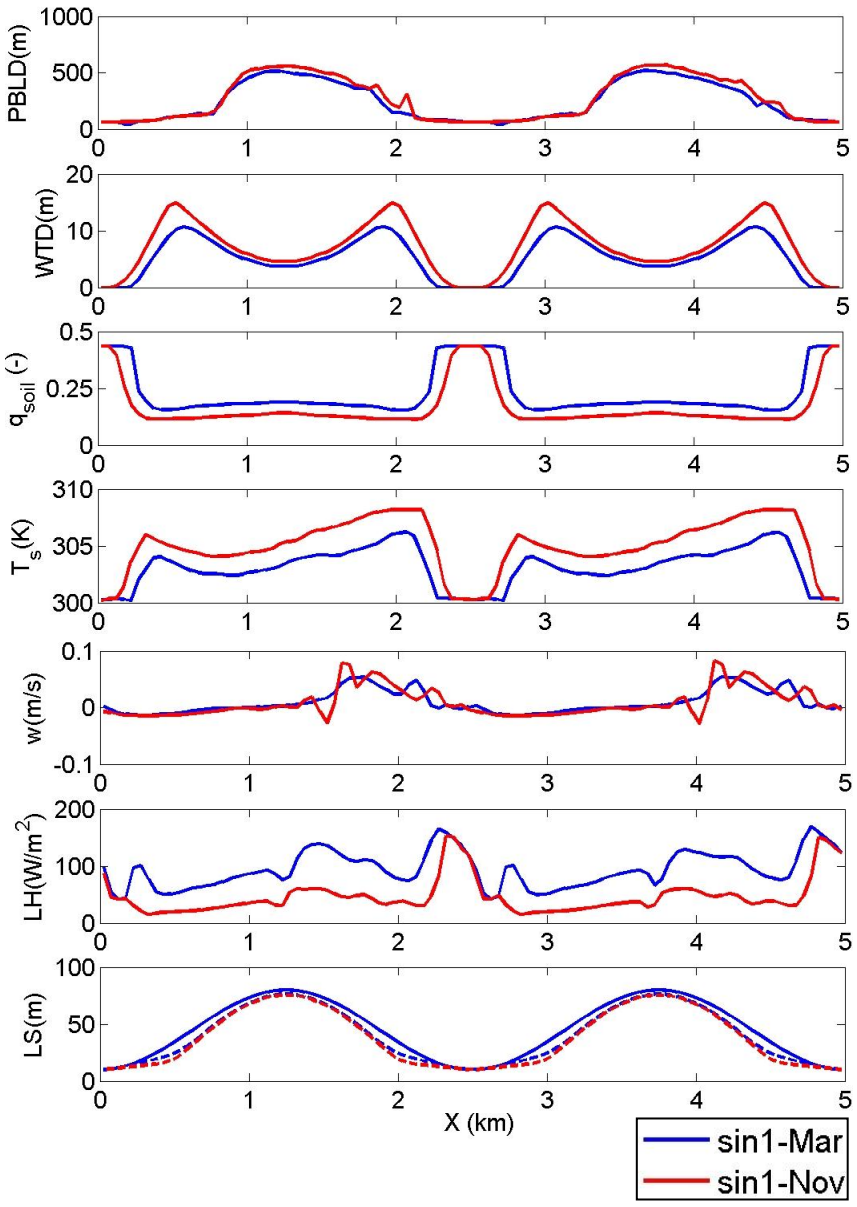


**Figure 3.21:** Profiles at **10 am** of boundary layer depth (PBLD), water table depth (WTD), soil moisture at the land surface ($q_{soil}$), land surface temperature (Ts), vertical wind velocity (w), latent heat flux (LH), and land surface elevation (LS) for cases: sin1_Mar and sin1_Nov. Dashed lines in bottom panel show water table elevation (WT) for the two cases.

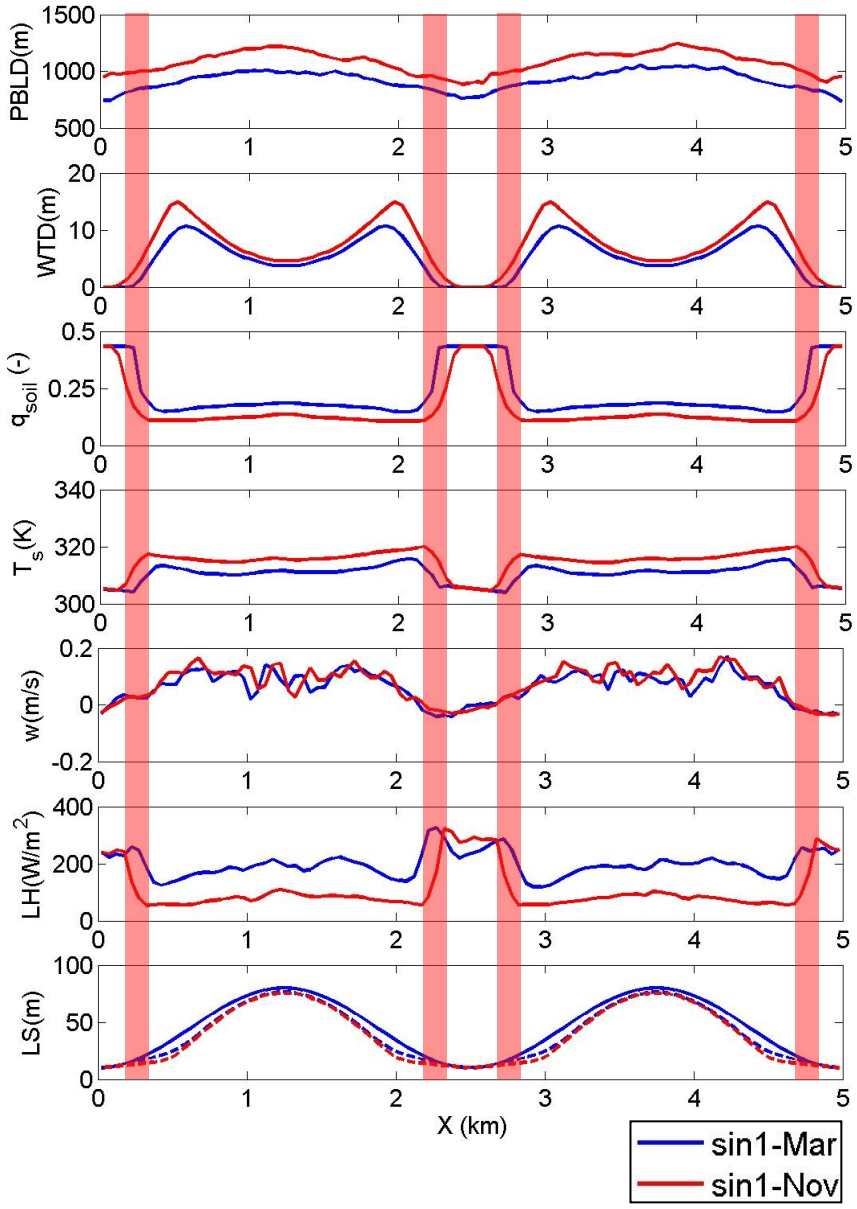


**Figure 3.22:** Profiles at **noon** of boundary layer depth (PBLD), water table depth (WTD), soil moisture at the land surface ($q_{soil}$), land surface temperature (Ts), vertical wind velocity (w), latent heat flux (LH), and land surface elevation (LS) for cases: sin1_Mar and sin1_Nov. Dashed lines in bottom panel show water table elevation (WT) for the two cases. Red highlighted areas show transition zones for case sin1_Nov.

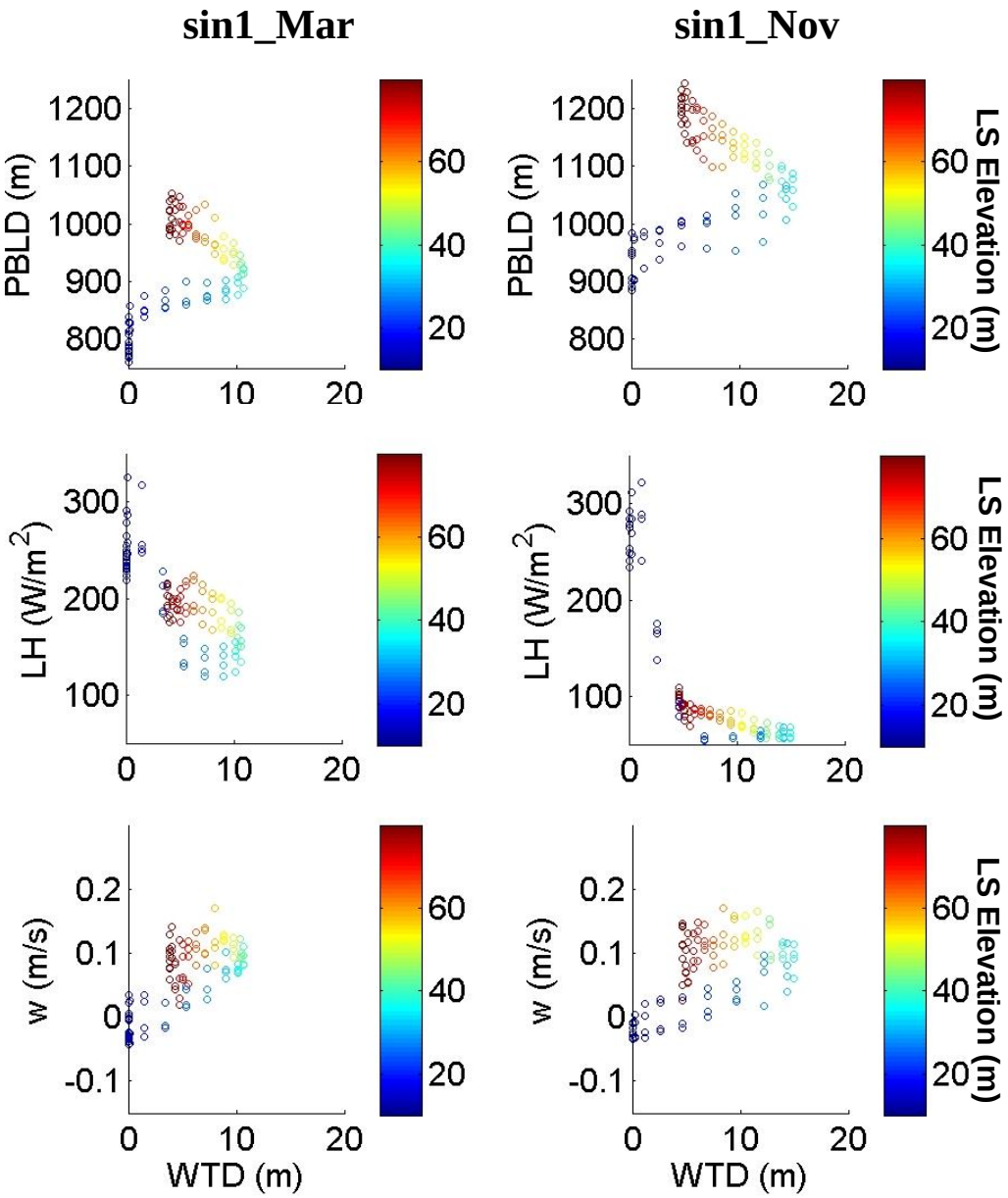


**Figure 3.23:** Scatter plots of boundary layer depth (PBLD), latent heat flux (LH), and vertical wind velocity at the land surface (w) versus water table depth (WTD) for cases: sin1_Mar and sin1_Nov. Scatter points are color coded by land surface (LS) elevation (colorbar).

## 3.6 Conclusions

Idealized atmospheric simulations, initialized with realistic soil moisture profiles from the coupled land surface-groundwater model PF.CLM, were used here to investigate the role of surface soil moisture, terrain, and the indirect effects of subsurface properties on the development of the atmospheric boundary layer. These cases allow us to determine the relative importance of each effect under various conditions. They also demonstrate how terrain and soil moisture heterogeneity simultaneously affect the development of the boundary layer through the land surface temperature and moisture fluxes. The three-zone structure observed in chapter 2 also appears in these atmospheric simulations and this directly controls surface-atmospheric feedbacks. Conclusions are drawn in response to the research questions posed at the beginning of the chapter:

*1. What is the relative importance of terrain and soil moisture variability on the development and structure of the atmospheric boundary layer? And what times within a diurnal cycle show stronger surface-atmospheric feedbacks?*

Terrain affects the boundary layer development by inducing variable heating and cooling at the land surface which drives thermally-forced winds. Effects of terrain on the convective boundary layer development are stronger during morning hours when the nocturnal stable boundary layer is destroyed. This effect is more pronounced when the difference in soil moisture between wet and dry patches is greater which implies that soil moisture heterogeneity may enhance the effect of terrain on PBL height and development. In the afternoon when the land surface heats more evenly, soil moisture effects overcome terrain effects. A wetter land surface induces higher evaporation rates and thus higher moisture fluxes into the atmosphere. A drier land surface, on the other hand, implies more heating, increasing thermals from the land surface and an upward net heat flux. This positive correlation increases as the day progresses and more heating occurs. The soil moisture signatures gradually disappear at the end of the day as the land surface starts to cool, turbulent motions die off, and a nocturnal stable layer develops.

*2. How do subsurface properties (reflected in soil moisture initialization profiles) affect the structure and depth of the PBL?*

The simulations show that saturated hydraulic conductivity and porosity can significantly affect soil moisture and hence boundary layer development. Initialization profiles obtained from offline spinup cases with higher conductivity and porosity values had more heterogeneous soil moisture profiles at the land surface. This dictates the extent of the three-zone structure and results in sharper transition zones which exhibit increased sensitivity of land surface heat and moisture fluxes to soil moisture profiles at the land surface. This is reflected in the structure of the PBL and its positive correlation to water table depth within the transition zones. The effect of soil moisture however becomes less important outside the transition zone, particularly elevations higher than the transition zone. Terrain effects dominate within this decoupled region and have a more pronounced effect on PBL depth which now has a negative correlation to water table depth.

Water retention properties of the subsurface also have an effect, though less pronounced than that of conductivity and porosity, on developing convective cells and the resulting PBL depth.

*3. Can we gain a better understanding of the processes which drive the atmospheric boundary layer by initializing atmospheric simulations with detailed soil–moisture profiles obtained from offline-simulations using realistic terrain and subsurface properties, rather than using uniform or simplified soil moisture profiles?*

Results demonstrate that even when a fully coupled subsurface-surface-atmospheric simulation is not computationally feasible; using soil moisture initialization profiles (obtained from coupled offline subsurface-land surface simulations) have a significant effect on the simulated convective boundary layer. The development and depth of the simulated PBL in this case carries a clear signature of land surface conditions which in turn reflects water table dynamics and subsurface properties more realistically than when using a simplified wet or dry soil moisture field.

This is the first time, to our knowledge, that these land-atmosphere connections have been explicitly demonstrated and hence present unique contributions. In reality it may not be easy to isolate effects of terrain and soil moisture variability on the boundary layer. Understanding how these effects work in an idealized setting brings us a step closer to interpreting their role in driving boundary layer development in a real watershed. In the next chapter, the fully coupled subsurface-land-surface-atmospheric code PF.ARPS is used to simulate the Little Washita watershed in Oklahoma to incorporate all the feedbacks studied in chapters 2 and 3 in a real setting. Results are compared to non-coupled atmospheric simulations of the same watershed.

# Chapter 4

## Coupled Subsurface-Land Surface-Atmospheric Simulations of a Real Watershed

Results in chapter 3 demonstrate how land surface heating and cooling control the development of convective circulations which in turn determine the structure of the PBL. In this chapter, these effects are examined under real weather conditions and real terrain. The Little Washita watershed in Oklahoma is simulated using the mesoscale atmospheric model, ARPS, in three different configurations. First, ARPS is run with NARR soil moisture (the default configuration). Second, ARPS is initialized with realistic soil moisture conditions resulting from offline spinups using PF.CLM. Third, PF.ARPS is used in coupled mode to represent the coupled atmospheric-surface-subsurface, initialized with the PF.CLM soil moisture from the spinups. NARR time-variant boundary conditions are used throughout the simulation time of 4 days for all three cases. Results show small differences between the three runs, particularly between PF.ARPS and ARPS initialized with PF.CLM soil moisture on one hand, and the ARPS case initialized with NARR soil moisture. A scaling analysis demonstrates that the lateral boundary conditions dominate over land surface fluxes, making the simulations more similar than in previous work with closed boundaries. The differences between the PF.ARPS and ARPS runs show the significance of soil moisture initialization in atmospheric simulations. Particularly in cases where a computationally expensive, fully coupled modeling approach is not feasible, employing more realistic soil moisture conditions at the land surface does make a difference in model results. Furthermore, results from the fully coupled PF.ARPS simulation show a strong correlation between water table depth and boundary layer depth, as expected based on results from Chapters 2 and 3.

### 4.1 Introduction

The importance of land surface processes to the overlying planetary boundary layer (PBL) has long been recognized in the literature (Pielke, 2001). While changes in the Earth's surface can result in significant changes in the surface energy and moisture budgets; water table dynamics also have an effect on land surface energy balance and thus may affect the PBL (Yeh and Eltahir 2005, Kollet and Maxwell 2008, Seuffert et al. 2002). Yeh and Eltahir (2005) addressed errors in predicted land surface fluxes especially for shallow water table areas in humid regions by developing a simple unconfined aquifer model and interactively coupling it to a land surface scheme. They tested this coupled model in Illinois and were able to show the importance of the presence of a shallow water table in affecting the near-surface soil moisture profile, and hence the numerous hydrological processes associated with the soil wetness condition. Kollet & Maxwell (2008) studied the influence of groundwater dynamics on the energy balance at the land surface for the Little Washita watershed in Oklahoma using the three-dimensional, variably-saturated groundwater code ParFlow coupled to the Common Land Model (PF.CLM). They used spatially distributed soil cover information for the top soil layer. The remaining subsurface layers were modeled as homogeneous. Their results show that components of the energy balance are most sensitive to groundwater dynamics if the water table is neither too

shallow nor too deep, but within a range in between called the critical depth. A very shallow water table makes the land surface non-moisture limited while a very deep water table is essentially decoupled from the land surface. The critical zone forms the transition between these two cases and it is within this zone that small changes in water table depth result in significant vertical redistribution of soil moisture at the land surface and thus causing significant changes of land surface mass and energy fluxes. The critical zone is studied in detail in this research for a range of cases with varying subsurface layering, properties, land forms, vegetation, and climatic forcing (as presented in chapter 2). Terrain, subsurface layering, and properties are shown to have great significance in changing water table dynamics, its coupling to land surface energy fluxes, and thus to the location and extent of the critical zone along a hillside.

Effects of water table depth have been shown to extend to the atmospheric boundary layer (York et al. 2002, Maxwell et al. 2007). York et al (2002) developed a coupled aquifer-land-surface-atmospheric model to demonstrate that a physically based groundwater model can provide insights into groundwater-atmosphere interactions on decadal timescales. Their model consisted of a single column atmospheric model coupled via a land surface model to a single layer groundwater model. They investigated effects of aquifer levels on evapotranspiration in a watershed in northeastern Kansas and showed that seasonal and inter-annual feedbacks between water levels and atmospheric forcing exist. Maxwell et al. (2007) used a 3D, fully coupled, groundwater-atmospheric flow model (PF.ARPS) to study the influence of terrain and soil moisture variability on atmospheric boundary layer forcing under idealized conditions in the Little Washita watershed in Oklahoma. They detected a close relationship between water table depth and boundary layer height such that regions with a shallower water table have wetter soil moisture and cooler soil temperatures and hence a lower boundary layer height. They also found that these feedbacks become stronger during early morning hours as the convective boundary layer is developing from its stable nocturnal form.

Accordingly, changes in landscape properties (land form and surface soil moisture) affect the climate system as much as atmospheric processes such as cloud activity, energy and moisture transport (Pielke, 2001). Despite numerous field and modeling studies, however, the connection between the land surface and the atmosphere remains difficult to quantify. In particular, with real terrain and atmospheric conditions, it can be difficult to isolate the role of land-atmosphere feedbacks if other effects are dominant.

Maxwell et al. (2007), mentioned above, specifically chose to turn off lateral boundary forcing so that the influence of the soil moisture on the atmosphere would not be overshadowed by synoptic winds. In this work, we include time-variant lateral boundary forcing for the same Little Washita domain to simulate realistic conditions. We thus explore the effect of including a dynamic representation of subsurface hydrology and water table on subsurface-land-surface feedbacks into the atmospheric boundary layer. The following key questions are used to guide the simulations and analysis presented in this chapter: (1) What are the effects of lateral boundary forcing compared to effects of the land surface conditions? (2) Which times within the diurnal cycle and locations within the watershed show stronger feedbacks between the water table and the atmospheric boundary layer? (3) How does a storm system affect the coupling and which days show stronger feedback: before, during, or after a storm? We begin with a

description of the models used here, the Little Washita watershed, and the different cases being simulated and compared.

## 4.2 Models

### 4.2.1 The Advanced Regional Prediction System (ARPS)

ARPS is a parallel, meso-scale atmospheric model designed for prediction of convective storms and serves as an effective tool for studying the dynamics and predictability of storm-scale weather in both idealized and more realistic settings. It was developed at the Center for Analysis and Prediction of Storms (CAPS) at the University of Oklahoma (Xue et al. 2000, Xue et al. 2001). ARPS solves the three-dimensional, compressible, non-hydrostatic, spatially-filtered Navier–Stokes equations and can be run in large-eddy simulation (LES) mode. Its governing equations (see Appendix B) employ a terrain-following curvilinear coordinate system and include equations for conservation of mass, momentum, heat, water (vapor, liquid and ice), turbulent kinetic energy (TKE), and the equation of state of moist air. ARPS employs high-order monotonic advection schemes for scalar transport and fourth-order central differencing advection schemes for other variables. A split-explicit time advancement scheme is used with leapfrog on the large time steps, and a forward-backward scheme for the smaller timesteps used to integrate the acoustic terms in the equations.

### 4.2.2 Coupled subsurface-surface-atmospheric model (PF.ARPS)

The variably-saturated groundwater flow model ParFlow coupled to the atmospheric model ARPS is used here to simulate the hydrologic cycle in a more dynamic and coupled manner. ParFlow solves the three-dimensional Richards equation and has an integrated overland boundary condition in which ParFlow explicitly resolves streamflow by solving the kinematic wave equation (Kollet and Maxwell, 2006). ParFlow uses a very robust parallel, globalized Newton method coupled to a multigrid-preconditioned linear solver (Ashby and Falgout, 1996; Jones and Woodward, 2001) and is implemented here in transient mode. The pressure-saturation relationship is obtained from the vanGenuchten formulation (Van Genuchten 1980). An implicit backward Euler scheme in time is used for both the subsurface and overland flow components. A cell-centered finite difference scheme in space is used for the groundwater flow solution while an upwind finite volume in space is used for the land surface solution. ParFlow solves for water pressure in the subsurface and gives the saturation field (from which the water table can be determined) at every time step in the simulation. Input parameters include subsurface hydraulic properties (e.g. saturated hydraulic conductivity, porosity) and land surface properties (vanGenuchten parameters, manning's coefficient, and surface slopes).

Coupling between the two codes is performed by implementing ARPS as a subroutine in ParFlow, and involves the simultaneous solution of the three-dimensional groundwater equations in ParFlow and the three-dimensional atmospheric flow equations in ARPS (Maxwell et al. 2007). The ARPS land surface model comprises the interface between the two models such that the two top soil layers in ARPS are numerically overlaid with the two top soil layers in ParFlow. The original land surface model in ARPS passes surface momentum, heat and moisture fluxes

between ParFlow and ARPS, and the subsurface hydrology in the land surface model is now entirely replaced by ParFlow (Figure 4.1).

An operator-splitting approach is applied which allows ParFlow to honor either the same time step as ARPS or run at a larger time step. The coupled solution begins with explicit advancement of ARPS over the ParFlow time step. Fluxes relevant to ParFlow (such as infiltration and evaporation) are integrated within ARPS over the ParFlow time step and then used to provide surface fluxes over the next time step for implicit time advancement of ParFlow. ParFlow now provides the soil moisture field and passes it through the land surface model to be used in the next ARPS internal time step. The coupled model is mass and energy conservative.

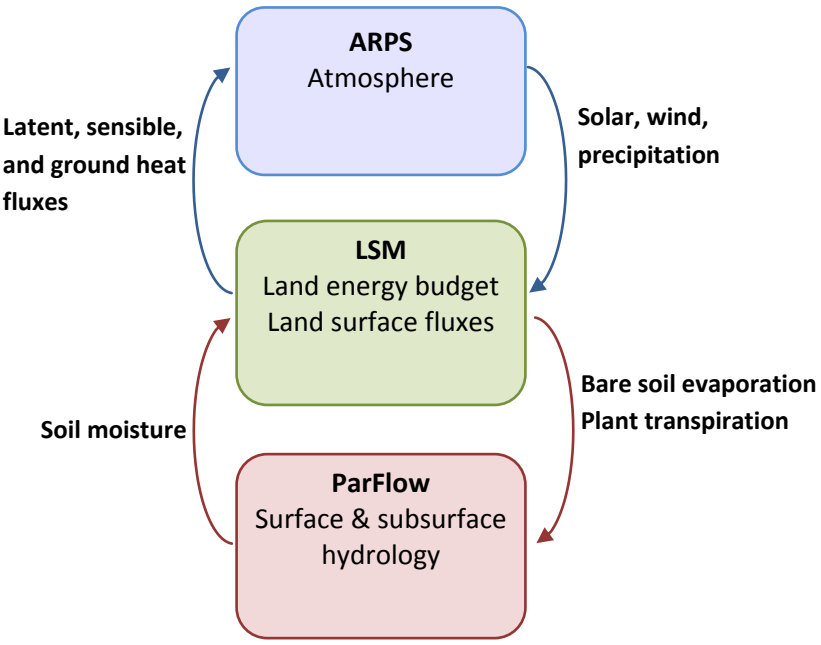


**Figure 4.1**: Coupled model processes in PF.ARPS (adapted from Maxwell et al. 2007).

## 4.3 The Little Washita watershed

The site being investigated is the Little Washita watershed located in the Southern Great Plains in central Oklahoma (Figure 4.2). This watershed has been the subject of many previous studies and has an exceptionally extensive observational dataset of shallow subsurface, surface, and atmospheric data ideal for validation. The simulations presented here build upon the work of Maxwell et al. (2007) and Maxwell and Kollet (2008) who investigated quasi-idealized conditions in the Little Washita. In the simulations presented here, three-dimensional grid nesting is used to provide the model with real atmospheric initial conditions and transient boundary conditions of wind, potential temperature, and humidity during summer 2003 when datasets from multiple field experiments are available.

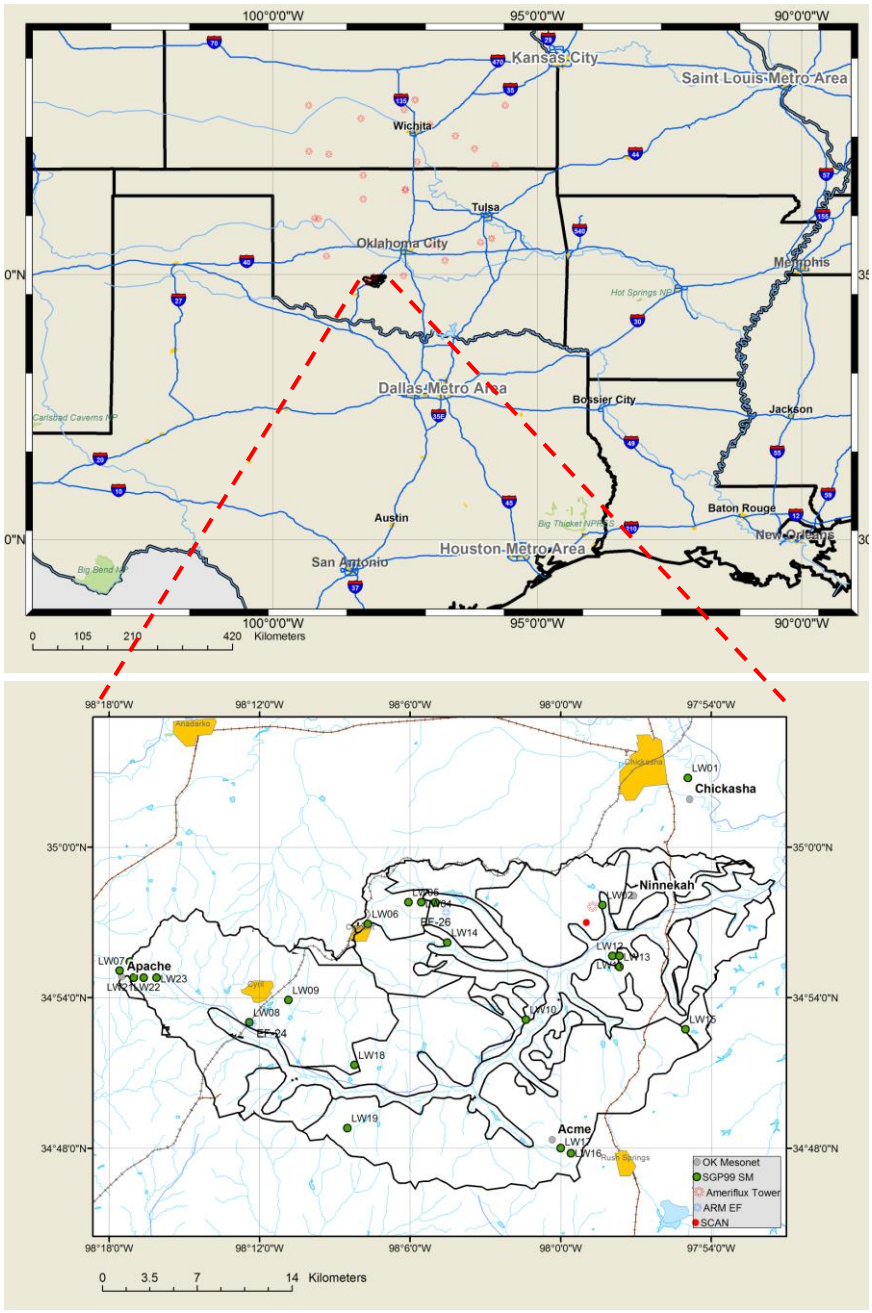


**Figure 4.2**: Location of the Little Washita watershed within the state of Oklahoma (Kollet and Maxwell, 2008).

### 4.3.1 Model setup and grid

The watershed has an area of approximately 600 km$^2$. The model domain was extended beyond the boundaries of the watershed to allow for the hydraulic surface and subsurface conditions to

develop naturally in the model during the spinup process (section 4.3.4). Grid nesting was used to model the watershed at a horizontal resolution of 1 km (from the NARR resolution of 9 km) using 45 x 32 cells in x and y, respectively. Vertical grid stretching is used in the atmospheric part of the model which has 50 vertical grid points. Vertical spacing of 40 m is used near the ground which is stretched to an average of 400 m spacing over the 20 km domain height in ARPS. The subsurface domain has uniform 0.5 m spacing and 390 grid points in the vertical. This gives a maximum subsurface depth of 195 m depth which is suitable for modeling deep groundwater as well as insuring that the lower boundary of the model does not affect processes at the land surface.

The land surface is defined as the upper boundary of the groundwater model and is generated from a digital elevation model as shown in Figure (4.3). ParFlow allows for an overland flow boundary condition to be used at the land surface (Kollet and Maxwell, 2006). No flow boundary conditions are used on all other sides of the subsurface model. Grass is the main vegetation type in the Little Washita with some scattered shrubs and trees. Soil types are mostly loamy sand, and sand, with small areas of silt loam (Figure 4.4). As mentioned previously, this model setup is based on simulations performed by Maxwell et al. (2007) for the Little Washita. Although Maxwell et al. studied a fully convective atmospheric boundary layer by initializing their model with quiescent winds and a sounding profile, the simulations presented here are provided with time-variant atmospheric conditions at the boundaries to study the effects of a real weather system passing over the domain.

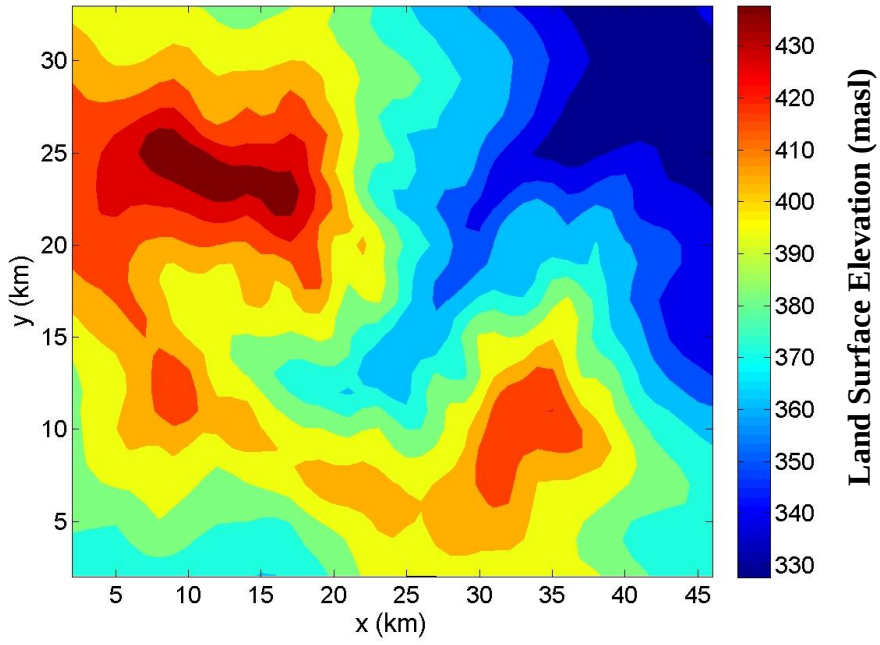


**Fig 4.3:** Land surface elevation in meters above sea level for the model domain.

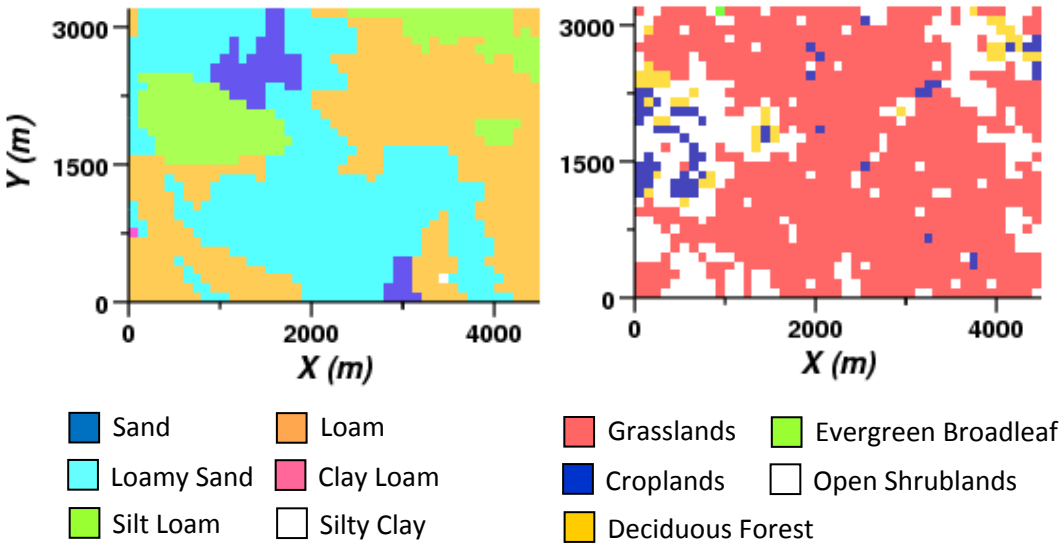


**Fig 4.4:** Plot of spatially distributed (a) soil type and (b) vegetation type for the simulated domain.

### 4.3.2 Atmospheric, surface and subsurface input data

Surface and subsurface model inputs, based on values used in Maxwell and Kollet (2008) and Maxwell et al 2007, included spatially distributed land cover and soil types, topography, and subsurface properties (saturated hydraulic conductivity, porosity, and vanGenuchten parameters). The subsurface model is designed with spatially distributed soil and vegetation types at the land surface, and uniform subsurface properties throughout the rest of the domain. Since the top two soil layers are numerically overlaid with the two soil layers in ARPS, soil and vegetation types were derived from the USGS categories used by ARPS (Figure 4.4). Subsurface parameter ranges in Schaap and Leij (1998) were used to match the ARPS categories to vanGenuchten parameters used in ParFlow. These parameters correspond to sandy loam which is the representative soil type for the watershed. The following effective properties are used for the deeper subsurface: saturated hydraulic conductivity = 5.6 x10-5 m/s, porosity = 0.4, vanGenuchten $\alpha$ = 3.5 $m^{-1}$, vanGenuchten n = 2, and relative residual water saturation = 0.2. Land surface slopes are calculated from the digital elevation model (figure 4.3) and input into ParFlow. A uniform Manning's coefficient, chosen as a mid-range literature value, is applied at the land surface.

### 4.3.3 Simulation cases

The Little Washita watershed is simulated here with three different model configurations to study the sensitivity of PBL to soil moisture heterogeneity at the land surface and water table depth, and to dynamic land-atmosphere feedbacks. In these cases, the relative effects of weather fronts to land surface forcing are studied by using real-time NARR synoptic forcing data to

initialize the model and as time-variant boundary conditions during the 4-day simulation period. The three simulations cases are described below:

1. In the first simulation case, the Little Washita is modeled using the uncoupled atmospheric model ARPS. This model is initialized with a soil moisture field interpolated from NARR (default configuration).

2. The second simulation case is also performed using uncoupled model ARPS. Offline spin-ups, however, using the coupled land surface-subsurface model PF.CLM are used here to provide soil moisture fields for initializing the land surface.

3. The third simulation case is performed using the coupled code PF.ARPS, allowing continuous feedbacks between the subsurface and the atmosphere. The model is initialized with soil moisture and subsurface pressure fields resulting from the PF.CLM offline spinup of the watershed (i.e. same soil moisture initialization as in case 2 above).

A schematic clarifying the three cases and initialization fields used for each case is shown in Figure 4.5. The offline spinup mentioned in 2 and 3 above is performed using the coupled surface-subsurface model, PF.CLM, as explained in the next section. The three cases are hereafter named arpsnarr, arps, pfarps. The arps case is designed to show effects of using a more realistic soil moisture initialization for a non-coupled atmospheric model when a fully coupled simulation is not computationally feasible. Comparison of cases arps and pfarps will highlight the effect of dynamic land-atmosphere feedbacks, given the same initial conditions.

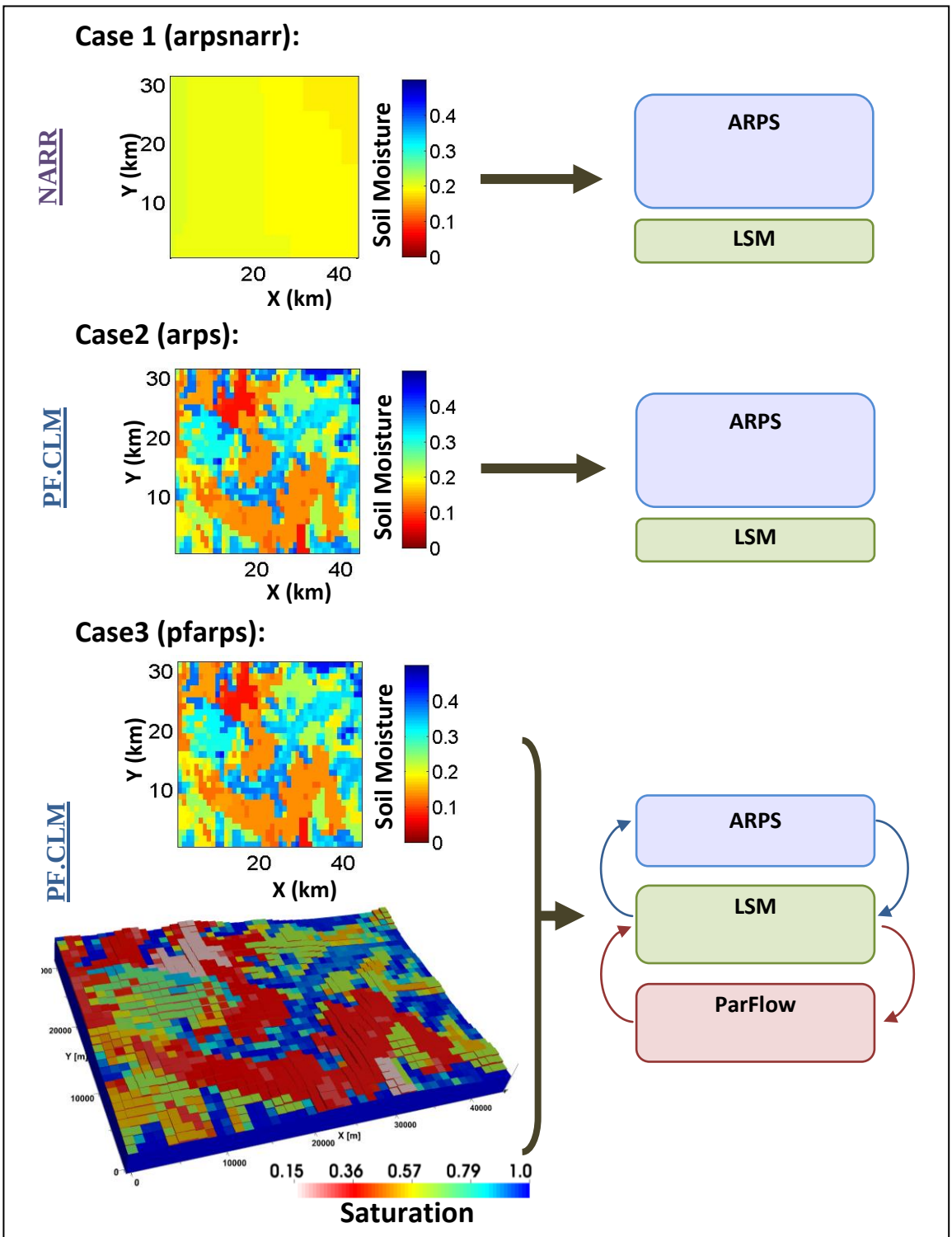


**Figure 4.5:** Schematic showing soil moisture initialization fields and model used for each of the three Little Washita simulation cases. The initialization subsurface saturation field for case 3 is also shown.

### 4.3.4 Soil moisture initialization (Offline spin-ups)

PF.CLM is used here to obtain realistic soil moisture and pressure fields to initialize the pfarps and arps cases presented in the previous section. This was done by Ian Ferguson (Colorado School of Mines) who initialized the model with WY1999 conditions and used NLDAS (North American Land Data Assimilation System) spatially distributed forcing for the 1998-1999 water year to spinup the model. The forcing dataset includes surface air temperature, incoming radiation, precipitation, pressure, humidity, wind speed and direction. The model was run repeatedly until the water and energy balances converge and the system reaches dynamic equilibrium. The spinup was then extended from 1999 to the year 2003 by performing a transient run while forced with continuous NLDAS atmospheric conditions. Land surface input parameters for the PF.CLM model included topography, spatially distributed land cover and soil types, while the subsurface component consisted of a homogeneous geologic formation. This is the setup used herein for the ARPS and PF.ARPS simulations.

It should be noted that the simulations presented here did not undergo a calibration process. The offline spinup is preformed to allow for hydrologic time and allow the model to develop its natural hydrologic state given a set of atmospheric conditions. This replaces the need to calibrate by allowing the model to behave in a more physical manner and distribute the water table over time (Maxwell et al, 2007; Maxwell and Kollet, 2008). Figure 4.6 shows the soil moisture distribution for the top two soil layers resulting from the PF.CLM offline spinup. This distribution results from having real terrain and variable soil type and vegetation at the land surface. The soil moisture fields in Figure 4.6 are extracted at 7pm on June 24$^{th}$, 2003, which is when the three simulation cases are started. The spinup process also produces saturation and pressure fields for the subsurface. These can be used to extract water table depth contours for the domain as seen in Figure 4.7a which indicates the spinup yields shallow water table depths at and around the valleys and deeper water table at higher elevations. Figure 4.7b shows the saturation field for a y-cross section into the domain. The water table is apparent here as the top boundary of the fully saturated (blue) region.

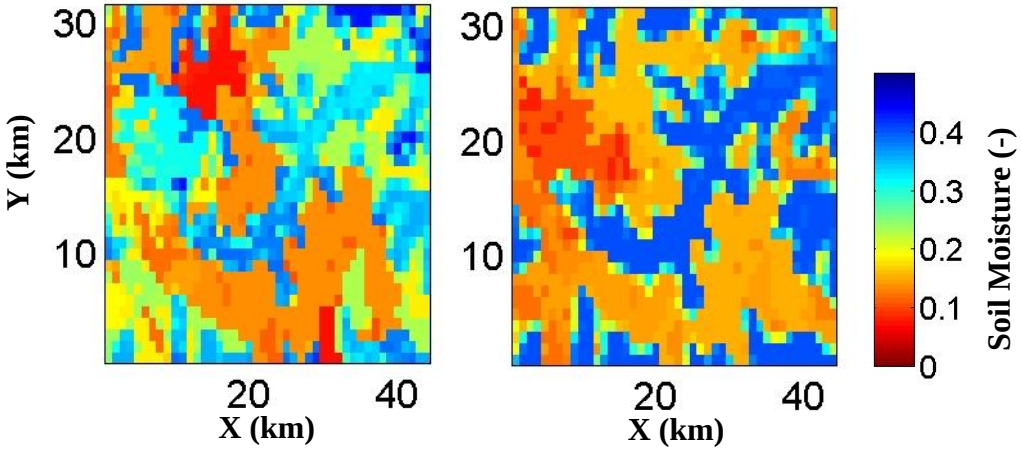


**Figure 4.6**: Soil moisture distribution at 7pm (CST) on June 24$^{th}$, 2003, for top two soil layers resulting from the PF.CLM offline spinup.

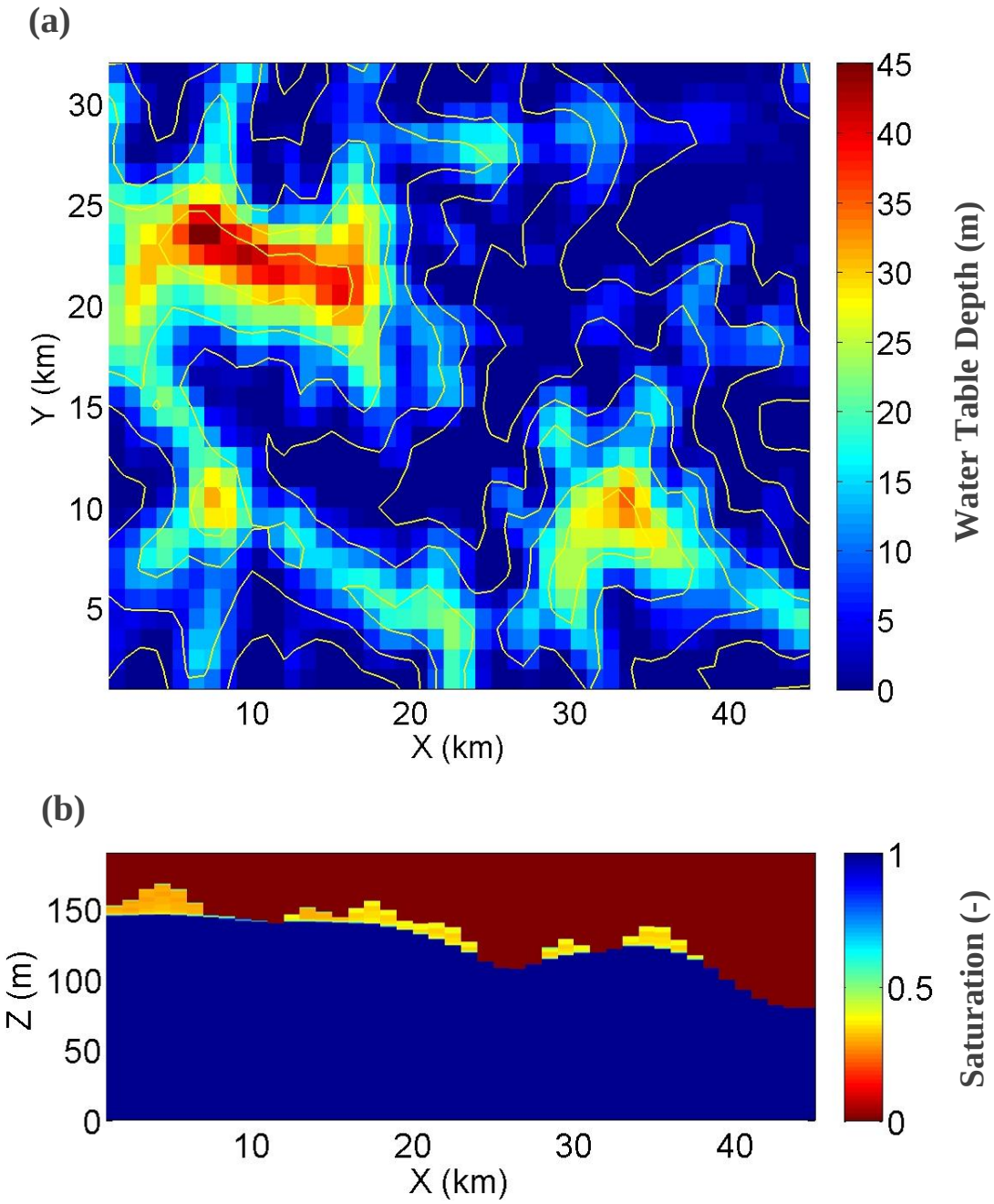


**Figure 4.7**: Results from the PF.CLM offline spinup: (a) water table depth distribution with terrain contours overlayed (b) saturation field at y=15km.

## 4.4 Simulation Results

The simulations are run for four days during the month of June; from 7pm on June 24th to 7pm on June 28th 2003. This period of time is chosen because it includes a single storm event preceded and followed by a few days with no rain. The goal is to observe wetting and drying behavior within the watershed and how this behavior might affect the coupling between PBL depth and water table depth. In the following sections, simulation results from the three cases explained in section 4.3.3 are compared to observation data in the watershed. Cross comparisons between the cases are presented to demonstrate differences in model outcome based on soil moisture initialization and the inclusion of a dynamic subsurface. Furthermore, correlations between water table depth and boundary layer depth are extracted from the PFARPS simulation (case 3) for different times of the simulation period.

### 4.4.1 Comparisons to observation data

Many field measurement campaigns have been conducted at the Little Washita watershed which focused on measurements of streamflow, shallow soil moisture, soil temperature, and variables of the atmospheric boundary layer. As a result, this watershed has a number of unique data sets ideal for validating a coupled study as presented here. It should be noted that although USGS groundwater wells are available within the watershed, these measurements are not frequent enough to validate the simulations presented here at an hourly timescale during June, 2003 (only one groundwater measurement was obtained during that year).

In this section, results from the three simulation cases are validated against observations of land surface temperature, soil moisture, near-surface ambient temperature, rainfall, wind velocity, and directions through sounding profiles and time series during the four days of simulation. Observation data sets are obtained from the Norman sounding station near the LW, the Agricultural Research Service's (ARS) micronet data, and the Soil Moisture Experiment 2003 (Jackson et al, 2007).

**Sounding Profiles:**

Potential temperature, wind speed and direction sounding profiles are compared to profiles measured from nearby soundings in Norman, OK. The observation data is available every 12 hours during the four days of simulation. These are shown in Figures 4.8 and 4.9 for June 25th and the morning of June 27th while the full series of sounding profiles is shown in Appendix C (Figures C1 through C6). The profiles demonstrate good agreement between the three cases and observed data. It should be noted that Norman is the nearest sounding station to the LW watershed, and since no sounding data was available within the model domain, the data is compared against soundings extracted at x=15km and y=15km. This representative point (about 72 km (45 miles) away from Norman) is chosen since it is within the middle region of the domain (i.e. far enough from the boundaries), yet not at an extreme location such as a peak or valley location.

Potential temperature soundings show a well-mixed PBL with greater depth during evenings (at 7pm) than morning hours, which show the remainder of the nocturnal, stable and shallow boundary layer (Figure 4.8). Although the observed sounding is measured outside the model domain, the simulation profiles follow observations quite well. Note that all three simulation cases show similar potential temperature throughout the 4 days (full series of potential temperature soundings are shown in Appendix C; Figures C1 and C2). The only apparent differences appear close to the land surface and are observed most clearly at 24 hours simulation time on the evening of June 25$^{th}$ which is when the storm event takes place and on the morning of June 27$^{th}$ (Figure 4.8). Looking at the wind profiles (Figure 4.9), we see the three cases produce similar results during evening times. As with the potential temperature profiles, however, differences are seen on the evening of June 25$^{th}$ just before the storm event (full series of wind profiles are shown in Appendix C; Figures C3 through C6).

Although lateral boundary conditions have a dominant effect on the sounding profiles shown here (particularly on the wind profiles), the findings of Maxwell et al (2007) that early morning hours are most important in terms of coupled behavior and show strongest feedbacks between the atmosphere and land surface are still observed, particularly in the morning of June 27$^{th}$. These differences occur during the drying period following three storm events. These profiles indicate that rainfall and wetting/drying periods also have a direct influence (as well as the diurnal cycle) on effects of land surface forcing particularly with respect to synoptic forcing effects.

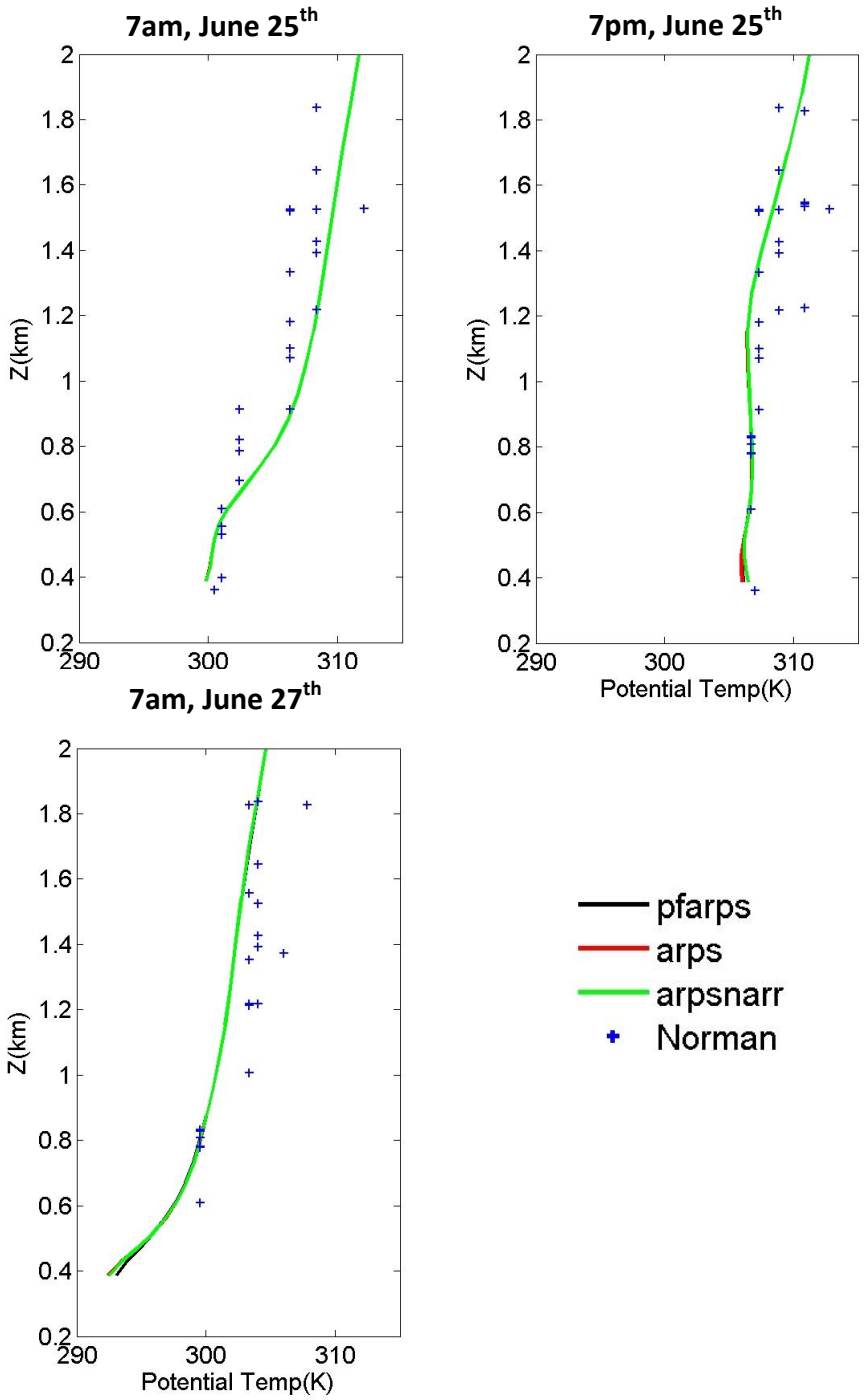


**Figure 4.8**: Potential Temperature sounding profiles on June 25th (7am and 7pm) and June 27th (7am), extracted at x=15km and y=15km. Observed soundings at the Norman station near the watershed are also shown.

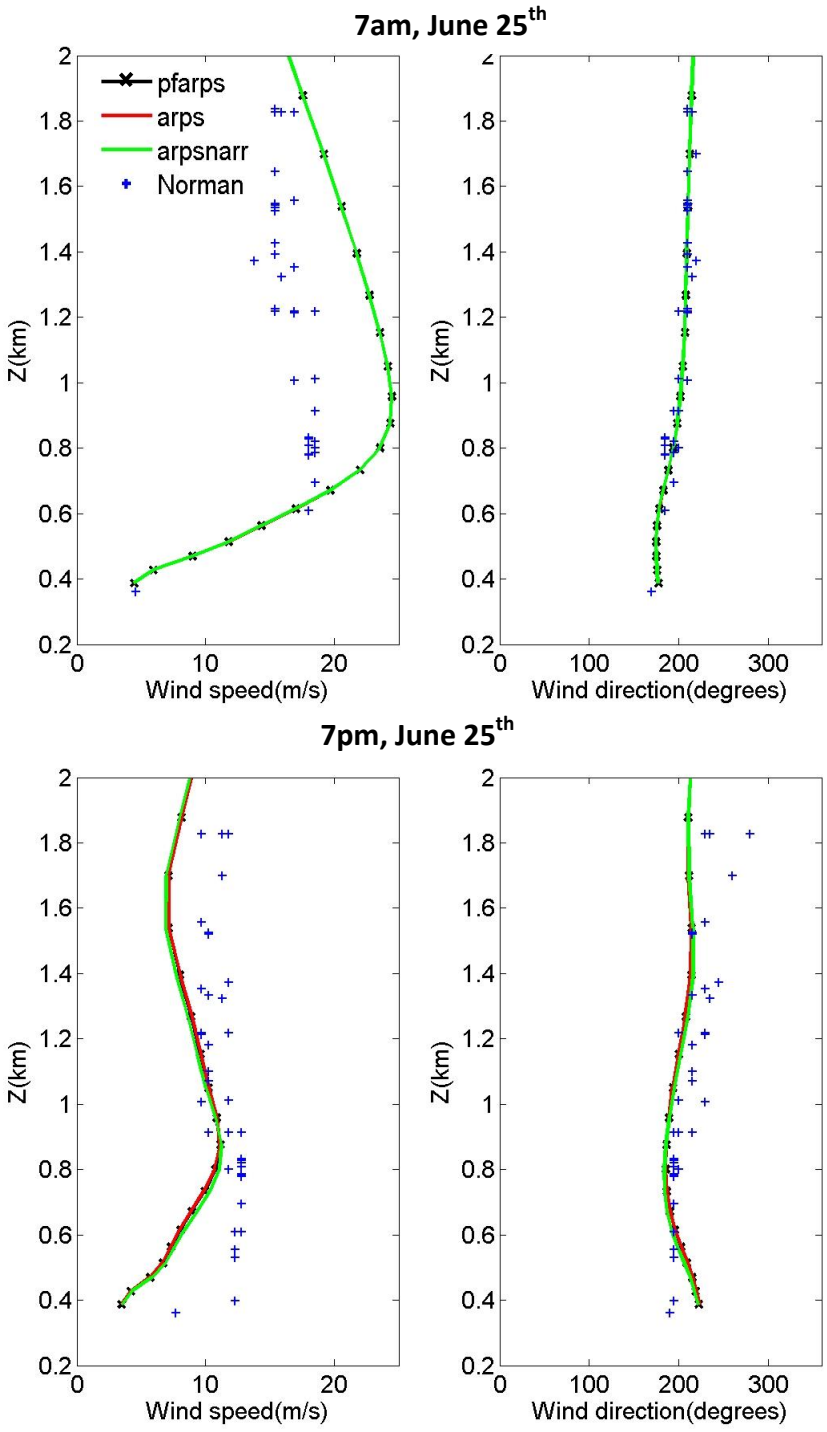


**Figure 4.9**: Wind speed and direction sounding profiles on June 25th (7am and 7pm) extracted at x=15km and y=15km. Observed soundings at the Norman station near the watershed are also shown.

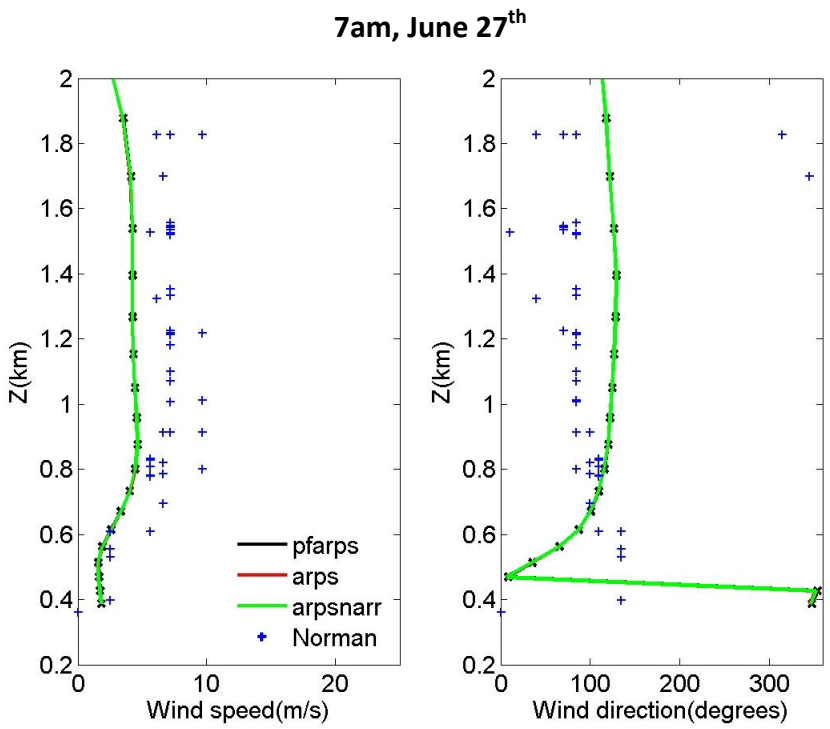


**Figure 4.9 Cont'd**: Wind speed and direction sounding profiles on June 27th (7am) extracted at x=15km and y=15km. Observed soundings at the Norman station near the watershed are also shown.

**Surface Data:**

The USDA Agricultural Research Service (ARS) monitors meteorological conditions in the Little Washita watershed through a 42 micronet station network (Figure 4.10). These stations provide hourly values of incoming solar radiation, ambient temperature, rainfall, and soil temperature. Although soil moisture measurements were not available for June, 2003, through the ARS dataset, these were obtained through the SMEX03 experiment (as shown in the following section) for validation against the simulation results.

The ARS data set is used here to compare time series of solar radiation, ambient temperature, rainfall, and soil temperature against simulated values in the three study cases. Figures 4.11 and 4.12 show these comparisons at two of the ARS micronet stations. A quick look at these figures shows good general agreement with measured data. The NARR forcing however does not produce rainfall events accurately as there is a few hours' shift in predicting the storm event (starting around 24 hours of simulation time) within the models. There is also a lag in ambient temperature trends which becomes less during dry times (i.e. before the storm event and during

the drying phase afterwards). The same lag is observed in the solar radiation trend which indicates the NARR forcing does not provide the right cloud cover. The fit between observed and simulated solar radiation timeseries thus improves during drier times.

Quick comparisons of Figures 4.11 and 4.12 indicate the three simulation cases produce almost identical results; however a closer look shows some consistent differences. For instance, arpsnarr tends to overestimate ambient temperature during the daytime (starting with morning hours) at station A135 (Figure 4.11) located around the Little Washita valley. Cases pfarps and arps produce similar results at this station because they have similar soil moisture initializations while arpsnarr has drier soil in this region. The effect of soil moisture initialization however doesn't matter as much at higher elevation stations such as A148 (Figure 4.12) which demonstrates similar results between all three cases even during daytime hours.

Although the simulation differences shown here are not very large (this will be discussed in the next two sections), their consistency between station locations nonetheless indicates a spatial and temporal trend in the dependence of heat fluxes on conditions at the surface and in the subsurface. Station locations with deep water table demonstrate smaller differences between the three simulation cases since these locations tend to have a drier land surface which is decoupled from the subsurface. On the other hand, differences between the model cases are greater at and around valley locations with shallow water table depth because the arpsnarr case has drier soil moisture at these locations than pfarps and arps cases. . This means that initializing with a realistic soil moisture field (such as in the pfarps or arps simulation cases) has a greater impact within regions of shallower water table. Furthermore, applying a coupled model (such as PFARPS) appears to have an impact within small transitional (partly-saturated) areas next to the river valley. In general, these differences, which appear in the morning and increase towards the afternoon, are emphasized during drying periods but smoothed out during wet periods (e.g. ambient temperature profiles in Figures 4.11 and 4.12).

This agrees with the findings of the previous two chapters and is observed when looking at soil temperature time series. Most of the ARS stations show differences in soil temperatures between pfarps and arpsnarr. These mostly occur at and around the valley and some of the stations in transition zones between high and low elevations. Figure 4.13 shows soil temperature time series at the same two stations chosen in the previous plots. We first notice that the deep simulated soil moisture (for the second soil layer) follows observed trends while the shallow simulated soil moisture shows greater fluctuations than observed. Observed soil temperatures are measured at depths of 5, 10, 15, and 30cm. Most of these are shallower than the cell center of the top soil layer (0.25m deep). These fluctuations in top soil temperature are observed here because the top soil layer in the model is affected by atmospheric temperature more than the deep layer. Since it takes longer for heat fluctuations from the land surface to diffuse down to the deep layer, we see a damped and delayed signature here which better matches observed values. Nonetheless, the shallow soil moisture profiles show differences between simulated cases more clearly. Both stations A135 and A148 show that arpsnarr tends to exaggerate the land surface temperature more than pfarps which is consistent with drier soil moisture for the arpsnarr case. On the other hand, soil temperatures in the arps case (initialized with PF.CLM soil moisture) appear to be most sensitive to location within the watershed. At the valley station of A135, arps results are most similar to pfarps results, while at station A148, which is located at a higher elevation, arps

results slowly shift from the pfarps trend to match the arpsnarr case by the third and fourth simulation days. This is attributed to the fact that although the arps case is initialized with a realistic soil moisture field, it cannot sustain the soil moisture without a coupled subsurface component and this shows most clearly at higher elevations with deeper water table.

Another trend observed in Figure 4.13 is the effect of the rain event at the start of the second day. This suppresses most differences between the models and shows a relatively more uniform trend at the land surface. Another thing to notice is that the model differences are maintained during the night. Because pfarps has a dynamic subsurface component, it can maintain soil moisture within the valley and surrounding locations and thus maintain a higher soil temperature during the night. This means that the nocturnal difference between the three cases is expected to increase with elevation to a certain extent. For example, greater nighttime differences are observed at station A148 compared to station A135 (Figure 4.13).

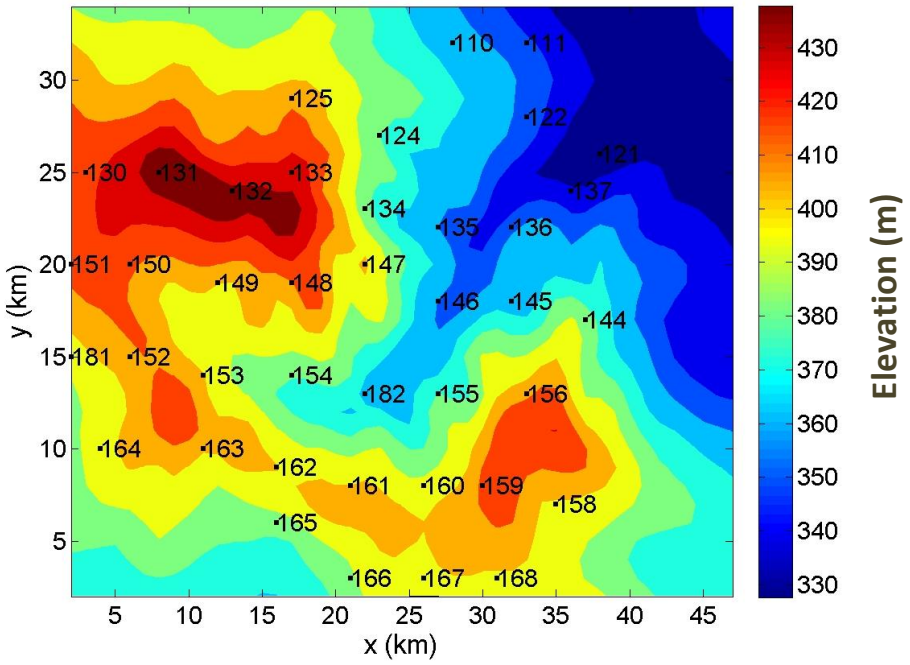


**Figure 4.10**: ARS micronet station locations within model domain. Color bar and contours show land surface elevation (m). Each station ID is indicated next to its location.

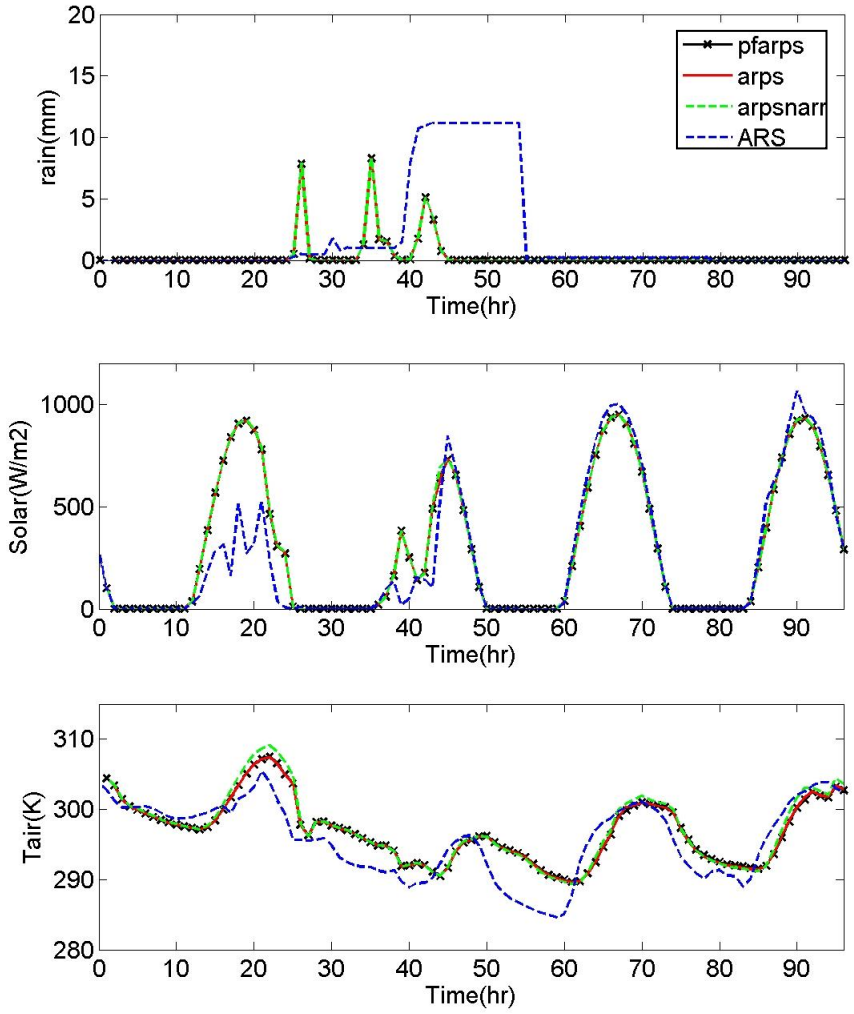


**Figure 4.11**: Time series of precipitation, solar radiation, and air air temperature at the land surface at ARS micronet station A135 for the three simulation cases and ARS observations.

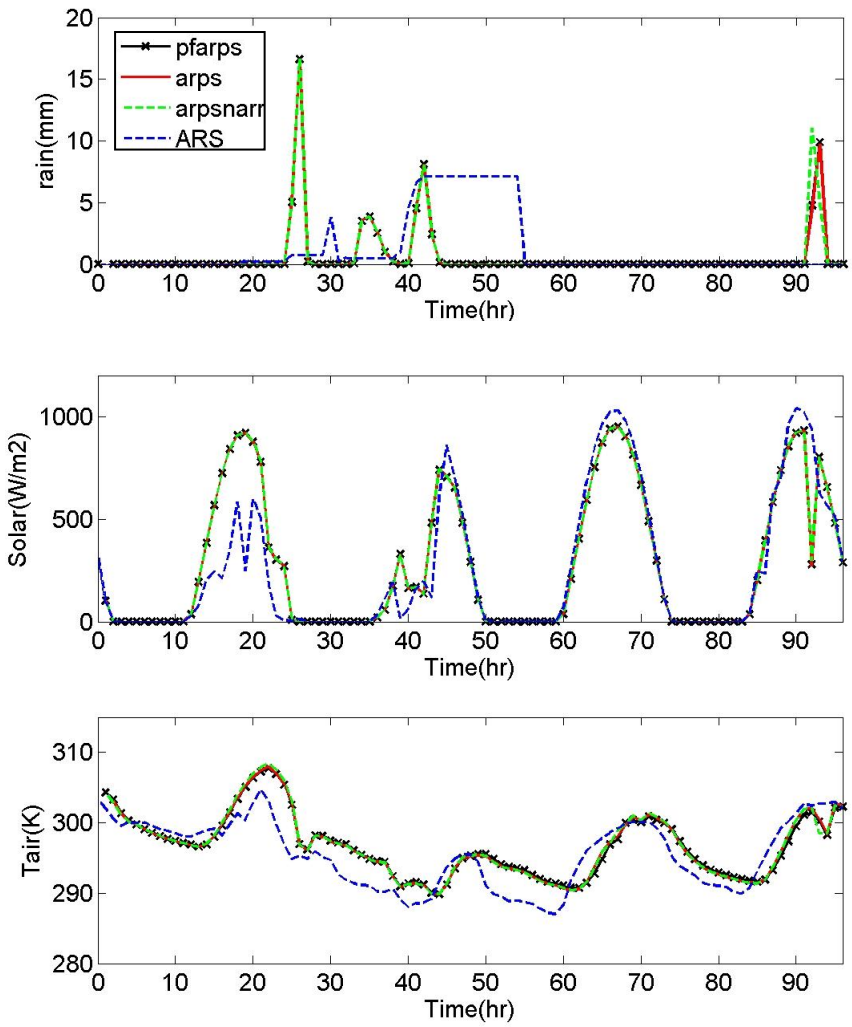


**Figure 4.12**: Time series of precipitation, solar radiation, and air temperature at the land surface at ARS micronet station A148 for the three simulation cases and ARS observations.

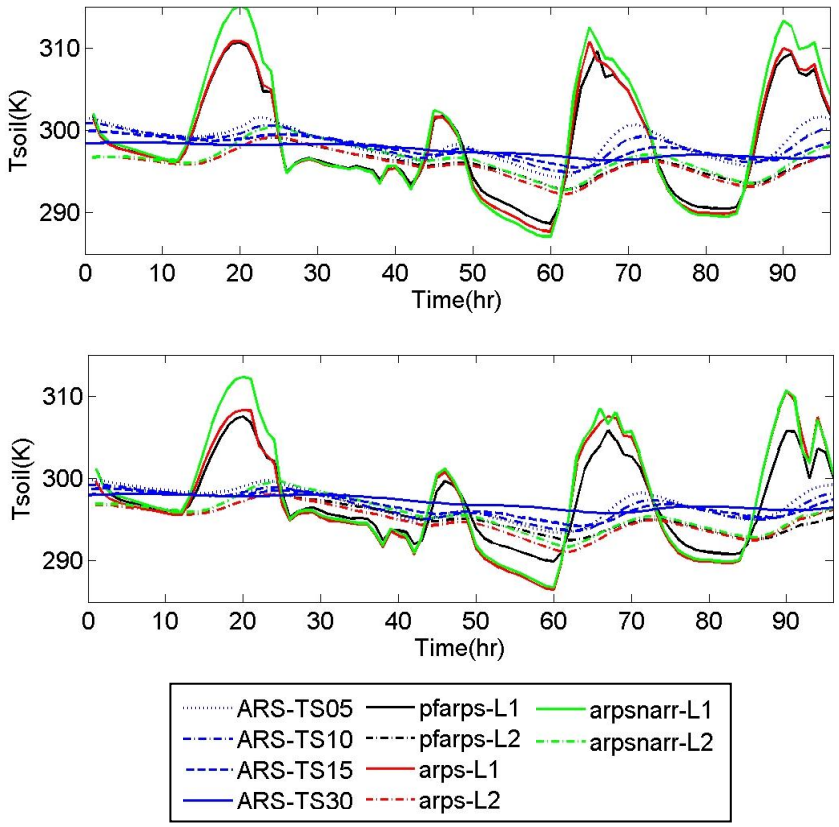


**Figure 4.13**: Time series of observed and simulated (top two soil layers) soil temperature (Tsoil) at ARS micronet stations: (a) A135 and (b) 148. L1: top soil layer; L2: Second soil layer; ARS-TS05, 10, 15, and 30: ARS observed soil temperature at 5, 10, 15, and 30 cm deep, respectively.

**Soil Moisture**:

The National Snow and Ice Data Center (NSIDC) conducted the Soil Moisture Experiment 2003 (SMEX03) in Oklahoma between June 23rd and July 18th, 2003 (Jackson et al, 2007). In situ field measurements were conducted within the Little Washita watershed. These included soil moisture measurements at 10 of the micronet stations shown in Figure 4.10. Figure 4.14 shows the measured timeseries against simulated values for the top soil layer at four micronet stations with varying locations; a valley station (A146), a station at a transitional location close to the valley (A144), and two transitional stations at higher-elevations (A133 and A149). It should be noted here that the observed soil moisture measurements are taken at 5 cm depth, while the top soil layer for simulated soil moisture values has a 0.5m thickness and thus has its cell center at 0.25 below the land surface. Furthermore, differences between simulated and observed rainfall will bias the timing of soil moisture changes as shown here. Another factor to take into account when comparing simulated soil moisture values to observations is the large difference in lateral scale between measurements and the 1 km model grid size used here. Local heterogeneities and subsurface properties are likely to dominate observed soil moisture values, particularly local porosity (Kollet and Maxwell, 2008). Effective porosity and subsurface properties used over the 1 km model grid will change the magnitude of soil moisture significantly when compared to local measurements.

Even though simulated values might not exactly match observed values, the trends are still an important indication of wetting/drying behavior within the models. All three simulated cases appear to exaggerate soil moisture values in the valley (Figure 4.14c) and the low-transition station (Figure 4.14b). Saying that, however, pfarps has a similar wetting/drying behavior as the observed timeseries at the low transition station A144 (Figure 4.14b), while arps and arpsnarr soil moistures tend to drop more rapidly with time since they do not have a dynamic subsurface component and thus cannot maintain soil moisture as well as pfarps during the drying periods. Pfarps compares better to observed soil moisture trends and values at the high-transition stations, particularly at A133 (Figure 4.14a) while arps and arpsnarr overestimate the shallow soil moisture at this station.

In summary, the simulation cases capture the general patterns of the observed data. Effects of coupling the subsurface to the atmosphere and initializing with a realistic soil moisture field become clearer when comparing against land surface measurements such as near surface winds and ambient temperature, soil moisture and soil temperature. However, the models give similar results within the atmosphere except for small differences very near the surface. In the following sections, the three simulation cases as well as differences at the land surface and within the atmosphere are presented more thoroughly and reasons behind these similarities are discussed.

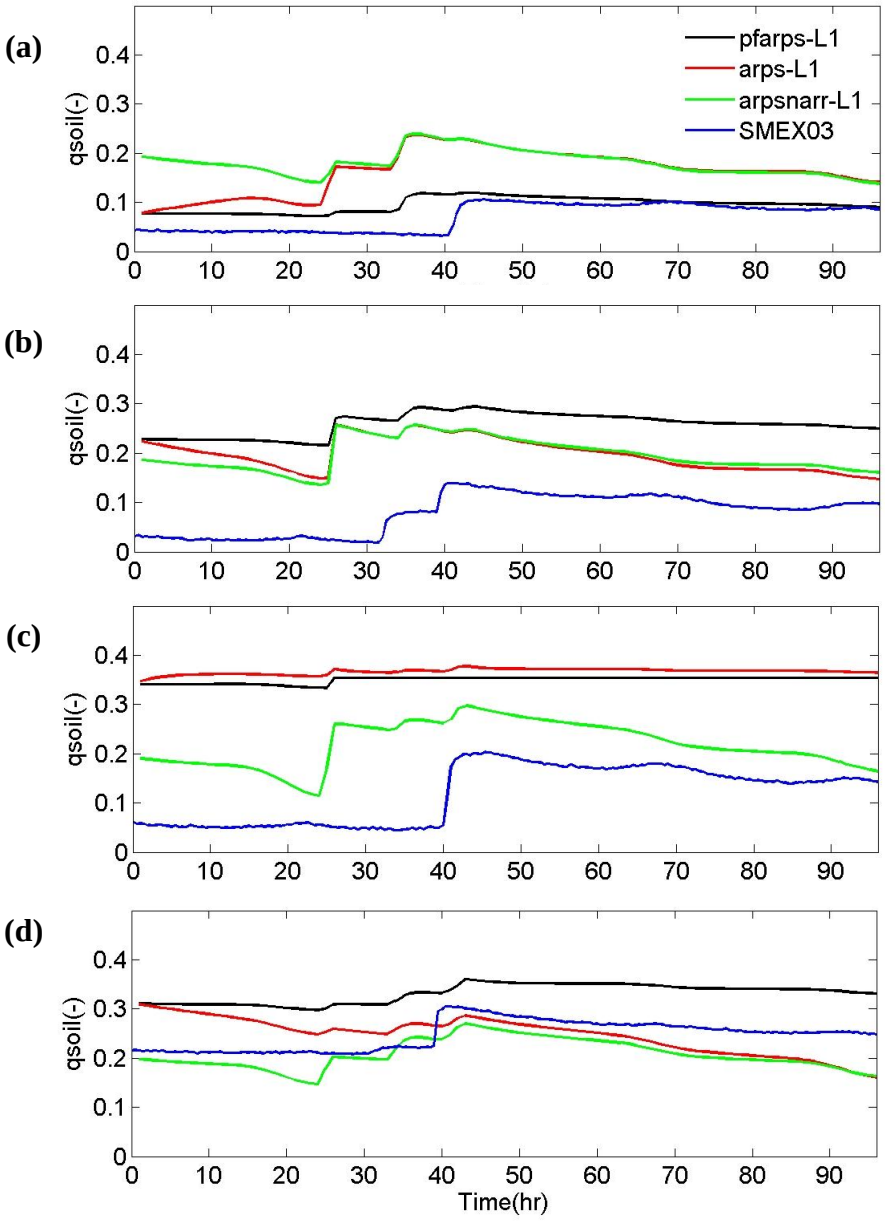


**Figure 4.14**: Time series of soil moisture for the top soil layer of the three simulations and observed soil moisture (at 5cm depth) from the SMEX03 micronet stations: (a) A133, (b) A144, (c) A146, (d) A149.

### 4.4.2 Rainfall Events

Four rainfall events are produced within the four simulation days for all three cases. The first rainfall event is discussed here (Figure 4.15) while the rest of the storms are included in Appendix C (Figures C7 through C9). The first three events are observed at the ARS micronet stations presented in the previous section (Figures 4.11 and 4.12), often as a more continuous rainfall event. These events are different than the fourth storm which is more localized and concentrated around the middle of the watershed (Figure C9).

The first simulation rainfall event starts at 7pm on the second day (June 25$^{th}$) and is shown in Figure 4.15 as a storm front coming from the south-west direction into the watershed. Cloud cover at the land surface is also shown as total cloud water mixing ratio (qc) summed in the vertical direction. This weather front is seen more clearly when looking at contours of wind speed in the X and Z-directions. These are shown at 7, 8, and 9 pm as XZ sections at y=15km in Figure 4.16. The circulation trends shown in Figure 4.16 are of a different nature than the convective circulations presented in Chapter 3 for the sinusoidal hills. By the time this storm starts (8pm) any daytime convective circulations have mostly been mixed into the evening residual layer and thus the circulations occurring here are mostly caused by synoptic forcing from the boundaries.

The three simulation cases show very similar wind and rainfall trends which is why only pfarps results are shown in Figures 4.15 through 4.17. The reason behind the generally small differences observed so far in atmospheric conditions (rainfall, winds, ambient temperature) between the three simulation cases is the effect of real-time NARR forcing at the lateral boundaries (this is further discussed throughout the following sections). Nonetheless, there are some differences particularly in rainfall magnitude during the first storm (Figure 4.17) and the location of the localized storm on the fourth day (shown in Appendix C, Figures C10 and C11). Looking at Figure 4.17, the three plots show rainfall differences between the three simulated cases indicated on the plots as (pfarps-arps), (pfarps-arpsnarr), and (arps-arpsnarr). This figure shows the major differences here are between the coupled pfarps case and the two non-coupled cases; arps and arpsnarr. Differences in rainfall, however, increase with changing soil moisture patterns at the land surface and are an order of magnitude greater during the fourth storm (Figures C10 and C11). To emphasize the connection between atmospheric divergence among cases and soil moisture differences at the land surface, maximum differences in rainfall and soil moisture are plotted in figure 4.18. The timeseries show the maximum difference over the domain area between each of the two simulation cases. The figure demonstrates how rainfall resets land surface effects and thus reduces differences between cases. These differences increase again during drying periods and cause the divergence in rainfall behavior towards the end of the simulation period. Although the maximum differences shown in Figure 4.18 are small in magnitude, the integrated differences over the large domain area could amount to significant changes in water balance over the watershed.

Over time, subsurface physics in pfarps will maintain soil moisture at the land surface which arps alone cannot. This has an effect on divergence of atmospheric behavior between the models with time. The extent of this divergence depends on effects of lateral forcing with respect to land surface forcing. Since the cases presented here are simulated with real time forcing, land surface

effects generally play a smaller role as their effect is subdued by effects of lateral boundary forcing.

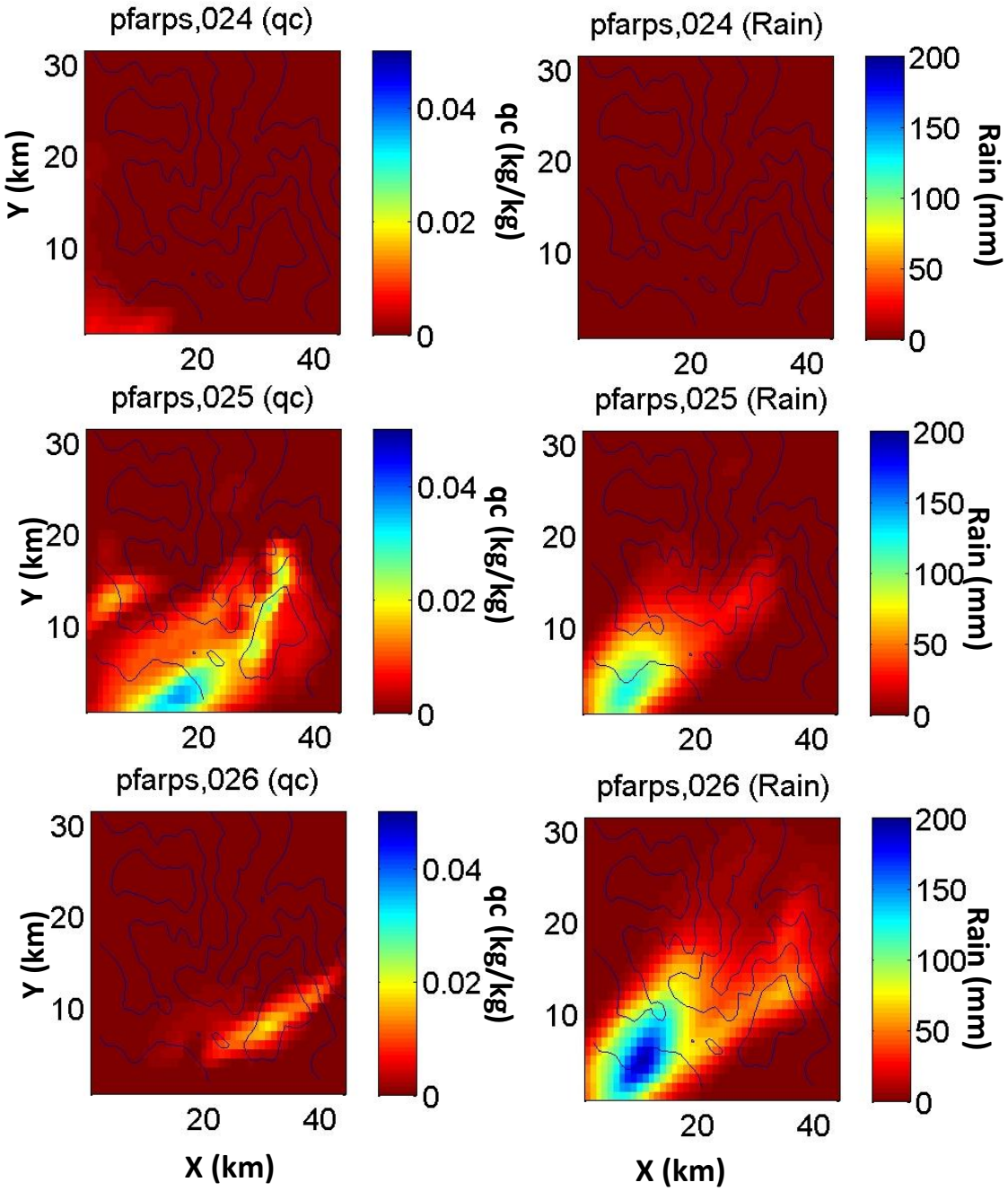


**Figure 4.15**: Cloud water mixing ratio (qc) and cumulative hourly rainfall for the pfarps simulation case at 7, 8 and 9pm on the June 25th (24, 25, and 26 hours of simulation). Contour lines show terrain.

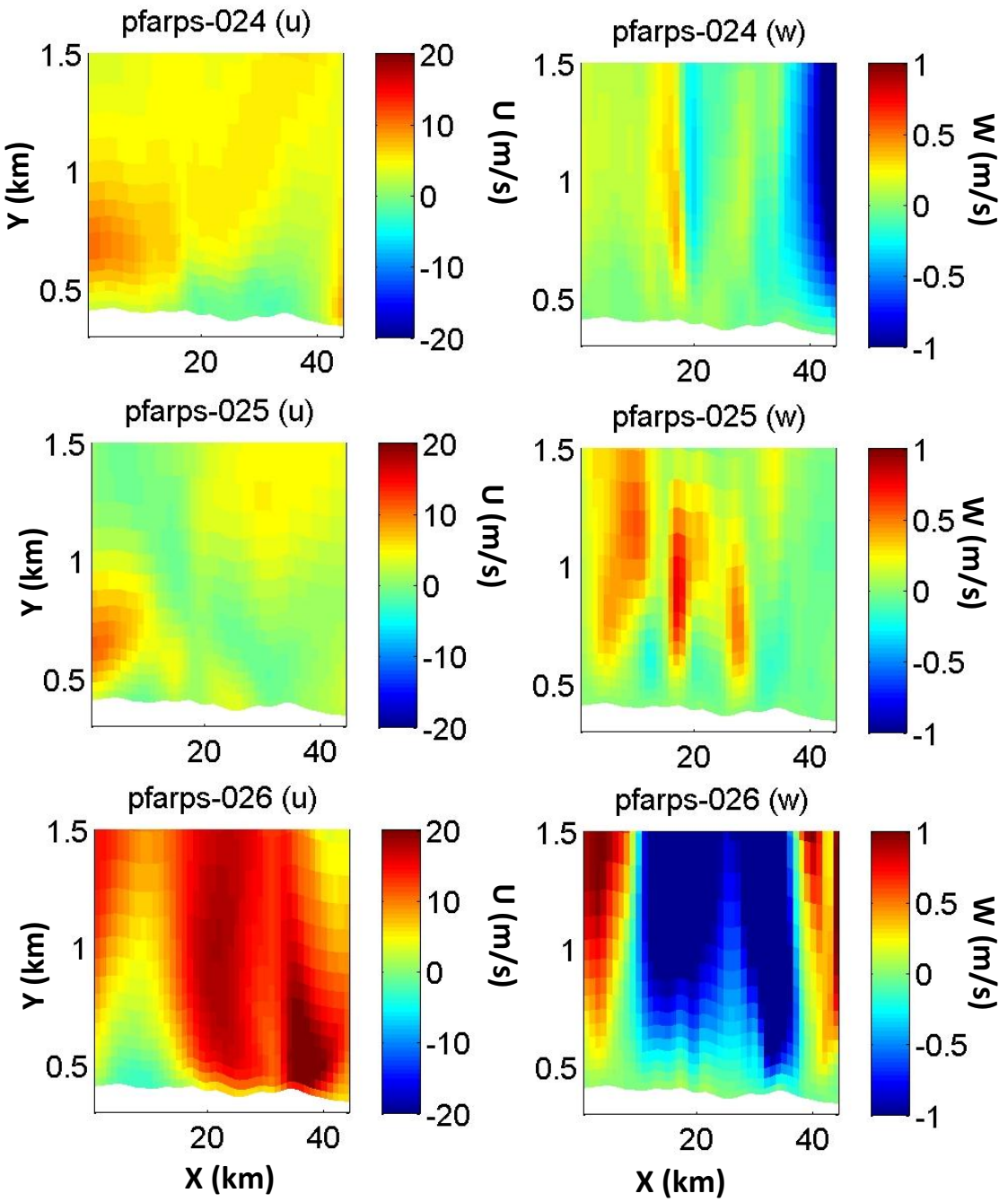


**Figure 4.16**: XZ sections of wind speed in the x and z-directions (U and W, respectively) at y=15km for the pfarps case at 7, 8 and 9pm on June 25$^{th}$ (24, 25, and 26 hours of simulation).

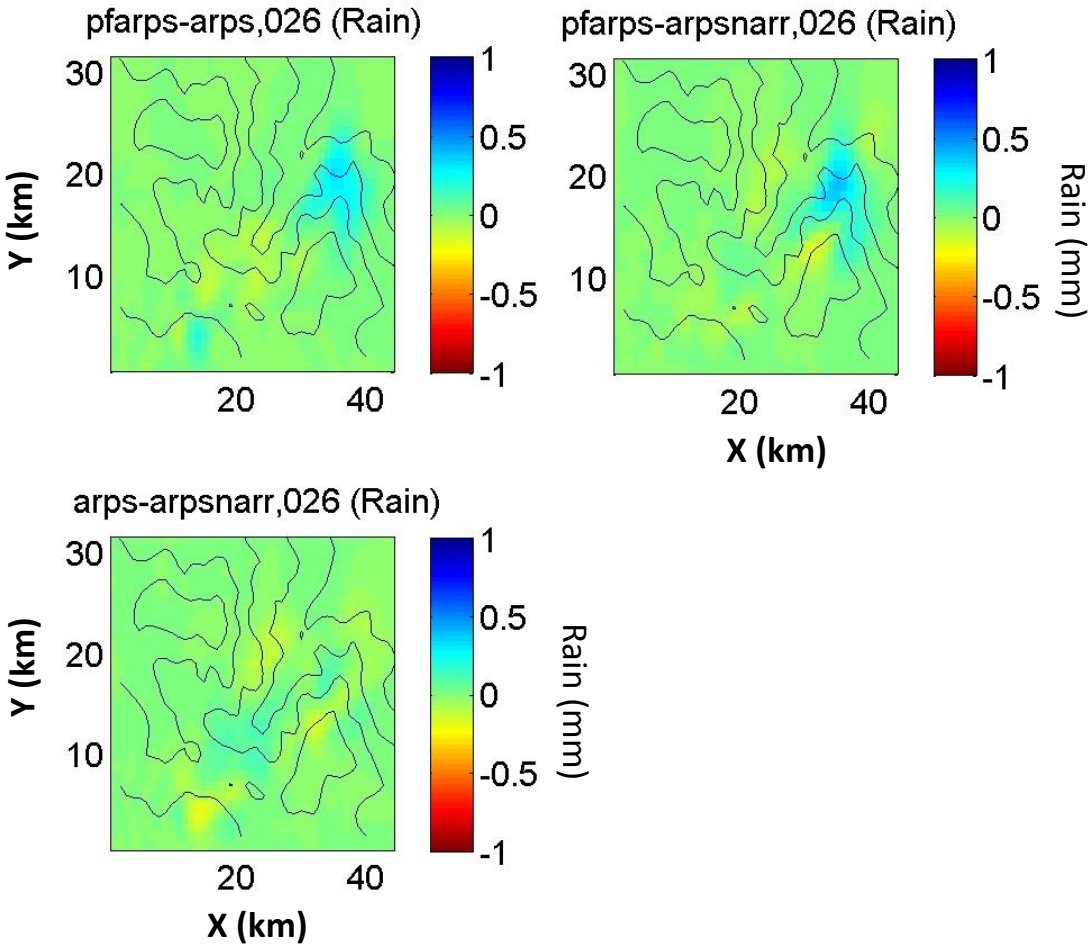


**Figure 4.17**: Differences in rainfall between the three simulation cases at 9pm on June 25th. Contour lines show terrain.

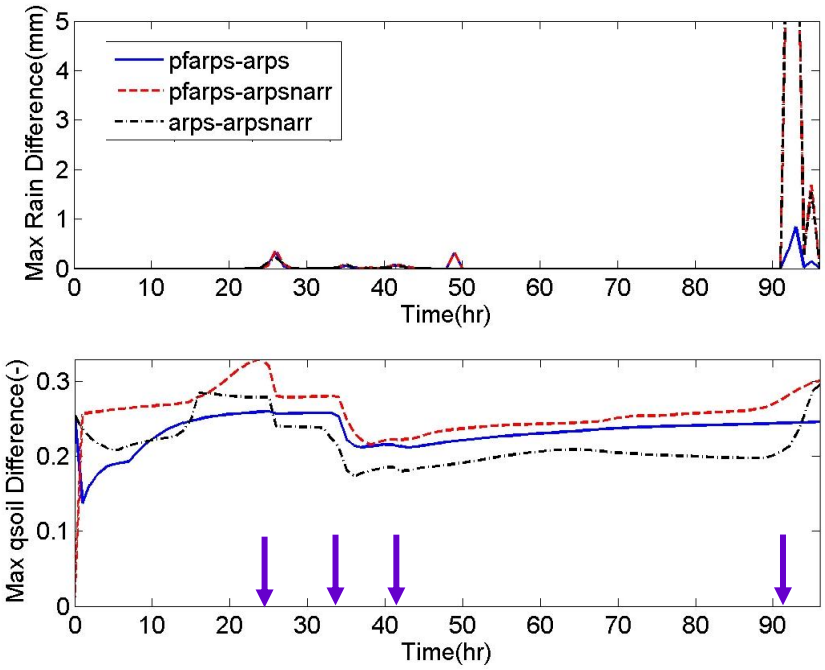


**Figure 4.18:** Rainfall and top soil moisture maximum differences between simulation cases over the domain area. Arrows indicate times at which rainfall events start.

### 4.4.3 Land surface comparisons

Despite the relatively small differences in atmospheric variables (e.g. rainfall) shown in previous sections, differences in land surface variables are greater. Looking at land surface energy fluxes for instance, the models show clear differences resulting from different soil moisture initializations. These differences are enhanced in the afternoon as the day progresses and the land surface warms up as shown in Figure 4.19 which shows snapshots at 4 pm (June 25$^{th}$) of latent heat flux and sensible heat flux contours for all three cases. Similar fluxes are observed for arps and pfarps cases as they are initialized with the same soil moisture fields obtained from offline spinups. Thus, both these cases show higher latent heat flux (and lower sensible heat flux) in the valley than the peaks. The arpsnarr case shows a more uniform flux distribution which follows the NARR soil moisture field used for initialization.

As there is not a lot of rain during these simulations, the soil moisture changes are very small, which is why the energy flux fields are quite similar between the pfarps and arps cases. There are however some differences between these two cases before, during and after the simulated storm (as shown in Figures 4.20 and 4.21). Figure 4.20a shows differences between the two cases at 4pm (June 25$^{th}$) and indicates more evaporation (locally up to a 600 W/m$^2$ difference in latent

heat flux) occurs in the valley for the pfarps case. This case takes lateral flow and water table fluctuations into account and can thus sustain more moisture as base flow in the valley. The arps case, on the other hand, does not distribute any water laterally and can only change soil moisture vertically through infiltration or evaporation.

Differences between the pfarps and arps cases are reduced once more (though still up to 400 $W/m^2$ difference in latent heat flux) as the land surface cools down in the evening (e.g. at 7pm prior to the storm, Figure 4.20b). As the land surface becomes wet during the storm, differences between cases are gradually smoothed out (e.g. at 9pm on June 25$^{th}$, Figure 4.20c). Note the changing colorbar scale in Figure 4.20. As the land surface remains cool during the night, rainfall effects are still there the next morning and differences in heat fluxes between cases are not as enhanced at 10am on the morning after the storm as they were at 10am on the previous day after dry period (Figure 4.21, with differences up to 100 $W/m^2$ in latent heat flux). Maximum differences in land surface energy fluxes between the three simulation cases are shown in Figure 4.22. In general the differences increase during dry periods, and are smoothed out by rainfall events which resets the soil moisture at the land surface. Smaller differences are observed between pfarps and arps cases because both these cases are initialized with similar soil moisture fields. Differences between these two cases however increase towards the end of the simulation as the coupled processes in pfarps will sustain soil moisture that arps alone cannot, thus causing the divergence in energy fluxes with time.

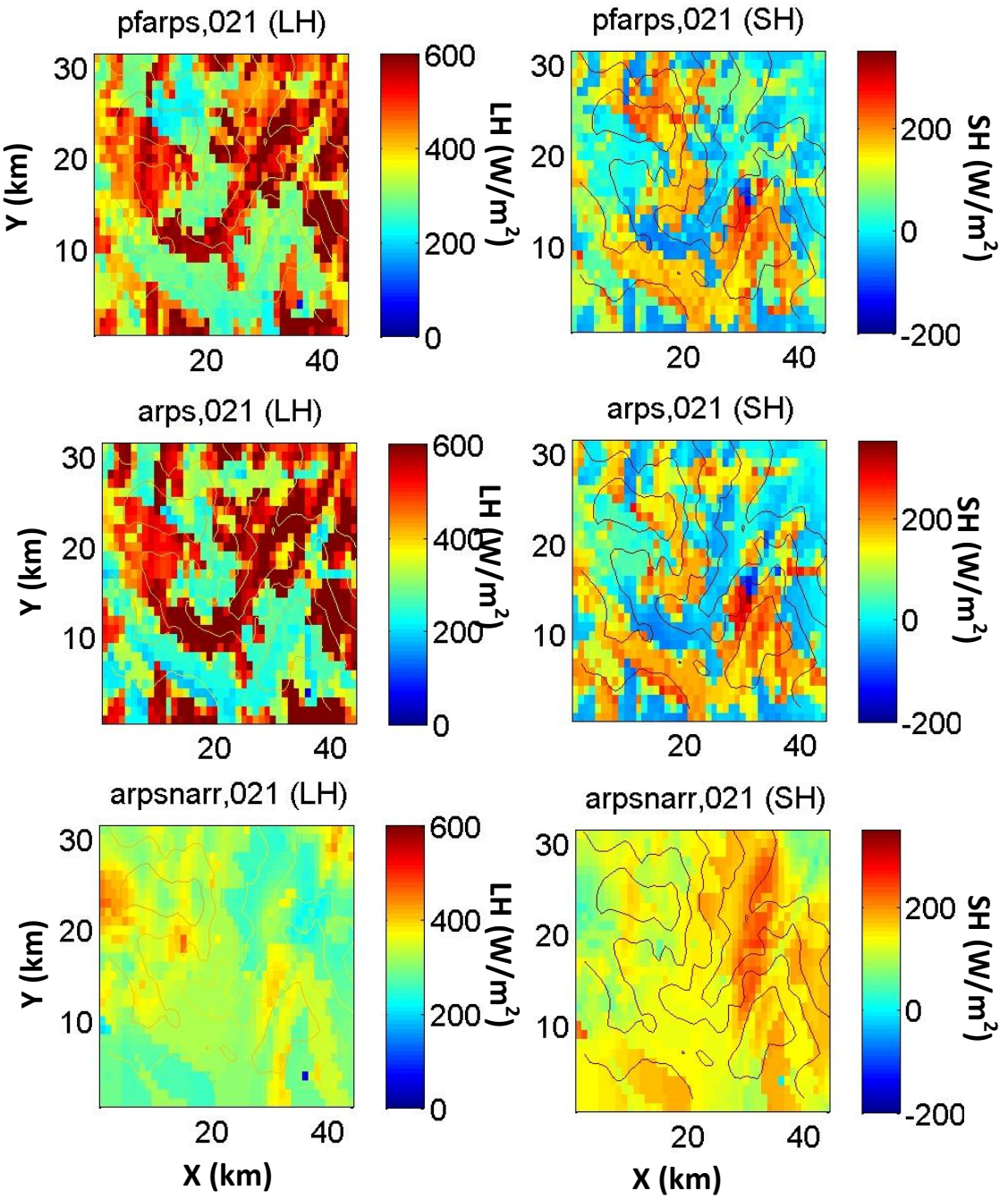


**Figure 4.19**: Latent heat (LH) and Sensible heat (SH) fluxes at the land surface for the three simulation cases at 4pm on June 25th. Contour lines show terrain.

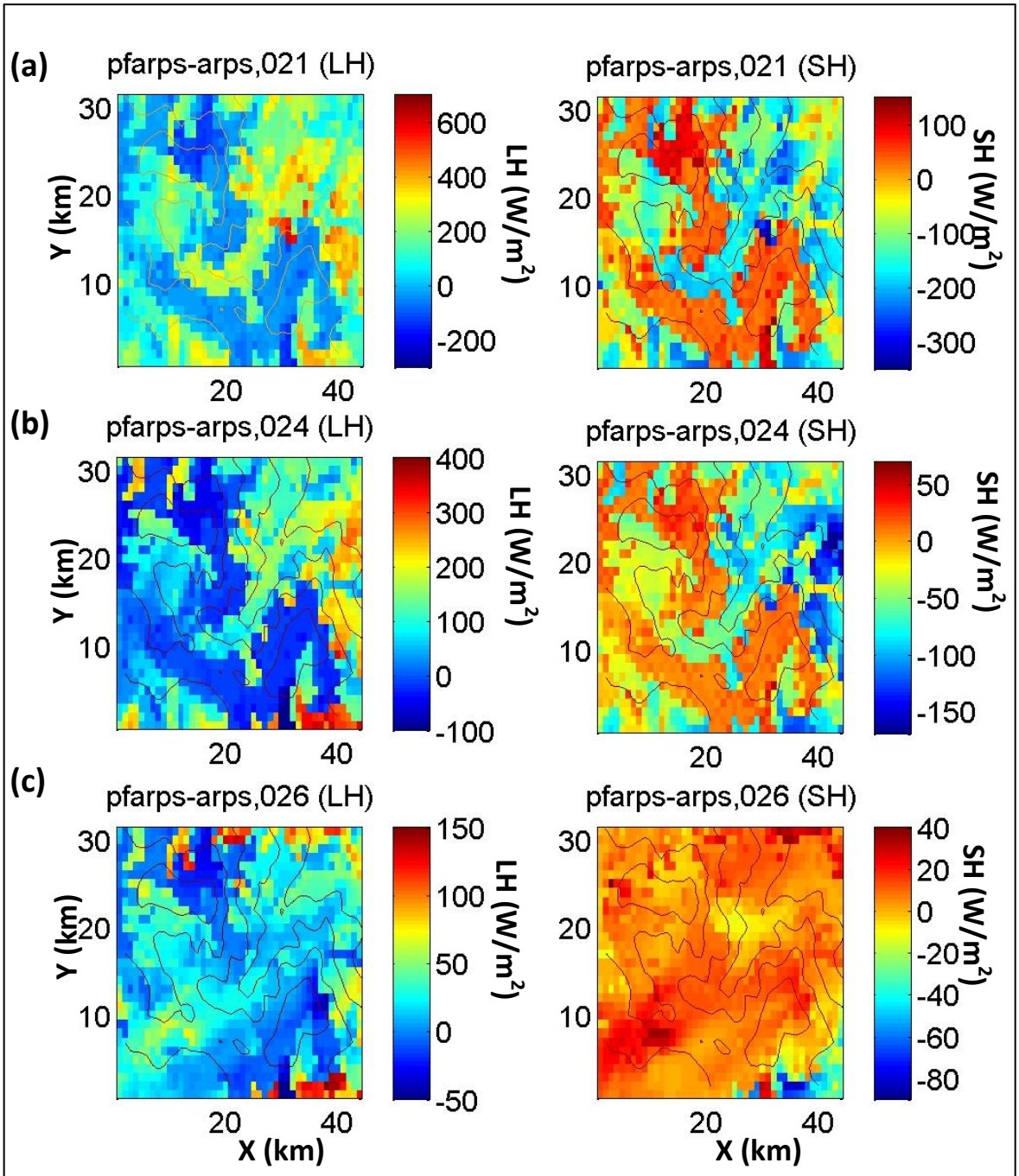


**Figure 4.20**: Differences in Latent heat (LH) and Sensible heat (SH) fluxes at the land surface between the pfarps and arps simulation cases at (a) 4pm, (b) 7pm, and (c) 9pm on June 25th. Contour lines show terrain. Note the different colorbar scales.

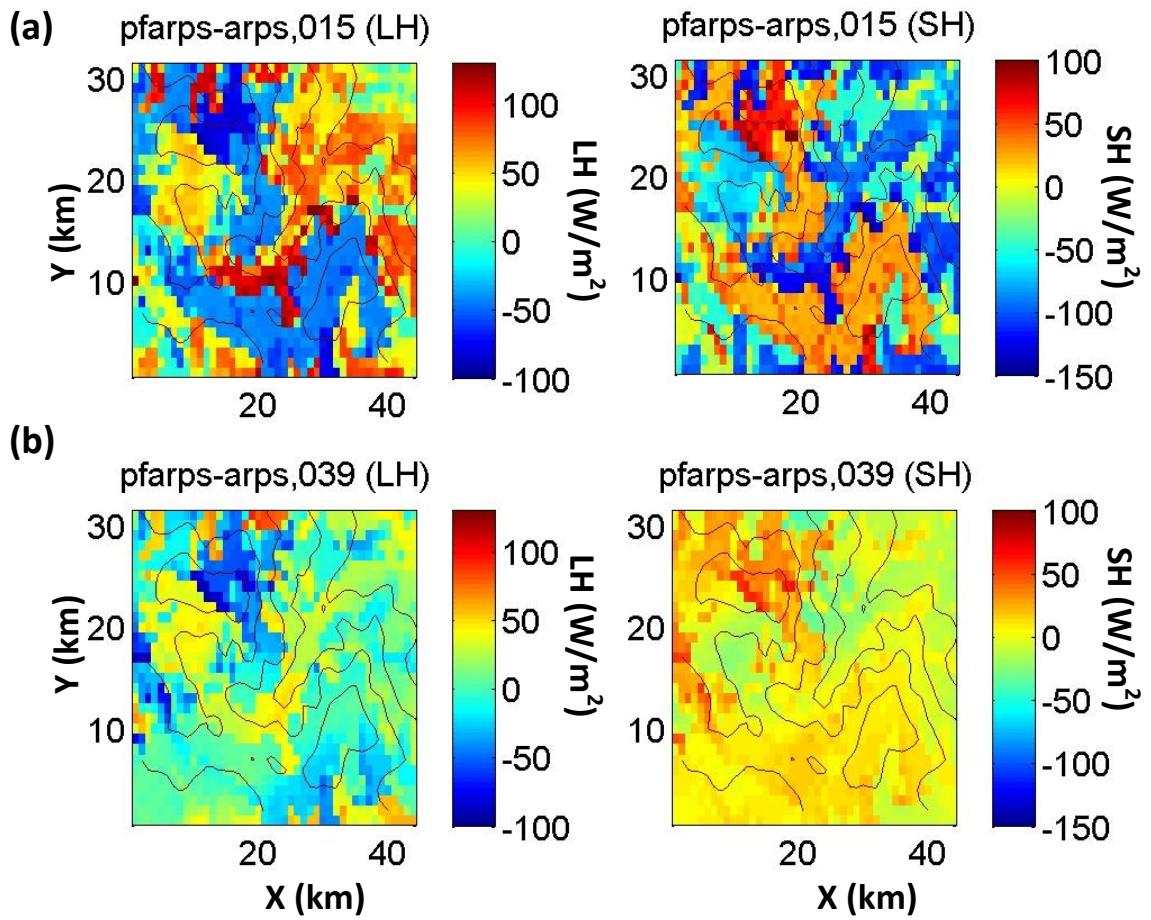


**Figure 4.21**: Differences in Latent heat (LH) and Sensible heat (SH) fluxes at the land surface between the pfarps and arps simulation cases at (a) 10 am on June 25th and (b) 10 am on June 26th. Contour lines show terrain.

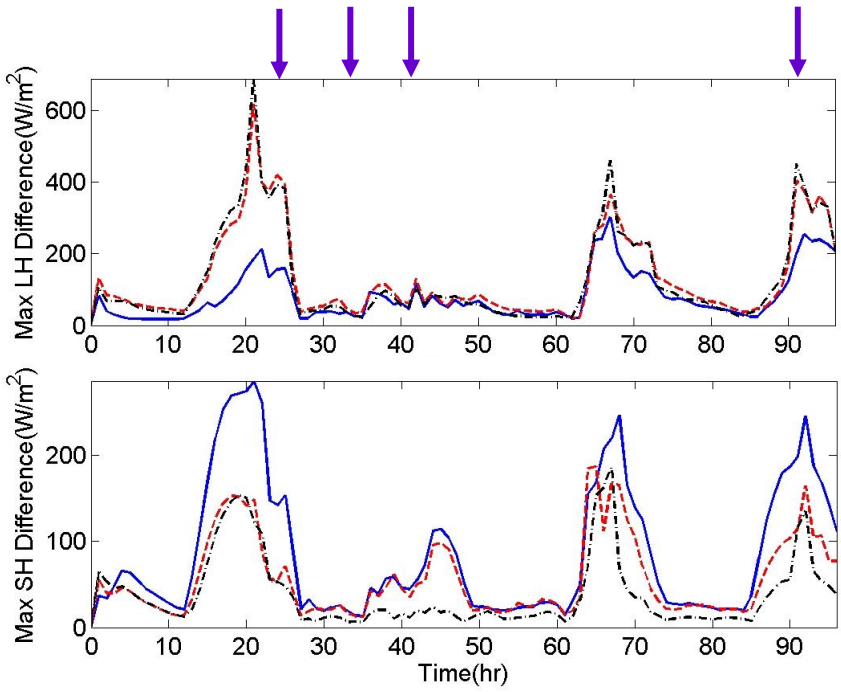


**Figure 4.22**: Latent heat (LH) and sensible heat (SH) flux maximum differences between simulation cases over the domain area. Arrows indicate times at which rainfall events start.

### 4.4.4 Effects of Boundaries vs. Land Surface

Despite the clear differences presented in the previous section in land surface variables, such as soil moisture and energy fluxes, the three simulation cases showed relatively small differences in atmospheric variables such as winds, potential temperature, rainfall, and cloud cover. To verify the extent of land surface effects on these simulations, two more simulation tests were run with the non-coupled atmospheric code ARPS. The first was initialized with uniform soil moisture at half saturation throughout the domain. The second test case was run with surface physics turned off entirely. These cases are named: uniform and nosfcphy, respectively, and are compared herein against the arps case initialized with PF.CLM soil moisture. Potential temperature and water vapor mixing ratio sounding profiles are extracted at x = 15 km and y = 15 km for the two test cases and compared against the arps simulation case in Figure 4.23 on the morning before the first storm (10am June 25$^{th}$), during the first storm (8pm June 25$^{th}$), and the morning after the storm (10am June 26$^{th}$).

What we notice here is that the NARR lateral boundary forcing has a greater effect on the atmospheric behavior in these cases than conditions at the land surface. Even when turning off surface physics entirely, differences between arps and nosfcphy cases do not appear beyond an

elevation of about 1 km (Figure 4.23). Despite this dominant effect of the boundaries, we see that soil moisture initialization does have an effect closer to the land surface as seen in the water vapor mixing ratio soundings for the arps and uniform cases during the storm (Figure 4.23b). A similar effect was observed in the numerical experiments of Avissar and Schmidt (1998) and Raasch and Harbusch (2001) who demonstrated that a background wind speed higher than 5 m/s can minimize the effect of surface heterogeneity. They also found that the degree of reduction however depends on wind direction relative to the heterogeneity orientation.

To further investigate the effects of lateral boundary forcing versus land surface forcing, horizontal advection and vertical diffusion timescales are compared for the three simulation cases to further understand the relative effects of lateral boundary forcing and land surface forcing in these simulations. The horizontal advection timescale ($T_{adv}$) indicates how long it takes flow to travel laterally across the domain from the boundaries, while the vertical diffusion timescale ($T_{diff}$) represents the time it takes information to travel vertically from the land surface to the top of the PBL. These timescales are defined herein as follows:

$$T_{diff} = H^2 / \nu_T \qquad \text{(Equation 4.1)}$$

$$T_{avd} = L/U \qquad \text{(Equation 4.2)}$$

Where:

H: is the average PBL depth (m),
$\nu_T$: is the average vertical eddy viscosity within the PBL ($m^2/s$),
L: Length scale, taken here as the horizontal domain length, and
U: is the average horizontal wind speed within the PBL.

Results (shown for all three simulation cases in Figure 4.24) indicate that both timescales are of the same order of magnitude during the daytime and dry nights (first and second nights). These timescale trends however are affected by several factors including the diurnal cycle, rainfall events, and wetting/drying behavior. Rainfall has a direct effect on increasing the vertical diffusion timescale particularly on the third and fourth nights following rainfall events. The land surface is wetter during the third night than it was during the first simulation night for instance. This extra moisture cools the land surface and thus inhibits convective circulations which increase the time it takes for diffusive motions to reach the PBL top from the land surface. This same effect is observed in all three simulation cases.

Effects of the diurnal cycle are more apparent during the drying period after the second day. The longer advective timescales during mornings on the third and fourth days indicate weaker synoptic forcing which picks up during the afternoon and evening times on those days. Vertical diffusion motions however are weakest during the night, and it is when these motions are breaking from their stable nocturnal state during morning hours that they overcome the synoptic forcing effects. This is seen for example on the morning of the third day in the figure when the diffusion and advection timescale curves intersect (at ~62 hours of simulation).

The purpose of these simple scaling estimates is to obtain an order of magnitude of these timescales and their relative importance during different times during the simulation. The fact that both timescales have similar orders of magnitude during most times indicates that both lateral boundary forcing and land surface forcing are significant. This does not imply however that one of these forcings cannot have a larger potential to cause change within the PBL than the other (as seen in the results of previous sections where lateral boundary conditions have a greater effect on PBL processes during most times). If the horizontal domain was larger however, the lateral boundary effect is reduced in comparison to land surface forcing. According to Warner et al (1997), effects of lateral boundary conditions (LBC) can be reduced by distancing the boundaries from the central part of the computational area so that their influence does not penetrate to the main part of the simulation. This was tested here by running three more simulation tests with double the grid size of the original three simulation cases. The three larger test cases are simulated using uncoupled ARPS and are named as follows based on the soil moisture initialization:

1. *wet*: almost saturated land surface
2. *dry*: $q_{soil}=0.1$
3. *narr*: initialized with NARR soil moisture field.

Results are shown in Figure 4.25 in which wind speed and direction sounding profiles for the three larger-domain cases are compared against the three original simulation cases (pfarps, arps, and narr). The soundings clearly show that land surface forcing effects are observed at much higher elevations within the PBL in the larger domain than in the original domain. In general, the larger domain does produce greater differences between the three simulation cases (wet, dry, and narr). These differences increase during dry times and during the day. Vice versa, differences are smoothed out after rain events and during night.

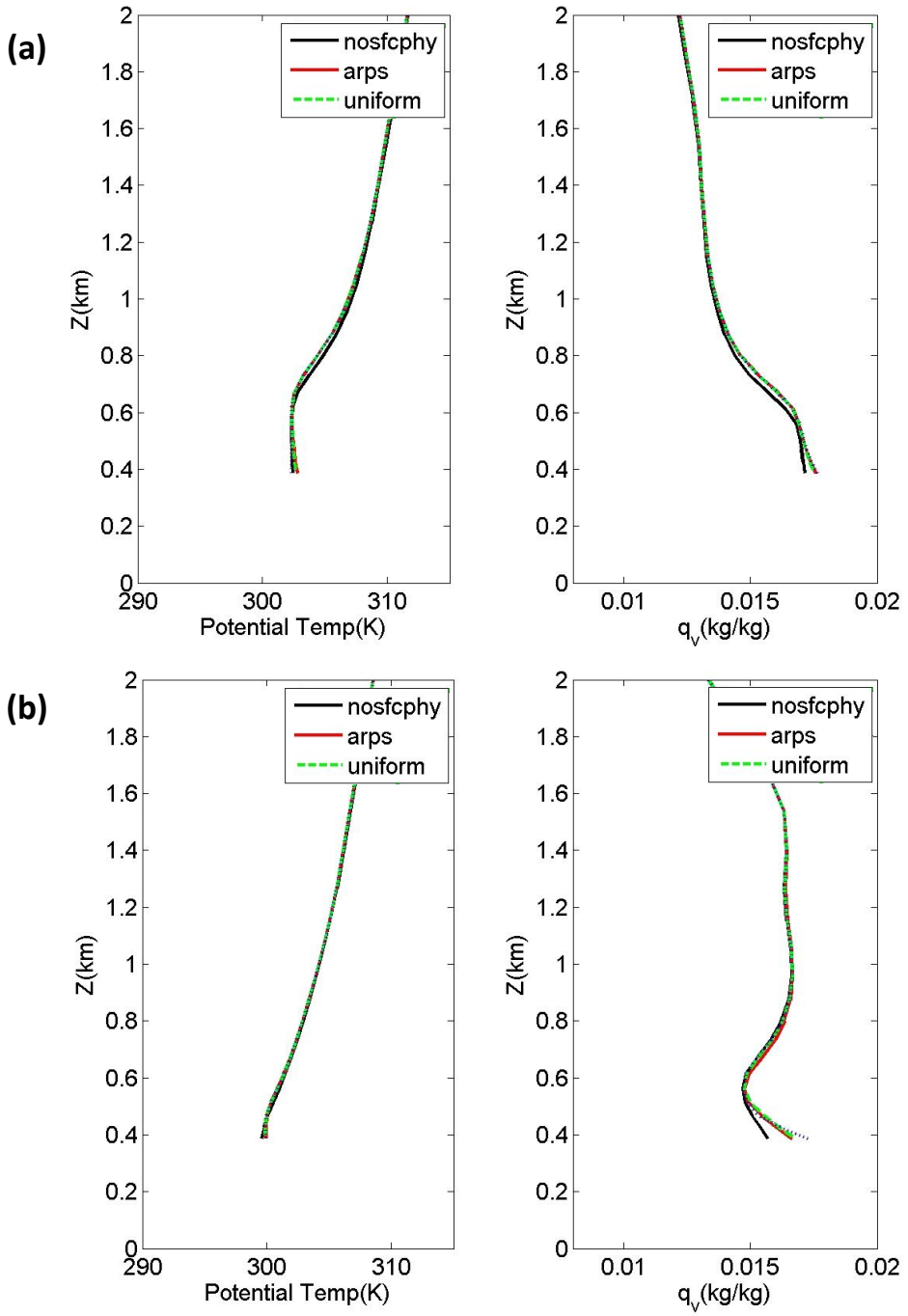


**Figure 4.23**: Potential temperature and water vapor mixing ration sounding profiles for the two tests (uniform and sfcphy) compared against the arps case at: (a) 10am June 25th (b) 8pm June 25th.

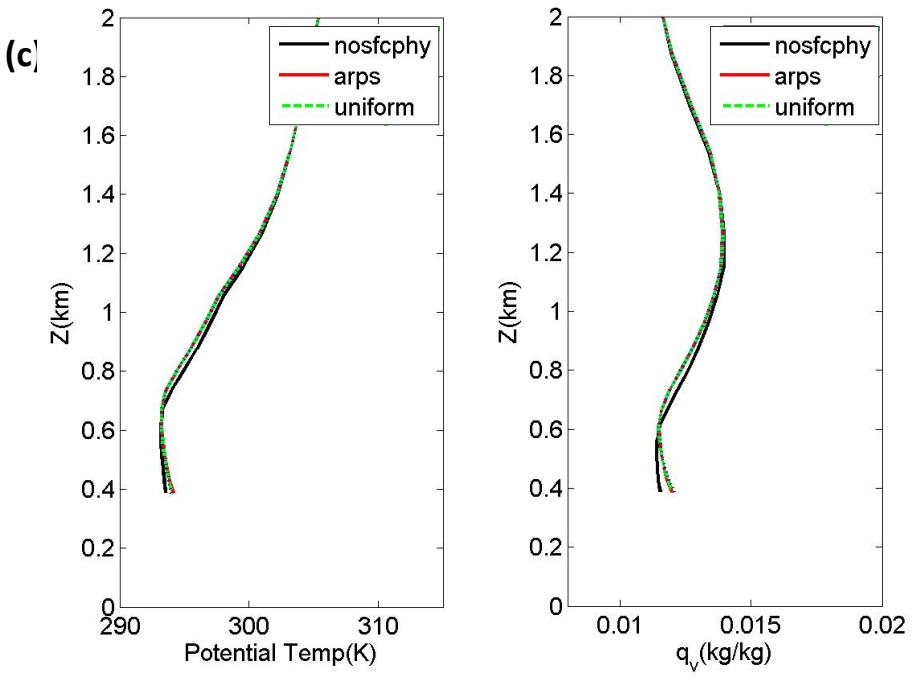


**Figure 4.23 Cont'd**: Potential temperature and water vapor mixing ration sounding profiles for the two tests (uniform and sfcphy) compared against the arps case at: (c) 10 am June 26th

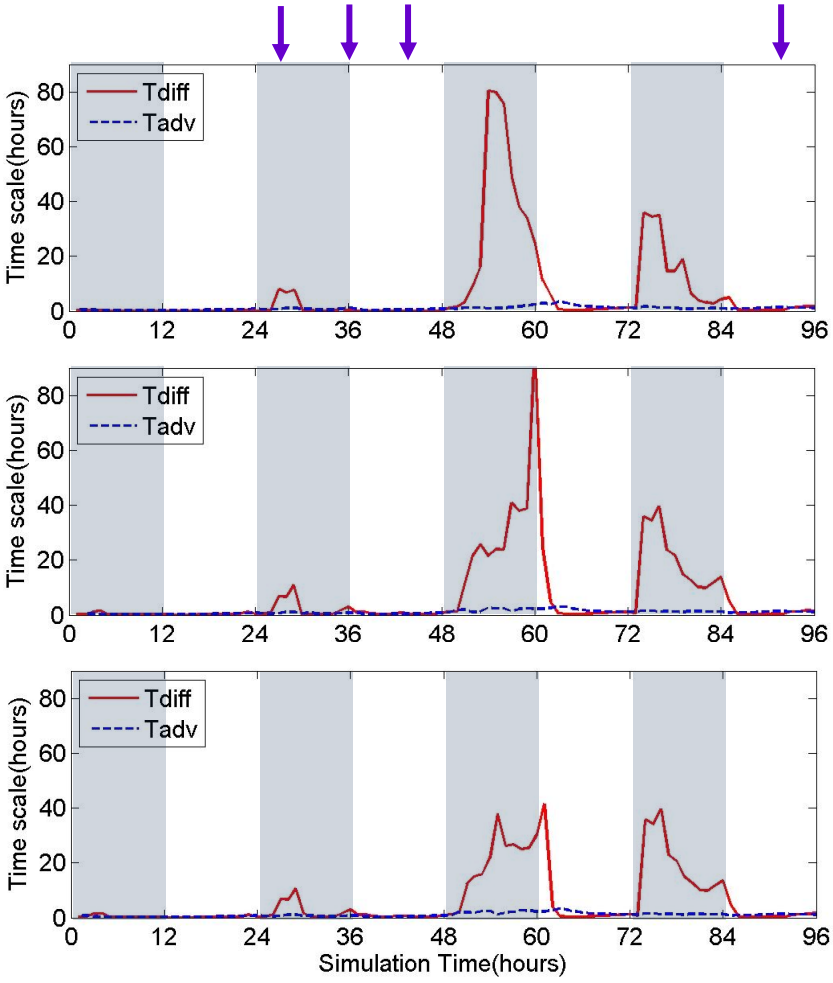


**Figure 4.24:** Vertical diffusion and horizontal advection timescales for the three simulation cases: (a) pfarps, (b) arps, and (c) arpsnarr. Shaded areas represent night times (7pm to 7am) and arrows indicate peaks of the four rainfall events.

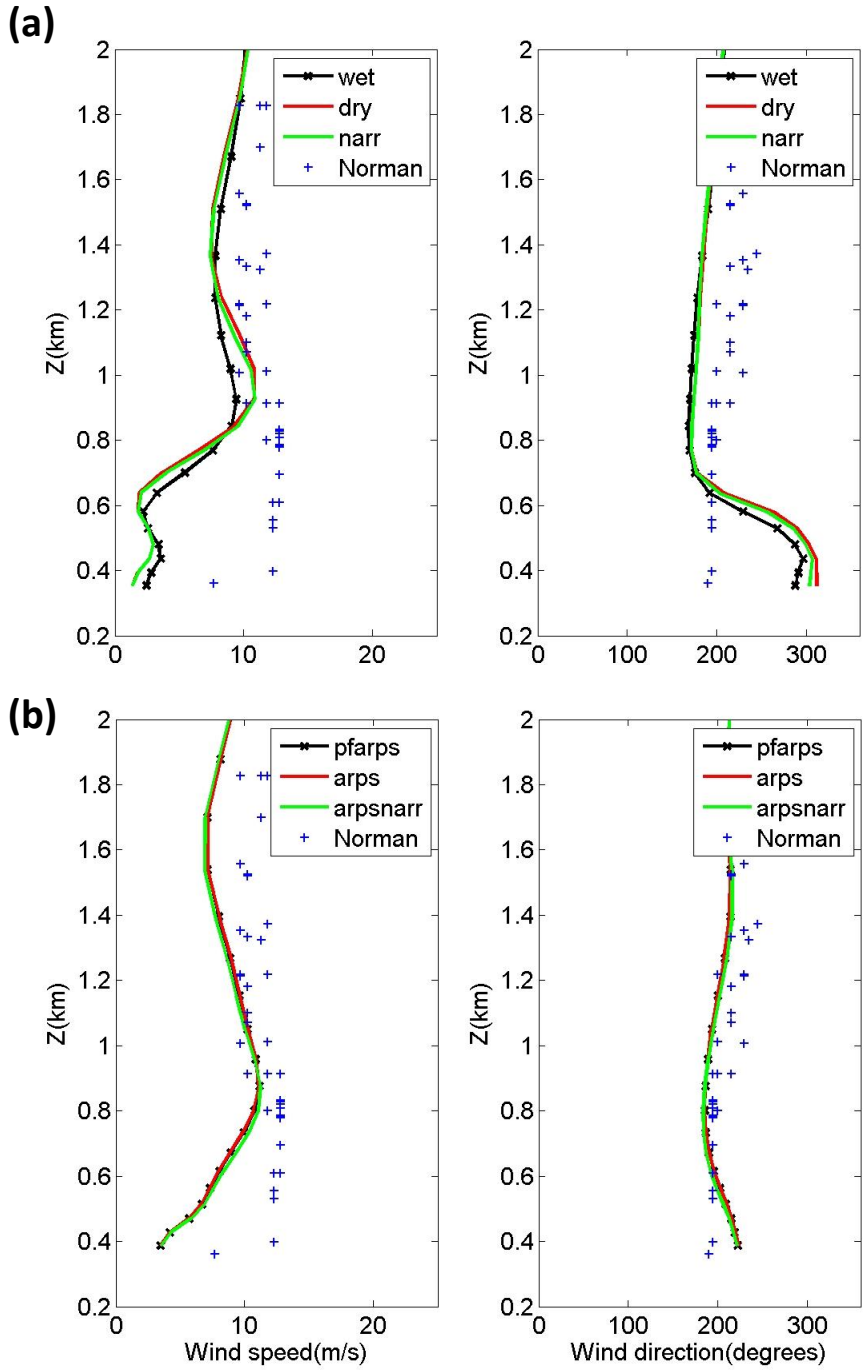


**Figure 4.25:** Sounding profiles of wind speed and direction at 7pm on June 25th for: (a) larger domain simulation cases and (b) original domain simulation cases. Observed soundings at Norman station are indicated on the plot.

### 4.4.5 Fully coupled model: PBL and WTD feedbacks

To investigate the coupling between subsurface, surface, and atmospheric processes in the LW watershed, the coupled model results (pfarps) are analyzed and scatter plots are generated of water table depth versus planetary boundary layer depth (PBLD), vertical wind speeds (w), top soil moisture (qs-L1) and temperature (Ts-L1), latent heat (LH) and sensible heat (SH) fluxes at the land surface. Figures 4.26 and 4.27 show averaged scatter plots for the first (13 to 24 hours) and third (37 to 48 hours) simulation days, respectively. Results indicate that although synoptic winds and lateral boundary forcing have a large effect, some of the subsurface-surface-atmosphere feedbacks observed in chapters two and three are seen here during dry times of the simulation period (i.e. during the first day). For instance, effects of water table depth on land surface energy fluxes are observed most clearly during the first day of simulation before any rainfall events as shown in Figure (4.26). Soil moisture at the land surface for the pfarps case is closely related to water table depth (Figure 4.26f) as it results from an offline spinup with an active water table. This connection translates to energy fluxes at the land surface. While LH and SH are decoupled from WTD at locations with a deep water table, a transition zone behavior can be seen (following conclusions of chapter 2) in Figures 4.26c and 4.26d such that a negative correlation for LH and a positive correlation for SH are observed in regions around the river valley with shallow water table. Feedbacks between WTD and land surface energy fluxes are translated to a positive correlation with PBLD (Figure 4.26a). Wetter valleys have enhanced evaporation, a cooler land surface, and thus reduced heating of air which results in a lower boundary layer depth. On the other hand, a deep water table means a drier land surface, which results in warmer soil particularly during the day (Figure 4.26e). A warm land surface enhances convective motions and thus increases the boundary layer height. This correlation is most clear during dry periods (first 24 hours of simulation) but is also observed during other times.

Rainfall on the second and third days has the effect of reducing these coupling effects as it makes the soil moisture distribution at the land surface more uniform (Figure 4.27f). This directly affects land surface energy fluxes and their correlation to water table depth (Figures 4.27c and 4.27d). As rainfall reduces subsurface-surface feedbacks, this behavior is also extended to the PBLD (Figure 4.27a) and although the correlation to WTD is still observed, it is not as strong as it is on the first day before rainfall. The correlation between vertical winds at the land surface and water table depth however is enhanced during wet periods (Figure 4.27b), particularly during night times as shown in the instantaneous scatter plot (Figure 4.28b) at 4am during the third night of simulation.

The dependence on soil type is very clear here particularly in land surface energy fluxes and soil temperature (Figure 4.26). Silt and loam soils can hold more water and thus exhibit greater latent heat and lower sensible heat fluxes than sandy soil (Figures 4.26c and 4.26d). Drier sandy soils thus heat faster during the day than silt and loam soil types as seen in Figure 4.26e. Soil type also has some effect on the PBLD-WTD correlation, however a larger dependence on terrain is observed during most times (e.g. Figure 4.28a) such that valley locations exhibit a shallower PBLD than peaks with deep WTD. This is in agreement with results from chapter 3 in which the effects of terrain-induced variable heating and cooling were demonstrated for sinusoidal hills. These effects were shown to increase with increasing soil moisture heterogeneity, and this aligns

with what is observed here such that the WTD-PBLD correlation is enhanced during dry times which exhibit greater differences between saturated valleys and dry peaks.

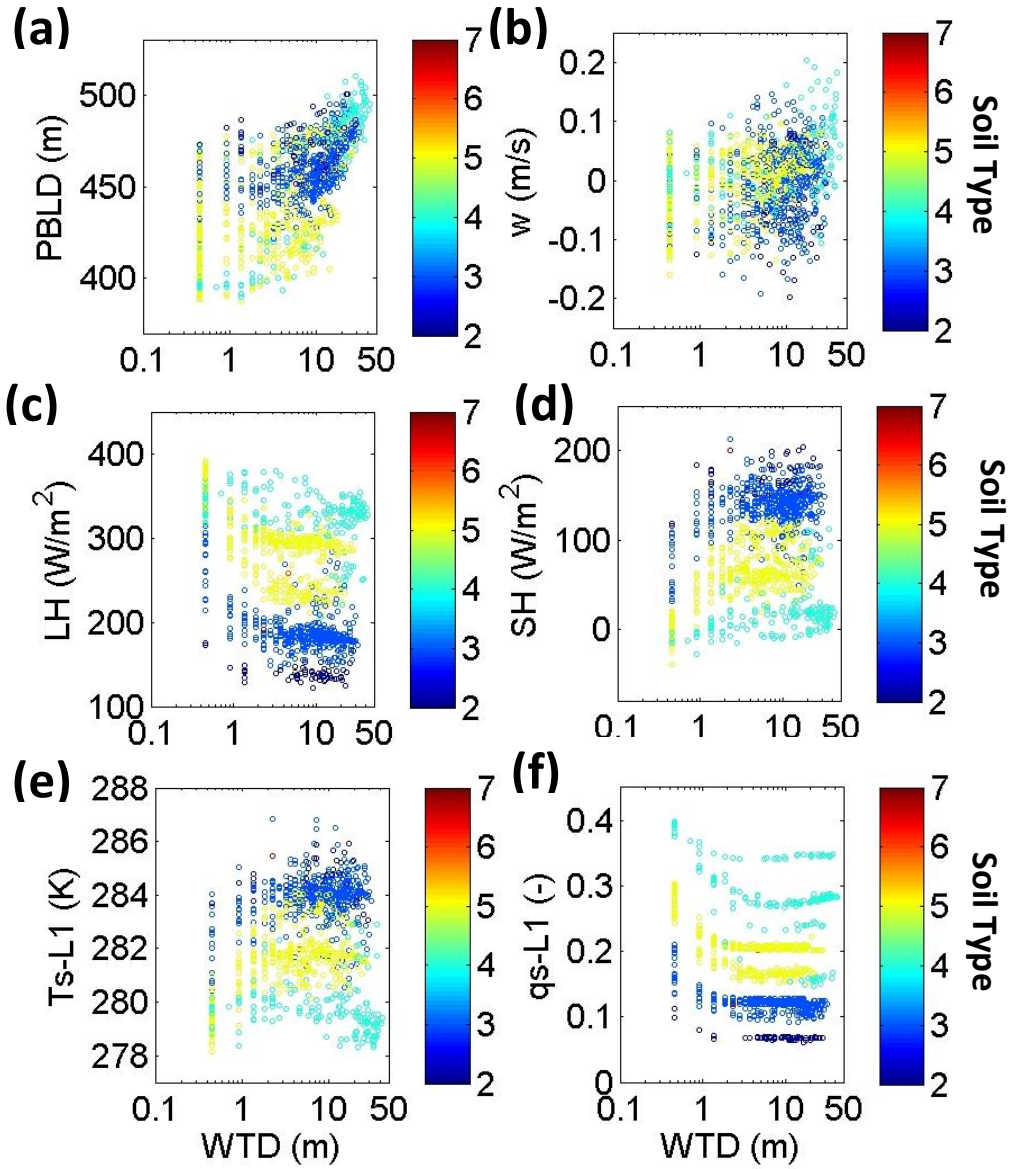


**Figure 4.26**: Scatter plots of: (a) PBL depth (PBLD), (b) vertical wind speed (w), (c) latent heat flux (LH), (d) sensible heat flux (SH), (e) top soil temperature (Ts-L1), and (f) moisture (qs-L1) versus water table depth (WTD). Values are averaged over the first day of simulation (hours 13 to 24). Color bar indicates soil type (2: sand, 3: Loamy sand, 4: Silt Loam, 5: Loam, 6: Clay Loam, 7: Silty Clay).

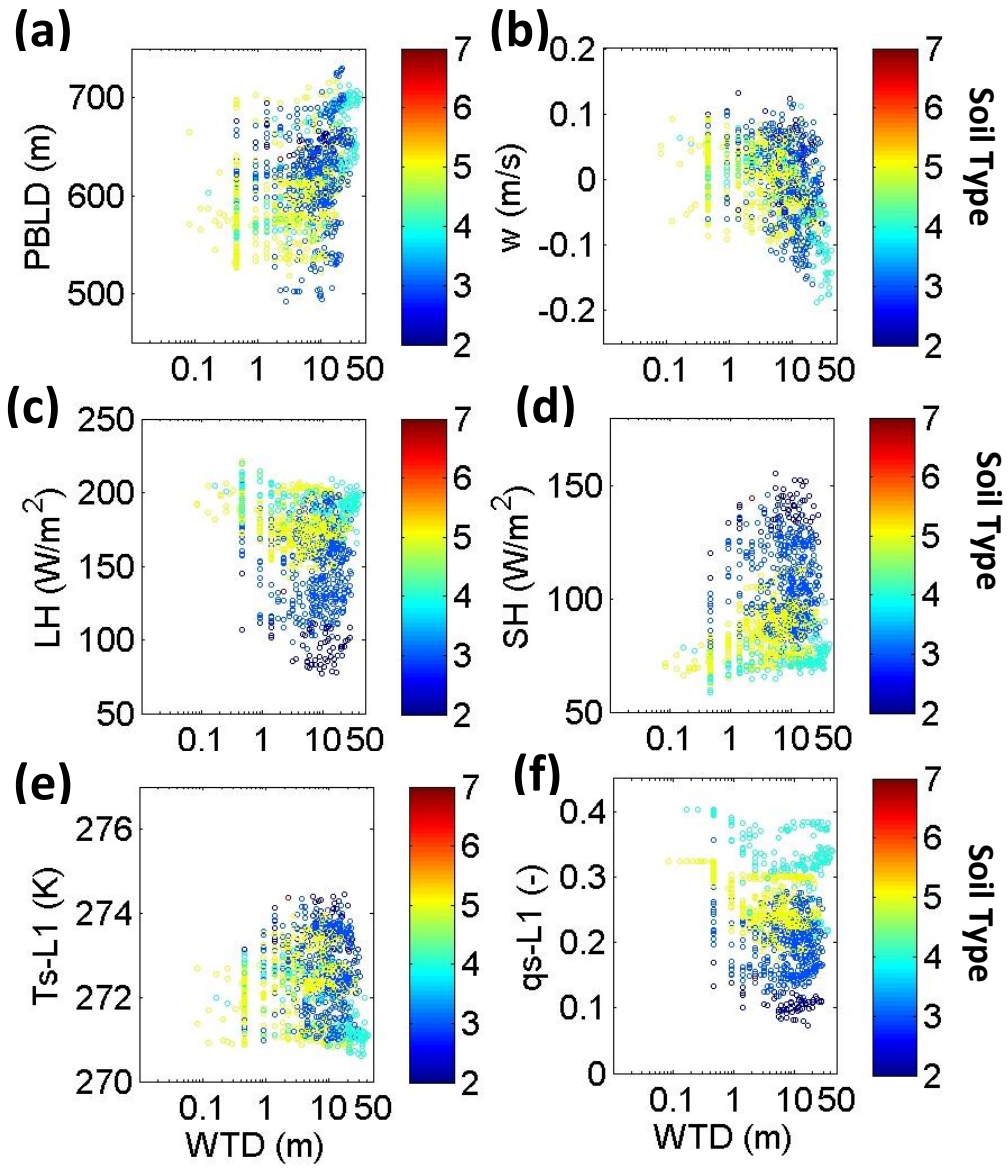


**Figure 4.27**: Scatter plots of: (a) PBL depth (PBLD), (b) vertical wind speed (w), (c) latent heat flux (LH), (d) sensible heat flux (SH), (e) top soil temperature (Ts-L1), and (f) moisture (qs-L1) versus water table depth (WTD). Values are averaged over the second day of simulation (hours 37 to 48). Color bar indicates soil type (2: sand, 3: Loamy sand, 4: Silt Loam, 5: Loam, 6: Clay Loam, 7: Silty Clay).

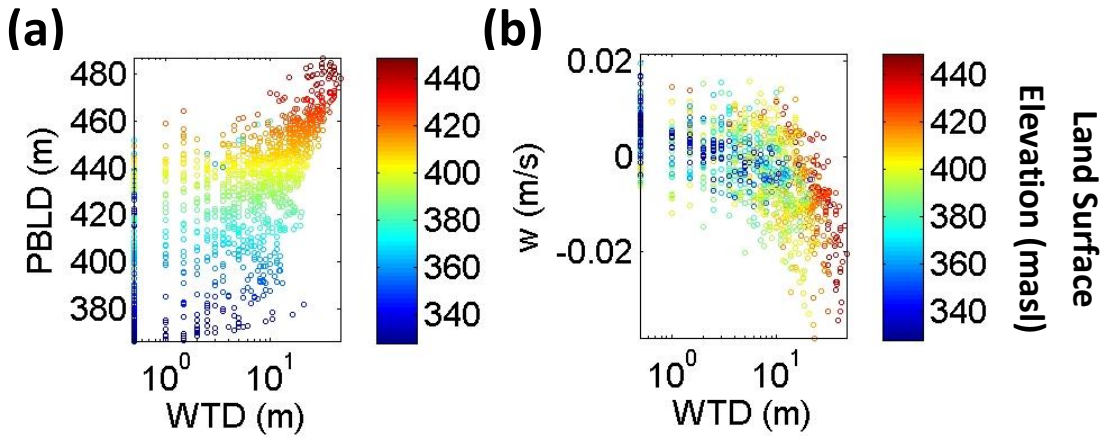


**Figure 4.28**: Instantaneous scatter plot of: (a) PBL depth (PBLD) and (b) vertical wind speed (w) versus water table depth (WTD) at 4 am during the third simulation night (June 27th). Color bar indicates land surface elevation (masl).

### 4.4.6 Fully coupled model: Streamflow results

Simulated pressure field for the pfarps case was used to calculate total outflow from the LW basin. This was compared to observed streamflow at the USGS stream gauging station (07327550) on the Little Washita River East of Ninnekah, as shown in Figure 4. 29. The figure demonstrates little agreement between simulated and observed streamflow and this is mainly attributed to the large lateral grid scale of 1km which makes it harder for the model to fully capture low flow conditions. There is also a few hours' lag in predicting rainfall events in the model (Figure 4.29a) as the NARR forcing does not produce rainfall events accurately. This affects the timing of the peak streamflow here and is the reason why it does not occur around the same time as observed streamflow. Another thing to be considered here is although subsurface properties were adjusted slightly to better match observed data, the model was not really calibrated during the spinup process. Kollet and Maxwell (2008) made a similar comparison for their spinup results of the LW basin for the 1998-1999 water year. Their comparison showed reasonable agreement for stream discharge except during low flow conditions between July and September. A similar effect is seen here during the end of June and although the LW valley is maintained at saturated or near-saturated conditions during the simulation, periods of no-flow from the basin outlet are mainly attributed to the large grid scale and the model being unable to resolve low flows.

It should be noted that the timing of the simulations in June was particularly chosen to observe effects of wetting and drying on coupled interactions between subsurface, surface, and the atmosphere, an effect that would have been much harder to observe during the wet season with larger rainfall events.

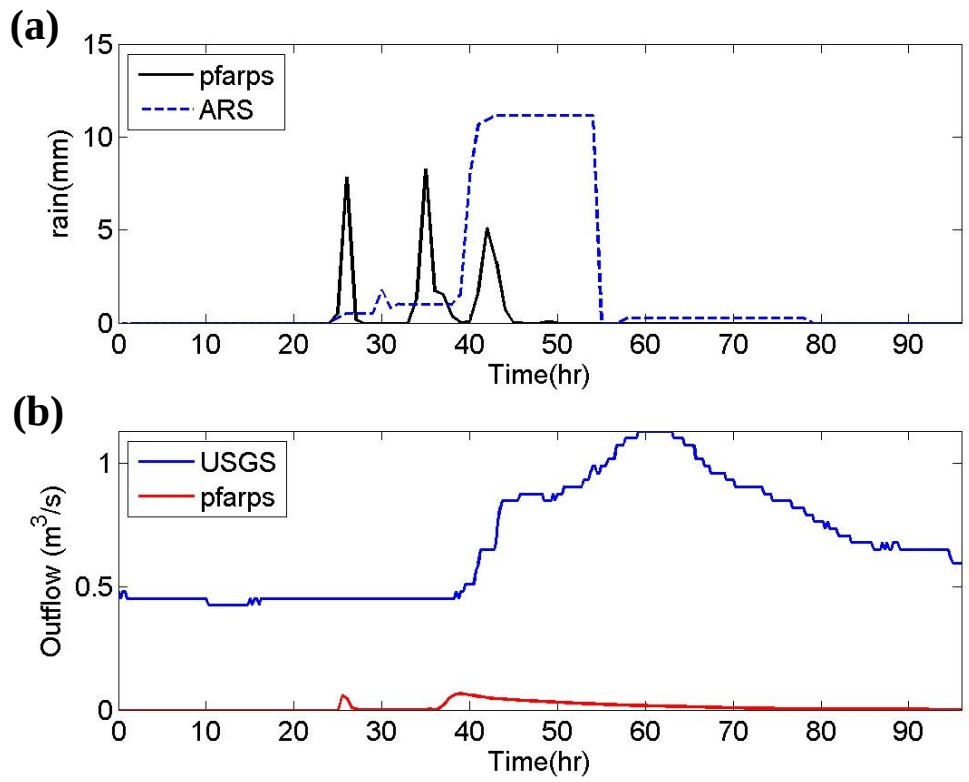


**Figure 4.29**: (a) Observed (ARS) and simulated (pfarps) rainfall at ARS station A135, (b) observed (USGS) and simulated (pfarps) hydrographs for the LW watershed basin.

## 4.5 Conclusions

To investigate feedbacks between subsurface and atmosphere under real weather conditions, the Little Washita watershed in Oklahoma was simulated using the coupled subsurface-surface-atmospheric code, PFARPS, and the uncoupled mesoscale atmospheric code ARPS. Effects of soil moisture initialization were also studied by initializing simulations both with a realistic soil moisture distribution resulting from an offline spinup and a more uniform NARR distribution. The model results were in general agreement with field observations (in particular for the atmosphere), with better agreement when the offline spinup data were used to initialize the land surface. The following conclusions are made in response to the research questions posed earlier in the chapter:

*(1) What are the effects of lateral boundary forcing compared to effects of the land surface conditions?*

Comparing simulation results over 4 days demonstrates that despite large differences in surface fluxes, the effects of lateral boundary forcing dominate and create relatively small differences in the lower part of the atmospheric boundary layer. For example, errors in the timing of the storm system (compared to observations) propagate into the higher resolution domains due to the lateral boundary forcing. This forcing dominates the evolution of atmospheric variables such as wind speed, potential temperature, and rainfall events. Nonetheless, small differences in the atmosphere are visible up to about 1 km above ground level. For instance, differences in potential temperature and horizontal wind speeds of up to 2 K and 5 m/s, respectively, are observed between simulation cases, particularly between the pfarps and arpsnarr cases. These near-surface differences can have significant effects on scalar fluxes, such as moisture and air pollutant transport. The near-surface region of the atmospheric boundary layer is also of great importance in wind energy predictions, which require high accuracy in wind speed values below about 200 m.

*(2) Which times within the diurnal cycle and locations within the watershed show stronger feedbacks between the water table and the atmospheric boundary layer?*

Effects of coupling the subsurface to the land surface and atmosphere are mostly observed during dry daytime periods, particularly early morning hours. For instance, differences in land surface energy fluxes between the simulation cases are observed early in the morning and increase during the afternoon as the land surface warms up, reaching a maximum difference in latent heat flux of 600 $W/m^2$ on a dry day. This large increase in evaporation is observed in the coupled case and is a direct effect of having lateral flow taken into account which allows more moisture to be sustained in the valley as base flow. Furthermore, coupled feedbacks and soil moisture initialization become most important within small transitional (partly-saturated) areas around the river valley. These locations lie in between saturated valley regions and higher elevation regions with drier land surface which are decoupled from the subsurface. For instance, scatter plots of land surface and atmospheric variables versus water table depth demonstrate a negative correlation for LH and a positive correlation for SH within these transitional zones during the day. These correlations are reflected in soil temperature and heating at the land surface and thus in the boundary layer development and depth.

*(3) How does a storm system affect the coupling and which days show stronger feedback: before, during, or after a storm?*

Coupled subsurface-surface-atmosphere feedbacks, which appear in the morning and increase towards the afternoon, are emphasized during dry periods but are smoothed out during and after storm events. As the land surface becomes wet during a storm, soil moisture at the land surface is reset and differences in land surface variables are gradually smoothed out. These differences emerge once more as the rain effects gradually dry out. For instance, differences in land surface

energy fluxes are reduced after the storm events and only reach a maximum of 100 W/m$^2$ on the morning after the storm events (compared to 600 W/m$^2$ on the morning before the storm).

In general, a better agreement with observations was achieved by initializing the model with a more realistic soil moisture field as in the arps and pfarps cases. The greatest differences between the three simulation cases lie in heat fluxes, soil moisture, and ground surface temperature. This shows the significance of soil moisture initialization in atmospheric simulations, particularly in cases where a computationally expensive, fully coupled modeling approach is not feasible, employing more realistic soil moisture conditions at the land surface does make a difference in model results. It should be noted however that a non-coupled atmospheric model, even when initialized with a realistic soil moisture distribution, cannot sustain soil moisture without a coupled subsurface component particularly at higher elevations with deeper water table.

It is worth mentioning that although the Little Washita is a heavily studied site and one rarely finds this amount of multidisciplinary data in a single site, it can still be challenging to match the time scale of the model to the time scale of observations. For instance, in order to fully investigate the storm system passing through the watershed, a much shorter simulation time is needed than that required to capture water table changes. The simulations presented here are for 4 days, while only a few groundwater measurements are taken within any single year which is not enough to validate water table trends in the aquifer. This points to the need for further simultaneous and co-located subsurface and atmospheric measurements.

# Chapter 5

# Conclusions and Recommendations

The work presented here aims to increase our understanding of subsurface-land surface-atmospheric interactions and the two way feedbacks between water table dynamics and atmospheric boundary layer processes. The coupled models implemented in this work (PF.CLM and PF.ARPS) are valuable research tools and are used herein to study effects of terrain, subsurface formation, land cover, and climate on water table dynamics, energy fluxes at the land surface, and how these impact the development and structure of the atmospheric boundary layer. These effects were investigated for idealized cases and a real watershed. Conclusions were made regarding times within a diurnal cycle and locations within a watershed which demonstrate strong coupling between the subsurface and the atmosphere. These are summarized herein and recommendations are made for future research efforts.

## 5.1 Summary and Conclusions

To further understand factors affecting interactions between subsurface, land surface, and the atmosphere, this fully coupled system was studied in two stages. Subsurface-land surface coupling was investigated first for a range of idealized cases in chapter 2 with the purpose of isolating factors which significantly affect the coupling. Results from chapter 2 were then used to initialize a range of idealized atmospheric simulations in chapter 3 and study the second part of the coupled system; land surface-atmospheric coupling. Conclusions obtained from the idealized cases in chapters 2 and 3 were used to investigate a fully coupled simulation of the Little Washita watershed in Oklahoma. This was compared against non-coupled atmospheric simulations of the Little Washita to glean the benefits of having a fully coupled model of a hydrologic system.

In chapter 2, the role of terrain and subsurface heterogeneity on the interactions between groundwater dynamics and land surface energy fluxes was investigated using idealized simulations and the groundwater-surface water coupled code PF.CLM. Results show that different land forms and subsurface properties produce very different water table dynamics and land surface flux responses to atmospheric forcing. Critical zones along a hillside with stronger interactions between water table depth and land surface energy fluxes were identified. Subsurface formations and properties had the greatest effect on location and extent of these critical zones. Changes in land form and land surface slope also had a significant effect by influencing the fraction of rainfall contributing to overland flow versus infiltration. While effects of vegetation and climate extended to the energy balance at the land surface and water table dynamics, respectively, their effect on the coupling between water table depth and land surface energy fluxes was limited compared to land form and subsurface properties.

Chapter 3 focused on the connection between the land surface and atmosphere by looking into effects of terrain, soil moisture heterogeneity, and the indirect effects of subsurface properties and water table depth on the development and behavior of the atmospheric boundary layer. This

was done by simulating a set of 3D idealized numerical experiments using the non-coupled mesoscale atmospheric model ARPS. Results demonstrate that effects of terrain are strongest during early morning hours as the stable nocturnal boundary layer is destroyed by convective circulations resulting from variable heating and cooling at the land surface. Increasing soil moisture heterogeneity enhances the terrain signature on PBL height and development during morning hours, but eventually overcomes it in the afternoon when the land surface heats more evenly. These relative effects are influenced by subsurface properties and water table dynamics which dictate the location and extent of the critical zone with strongest coupling between water table depth and land surface energy fluxes (as described in chapter 2). Soil moisture variability for instance has a larger effect on PBL depth within the transition zone while terrain effects dominate at higher elevations outside the transition zone. This results in a positive correlation between PBL depth and water table depth within the transition zone, but a negative correlation appears at higher elevations within the decoupled zone.

These effects were examined under real weather conditions and real terrain for the Little Washita watershed in chapter 4. Three simulations of the Little Washita were conducted and compared; an atmospheric non-coupled simulation using ARPS initialized with NARR soil moisture conditions, an atmospheric non-coupled simulation using ARPS initialized with realistic soil moisture conditions resulting from PF.CLM offline spinups; and a fully coupled subsurface-surface-atmospheric simulation using PF.ARPS also initialized with realistic soil moisture conditions resulting from PF.CLM offline spinups. Coupled subsurface-surface-atmosphere feedbacks were mostly observed during dry daytime periods, particularly early morning hours. Storm events can reset land surface soil moisture and thus smooth out the signature of subsurface conditions and terrain on land surface energy fluxes and the atmospheric boundary layer. These feedbacks however emerge once more during dry periods, particularly within small transitional (partly-saturated) areas around the river valley. These correspond to the critical zone described in chapter 2, and demonstrate a strong correlation between water table depth on one hand, and land surface energy fluxes, soil temperature, and PBL depth on the other hand.

The greatest differences observed between these three simulation cases were in heat fluxes, soil moisture, and ground surface temperature. Simulation results were in better agreement with field observations when the realistic PF.CLM soil moisture field was used to initialize the land surface. This shows the significance of soil moisture initialization in atmospheric simulations particularly in cases where a fully coupled modeling approach is not feasible, employing a more realistic soil moisture field which takes into account subsurface conditions greatly improves model results. It should be noted however that a non-coupled atmospheric model cannot sustain soil moisture without a coupled subsurface component particularly at higher elevations with deeper water table.

This is the first time, to our knowledge, that these subsurface-surface-atmosphere connections have been explicitly demonstrated for a range of cases and conditions as presented here. This work hence presents unique contributions to the connection between water table dynamics and planetary boundary layer development. In reality, it is not easy to isolate effects of terrain, soil moisture variability, and subsurface conditions on the atmospheric boundary layer, but results from the idealized simulations have proven valuable in explaining these feedbacks for the Little Washita watershed. Although these simulations do not cover all possible cases of terrain and

subsurface heterogeneities, the results reached in this work are meant to provide a platform upon which other case studies can build.

## 5.2 Recommendations

Given the improved results obtained from including subsurface processes and more realistic soil moisture conditions at the land surface, this work demonstrates that such conditions should not be ignored in atmospheric simulations. Even when a fully coupled approach is computationally expensive to implement, our results demonstrate that using a separate groundwater-surface water model to obtain soil moisture field initializations for an atmospheric simulation can greatly improve model results and agreement with observations. Land surface forcing was shown to have a great effect on potential temperature and horizontal wind speeds within the near-surface region of the PBL, thus rendering these interactions significant for moisture and air pollutant transport studies as well as wind energy predictions.

The simulations presented here do not cover all possible scenarios of climate, land cover, terrain, and subsurface conditions. More work is needed to fully understand subsurface-land surface-atmospheric interactions and conditions which make them most significant. Studies looking into subsurface, land surface, and/or atmospheric interactions however can be limited by the lack of sites with coexisting observations to validate coupled models. There is a need for more extensive field campaigns which consider taking measurements of land-energy and hydrologic variables as well as characterizing subsurface heterogeneity. The findings presented here may be used to guide the temporal and spatial resolution of observations in such field campaigns. For instance, horizontal layering, land surface slope, and bedrock layer depth had the largest effects on the coupling strength between subsurface and land surface and thus should be taken into consideration when designing field measurements.

# References


Ashby SF and Falgout RD, "A parallel multigrid preconditioned conjugate gradient algorithm for groundwater flow simulations", Nuclear Science and Engineering, 124(1): 145-159, 1996.

Avissar, R. and Pielke, R. A., "A parameterization of heterogeneous land-surface for atmospheric numerical models and its impact on regional meteorology", Monthly Weather Review, 117, 2113–2136, 1989.

Baldocchi, D. and Harley, P., "Scaling carbon dioxide and water vapour exchange from leaf to canopy in a deciduous forest. I. Leaf model parameterization", Plant Cell and Environment: 18, 1146–1156, 1995.

Batchelor GK, "An Introduction to Fluid Dynamics", Cambridge: Cambridge University Press, 1967.

Betts AK, Ball JH, Beljaars ACM, Miller MJ, and Viterbo PA, "The land surface-atmosphere interaction: A review based on observational and global modeling perspectives", Journal of Geophysical Research 101(D3): 7209–7225, 1996.

Bhumralkar CM, "Numerical experiments on the computation of ground surface temperature in an atmospheric general circulation model", Journal of Applied Meteorology 14: 1246–1258, 1975.

Blackadar AK, "Modelling the nocturnal boundary layer". In Proceedings of the Third Symposium on Atmospheric Turbulence, Diffusion and Air Quality, American Meteorological Society: Boston, MA; 46–49, 1976.

Chen X and Hu Q, "Groundwater influences on soil moisture and surface evaporation", Journal of Hydrology, 297: 285–300, 2004.

Chow FK, Kollet SJ, Maxwell RM, Duan Q, "Effects of soil moisture heterogeneity on boundary layer flow with coupled groundwater, land-surface, and mesoscale atmospheric modeling". In: Proceedings of the 17th symposium on boundary layers and turbulence. Paper 5.6. American Meteorological Society. p. 6, 2006.

Chow FK, Weigel AP, Street RL, Rotach MW, Xue M., "High-resolution large-eddy simulations of flow in a steep Alpine valley. Part I: methodology, verification, and sensitivity experiments", Journal of Applied Meteorology and Climatology, 45:63–86, 2006.

Clark DB, Taylor CM, Thorpe AJ, "Feedback between the Land Surface and Rainfall at Convective Length Scales", Journal of Hydrometeorology, 5: 625-639, 2004.

Cowan, IP, “Mass, heat and momentum exchange between stands of plants and their atmospheric environment”, Quarterly Journal of the Royal Meteorological Society, Volume 94 (402): 523–544, 1968.

Dai, Y. J., et al, The Common Land Model, Bulletin of the American Meteorological Society, 84(8), 1013–1023, 2003.

Da Silva RR & Avissar R, “Regional Impacts of Future Land-Cover Changes on the Amazon Basin: Wet-Season Climate”, Journal of Climate, 21: 1153-1170, 2008.

Dawson C, “A continuous/discontinuous Galerkin framework for modeling coupled subsurface and surface water flow”, Computational Geosciences, 12(4): 451–472, 2008.

Deardorff JW, “Efficient prediction of ground surface temperature and moisture with inclusion of a layer of vegetation”. Journal of Geophysical Research, 83: 1889–1903, 1978.

Dickinson RE, Henderson-Sellers A, Kennedy PJ, and Wilson MF, “Biosphere–Atmosphere Transfer Scheme (BATS) for the NCAR Community Climate Model”, NCAR Technical Note TN-275 + STR, 1986.

Dickinson RE, Henderson-Sellers A, and Kennedy PJ, “Biosphere–Atmosphere Transfer Scheme (BATS) Version 1e as coupled to the NCAR Community Climate Model”, NCAR Technical Note, NCAR, TN383+STR, 1993

D'Odorico P and Porporato A, “Preferential states in soil moisture and climate dynamics”, Proceedings of the National Academy of Sciences, 101(24): 8848–8851, 2004.

Ebel BA, Mirus BB, Heppner CS, VanderKwaak JE , and Loague K, “First-order exchange coefficient coupling for simulating surface water–groundwater interactions: Parameter sensitivity and consistency with a physics-based approach”, Hydrological Processes, 23(0–0): DOI: 10.1002/hyp.7279, 2009.

Fan Y, Miguez-Macho G, Weaver GP, Walko R, and Robock A, “Incorporating water table dynamics in climate modeling: 1. Water table observations and equilibrium water table simulations”, Journal of Geophysical Research, 112, D10125, doi:10.1029/2006JD008111, 2007.

Fiori A and Russo D, “Numerical analyses of subsurface flow in a steep hillslope under rainfall: The role of the spatial heterogeneity of the formation hydraulic properties”, Water Resources Research, 43, W07445, doi:10.1029/2006WR005365, 2007.

Freeze RA, “Role of subsurface flow in generating runoff 1. Base flow contributions to channel flow”, Water Resources Research 8: 609–624, 1972.

Freeze R.A., and Harlan R.L., “Blueprint for a physically-based digitally-simulated hydrologic response model”, Journal of Hydrology, 9: 237-258, 1969.

Freeze RA and Witherspoon PA, "Theoretical Analysis of Regional Groundwater Flow: 1. Analytical and Numerical Solutions to the Mathematical Model", Water Resources Research, 2(4): 641-656, 1966.

Furman, A., "Modeling Coupled Surface–Subsurface Flow Processes: A Review", Vadose Zone Journal, 7:741–756, 2008.

Graham, D.N. and Butts, M.B. "Flexible integrated watershed modelling with MIKE SHE, in: Watershed Models", edited by: Singh, V. P. and Frevert, D. K., CRC Press, Boca Raton, Chapter 10, 245–272, 2006.

Gu, L., Shugart, H., Fuentes, J., Black, T., and Shewchuk, S., "Micrometeorology, biophysical exchanges and NEE decomposition in a two-storey boreal forest – development and test of an integrated model", Agricultural and Forest Meteorology: 94, 123–148, 1999.

Gulden LE, Rosero E, Yang ZL, Rodell M, Jackson CS, Niu GY, Yeh PJ, and Famiglietti J, "Improving land-surface model hydrology: Is an explicit aquifer model better than a deeper soil profile?", Geophysical Research Letters, 34, L09402, doi:10.1029/2007GL029804, 2007.

Haltiner GJ and Williams RT, "Numerical Prediction and Dynamic Meteorology", New York: Wiley and Sons, 1980.

Jackson T, Cosh M, Starks P, and Heathman G, "SMEX03 Little Washita Micronet Soil Moisture Data: Oklahoma". Boulder, Colorado, USA: National Snow and Ice Data Center. Digital media, 2007.

Jones JE and Woodward CS, "Newton-Krylov-multigrid solvers for large-scale, highly heterogeneous, variably saturated flow problems", Advances in Water Resources, 24: 763-774, 2001.

Kim CP, Salvucci GD, and Entekhabi D, "Groundwater-Surface water interaction over simple hillslopes", Hydrology and Earth Systems Science, 3(3): 375-384, 1999.

Kollet SJ, Cvijanovic I, Schüttemeyer D, Maxwell RM, Moene AF, and Bayer P, "The Influence of Rain Sensible Heat, Subsurface Heat Convection, and the Lower Temperature Boundary Condition on the Energy Balance at the Land Surface", Vadose Zone Journal, doi:10.2136/vzj2009.0005, 2009.

Kollet, S.J., and Maxwell, R.M., "Integrated surface-groundwater flow modeling: A free-surface overland flow boundary condition in a parallel groundwater flow model", Advances in Water Resources, 29:945–958, 2006.

Kollet SJ and Maxwell RM, "Capturing the influence of groundwater dynamics on land surface processes using an integrated, distributed watershed model", Water Resources Research, 44(2), W02402, 2008.

Koster, RD, PA Dirmeyer, Z Guo, G Bonan, E Chan, P Cox, CT Gordon, S Kanae, E Kowalczyk, D Lawrence, P Liu, C Lu, S Malyshev, B McAvaney, K Mitchell, D Mocko, T Oki, K Oleson, A Pitman, YC Sud, CM Taylor, D Verseghy, R Vasic, Y Xue, and T Yamada, "Regions of Strong Coupling Between Soil Moisture and Precipitation", Science, 305: 1138-1140, 2004.

Levine JB and Salvucci GD, "Equilibrium analysis of groundwater-vadose zone interactions and the resulting spatial distribution of hydrologic fluxes across a Canadian prairie", Water Resources Research, 35(5): 1369-1383, 1999.

Legg BJ, Long IF, Turbulent diffusion within a wheat canopy, II: results and interpretation. Quarterly Journal of the Royal Meteorological Society 101: 611–628, 1975.

Liang X, Xie Z, and Huang M, "A new parameterization for surface and groundwater interactions and its impact on water budgets with the variable infiltration capacity (VIC) land surface model", Journal of geophysical research, 108, NO. D16, 8613, doi:10.1029/2002JD003090, 2003.

Loague K, Heppner CS, Mirus BB, Ebel BA, Ran Q, Carr AE, BeVille SH, and VanderKwaak JE, "Physics-based hydrologic-response simulation: foundation for hydroecology and hydrogeomorphology", Hydrological Processes 20: 1231–1237, 2006.

Loague K and VanderKwaak JE, "Physics-based hydrologic response simulation: platinum bridge, 1958 Edsel, or useful tool", Hydrological Processes 18: 2949–2956, 2004.

Manabe, S., Climate and the ocean circulation. "The atmospheric circulation and hydrology of the Earth's surface", Monthly Weather Review: 97, 739–774, 1969.

Manabe S, Smagorin J, Holloway JL, and Stone HM, "Simulated climatology of a general circulation model with a hydrologic cycle", Monthly Weather Review 98(3): 175– 212, 1970.

Maxwell, R.M., "Coupled surface–subsurface modeling across a range of temporal and spatial scales", Vadose Zone Journal, 8(4):823–824, 2009.

Maxwell RM, Chow FK, Kollet SJ, "The groundwater-land-surface-atmosphere connection: Soil moisture effects on the atmospheric boundary layer in fully-coupled simulations", Advances in Water Resources, 30(12): 2447-2466, 2007.

Maxwell RM and Kollet SJ, "Interdependence of groundwater dynamics and land-energy feedbacks under climate change", Nature Geoscience, 1: 665-669, 2008a.

Maxwell RM and Kollet SJ, "Quantifying the effects of three-dimensional subsurface heterogeneity on Hortonian runoff processes using a coupled numerical, stochastic approach", Advances in Water Resources, 31: 807–817, 2008b.

Maxwell RM, Miller NL, “Development of a coupled land surface and groundwater model”, Journal of Hydrometeorology, 6(3): 233-247, 2005.

Monteith, J. L., “Evaporation and the environment, in: The State and Movement of Water in Living Organisms”, edited by: Fogg, G. E., 19th Symposium of the Society for Experimental Biology, University Press, Cambridge, 205–234, 1965.

Monteith JL, and Szeicz G, “Radiative temperature in the heat balance of natural surfaces”, Quarterly Journal of the Royal Meteorological Society 88: 496–507, 1962.

Morita, M., and Yen, B. C., “Modeling of conjunctive two-dimensional surface-three-dimensional subsurface flows”. Journal of Hydraulic Engineering, ASCE, 128(2):184–200, 2002.

Overgaard, J., Rosbjerg, D., and Butts, M. B., “Land-surface modelling in hydrological perspective – a review”, Biogeosciences: 3, 229–241, 2006.

Panday S. and Hyuakorn P. S., “A fully coupled physically-based spatially distributed model for evaluating surface/subsurface flow”, Advances in Water Resources: 27, 361–387, 2004.

Penman H. L., “Natural evaporation from open water, bare soil and grass”, Proceedings of the Royal Society of London A: 193, 120–146, 1948.

Pitman AJ and Henderson-Sellers A, “Simulating the diurnal temperature range: Results from Phase 1 (a) of the Project for Intercomparison of Landsurface Parameterization Schemes (PILPS)”, Atmospheric Research, 37: 229-245, 1995.

Qu Y and Duffy CJ, “A semidiscrete finite volume formulation for multiprocess watershed simulation”, Water Resources Research, 43: W08419, 2007.

Richards LA, “Capillary conduction of liquids through porous media”, Physics, 1: 318-33, 1931.

Salvucci GD and Entekhabi D, “Hillslope and climatic controls on hydrologic fluxes”, Water Resources Research, 31(7): 1725-1739, 1995.

Schaap MG, and Leij FJ, “Database-related accuracy and uncertainty of pedotransfer functions”, Soil Science, 163(10): 765-779, 1998.

Sellers PJ, Mintz Y, Sud YC, and Dalcher A, “A Simple Biosphere model (SiB) for use within general circulation models”, Journal of the Atmospheric Sciences 43: 505–531, 1986.

Seuffert G, Gross P, Simmer C, and Wood EF, “Influence of hydrologic modeling on the predicted local weather: two-way coupling of a mesoscale weather prediction model and a land surface hydrologic model”, Journal of Hydrometeorology, 3, 2002.

Sharman RD, Keller TL, and Wurtele MG, “Incompressible and anelastic flow simulations on numerically generated grids”, Monthly Weather Review, 116: 1124-1136, 1988.

Shawcroft, RW, ER Lemon, LH Allen Jr., DW Stewart and SE Jensen, "The soil-plant-atmosphere model and some of its predictions", Agricultural Meteorology, 14(1-2: 287-307, 1974.

Shuttleworth, W. J. and Wallace, J. S., "Evaporation from sparse crops – an energy combination theory", Quarterly Journal of the Royal Meteorological Society: 111, 839–855, 1985.

Stull, R. B., "An introduction to boundary layer meteorology". Boston: Kluwer Academic Publishers, 1988.

Sulis, M., Meyerhoff, S., Paniconi, C., Maxwell, R.M., Putti, M., Kollet, S.J., "A comparison of two physics-based numerical models for simulating surface water–groundwater interactions", Advances in Water Resources, doi: 10.1016/j.advwatres.2010.01.010, 2010.

Sullivan, P. P., Moeng, C. H., Stevens, B., Lenschow, D. H., and Mayor, S. D., "Structure of the entrainment zone capping the convective atmospheric boundary layer". Journal of the Atmospheric Sciences, 55: 3042–3064, 1998.

Taylor CM, and Lebel T, "Observational Evidence of Persistent Convective-Scale Rainfall Patterns", Monthly Weather Review, 126: 1597-1607, 1998.

Therrien R, McLaren RG, Sudicky EA, Panday SM, "HydroGeoSphere: A Three-Dimensional Numerical Model Describing Fully-Integrated Subsurface and Surface Flow and Solute Transport", Groundwater Simulations Group, University of Waterloo: Waterloo, 322, 2005.

Thom AS, "Momentum, mass and heat exchange of vegetation", Quarterly Journal of the Royal Meteorological Society 98: 124–134, 1972.

Toth J, "A Theoretical Analysis of Groundwater Flow in Small Drainage basins", Journal of Geophysical Research, 68(16): 4795-4812, 1963.

Van Genuchten, "A closed-form equation for predicting the hydraulic conductivity of unsaturated soils", Soil Science Society of America Journal 44:892–898, 1980.

VanderKwaak JE, "Numerical simulation of flow and chemical transport in integrated surface-subsurface hydrologic systems", PhD Dissertation, University of Waterloo, Waterloo, 217, 1999.

VanderKwaak, J.E., and Loague, K., "Hydrologic-response simulations for the R-5 catchment with a comprehensive physics-based model", Water Resources Research, 37:999–1013, 2001.

Waggoner, PE, GM Furnival, WE Reifsnyder, "Simulation of the microclimate in a forest", Forest Science, Volume 15(1): pp. 37-45(9), 1969.

Xue M, Droegemeier KK, and Wong V, "The advanced regional prediction system (ARPS) – A multi-scale nonhydrostatic atmospheric simulation and prediction model. Part I: Model dynamics and verification", Meteorology and Atmospheric Physics, 75: 161-193, 2000.

Xue M, Droegemeier KK, Wong V, Shapiro A, Brewster K, Carr F, Weber D, Liu Y, and Wang D, "The advanced regional prediction system (ARPS) – A multi-scale nonhydrostatic atmospheric simulation and prediction tool. Part II: Model physics and applications", Meteorology and Atmospheric Physics, 76: 143-165, 2001.

Yang ZL, Dickinson RE, Henderson-Sellers A and Pitman AJ, "Preliminary study of spin-up processes in land surface models with the first stage data of Project for Intercomparison of Land Surface Parameterization Schemes Phase 1(a)", Journal of Geophysical Research 100(D8): 16,553-16,578, 1995.

Yeh PJ and Eltahir EAB, "Representation of Water Table Dynamics in a Land Surface Scheme. Part I: Model Development", Journal of Climate, 18:1861-1880, 2005.

York PJ, Person M, Gutowski WJ, Winter TC, "Putting aquifers into atmospheric simulation models: an example from the Mill Creek Watershed, northeastern Kansas", Advances in Water Resources, 25: 221-238, 2002.

# Appendix A

## PF.CLM Governing Equations

The governing equations for the coupled code include mass and energy balance at the land surface and mass balance in the subsurface (Kollet and Maxwell, 2006 and 2008). The mass balance for both surface and subsurface is solved by ParFlow while the energy balance at the land surface is solved by CLM. The full set of equations is presented briefly here for completeness.

**Surface and Subsurface Mass Balance:** In this formulation, the surface water equations are implemented as a boundary condition to the subsurface governing equation. The subsurface mass balance can be expressed by the three-dimensional Richards' equation (Richards, 1931):

$$S_s S_w \frac{\partial \psi_p}{\partial t} + \phi \frac{\partial S_w(\psi_p)}{\partial t} = \nabla \cdot q + q_s + \frac{q_e}{m'} \qquad \text{(A.1)}$$

where $S_s$ is the specific storage [$m^{-1}$], $S_w$ is the relative saturation [-], $\psi_p$ is the soil pressure head [m], t is time [s], $\phi$ is the porosity [-], q is the water flux [m/s], and $q_s$ is a general source/sink term [$T^{-1}$], $q_e$ is the exchange rate with the land surface [L/T], and m' is the thickness of an interface separating the surface and subsurface [L]. If the change in vertical momentum is neglected, the two dimensional conservation of mass at the land surface can be expressed as (Kollet and Maxwell, 2006):

$$\frac{\partial \psi_s}{\partial t} = \nabla \bullet \vec{v} \psi_s + q_r(x) + q_e(x) \qquad \text{(A.2)}$$

where t is time [T], $\psi_s$ is the ponding depth of water at the land surface [L], $\vec{v}$ is the depth averaged surface water velocity [L/T], $q_r$ is the source/sink rate (i.e. rainfall/evaporation) [L/T], and $q_e$ is the surface-subsurface water exchange rate [L/T]. The coupling in surface-subsurface integrated models occurs through the surface-subsurface water exchange rate ($q_e$ in equations 1 and 2). Specifying this exchange rate is the main problem being solved in these integrated models and therefore forms the main difference between the first-order exchange coefficient approach and the surface-subsurface continuity of pressure and flux boundary condition.
The water flux, q, in equation 1 can be expressed using unsaturated Darcy's law as:

$$q = -k(x) k_r(\psi) \nabla(\psi - z) \qquad \text{(A.3)}$$

where k is the saturated hydraulic conductivity [L/T], $k_r$ is the relative permeability [-], and z is depth below the land surface [L]. The Van Genuchten formulation is used here to relate relative (unsaturated) permeability, $k_r$ [-] and relative saturation, $S_w$ [-], to the subsurface pressure head, $\psi_p$ [L], as follows (Van Genuchten, 1980):

$$S_w(\psi_p) = \frac{S_{sat} - S_{res}}{(1 + (\alpha\psi_p)^n)^{(1-1/n)}} + S_{res} \tag{A.4}$$

$$k_r(\psi_p) = \frac{\left(1 - \frac{(\alpha\psi_p)^{(n-1)}}{(1 + (\alpha\psi_p)^n)^{(1-1/n)}}\right)^2}{(1 + (\alpha\psi_p)^n)^{\frac{(1-1/n)}{2}}} \tag{A.5}$$

where $\alpha$ [$L^{-1}$] and $n$ [-] are the Van Genuchten soil parameters, $S_{sat}$ [-] is the saturation at saturated conditions and $S_{res}$ [-] is the residual saturation. $S_{res}$ ranges from zero (for completely dry soil) to one (for fully saturated soil) while $S_{sat}$ has the value of one. Neumann boundary conditions are applied:

$$-k(x)k_r\nabla(\psi_p - z) = q_{bc} \tag{A.6}$$

The overland flow equations can be implemented into the Richards equation by applying the assumption of pressure and flux continuity at the land surface which basically states that the surface and subsurface pressures and fluxes are equal at the land surface. Thus, the conservation of mass (equation 2) can be solved for $q_e$ using the continuity of pressure ($\psi_s=\psi_p=\psi$) at the land surface:

$$q_e(x) = \frac{\partial \|\psi,0\|}{\partial t} - \nabla \bullet \left(\vec{v}\ \|\psi,0\|\right) - q_r(x) \tag{A.7}$$

where $\|\psi,0\|$ is the greater of $\psi$ and 0. Applying continuity of flux ($q_{bc} = q_e$) at the land surface and substituting for $q_{bc}$ in equation 6 gives:

$$-k(x)k_r\nabla(\psi_p - z) = \frac{\partial \|\psi,0\|}{\partial t} - \nabla\vec{v}\ \|\psi,0\| - q_r(x) \tag{A.8}$$

Equation 8 represents the new head-dependent boundary condition, which now accounts for the exchange flux, $q_e$, and simultaneously describes the surface and subsurface domains at the land surface. This new formulation accounts for movement of ponded water at the ground surface and removes the need to apply first order exchange coefficients to describe the exchange flux $q_e$. The Richard's equation (1) can now be expressed as (Kollet and Maxwell, 2006):

$$S_s S_w \frac{\partial \psi_p}{\partial t} + \phi \frac{\partial S_w}{\partial t} = \nabla.[k(x)k_r(\psi)\nabla(\psi - z)] + q_s \tag{A.9}$$

**Land Surface Energy Balance**: The energy balance at the land surface, as provided by CLM, is a function of soil moisture and can be expressed as (Maxwell and Miller, 2005; Kollet and Maxwell, 2008; Kollet et al, 2009):

$$Rn(\theta) = H(\theta) + LE(\theta) + G(\theta) \quad \text{(A.10)}$$

Where Rn is net radiation [W/m$^2$], $\theta$ is the soil moisture at the land surface [kg/kg] estimated by ($S_w$*$\phi$), H is the sensible heat flux [W/m$^2$], LE is latent heat flux [W/m$^2$], and G is ground heat flux [W/m$^2$]. Sensible heat flux includes heat flux from the canopy [$H_c$] and the ground [$H_g$] which are expressed as:

$$H = H_c + H_g \quad \text{(A.11)}$$

$$H_c = \sigma_f \; L_{SAI} \; \rho_a \; c_p \; r_b \; (T_c - T_{af}) \quad \text{(A.12)}$$

$$H_g = \sigma_f \; \rho_a \; c_p \; C_{soilc} u_{af} \; (T_g - T_{af}) \quad \text{(A.13)}$$

Where $\sigma_f$ is the vegetation fraction [-], $L_{SAI}$ is the stem plus leaf area index [m$^2$/m$^2$], $\rho_a$ is the intrinsic density of air [kg/m$^3$], $c_p$ is the specific heat of dry air [J/kg.K$^2$], $r_b$ is the leaf boundary resistance [s/m], $C_{soilc}$ is the transfer coefficient between the canopy air and underlying ground, $u_{af}$ is the magnitude of the wind velocity incident on the leaves [-], $T_c$ is the leaf temperature [K], $T_g$ is the ground surface temperature [K], and $T_{af}$ is the air temperature in the canopy space [K].
The latent heat flux is expressed as: LE = $L_v$E where $L_v$ is the latent heat of evaporation [J/kg] and E is the sum of the evaporation from the canopy, Ec [kg/m$^2$s] and from the ground, Eg [kg/m$^2$s]:

$$E = E_c + E_g \quad \text{(A.14)}$$

$$E_g = \rho_a \frac{(q_g - q_a)}{r_d} \quad \text{(A.15)}$$

where $\rho_a$ is the intrinsic density of air [kg/m$^3$], $q_g$ is the specific humidity of air at the ground surface [kg/kg], $q_a$ is the specific humidity of air at reference height $z_q$ obtained from atmospheric forcing [kg/kg], and $r_d$ is the aerodynamic resistance of evaporation between the atmosphere at $z_q$ [s/m]. Evaporation from the canopy ($E_c$) is the sum of evaporation from wet foliage $E_w$ [kg/m$^2$s] and transpiration $E_{tr}$ [kg/m$^2$s]:

$$E_c = E_w + E_{tr} \quad \text{(A.16)}$$

Where:

$$E_{tr} = \sigma_f \; L_{SAI} \; \delta(E_f^{pot}) L_d \frac{r_b}{r_b + r_s} \quad \text{(A.17)}$$

$$E_w = \sigma_f \; L_{SAI} \; \left[1 - \delta(E_f^{pot})(1 - \tilde{L}_w)\right] \; E_f^{pot} \quad \text{(A.18)}$$

$\sigma_f$ is the vegetation fraction [-], $\delta$ is the step function ($\delta$=1 for positive arguments and $\delta$=0 for zero and negative arguments), $E_f^{pot}$ is the potential evaporation from wet foliage [kg/m$^2$s], $L_d$ is

the dry fraction of foliage surface [-], $r_b$ is the conductance of heat and vapor flux from leaves [s/m], $r_s$ is the stomatal resistance [s/m], and $\widetilde{L}_w$ is the wetted fraction of the canopy [-]. The ground heat flux, G, is expressed by the one dimensional transient heat conduction equation:

$$G = \lambda \Delta T \tag{A.19}$$

where λ is the soil thermal conductivity [W/mK], and T is subsurface temperature [K].
Finally, the net radiation (Rn) is expressed as:

$$R_n = S_{n,c} + S_{n,g} + L_a^{\downarrow} - L^{\uparrow} \tag{A.20}$$

where $S_{n,c}$ is the solar radiation absorbed by vegetation [W/m$^2$], $S_{n,g}$ is the solar radiation adsorbed by the ground [W/m$^2$], $L_a^{\downarrow}$ is the incoming atmospheric long wave radiation [W/m$^2$], $L^{\uparrow}$ is the outgoing long wave radiation [W/m$^2$]. These terms are obtained by the following expressions:

$$S_{n,c} = \sigma_f \sum_{\Lambda,\mu} F_{\Lambda,\mu} \; S_{\Lambda,\mu}^{\downarrow} \tag{A.21}$$

$$S_{n,g} = S_n - S_{n,c} \tag{A.22}$$

$$S_n = \sum_{\Lambda,\mu} (1 - \overline{\alpha}_{\Lambda,\mu}) \; S_{\Lambda,\mu}^{\downarrow} \tag{A.23}$$

where $S_{n,c}$ is the net solar radiation absorbed by the canopy [W/m$^2$], $F_{\Lambda,\mu}$ is the fraction of solar radiation absorbed by canopy [-], and $S_{\Lambda,\mu}^{\downarrow}$ is the component of the incident solar radiation visible (beam and diffuse) and near-infrared (beam and diffuse) [W/m$^2$], $S_n$ is the net solar radiation absorbed by the land surface [W/m$^2$], $S_{n,g}$ is the net solar radiation absorbed by the ground [W/m$^2$], and $\overline{\alpha}_{\Lambda,\mu}$ is the weighted surface albedo over the grid [-].
The coupling between CLM and ParFlow is maintained through the source/sink term in the Richard's equation ($q_s$ in equations 1 and 9) and the dependence of energy variables in equation 10 on soil moisture θ. The source/sink term $q_s$ is expressed as:

$$q_s = LE(\theta) + q_g \tag{A.24}$$

where $q_g$ [s$^{-1}$] is the flux of water infiltrating at the land surface due to precipitation and canopy throughfall and/or surface runoff. It should be noted that $q_g$ here is specifically the total throughfall and not explicitly runoff or infiltration. Once water hits the ground, the overland flow formulation in ParFlow takes over and divides the throughfall into either infiltration or overland flow. A more extensive explanation of the coupling in PF.CLM can be found in Maxwell and Miller (2005), and Kollet and Maxwell (2008).

# Appendix B

## ARPS Governing Equations

The governing equations for the nonhydrostatic atmospheric prediction model ARPS consist of a fully compressible system of equations solved using the split-explicit time integration method. These include the conservation equations of six entities: momentum, heat, mass, total water substance (water vapor, liquid and ice), turbulent kinetic energy (TKE), and the equation of state of moist air. For the ARPS system, potential temperature is used instead of temperature for the conservation of adiabatic processes. The original Navier-Stokes equations (Batchelor, 1967) are used to predict the pressure gradient force. Once potential temperature and pressure are predicted, density can be diagnosed using the equation of state (Xue et al. 2001).

A full derivation of the equations presented here and a description of the ARPS system can be found in Xue et al. 2000 and 2001. The ARPS governing equations are first written using a Cartesian coordinate system (*x,y,z*) and then transformed to a curvilinear terrain-following coordinate system ($\xi,\eta,\zeta$) which allows grid stretching in the vertical direction. In the following equations, the dot operator denotes total time derivative (e.g. $\dot{u} = du/dt$), and partial temporal or spatial derivatives are denoted by subscripts *t, x, y, z,* $\xi$, $\eta$, and $\zeta$. If the ellipticity of the earth is neglected, the following equations of motion can be obtained (Haltiner and Williams, 1980):

$$\dot{u} = -mp_x\rho^{-1} + (f + f_m)v - \tilde{f}w - uwa^{-1} + F_u \qquad \text{(Equation B1)}$$

$$\dot{v} = -mp_y\rho^{-1} - (f + f_m)u - vwa^{-1} + F_v \qquad \text{(Equation B2)}$$

$$\dot{w} = -p_z\rho^{-1} - g + \tilde{f}u + (u^2 + v^2)a^{-1} + F_w \qquad \text{(Equation B3)}$$

where *m* is the map projection factor, *p* is the total pressure, $\rho$ is the total density, $f$ and $\tilde{f}$ are the Coriolis parameter ( $f = 2\Omega\sin(\phi)$ and $\tilde{f} = 2\Omega\cos(\phi)$, where $\Omega$ is the angular rotation of the earth and $\phi$ is the earth latitude), *F* represents frictional forces, and *g* is the acceleration due to gravity. These equations assume a thin atmosphere such that the radius is replaced by the mean earth radius at sea level (*a*). The equations of state for moist air, mass continuity, heat energy conservation, and conservation of hydrometeor species are, respectively,

$$\rho = p(R_dT)^{-1}[1 - q_v(\gamma + q_v)^{-1}](1 + q_v + q_{li}) \qquad \text{(Equation B4)}$$

$$\dot{\rho} = -\rho\{m^2[(u/m)_x + (v/m)_y] + w_z\} \qquad \text{(Equation B5)}$$

$$\dot{\theta} = \dot{Q}(C_p \pi)^{-1} \qquad \text{(Equation B6)}$$

$$\dot{q} = S_q \qquad \text{(Equation B7)}$$

where $R_d$ is the gas constant for dry air (J/kgK), $T$ is the total temperature (K), $q_v$ is the water vapor mixing ratio (kg/kg), $\gamma = R_d/R_v$, $R_v$ is the gas constant for water vapor (J/kgK), $q_{li}$ is the total liquid and ice water mixing ratio (kg/kg), $\theta$ is total potential temperature (K), $C_p$ is the specific heat of dry air at constant pressure (J/kgK), $\pi = (p / p_0)^{Rd/Cp}$, $\dot{Q}$ and $S_q$ are sources of heat and moisture, respectively (Xue et al. 2000). The curvilinear coordinate system used to write ARPS prognostic equations is defined as:

$$\begin{aligned} \xi &= \xi(x) \\ \eta &= \eta(y) \\ \zeta &= \zeta(x,y,z) \end{aligned} \qquad \text{(Equation B8)}$$

Because the constant surfaces of $\xi$ and $\eta$ remain parallel to the constant $x$ and $y$ surfaces, this system is a special case of the fully three-dimensional curvilinear system. This transformation allows a domain with an irregular lower boundary (terrain) to be mapped onto a regular rectangular domain. Cartesian velocity components ($u$,$v$,$w$) are used as dependent variables. These can be transformed into contravariant velocity components ($U^c$,$V^c$,$W^c$) as (Sharman et al. 1988):

$$\begin{aligned} U^c &= uJ_3/\sqrt{G} = u/x_\xi \\ V^c &= vJ_4/\sqrt{G} = v/y_\eta \\ W^c &= (uJ_1 + vJ_2 + wx_\xi y_\eta)/\sqrt{G} \end{aligned} \qquad \text{(Equation B9)}$$

where $x_\xi$ and $y_\eta$ are grid stretching factors in the $x$ and $y$ directions. $J_1$, $J_2$, $J_3$, and $J_4$ are Jacobians of transformation and $\sqrt{G}$ is the determinant of the Jacobian matrix of transformation from the curvilinear system to the cartesian system. These are expressed as follows:

$$\begin{aligned} &J_1 = -z_\xi y_\eta, \qquad J_2 = -z_\eta x_\xi, \qquad J_3 = -z_\zeta y_\eta, \\ &J_4 = -z_\zeta x_\xi, \qquad \textit{and} \qquad \sqrt{G} = z_\zeta x_\xi y_\eta \end{aligned} \qquad \text{(Equation B10)}$$

In ARPS, atmospheric state variables and wind components are defined as the sum of a base (or reference) state and a deviation from the base state:

$$\varphi = \bar{\varphi}(z) + \varphi' \qquad \text{(Equation B11)}$$

The base state is assumed to be horizontally homogeneous (i.e. a function of z only) to avoid large cancellation errors associated with the explicit evaluation of its horizontal gradient in the curvilinear coordinate system. According to Xue et al. (2000), the choice of base state has a small effect on the final solution if high-order perturbations terms are retained. The base state must satisfy the hydrostatic relation:

$$\bar{p}_z = -\bar{\rho} g \qquad \text{(Equation B12)}$$

where $\bar{\rho}$ is the base-state density. The final governing equations are obtained by transforming equations B1 through B7 from Cartesian to curvilinear coordinates, in addition to the equation for sub-grid scale turbulent kinetic energy (TKE):

$$\begin{aligned}(\rho^* u)_t + m\bar{\rho}\rho^{-1}\{[J_3(p' - \alpha_\xi Div^*)]_\xi + [J_1(p' - \alpha_\xi Div^*)]_\zeta\} = \\ -ADV(u) + \rho^*(f + f_m)v - \tilde{f}w - uwa^{-1} + \sqrt{G}D_u\end{aligned} \qquad \text{(Equation B13)}$$

$$\begin{aligned}(\rho^* v)_t + m\bar{\rho}\rho^{-1}\{[J_4(p' - \alpha_\eta Div^*)]_\eta + [J_2(p' - \alpha_\eta Div^*)]_\zeta\} = \\ -ADV(v) - \rho^*(f + f_m)u - vwa^{-1} + \sqrt{G}D_v\end{aligned} \qquad \text{(Equation B14)}$$

$$\begin{aligned}(\rho^* w)_t + \bar{\rho}\rho^{-1}\{[x_\xi y_\eta (p' - \alpha_\zeta Div^*)]_\zeta + g\bar{\rho}\rho^{-1}\rho^*[p'(\gamma\bar{p})^{-1} - \theta'\bar{\theta}^{-1}]_\zeta\} \\ = -ADV(w) + g\bar{\rho}\rho^{-1}\rho^* B' + \rho^*\tilde{f}u + (u^2 + v^2)a^{-1} + \sqrt{G}D_w\end{aligned} \qquad \text{(Equation B15)}$$

$$\begin{aligned}(\sqrt{G}p')_t - \sqrt{G}\bar{\rho}gw + \rho c_s^2\{m^2[(\sqrt{G}U^c m^{-1})_\xi + (\sqrt{G}V^c m^{-1})_\eta + \\ (\sqrt{G}W^c)_\zeta]\} = -\{m[\sqrt{G}U^c p'_\xi + \sqrt{G}V^c p'_\eta + \sqrt{G}W^c p'_\zeta]\} + \\ \sqrt{G}\bar{\rho}c_s^2[\dot{\theta}\theta^{-1} + \dot{A}A^{-1}]\end{aligned} \qquad \text{(Equation B16)}$$

$$(\rho^*\theta')_t + \rho^* w\bar{\theta}_x = -ADV(\theta') + \sqrt{G}D_\theta + \sqrt{G}S_\theta \qquad \text{(Equation B17)}$$

$$(\rho^* q)_t = -ADV(q) + (\rho^* V_q q / z_\zeta)_\zeta + \sqrt{G} D_q + \sqrt{G} S_q \qquad \text{(Equation B18)}$$

$$(\rho^* E)_t = -ADV(E) + C + \rho^* [K_m |Def|^2 - 2/3 EDiv] - \rho^* C_\varepsilon l^{-1} E^{3/2} + 2\sqrt{G} D_E \qquad \text{(Equation B19)}$$

Where $c_s = (\gamma RT)^{1/2}$ is the full acoustic wave speed (m/s), $D_{ij}$ are deformation tensors ($s^{-1}$), $A = 1 + 0.61 q_v + q_{li}$, $E$ is the turbulent kinetic energy (TKE), $|Def|$ is the magnitude of the 3-D deformation, $C_\varepsilon$ =^ 3.9 at the lowest model level and 0.93 at other levels (Xue et al. 2000), and:

$$\rho^* = \bar{\rho}\sqrt{G}, \qquad U^* = \rho^* U^c,$$
$$V^* = \rho^* V^c, \qquad W^* = \rho^* W^c \qquad \text{(Equation B20)}$$

The advection operator ADV($\phi$) and the density weighted divergence Div$^*$ are defined as:

$$ADV(\phi) = m[U^* \phi_\xi + V^* \phi_\eta] + W^* \phi_\zeta = m^2 [(U^* \phi m^{-1})_\xi + (V^* \phi m^{-1})_\eta] + (W^* \phi)_\zeta - \phi \sqrt{G} Div^* \qquad \text{(Equation B21)}$$

$$Div^* = \nabla \cdot (\bar{\rho}\vec{V}) = 1/\sqrt{G} \{m^2 [(U^* m^{-1})_\xi + (V^* m^{-1})_\eta + W_\zeta^*]\} \qquad \text{(Equation B22)}$$

While Div in equation B20 is defined as $\nabla \cdot \vec{V}$.

# Appendix C

## Little Washita Simulation Results

This appendix contains extra results and comparisons from the Little Washita simulation cases than those presented in Chapter 4. The results included here show comparisons to observed soundings at Norman sounding station (Figures C1 through C6), snapshots of total rainfall and cloud water mixing ratio for the second (Figure C7), third (Figure C8), and fourth (Figure C9) rainfall events, and differences in total rainfall between the three simulation cases during the fourth simulation cases (Figures C10 and C11).

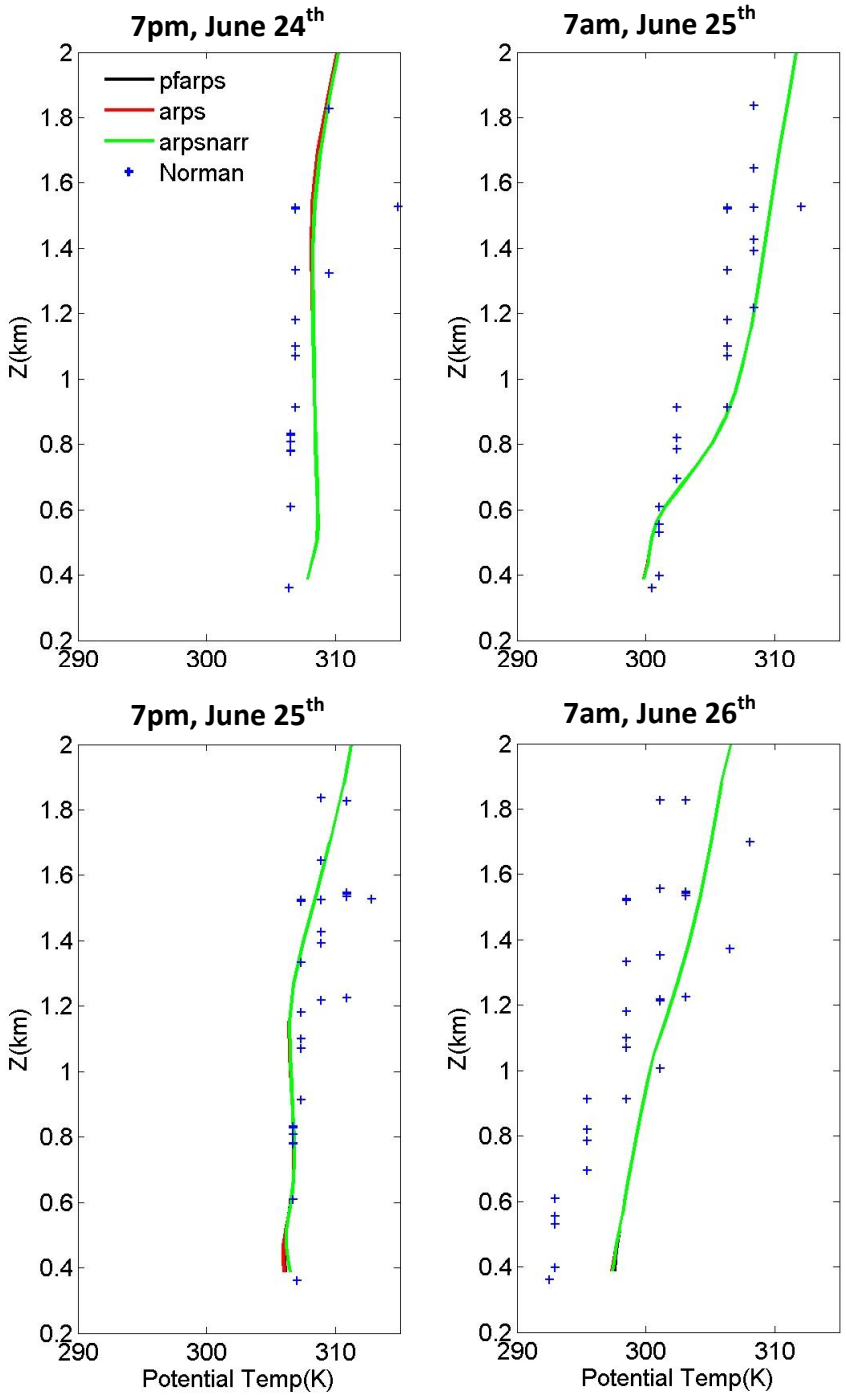


**Figure C1**: Potential Temperature sounding profiles for the first two days of simulation, extracted at x=15km and y=15km. Observed soundings at the Norman station near the watershed are also shown.

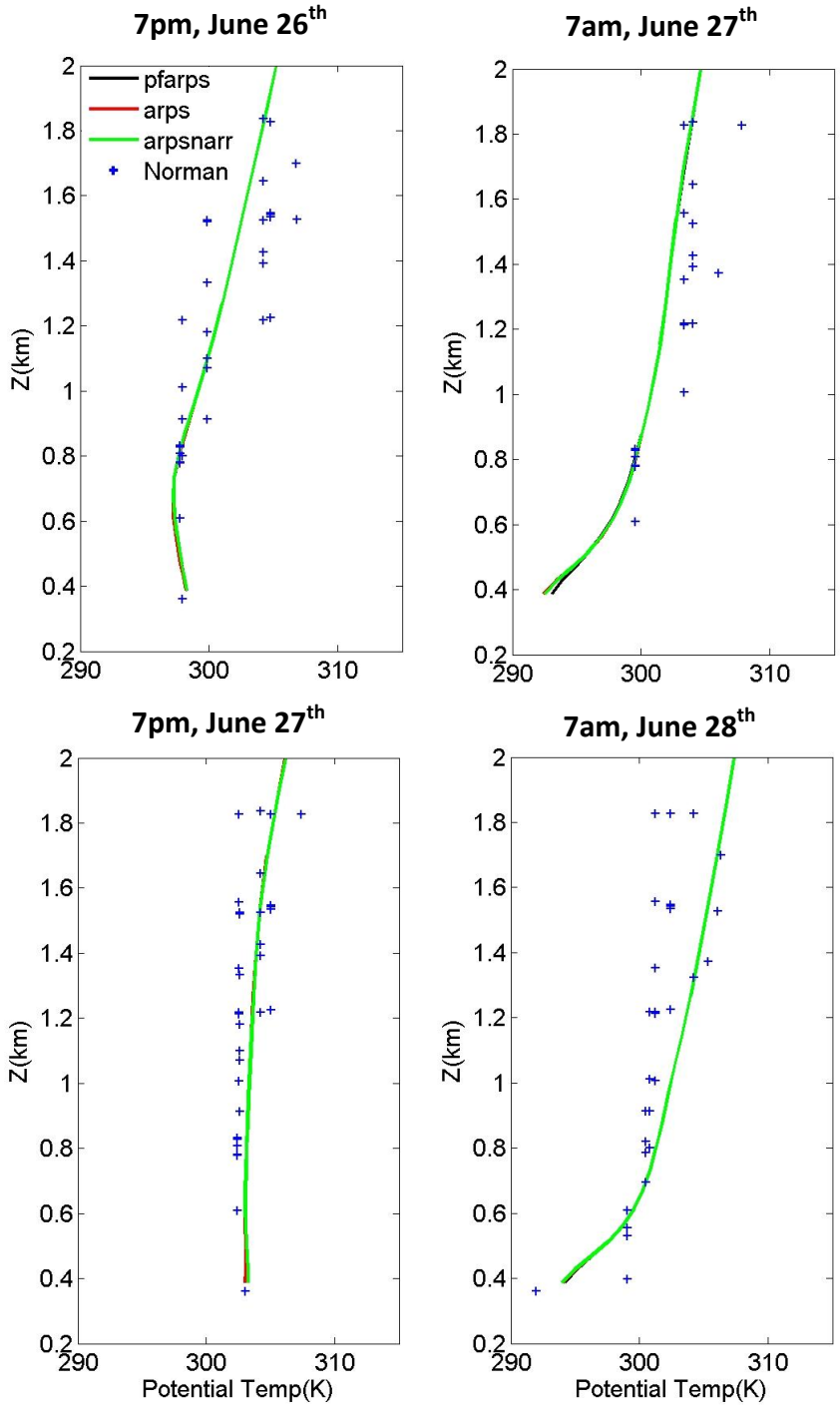


**Figure C2**: Potential Temperature sounding profiles for the third and fourth days of simulation, extracted at x=15km and y=15km. Observed soundings at the Norman station near the watershed are also shown.

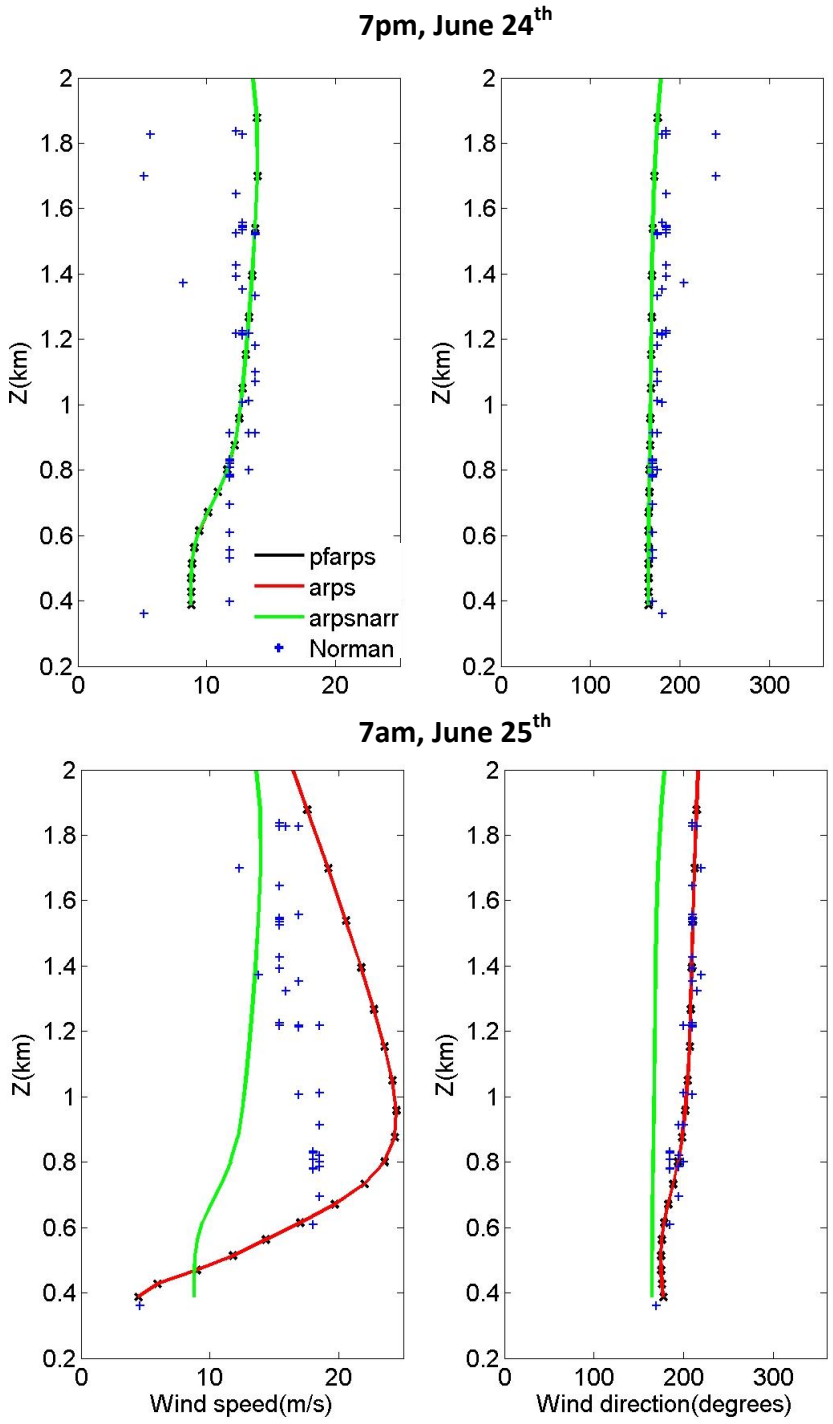


**Figure C3**: Wind speed and direction sounding profiles for the first day of simulation, extracted at x=15km and y=15km. Observed soundings at the Norman station near the watershed are also shown.

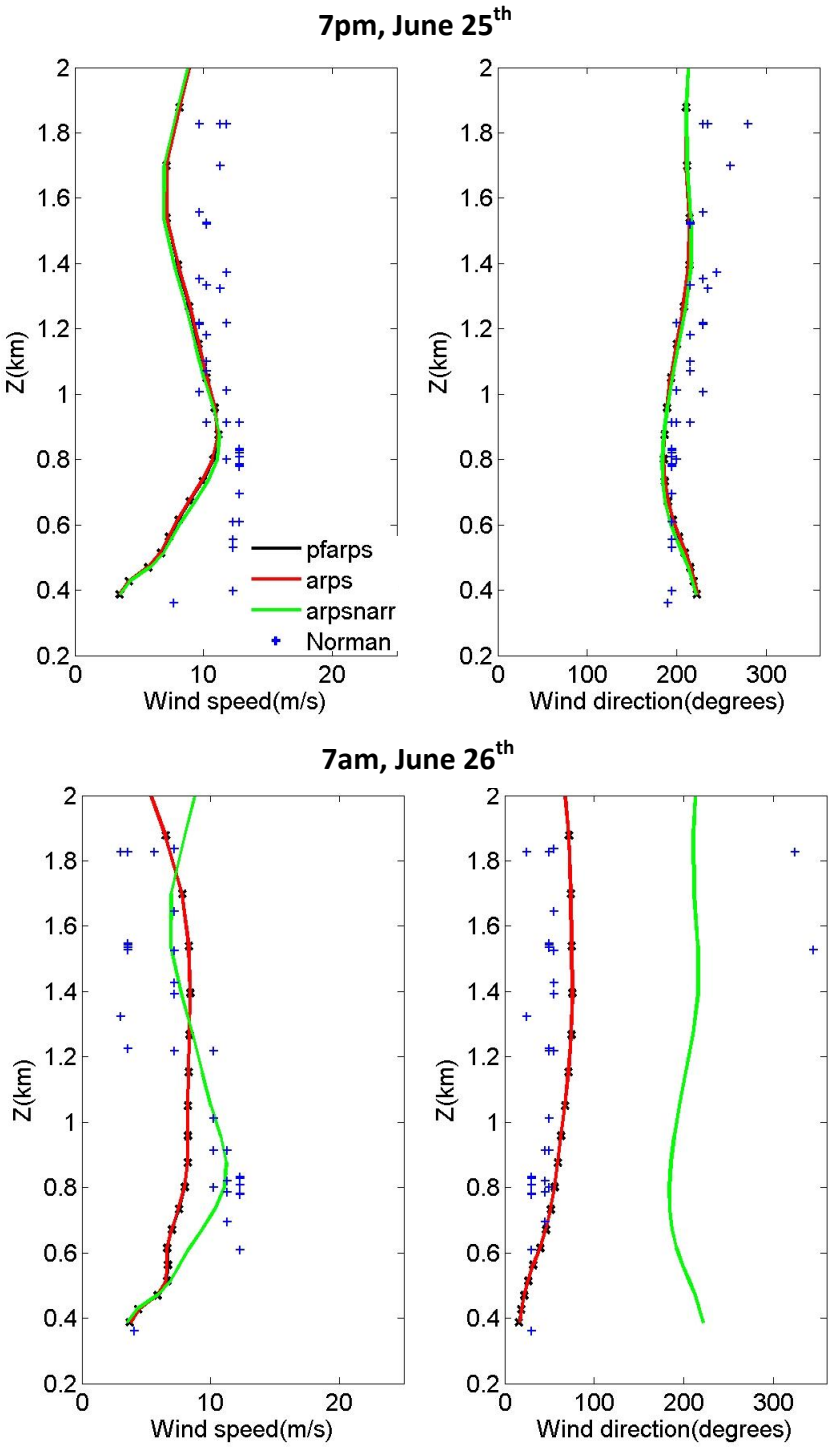


**Figure C4**: Wind speed and direction sounding profiles for the second day of simulation, extracted at x=15km and y=15km. Observed soundings at the Norman station near the watershed are also shown.

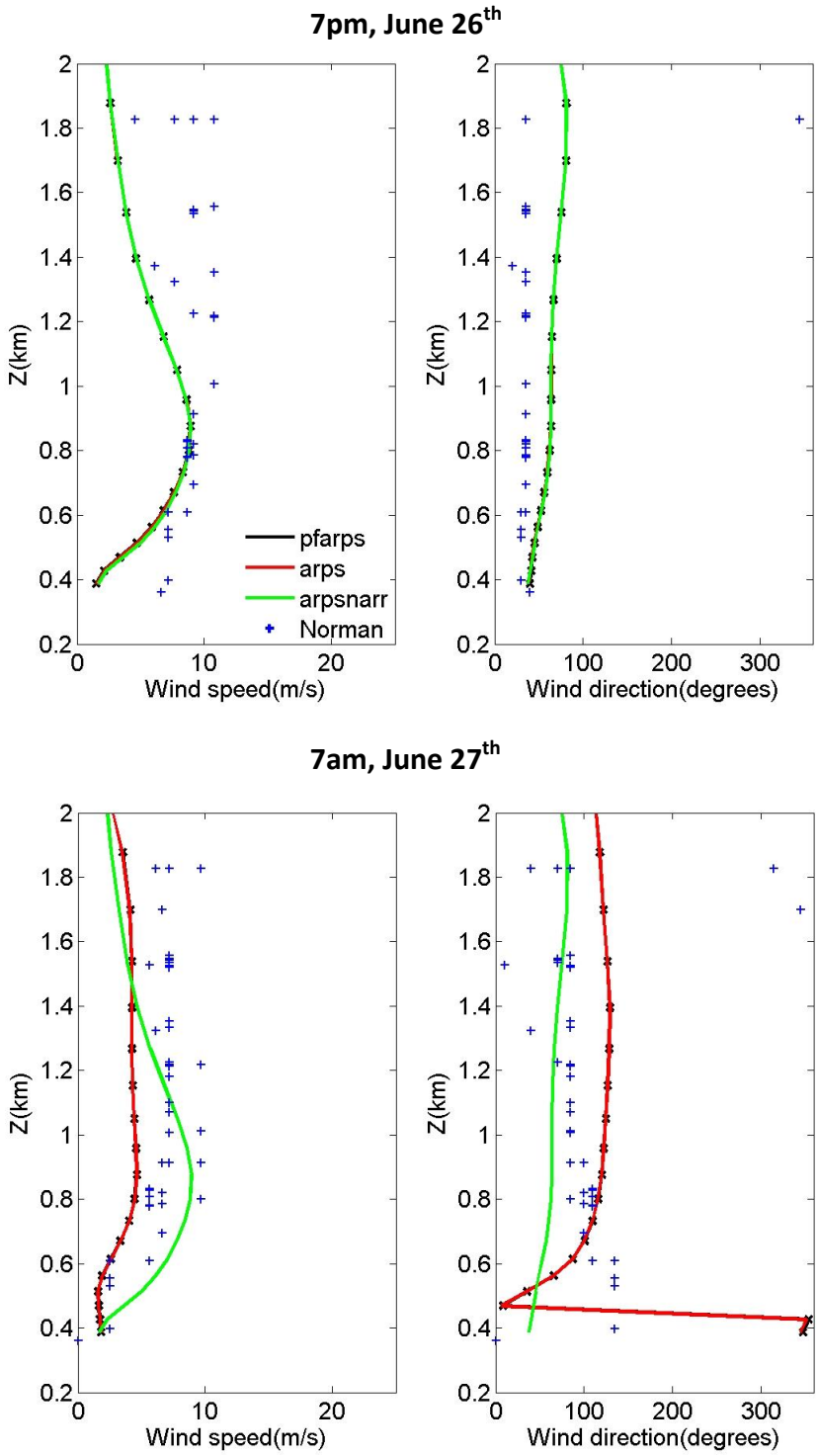


**Figure C5**: Wind speed and direction sounding profiles for the third day of simulation, extracted at x=15km and y=15km. Observed soundings at the Norman station near the watershed are also shown.

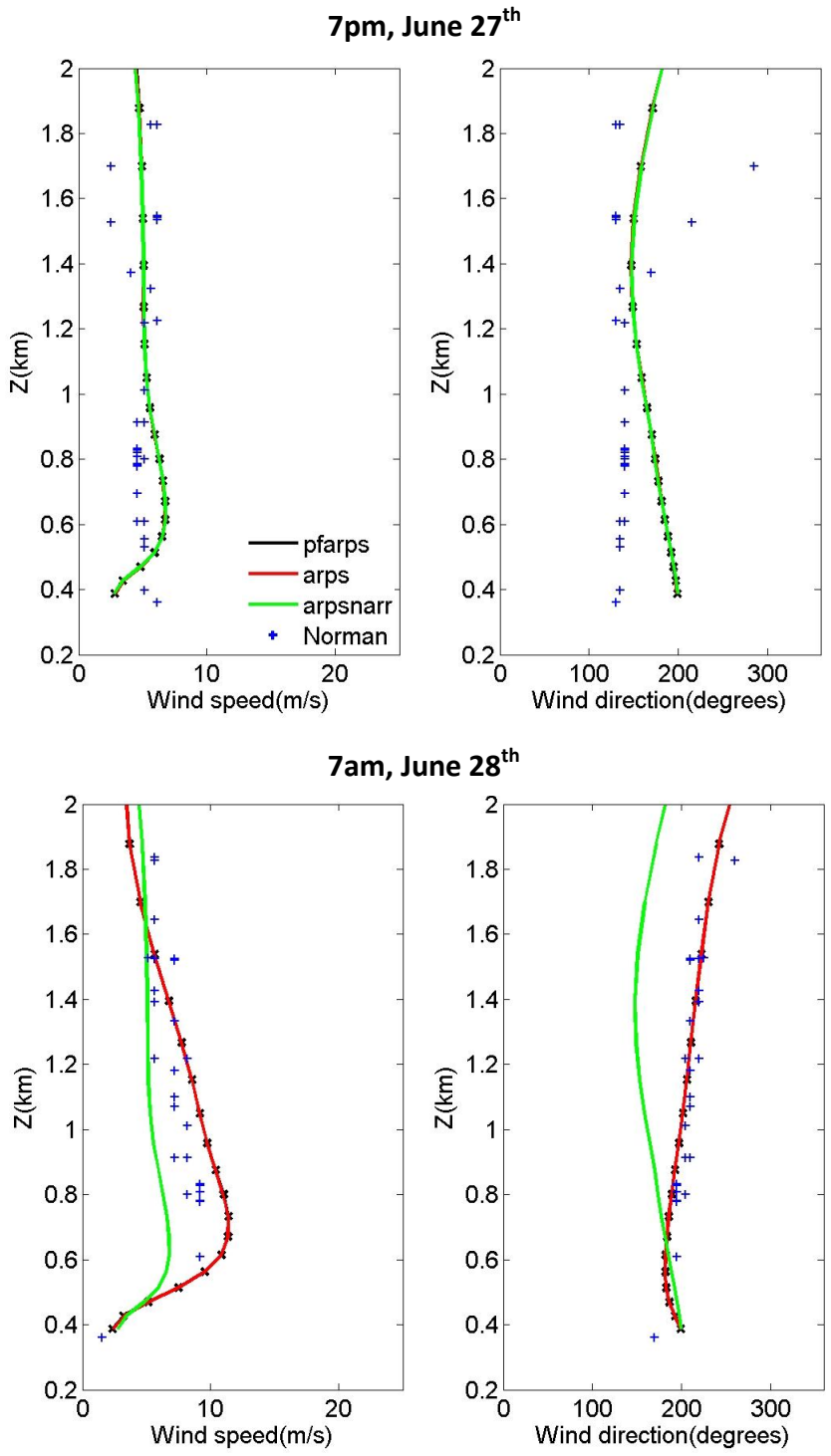


**Figure C6**: Wind speed and direction sounding profiles for the fourh day of simulation, extracted at x=15km and y=15km. Observed soundings at the Norman station near the watershed are also shown.

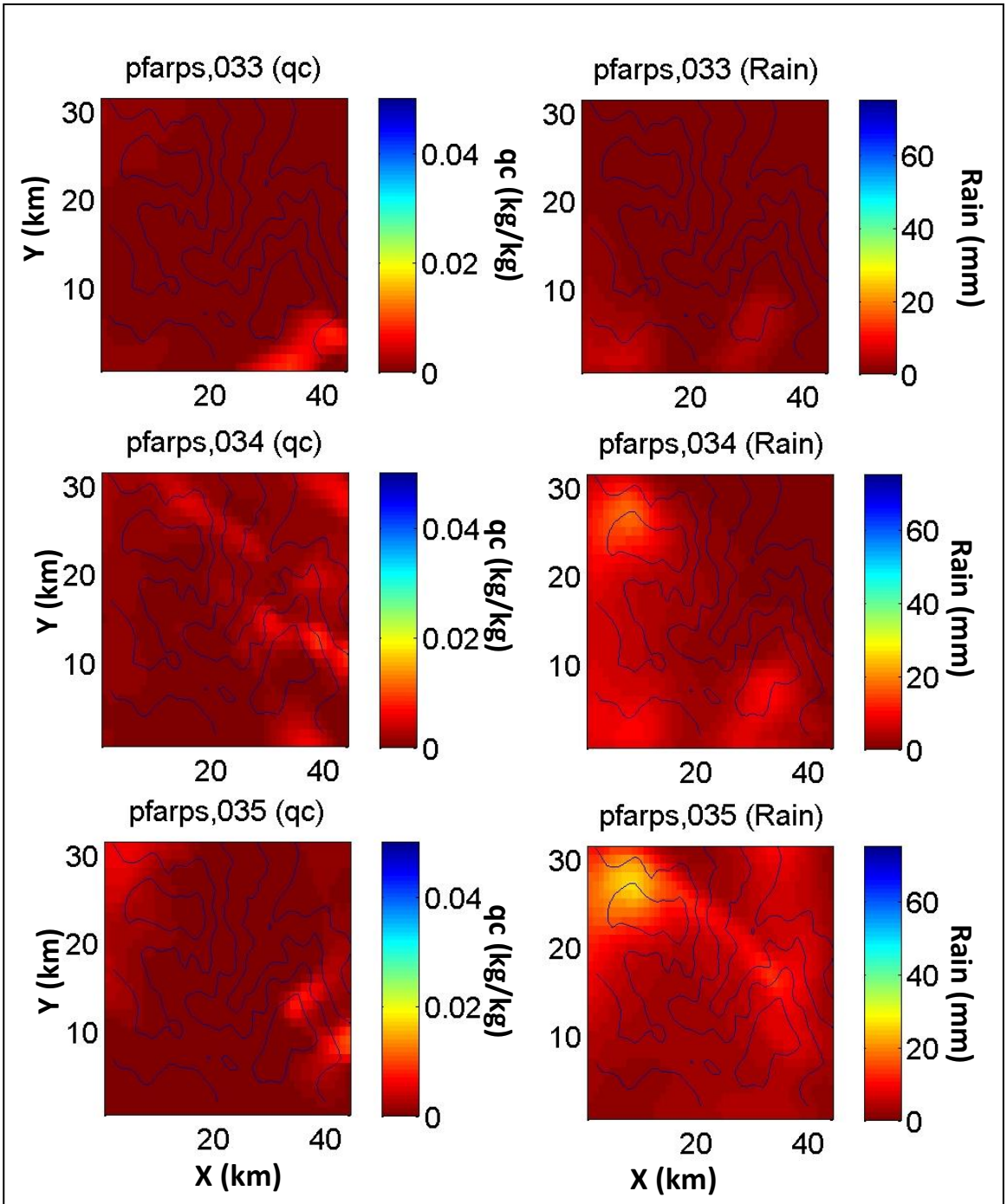


**Figure C7**: Cloud water mixing ratio (qc) and hourly rainfall for the pfarps simulation case at 4, 5, and 6 am on June 26th (33, 34, and 35 hours of simulation). Contour lines show terrain.

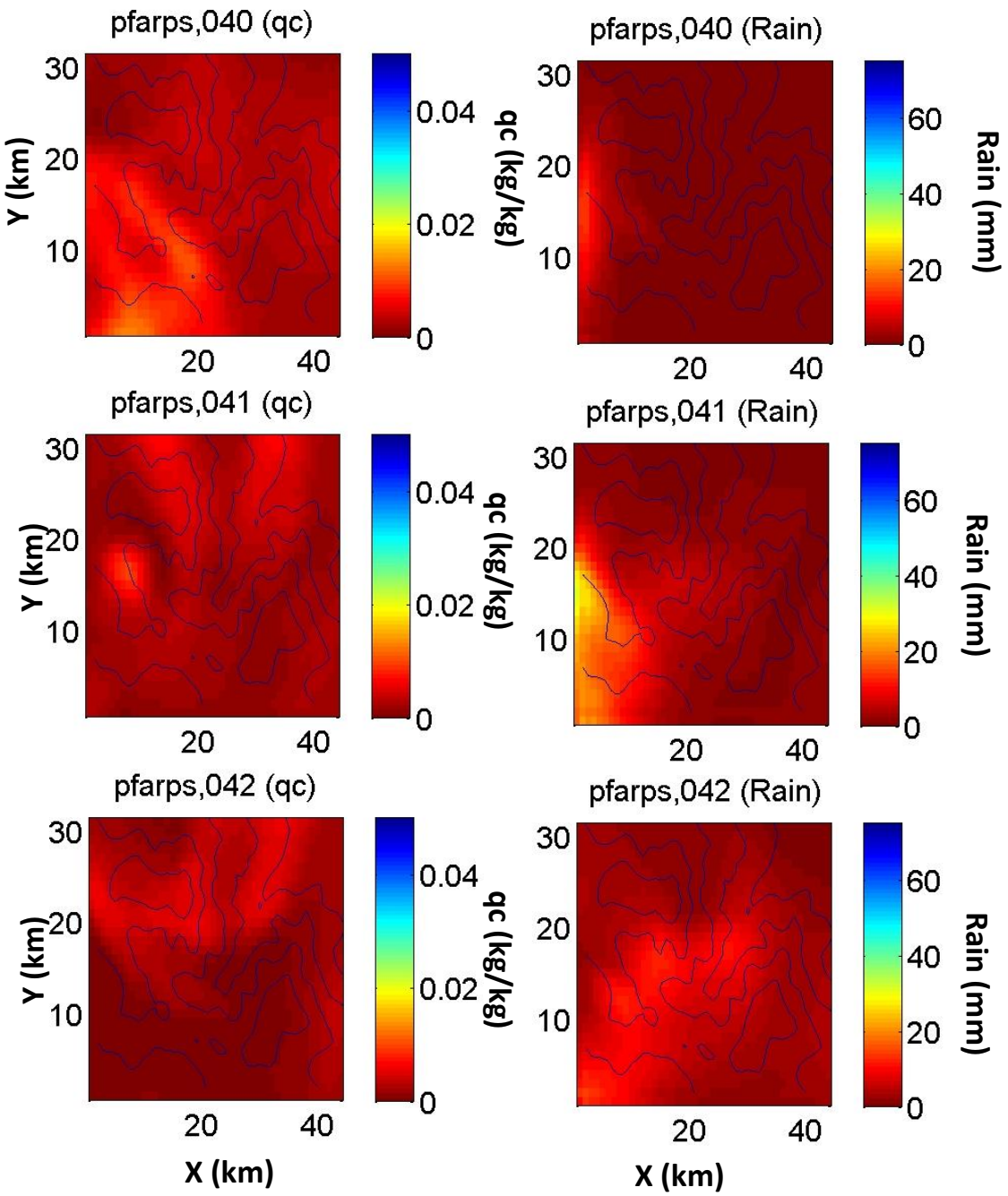


**Figure C8**: Cloud water mixing ratio (qc) and hourly rainfall for the pfarps simulation case at 11am, 12 and 1 pm on June 26$^{th}$ (40, 41, and 42 hours of simulation). Contour lines show terrain.

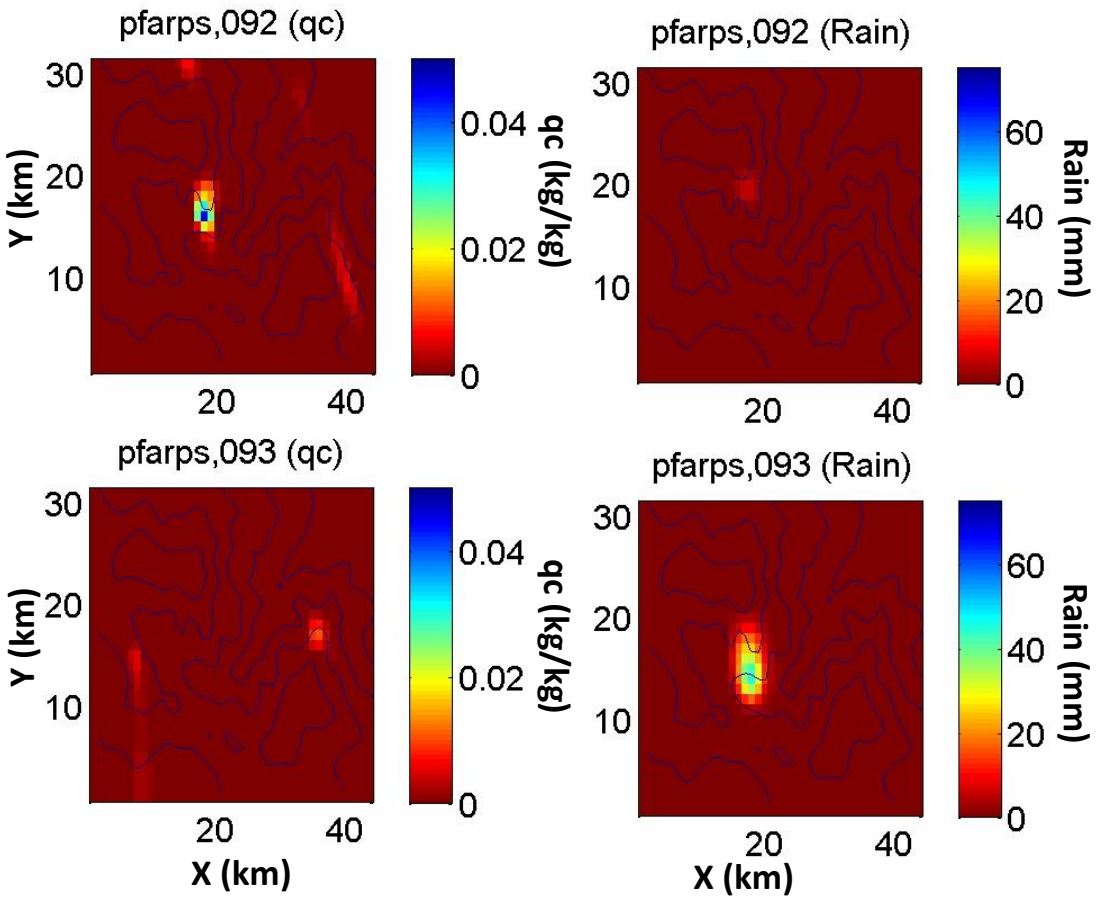


**Figure C9**: Cloud water mixing ratio (qc) and hourly rainfall for the pfarps simulation case at 3 and 4pm on June 28th (92 and 93 hours of simulation). Contour lines show terrain.

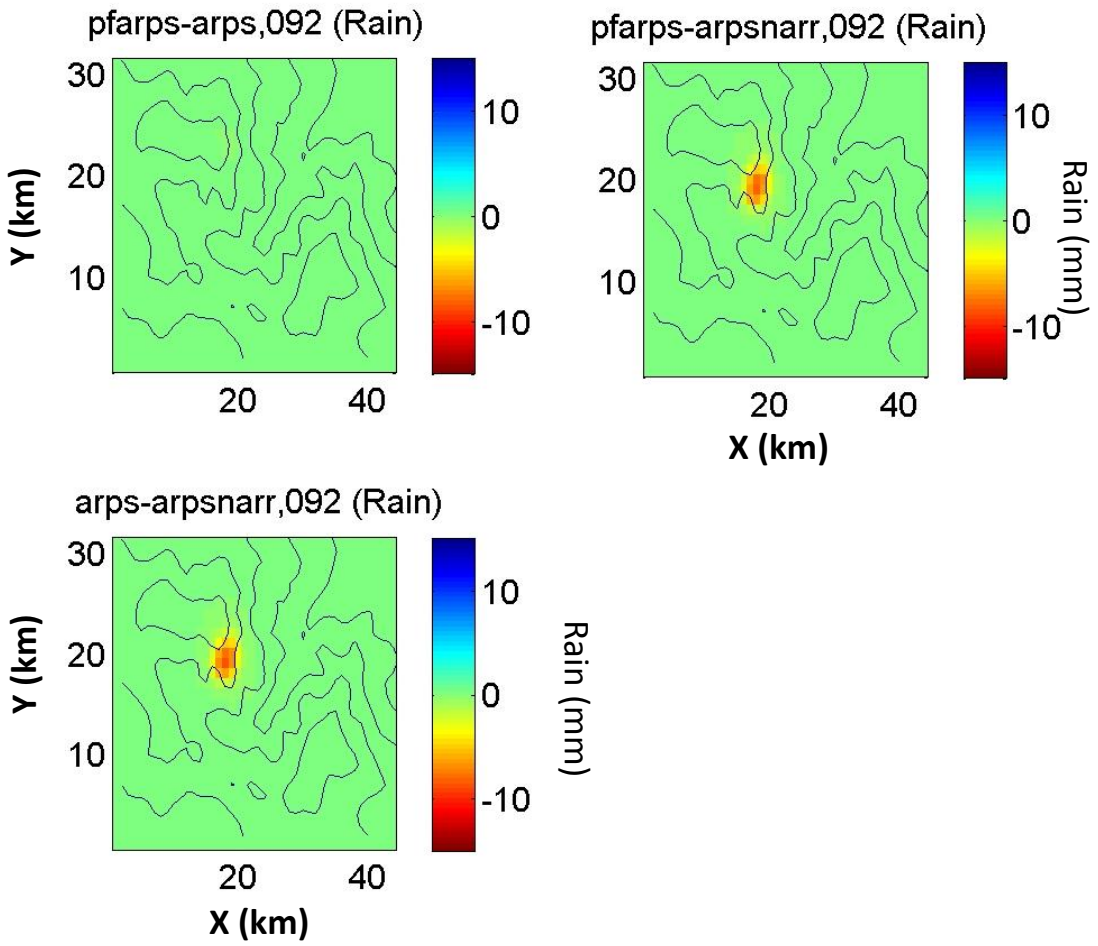


**Figure C10**: Differences in rainfall between the three simulation cases at 3pm on June 28th. Contour lines show terrain.

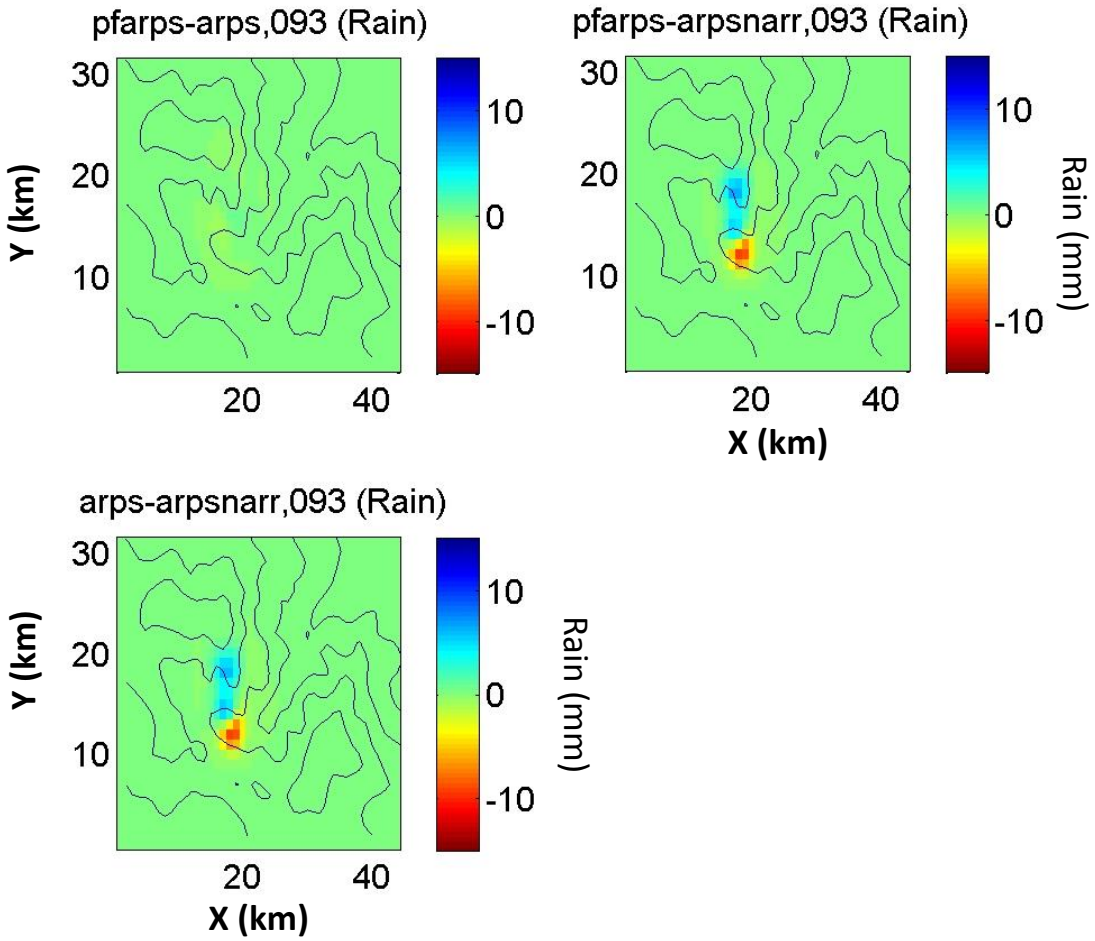


**Figure C11**: Differences in rainfall between the three simulation cases at 4pm on June 28th. Contour lines show terrain.